Time Reversal Optical Tomography and Decomposition Methods for Detection and Localization of Targets in Highly Scattering Turbid Media

by

Binlin Wu

A dissertation submitted to the Graduate Faculty in Physics in partial fulfillment of the requirements for the degree of Doctor of Philosophy, The City University of New York

2013

This manuscript has been read and accepted for the
Graduate Faculty in Physics in satisfaction of the
dissertation requirement for the degree of Doctor of Philosophy.

Professor Swapan K. Gayen

Date — Chair of Examining Committee

Professor Steven G. Greenbaum

Date — Executive Officer

Prof. Paul Gottlieb (CCNY Pathobiology)

Prof. Feng-Bao Lin (CCNY Civil Engineering)

Prof. Vladimir Petricevic (CCNY Physics)

Prof. Min Xu (Fairfield University Physics)
Supervisory Committee

THE CITY UNIVERSITY OF NEW YORK

Abstract

Time Reversal Optical Tomography and Decomposition Methods for Detection and Localization of Targets in Highly Scattering Turbid Media

By

Binlin Wu

Advisor: Professor S. K. Gayen

New near-infrared (NIR) diffuse optical tomography (DOT) approaches were developed to detect, locate, and image small targets embedded in highly scattering turbid media. The first approach, referred to as time reversal optical tomography (TROT), is based on time reversal (TR) imaging and multiple signal classification (MUSIC). The second approach uses decomposition methods of non-negative matrix factorization (NMF) and principal component analysis (PCA) commonly used in blind source separation (BSS) problems, and compare the outcomes with that of optical imaging using independent component analysis (OPTICA). The goal is to develop a safe, affordable, noninvasive imaging modality for detection and characterization of breast tumors in early growth stages when those are more amenable to treatment.

The efficacy of the approaches was tested using simulated data, and experiments involving model media and absorptive, scattering, and fluorescent targets, as well as, "realistic human breast model" composed of *ex vivo* breast tissues with embedded tumors. The experimental arrangements realized continuous wave (CW) multi-source probing of samples and multi-

detector acquisition of diffusely transmitted signal in rectangular slab geometry. A data matrix was generated using the perturbation in the transmitted light intensity distribution due to the presence of absorptive or scattering targets. For fluorescent targets the data matrix was generated using the diffusely transmitted fluorescence signal distribution from the targets. The data matrix was analyzed using different approaches to detect and characterize the targets.

The salient features of the approaches include ability to: (a) detect small targets; (b) provide three-dimensional location of the targets with high accuracy (~within a millimeter or 2); and (c) assess optical strength of the targets. The approaches are less computation intensive and consequently are faster than other inverse image reconstruction methods that attempt to reconstruct the optical properties of every voxel of the sample volume. The location of a target was estimated to be the weighted center of the optical property of the target. Consequently, the locations of small targets were better specified than those of the extended targets. It was more difficult to retrieve the size and shape of a target. The fluorescent measurements seemed to provide better accuracy than the transillumination measurements. In the case of *ex vivo* detection of tumors embedded in human breast tissue, measurements using multiple wavelengths provided more robust results, and helped suppress artifacts (false positives) than that from single wavelength measurements. The ability to detect and locate small targets, speedier reconstruction, combined with fluorophore-specific multi-wavelength probing has the potential to make these approaches suitable for breast cancer detection and diagnosis.

Dedicated to my parents,

my brothers Bintong, Binhao, and Binmeng,

my wife Xin Gao, and my son Maxwell (Yiu-Yiu)

谨献给我的父母

兄弟彬童、彬豪、彬蒙

妻子高新

及儿子优优

Acknowledgement

First, I would like to thank my advisor, Professor S. K. Gayen for his great support, guidance and comprehensive trainings from many aspects. He has provided me with the greatest help during my research and preparation of this dissertation. He has inspired and motivated me in pursing PhD degree and preparing for my future career. He has been teaching me how to do experiments, how to think as a physicist, how to write articles etc. He taught me the WAY to do things, and used himself as an example. It is very inspiring for me to see how carefully he handles experiments, analyzes data, evaluates results or problems, and writes articles. Particularly, I appreciate very much all the times that he worked with me so closely on the papers for hours and hours. I will always remember that. I can remember the path through which I was elevated from a new person to an "expert" in the field. Prof. Gayen is my advisor, beyond thesis. I would like to thank Prof. Gayen for his caring, and great help during all those difficult times.

I would also like to thank Dr. M. Alrubaiee, Dr. W. Cai, and Prof. M. Xu for all the trainings and discussions. Without the great help from them, there is no way I have made it here. Dr. Alrubaiee has given me hands-on training on experiments from day one since I joined the group. Dr. Xu's earlier work gave me formative education in this field. He has always been there to help proceed. I must give my special thanks to Dr. Cai. The original idea of TROT which is the major project in my dissertation was Dr. Cai's. I didn't find my direction in my research until I encountered this project.

I would like to thank Prof. Vladimir Petricevic, Prof. Prof. Feng-Bao Lin, Prof. Prof. Paul Gottlieb, and Prof. Min Xu for serving in my committee. I thank all of former and current ISUL fellows who have helped me in this work. I thank Ms. C.-H. Liu, Mr. G.-C.

Tang, Dr. X. Ni, Dr. Y. Pu, Dr. W. Wang, and Prof. R. R. Alfano for all the helps and useful discussions. I thank Mr. Yuri Bondasky, Dr. Alexei Bykov, Dr. Uladzimir Kartazayeu, Dr. Bidyut Das, Dr. Mikhail Yu. Sharonov and Dr. Alvin Katz for the help in experiments and useful discussions. I thank Dr. K. Sutkus, Ms. Joan Brijlall and Ms. Lauren Gohara for help every day in the group. I thank Ms. Sue Turner and Ms. Tonia Johnson for help in the department. I thank Mr. Daniel Moy, current executive officer of the GC physics program Prof. Steven Greenbaum, former executive officer Prof. Sultan Catto, and Prof. Brian Schwartz for the great helps in all these years during my PhD study. I thank Dr. Jason Koutcher, Dr. Ellen Ackerstaff, Mr. Mihai Coman (passed away), Ms. Mihaela Lupu, Dr. Ronald G. Blasberg, Dr. Inna Serganova, Dr. Pat Zanzonico, Ms. Valerie Longo for the trainings at Memorial Sloan Kettering Cancer Center (MSKCC). I would also like to thank my former fellows and Professors at Hunter College. I would like to thank Prof. Gregory Foster for the trainings and being my advisor for less than two years before he left Hunter. I thank Ms. Diane Rock and Ms. Patricia Harris for the help in arranging my teaching at Hunter. I thank Prof. Y. C. Chen and Prof. G. Gumbs at Hunter College, Prof. R. Khuri at Baruch College and Prof. V. P. Nair at City College for the helps in my study and teaching. I thank Dr. F. Kong, Dr. J. Xiao, Dr. L. Liu and Dr. Y. Zhou at Hunter College for helping me in my living since I first came to US. I thank my long-time friend and old classmate, Qiang Zhang for the help in everything.

After all these years pursuing my PhD degree, I have learned many other things besides physics. In particular, one is “big”, and the other, “small”. “Big” is for big picture. Without paying attention to the “big”, it is risky. I certainly have learned lessons for that

from my experience at Hunter College and IUSL. “Small” is for details. Success is in the details. This is one of the key things that have helped me make achievements.

I especially thank my families, including my wife Xin Gao, mom Zhiyu Yu, dad Jinsheng Wu, and brothers Bintong, Binhao, Binmeng for all the love, support, help and understandings. I also thank my wife’s parents and brother for their support and understanding.

My last thanks and love go to my precious, sweetheart, one-and-a-half-year-old son, Maxwell (Yiu-Yiu).

Financial support for this research was in part provided by US Army Medical Research and Materiel Command (USAMRMC) under Contract No. W81XWH-07-1-0454.

Time Reversal Optical Tomography and Decomposition Methods for Detection and Localization of Targets in Highly Scattering Turbid Media

Table of Contents

Abstract

Acknowledgements

Table of Contents

List of Tables

List of Figures

Chapter 1 Introduction 1

1.1. Introduction 1

1.2. Thesis statement 3

1.3. Background 4

1.3.1. Light propagation through turbid media 4

1.3.2. Optical imaging of breast cancer 9

1.3.3. Diffusion approximation and forward and inverse problems 12

1.3.4. Time reversal optical tomography 18

1.3.5. Decomposition methods based diffuse optical tomography 19

1.4. Thesis organization 19

References 21

Chapter 2 Time reversal optical tomography: locating small absorptive and scattering targets 31

2.1. Introduction 31

2.2. Theoretical formalism 33

2.2.1. Diffusion approximation, perturbation method and response matrix 33

2.2.2. Point spread functions 36

2.2.3. Time reversal and MUSIC 37

2.2.3.1. Well-resolved targets 38

2.2.3.2. Poorly-resolved targets and MUSIC 40

2.3. Algorithm 43

2.4. Testing TROT with simulated data 45

2.5. Testing TROT with experimental data 49

2.5.1. Experimental materials and methods 49

2.5.2. Data Processing and Analysis 51

2.5.3. Results 54

2.5.3.1. Single absorptive target at different depths 54

2.5.3.2. Resolving two absorptive targets 58

2.5.3.3. Single scattering target at different depths 61

2.6. Illumination and detection schemes 63

2.6.1. Noise 64

2.6.2. Results 68

2.7. Discussion 72

References 74

Chapter 3 Time reversal optical tomography: retrieval of properties of targets in turbid media 80

3.1. Introduction 80

3.2. Theoretical formalism 82

3.3. Simulations 88

3.3.1. Singular value decomposition and determination of signal subspace 89

3.3.2. Localization, property and size retrieval using simulated data 96

3.3.2.1. Single absorptive target 98

3.3.2.2. Single scattering target 102

3.3.2.3. Two absorptive targets 106

3.4. Experiments 111

3.4.1. Absorptive targets 111

3.4.2. Scattering target 119

3.5. Discussions 121

References 122

Chapter 4 Diffuse optical imaging using matrix decomposition methods 124

4.1. Introduction 124

4.2. Theoretical Formalism 125

4.2.1. Blind Source Separation problem 125

4.2.2. Diffuse optical imaging problem for absorptive and scattering targets 126

4.2.3. DOI as a BSS problem 127

4.2.4. Decomposition Methods 128

4.2.4.1. Independent Component Analysis (ICA) 129

4.2.4.2. Principal Component Analysis (PCA) 129

4.2.4.3. Nonnegative Matrix Factorization (NMF) 130
4.2.5. Backprojection 131
4.3. Simulative Study of Decomposition Methods 133
4.3.1. One absorptive target and one scattering target with ~ 4-cm separation 133
4.3.1.1. ICA Analysis 134
4.3.1.2. PCA Analysis 136
4.3.1.3. NMF Analysis 137
4.3.1.4. Results and discussions 138
4.3.2. One absorptive target and one scattering target with 2-cm separation 139
4.3.3. Two absorptive targets with 2-cm separation 144
4.3.4. Imaging extended targets 146
4.4. Experiments 158
4.4.1. Experimental materials and methods 158
4.4.2. Experimental Results 160
4.4.2.1. Absorptive targets 160
4.4.2.2. Scattering targets 169
4.5. Discussion 172
4.5.1. Computational complexity 172
4.5.2. Comparison of the decomposition methods 173
References 175
Chapter 5 Near-infrared optical imaging for detection of tumors in a "realistic model breast" 180
5.1. Introduction 180

5.2. Formalism 180

5.3. Experimental Methods and Materials 183

5.3.1. Experiments 183

5.3.1.1. NIR Imaging Experiments 183

5.3.1.2. MRI experiment 186

5.3.2. Analysis & Results 186

5.3.2.1. TROT analysis and results 186

5.3.2.2. NMF-OT and OPTICA analysis 190

5.3.2.3. MRI Results 197

5.4. Discussion 197

References 200

Chapter 6 Fluorescence imaging using time reversal optical tomography and non-negative matrix factorization 203

6.1. Introduction 203

6.2. Theoretical formalism 206

6.2.1. Fluorescence TROT 206

6.2.2. NMF-based Fluorescence Tomography 210

6.3. Experimental Materials and Methods 212

6.4. Analysis 216

6.4.1. Fluorescence TROT 217

6.4.2. NMF-based fluorescence tomography 217

6.5. Results 219

6.5.1. Single target 219

6.5.1.1. Fluorescence TROT 219

6.5.1.2. NMF-based fluorescence tomography 221

6.5.2. Two targets 225

6.5.2.1 Fluorescence TROT 225

6.5.2.2 NMF-based fluorescence tomography 230

6.6. Discussion 236

References 241

Chapter 7 Summary and Future work 246

7.1. Summary 246

7.2. Future work 246

Appendix A TROT Computer Program 249

Appendix B PCA and NMF based computer programs 257

Appendix C List of Patents, Publications and Presentations 271

Bibliography 274

List of Tables

2.1. Eigenvalues, pseudo spectrum and the corresponding positions. 48

2.2. Pseudo values associated with absorptive and scattering components at the peak position 55

2.3. Positions of one absorptive target located at different depths 56

2.4. Positions of two targets separated by different distances 61

2.5. Positions of one scattering target located at different depths 63

2.6. SDDS TROT retrieved target information 68

2.7. DSSD TROT retrieved target information 70

3.1. Retrieved optical absorption strength and FWHM of the pseudo spectrum with 0 noise 93

3.2. Retrieved optical absorption strength and FWHM of the pseudo spectrum with 20% additive Gaussian noise 96

3.3. Optical strength and size of an absorptive target 101

3.4. Optical strength and size of a scattering target 105

3.5. Optical strength and size of two absorptive targets 108

3.6. Retrieved target locations using 13 eigenvectors 115

3.7. Retrieved target locations using 2 eigenvectors 115

3.8. Retrieved optical strengths of the two targets 116

3.9. Estimated size and absorption coefficient of the targets 117

4.1. Positions and optical strengths retrieved using ICA, PCA and NMF algorithms 139

4.2. Positions and optical strengths retrieved using simulated data and ICA, PCA and NMF algorithms for one absorptive and one scattering point targets 143

4.3. Positions and optical strengths retrieved using simulated data and ICA, PCA and NMF algorithms for two absorptive point targets 146

4.4. Retrieved and known positions and absorption strength of the $2 \times 2 \times 2$ mm^3 target 151

4.5. Retrieved and known positions and absorption strength of the $10 \times 10 \times 10$ mm^3 target 151

4.6. Retrieved and known positions and absorption strength of the $20 \times 20 \times 20$ mm^3 target 151

4.7. FWHMs retrieved from the cross section images using ICA, PCA and NMF 157

4.8. Retrieved positions of the absorptive targets using ICA, PCA and NMF algorithms 163

4.9. FWHMs retrieved from the cross section images using ICA, PCA and NMF 166

4.10. Retrieved positions of the absorptive targets using ICA, PCA and NMF 168

4.11. Retrieved positions of the scattering targets using ICA, PCA and NMF algorithms 171

5.1. Coordinates (x, y, z) of the tumors retrieved by TROT 190

5.2. Target positions retrieved by NMF-OT and OPTICA 193

5.3. Estimated positions and dimensions of the targets using cross-section images 196

6.1. Known and TROT-retrieved target positions 220

6.2. TROT retrieved optical strength of the target 221

6.3. Known and NMF retrieved target positions 222

6.4. Known and NMF-retrieved optical strengths of the targets 222

6.5. Estimated target size using FWHM of the cross-section image of the targets 225

6.6. Known and retrieved target positions 227

6.7. Retrieved optical strengths of the targets 230

6.8. Known and NMF retrieved target positions 233

6.9. Retrieved optical strengths of the targets 233

6.10. Estimated target size using FWHM of the cross-section image of the targets 236

List of Figures

1.1. Absorption spectra of main constituents in human breast tissue: oxy-hemoglobin (HbO_2), deoxy-hemoglobin (Hb), fat, and water (H_2O). 7

1.2. Transmission spectrum of a 3 mm thick normal breast tissue sample showing absorption resonances of oxy-hemoglobin (1), fat (2), and water (3) superimposed on the losses due to scattering. 8

1.3. Anatomy of a female breast 10

2.1. (a) A plot of first twenty (20) eigenvalues on logarithmic scale. (b-e) 2-*D* slices of the pseudo spectrum on z = 9 mm, 15 mm, 21 mm, and 31 mm planes, respectively, showing the location of the six targets, where z = 21 mm shows a zoomed-in image of three difficult targets described in the text. 46

2.2. A schematic diagram of the experimental arrangement for imaging objects embedded in a turbid medium. (Key: CCD = charge coupled device, PC = personal computer) Inset (below) shows the 2-*D* array in the input plane that was scanned across the incident laser beam, and inset (right) shows a typical raw image. 51

2.3. A semi-log plot of eigenvalue spectrum with first 40 leading eigenvalues for the target at z = 30 mm. 54

2.4. Pseudo image of the target (left pane) and corresponding spatial intensity profiles (right pane) when the target is located at z = 30 mm: (a) experimental data; (b) simulation without any added noise; and (c) simulation with 20% Gaussian noise added. The pseudo values are calculated using Eq. (2.20). 57

2.5. (Experiment): TROT generated cross-section pseudo images when the targets are separated by 27.6 mm, 17.6 mm, and 12.6 mm are shown in (a), (c) and (e), 60

respectively; and pseudo-value profiles through the right target along *x*, *y* and *z* directions are shown in (b), (d) and (f), respectively. (Simulation): TROT generated cross-section pseudo image when two targets are separated by 12.6 mm is shown in (g) and the corresponding pseudo-value profiles are plotted in (h). In simulation 10% Gaussian noise is added for comparison with the experimental results. *P* is pseudo value calculated using Eq. (2.20).

2.6. Pseudo image of the target (a) and corresponding spatial intensity profiles (b) when the target is located at z = 30 mm: (a) and (b) experimental data; (c) and (d) simulation with 20% Gaussian noise added. *P* is pseudo value calculated using Eq. (2.20). 62

2.7. (a), (c) and (e) are the three singular components on the detector plane retrieved by SVD from simulated data with additive noise; (b), (d) and (f) are the corresponding components on the source plane. 65

2.8. (a), (c) and (e) are the three components on the detector plane with multiplicative noise; (b), (d) and (f) are the corresponding components on the source plane. 66

2.9. The singular values retrieved by SVD from simulative data with the presence of (a) additive and (b) multiplicative noise, respectively. 67

3.1. (a) and (b) are singular value spectra plotted in linear and logarithmic scales. 90

3.2. The pseudo images of the target generated using pseudo spectrum with 1, 3 and 100 eigen components shown in linear scale in (a), (c) and (e), respectively; and in log scale in (b), (d) and (f), respectively. (g) and (h) are the actual images of the point target and 20 mm × 20 mm target, respectively, for comparison. 91

3.3. Singular value spectrum in linear scale (a) and logarithmic scale (b). 94

3.4. The pseudo images of the target generated using 1, 3, 6 and 100 eigen components shown in linear scale in (a), (c), (e) and (g), respectively; and in logarithmic scale in (b), (d), (f) and (h), respectively. 95

3.5. (a) and (b) are singular value spectrum in linear and logarithmic scales respectively. (c) and (d) are axial and sagittal pseudo images of the absorptive target in logarithmic scale. (e) shows the isosurface for the "plateau" in the pseudo image (logarithmic scale). No noise was added to the simulated data. 99

3.6. (a) and (b) are singular value spectrum in linear and logarithmic scales respectively. (c) and (d) are axial and sagittal pseudo images of the absorptive target in logarithmic scale. (e) shows the isosurface for the FWHM in the pseudo image (logarithmic scale). (f) is the isosurface found using the local contour method in Eq. (3.6). 20% noise was added to the simulated data. 100

3.7. (a) and (b) are singular value spectrum in linear and logarithmic scales respectively. (c) and (d) are axial and sagittal pseudo images of the scattering target in logarithmic scale. (e) shows the isosurface for the FWHM in the pseudo image (logarithmic scale). No noise was added to the simulated data. 103

3.8. (a) and (b) are singular value spectrum in linear and logarithmic scales respectively. (c) and (d) are axial and sagittal pseudo images of the scattering target in logarithmic scale. (e) shows the isosurface for the FWHM in the pseudo image (logarithmic scale). (f) is the isosurface found using Eq. (3.6). 20% noise was added to the simulated data. 104

3.9. (a) and (b) are singular value spectrum in linear and logarithmic scales respectively. 107
(c) and (d) are sagittal pseudo images (logarithmic scale) of the two targets, respectively. (e) is the axial pseudo image (logarithmic scale) of the two targets at *z* = 20 mm. (f) shows the isosurface generated using the FWHM in the pseudo image.

3.10. (a) and (b) are singular value spectra in linear and logarithmic scales, respectively. 109
(c) and (d) are sagittal pseudo images (logarithmic scale) of the two targets, respectively. (e) is the axial pseudo image (logarithmic scale) of the two targets at *z* = 20 mm. (f) shows the isosurface generated using the FWHM in the pseudo image. (g) is the isosurface generated using the “local contour” method.

3.11. (a) and (b) are singular value spectrum in linear and logarithmic scales respectively. 112
(c) and (d) are pseudo images of the two targets generated using 2 eigen components and 13 eigen components, respectively. (e) shows the isosurface generated using the FWHM in the pseudo image. (f) is the isosurface generated using the “local contour” method.

3.12. (a) and (b) are singular value spectrum in linear and logarithmic scales respectively. 113
(c) and (d) are pseudo images of the two targets generated using 2 eigen components and 13 eigen components, respectively. (e) shows the isosurface generated using the FWHM in the pseudo image. (f) is the isosurface generated using the “local contour” method.

3.13. (a) and (b) are singular value spectrum in linear and logarithmic scales respectively. 114
(c) and (d) are pseudo images of the two targets generated using 2 eigen components and 13 eigen components, respectively. (e) shows the isosurface

generated using the FWHM in the pseudo image. (f) is the isosurface generated using the “local contour” method.

3.14. (a) and (b) are singular value spectrum in linear and logarithmic scales respectively. (c) and (d) are pseudo images of the two targets generated using 1 eigen component and 8 eigen components, respectively. (e) shows the isosurface generated using the FWHM in the pseudo image (logarithmic scale). (f) is the isosurface generated using the “local contour” method. 119

4.1. Light intensity distribution on the detector plane is recorded when a point source scans on the source plane. 134

4.2. ICA-based imaging of one absorbing and one scattering target ~4-cm apart: ICA extracted two-dimensional intensity distribution on the detector plane of: (a) the centrosymmetric component, (e) and (g) dumb-bell shaped components of the scattering target; and (i) the absorptive target. Similar intensity distribution on the source plane of: (b) the centrosymmetric, (f) and (h) dumb-bell shaped components of the scattering target, and (j) the absorptive target for comparison. Fits to the spatial intensity profiles on the detector plane along the white dashed line (shown in figures) of the centrosymmetric components of the scattering target are shown in (c), and that of the absorptive target is shown in (k). Corresponding fits to spatial profiles on the source plane are displayed in (d) and (l), respectively. 135

4.3. A logarithmic plot of the first 20 PCA eigenvalues 136

4.4. PCA-based imaging of one absorbing and one scattering target ~4-cm apart: PCA extracted two-dimensional intensity distribution on the detector plane of: (a) the 137

centrosymmetric component, (e) and (g) dumb-bell shaped components of the scattering target; and (i) the absorptive target. Similar intensity distribution on the source plane of: (b) the centrosymmetric, (f) and (h) dumb-bell shaped components of the scattering target, and (j) the absorptive target for comparison. Fits to the spatial intensity profiles on the detector plane along the white dashed line (shown in figures) of the centrosymmetric components of the scattering target are shown in (c), and that of the absorptive target is shown in (k). Corresponding fits to spatial profiles on the source plane are displayed in (d) and (l), respectively.

4.5. NMF-based imaging of one absorbing and one scattering target ~4-cm apart: NMF-extracted two-dimensional intensity distribution on the detector plane of: (a) the centrosymmetric component of the scattering target; (e) the absorptive target; and the corresponding distribution on the source plane of: (b) the centrosymmetric component of the scattering target; (f) the absorptive target. Fits to the corresponding spatial intensity profiles along the dashed line (shown in figures) are shown in (c), (d), (g) and (h), respectively. 138

4.6. ICA-based imaging of one absorbing and one scattering target 2-cm apart: ICIDs on the detector plane of (a) the absorptive target; (c) the centrosymmetric component; (e) and (g) dumb-bell shaped components of the scattering target; and the corresponding ICIDs on the source plane of: (b) the absorptive target; (d) the centrosymmetric component; (f) and (h) dumb-bell shaped components of the scattering target. 140

4.7. PCA-based imaging of one absorbing and one scattering target 2-cm apart: and 141

PCIDs on the detector plane of: (a) the absorptive target; (c) the centrosymmetric component; (e) and (g) dumb-bell shaped components of the scattering target; and the corresponding PCIDs on the source plane of: (b) the absorptive target; (d) the centrosymmetric component; (f) and (h) dumb-bell shaped components of the scattering target.

4.8. NMF-based imaging of one absorbing and one scattering target 2-cm apart: NCIDs on the detector plane of: (a) the absorptive target; (c) the centrosymmetric component of the scattering target; and the corresponding NCIDs on the source plane of: (b) the absorptive target; (d) the centrosymmetric component. 142

4.9. ICA-based imaging of two absorbing target 2-cm apart: (a) and (c) are the two ICIDs on the detector plane for the two targets. (b) and (d) are the two corresponding ICIDs on the source plane for the two targets. 144

4.10. PCA-based imaging of two absorbing target 2-cm apart: (a) and (c) are the two PCIDs on the detector plane for the two targets. (b) and (d) are the two corresponding PCIDs on the source plane for the two targets. 145

4.11. NMF-based imaging of two absorbing target 2-cm apart: (a) and (c) are the two NCIDs on the detector plane for the two targets. (b) and (d) are the two corresponding NCIDs on the source plane for the two targets. 145

4.12. ICA-based imaging of one $2 \times 2 \times 2$ mm^3 absorptive target: (a), (c) and (e) are the three ICIDs on the detector plane for the target. (b), (d) and (f) are the three corresponding ICIDs on the source plane for the target. 147

4.13. PCA-based imaging of one 2 × 2 × 2 mm^3 absorptive target: (a), (c) and (e) are the three PCIDs on the detector plane for the target. (b), (d) and (f) are the three corresponding PCIDs on the source plane for the target. 148

4.14. NMF-based imaging of one 2 × 2 × 2 mm^3 absorptive target: (a) and (b) are the NCIDs for the target on the detector plane and source plane, respectively. 149

4.15. ICA-based imaging of one 10 × 10 × 10 mm^3 absorptive target: (a), (c) and (e) are the three ICIDs on the detector plane for the target. (b), (d) and (f) are the three corresponding ICIDs on the source plane for the target. 149

4.16. PCA-based imaging of one 10 × 10 × 10 mm^3 absorptive target: (a), (c) and (e) are the three PCIDs on the detector plane for the target. (b), (d) and (f) are the three corresponding PCIDs on the source plane for the target. 150

4.17. NMF-based imaging of one 10 × 10 × 10 mm^3 absorptive target: (a) and (b) are the NCIDs for the target on the detector plane and source plane, respectively. 150

4.18. *L*-curve for back-projection of ICID, where *x* axis is the residue norm $||X_j(\boldsymbol{q} - \boldsymbol{q}_s, \boldsymbol{q}_s) - G_d(\boldsymbol{q} - \boldsymbol{q}_s)\,\chi_j(\boldsymbol{q})\,G^*(\boldsymbol{q}_s)||$ derived from Eq. (4.11a), and *y* axis is the solution norm $||\chi_j(\boldsymbol{q})||$. 152

4.19. (a) and (c) are cross-section images through the target, generated using the regularization parameter corresponding to the "corner" of the *L*-curve, and an optimized regularization parameter, respectively. (c) and (d) are the corresponding profiles through the maxima in the cross-section images. 153

4.20. (a) and (c) are cross-section images through the target, generated using the PCID and NCID. (c) and (d) are the corresponding profiles through the maxima in the cross-section images. 154

4.21. (a), (c) and (e) are cross-section images through the target generated using ICID, PCID, and NCID. (b), (d) and (f) are the corresponding profiles through the maxima in the cross-section images. 155

4.22. (a), (c) and (e) are cross-section images through the target generated using ICID, PCID, and NCID. (b), (d) and (f) are the corresponding profiles through the maxima in the cross-section images. 156

4.23. A schematic diagram of the experimental arrangement used for imaging objects embedded in a turbid medium. The inset at the bottom shows the 2D array in the input plane that was scanned across the incident laser beam; and the inset to the right shows a typical raw image recorded by the CCD. (CCD = charge coupled device, PC = personal computer) 159

4.24. ICA-based imaging of two absorptive targets ~5-cm apart: ICA-generated ICIDs on the detector plane are shown in (a) and (c) for target 1 and 2, respectively; corresponding Green's function fits to the horizontal spatial profiles through the dashed lines are shown in (b) and (d) for target 1 and 2, respectively. ICIDs on the source plane are shown in (e) and (g) for target 1 and 2, respectively; corresponding Green's function fits to the horizontal spatial profiles through the dashed line are shown in (f) and (h) for target 1 and 2, respectively. 161

4.25. PCA-based imaging of two absorptive targets ~5-cm apart: PCIDs on the detector plane are shown in (a) and (c) for target 1 and 2, respectively; and corresponding Green's function fits to the horizontal spatial profiles through the dashed line are shown in (b) and (d) for target 1 and 2, respectively. 162

4.26. NMF-based imaging of two absorptive targets ~5-cm apart: NCIDs on the detector plane are shown in (a) and (c) for target 1 and 2, respectively; corresponding Green's function fits to the horizontal spatial profiles through the dashed line are shown in (b) and (d) for target 1 and 2, respectively. 163

4.27. (a) and (c) are cross-section images of the two targets, respectively, generated using back-projection of ICIDs. (b) and (d) are the profiles through the maxima in the cross-section images, respectively. 164

4.28. (a) and (c) are cross-section images of the two targets, respectively, generated using back-projection of PCIDs. (b) and (d) are the profiles through the maxima in the cross-section images, respectively. 165

4.29. (a) and (c) are cross-section images of the two targets, respectively, generated using back-projection of NCIDs. (b) and (d) are the profiles through the maxima in the cross-section images, respectively. 165

4.30. ICA-based imaging of two absorptive targets 4-cm apart: (a) and (c) are the two ICIDs on the detector plane; (b) and (d) are the two ICIDs on the source plane. 167

4.31. PCA-based imaging of two absorptive targets 4-cm apart: (a) and (c) are the two PCIDs on the detector plane; (b) and (d) are the two PCIDs on the source plane. 167

4.32. NMF-based imaging of two absorptive targets 4-cm apart: (a) and (c) are the two NCIDs on the detector plane; (b) and (d) are the two NCIDs on the source plane. 168

4.33. ICA-based imaging of two scattering targets 4-cm apart: ICA-generated ICIDs on the detector plane are shown in (a) and (c); corresponding Green's function fits to the horizontal spatial profiles through the dashed line are shown in (b) and (d). 169

4.34. PCA-based imaging of two scattering targets 4-cm apart: PCIDs on the detector plane are shown in (a) and (c); corresponding Green's function fits to the horizontal spatial profiles through the dashed line are shown in (b) and (d). 170

4.35. NMF-based imaging of two scattering targets 4-cm apart: NCIDs on the detector plane are shown in (a) and (c); corresponding Green's function fits to the horizontal spatial profiles through the dashed line are shown in (b) and (d). 170

5.1. (a) Schematic diagram of the experimental arrangement. (Key: BC = beam collimator, CCD = charge coupled device, M = mirror.) Inset below shows the expanded view of the source (input) plane with the scanning grid points. (b) Photographs of the source plane (left) showing the scanned area, and detection plane (right) of the model breast sample. (c) (Upper pane) A typical raw CCD image of the detection plane, and how it is cropped and binned for analysis. 184

5.2. (a) and (c) are TROT-generated pseudo images at the z = 20.5 mm and 18.5 mm for the left and right tumors, respectively, using 750 nm; (b) and (d) are profiles of the pseudo image through the target along x(-), y(--) and z(-.) directions. 187

5.3. (a) and (c) are TROT-generated pseudo images for the left and right tumors using 800 nm; (b) and (d) are profiles of the pseudo image through the target along x(-), y(--) and z(-.) directions. 187

5.4. (a) and (c) are TROT-generated pseudo images for the left and right tumors using 830 nm; (b) and (d) are profiles of the pseudo image through the target along x(-), y(--) and z(-.) directions. 188

5.5. (a) The raw image which shows the tape placed on the exit surface of the sample. (b) TROT-generated pseudo image at z = 39 mm which the neighbor plane of the detector plane using 800 nm. 189

5.6. (a) and (c) are TROT-generated pseudo images for the left and right tumors using all three wavelengths; (b) and (d) are pseudo value profiles through the target along x(-), y(--) and z(-.) directions. 189

5.7. (a) and (c) are NCIDs of the left and right targets, respectively on the detector plane, for 750-nm measurements. (b) and (d) are Green's function fits of the profiles through the white lines. (e) and (f) are the corresponding NCIDs for the left and right targets, respectively on the source plane. 191

5.8. (a) and (c) are ICIDs of the left and right targets respectively on the detector plane, for 750-nm measurements. (b) and (d) are Green's function fits of the profiles through the white lines. 192

5.9. (a) and (c) are NCIDs of the left and right targets, respectively on the detector plane, for 800-nm measurements, and (b) and (d) are the corresponding ICIDs. 192

5.10. (a) and (c) are NCIDs of the left and right targets, respectively on the detector plane, for 830-nm measurements, and (b) and (d) are the corresponding ICIDs. 193

5.11. (a) and (c) are cross-section images of the left and right targets, respectively generated using backprojection of the NCIDs; (b) and (d) are the profiles through the maximum in the images, whose FWHMs are used to estimate the target dimensions. 194

5.12. (a) and (c) are cross-section images of the left and right targets, respectively generated using backprojection of the ICIDs; (b) and (d) are the profiles through the maximum in the images, whose FWHMs are used to estimate the target dimensions. 195

5.13. Magnetic resonance images of the left tumor and the right tumor pieces (LT: left tumor, RT: right tumor) 197

6.1. Multi-detector acquisition of fluorescence (wavelength, λ_m) intensity distribution on the detector plane following multi-source illumination (wavelength, λ_x) of the source plane of the sample. 205

6.2. (a) A schematic diagram of the experimental arrangement for imaging objects embedded in a turbid medium. [Key: NB = narrow band pass filter (830 nm), TS = translational stage, CCD = charge coupled device, PC = personal computer, SP = source plane, DP = detector plane] Inset (below) shows the 2-*D* array in the input plane that was scanned across the incident laser beam, and a typical raw image is shown in the PC monitor. (b) The absorption and fluorescence spectra of ICG in water. (c) A typical raw image detected by the CCD camera is cropped and binned. 213

6.3. Room-temperature (a) absorption spectrum, and (b) fluorescence spectrum of 1μM ICG aqueous solution. 214

6.4. TROT-reconstructed image at z = 30.5 mm using *fluorescence* data is shown in (a), and at z = 29.5.mm using transmission data shown in (b). 219

6.5. (a) and (b) are NCIDs retrieved from the fluorescence data corresponding to the target on the detector and source planes, respectively; (c) and (d) are least squares fits to the spatial profiles along the white dashed lines in (a) and (b), respectively. 221

6.6. (a) is the cross-section images at the z = 29.9 cm plane. (b) is the spatial profiles of the cross-sectiona image along the x and y directions shown by the white lines. 223

6.7. (a) and (b) are NCIDs retrieved from the transmission data corresponding to the target on the detector and source planes, respectively; (c) and (d) are least squares fits to the spatial profiles along the white dashed lines in (a) and (b), respectively. 224

6.8. (a) is the cross-section images at the z = 33.7 cm plane. (b) is the spatial profiles of the cross-sectiona image along the x and y directions shown by the white lines. 224

6.9. Eigenvalue spectrum of TR matrix 226

6.10. TROT-reconstructed pseudo image at z = 29.5 mm using *fluorescence* data. 226

6.11. TROT-reconstructed pseudo image at z = 29.5 mm using transmission data. 228

6.12. (a) and (b) are NCIDs corresponding to the left target on the detector plane and on the source plane, respectively; (c) and (d) are least squares fits to the spatial profiles along the white dashed lines in (a) and (b), respectively; (e) and (f) are NCIDs corresponding to the right target on the detector and source planes, respectively. 231

6.13. (a) and (b) are NCIDs corresponding to the left target on the detector and source planes, respectively; (c) and (d) are NCIDs corresponding to the right target on the detector and source planes, respectively. 232

6.14. (a) and (c) are cross sectional images at the z = 30.5 cm and 29.2 cm planes, respectively. (b) and (d) are spatial profiles of the cross sectional images along the x and y directions shown by the white lines. 234

6.15. (a) and (c) are cross sectional images at the z = 31.7 cm and 32.2 cm planes, respectively. (b) and (d) are spatial profiles of the cross sectional images along the x and y directions shown by the lines. 235

6.16. (a) The two curves show the peak values in the fluorescence signal using different ICG concentrations for the 1-cm-long and 2-cm-long fluorescent targets, respectively; (b), (c) and (d) show the fluorescence signal with ICG at concentrations of 20 nM, 50 nM, and 100 nM, respectively. 237

6.17. (a) shows measured fluorescence signal (o) and fitted curve (-) due to the ICG in the background medium at different concentrations. (b), (c) and (d) show different sections of the curve in (a). 239

Chapter 1

Introduction

1.1. Introduction

Optical imaging of targets embedded in a highly scattering turbid medium is an important area of contemporary research because of potential applications in a variety of areas, such as, detection of breast or prostate tumors in early growth stages, earth observation through cloud or fog cover, detection of mines in shallow coastal waters, underwater imaging, harbor defense, and military surveillance. [1-3] Of these, biomedical imaging using near-infrared (NIR) light has received particular attention for several reasons. First, commonly used biomedical imaging techniques, such as x-ray, computed tomography (CT), ultrasound, and magnetic resonance imaging (MRI) have important limitations. X-rays are high-energy radiation that could be harmful for prolonged exposure, and x-ray based methods cannot provide diagnostic information. Ultrasound provides structural information with inadequate spatial resolution and low specificity. MRI provides diagnostic information, but is often expensive. Optical imaging usually uses either visible or near-infrared non-ionizing light as the source. It is non-invasive, and may obtain spectral and functional information. It may be used for diagnosis if the spectral characteristics of the sample are obtained.

However, optical imaging of scattering medium, in particular, biological tissues has separate sets of challenges. In a biological tissue, light encounters wavelength-dependent absorption and strong scattering at all wavelengths, which lead to poor signal-to-noise ratio, as well as loss of phase coherence and polarization. As a consequence, distinct and sharp image of the targets may not be formed directly. Light propagation through optically-thick biological tissues involves

multiple scattering by tissue ultra-structures and may be treated as a diffuse transport problem. A commonly used theoretical framework for describing this light transport problem is provided by the radiative transport equation (RTE) [4], and for thick tissue, such as, a female human breast by the diffusion approximation (DA) [5-7] of RTE. The corresponding imaging approaches are commonly referred to as diffuse optical imaging (DOI) or diffuse optical tomography (DOT) [8-10]. DOI or DOT are image reconstruction approaches, also known as inverse image reconstruction (IIR) that make use of the knowledge of characteristics of the incident probing light, measurement of the diffusely propagating light emerging from the sample boundaries, average optical properties of the intervening medium, model for light propagation through the medium, and numerical algorithms to generate a map of the sample (such as, human breast) interior with targets (such as, tumor) appearing as localized inhomogeneities within the reconstructed sample volume.

The desired requirements of a useful and effective approach for optical breast imaging (also referred to as optical mammography) include ability to: (a) detect tumors at early development stages when those are small and more amenable to treatment; (b) provide location of the tumor and assessment of its size; (c) yield diagnostic information as to whether the tumor is malignant or benign. A number of continuous wave, frequency domain, and time-resolved experimental approaches and a variety of numerical algorithms have been developed over the years) [8-11]. Most of these approaches attempt to reconstruct optical properties of the sample, such as, scattering coefficient, absorption coefficient, anisotropy factor, and are computation intensive, and may not provide accurate target location. This thesis presents fast (less computation intensive) and accurate approaches for detection and localization of small targets.

1.2. Thesis statement

The objective of this thesis is to develop fast non-invasive diffuse optical imaging (DOI) modalities for detection, localization and potential diagnosis of tumors in human breast using near-infrared (NIR) light. Imaging of breast using light involves three components: experimental measurement of diffuse light that emerges from the breast when a part of it illuminated, theoretical model for light propagation through biological tissues, and numerical algorithms for identifying, locating, and characterizing the tumor. In this thesis, new novel diffuse optical imaging approaches are introduced and investigated using simulations and experiments. One approach is called time reversal optical tomography (TROT), which is an optical tomography method based on time reversal imaging and subspace-based algorithm. TROT is developed for imaging both point-like and extended targets in a highly scattering turbid medium. The other approach is optical imaging using decomposition methods. Decomposition methods including independent component analysis (ICA) [12-15], principal component analysis (PCA) [16, 17] and non-negative matrix factorization (NMF) [17-19] are thoroughly studied and compared. Three approaches are evaluated using simulations and transillumination experiments in which breast-simulating tissue phantom and *ex vivo* model human breast are used. The targets are considered as absorptive or scattering targets. For the experiment using human breast tissue, the results are compared to MRI images for validation.

All these methods are suited for fluorescence imaging [20-24]. Among the decomposition methods, NMF is particularly suited for fluorescence imaging, since the fluorescence signal is naturally positive and satisfies its non-negativity constraint. TROT and NMF-based fluorescence tomography approaches are developed, and tested in experiments using breast-simulating tissue phantom with embedded fluorescence targets.

The computational complexity of these methods is compared with other algorithms to prove that these alternative DOI methods are much faster than other model-based DOI methods.

1.3. Background

Since the DOI problem involves measurement of diffuse light on the boundary of a highly scattering turbid medium, such as human breast, in this section, the background knowledge about the key parameters of highly scattering media, particularly of human breast that determine the light propagation in the media are presented. The optical imaging methods that have been developed will be reviewed briefly, and the theoretical model for the diffusive optical imaging and the imaging approaches that we have developed will be introduced.

1.3.1. Light propagation through turbid media

When light propagates through a turbid medium, absorption and scattering process occur. Absorption [1] is the process when photons of appropriate energy are absorbed and cause atoms or molecules to make a transition from ground state to an excited state. Scattering [1] deviates light from incident direction. Multiple scattering randomizes the direction of the light propagation, as well as the phase and polarization. If the medium absorbs light, another process, fluorescence [25] may occur. Fluorescence is the process of photon emission that occurs when the atoms or molecules in an excited electronic state return to the ground state.

The optical properties of turbid media of concern are absorption length (l_a), scattering length (l_s) (also referred to as scattering mean free path), transport length (l_t) (also referred to as transport mean free path), and anisotropy factor (mean cosine of the angle of scattering), g. The absorption length (l_a) is the average distance a photon travels in the medium before it is absorbed, or the distance over which the intensity of the light source beam decreases to $1/e$ due to absorption. The length also depends on the chemical species, concentration and quantum yield

of the medium [26]. The absorption length is given by

$$l_a = 1/n\sigma_a \,, \tag{1.1}$$

where n is number density of the absorptive molecules, and σ_a is the effective absorption cross-section of the molecule. Another commonly used parameter directly related to absorption length is the absorption coefficient μ_a, the probability that a photon will be absorbed per unit length.

$$\mu_a = 1/l_a = n\sigma_a. \tag{1.2}$$

The scattering length (l_s) is the mean distance between scattering events and is inversely dependent on the density of the scattering particles and the scattering cross-section σ_s

$$l_s = 1/n\sigma_s \,, \tag{1.3}$$

where σ_s is the scattering cross-section. Another parameter that is directly related to l_s is scattering coefficient μ_s, the probability that a photon will be scattered per unit length.

$$\mu_s = 1/l_s = n\sigma_s. \tag{1.4}$$

σ_s depends on the shape and size of particles in comparison to the wavelength of the incident light and index of refraction with respect to the surrounding medium [27]. σ_s is given by the equation

$$\sigma_s = \int \sigma_d(\theta,\varphi)d\Omega = \int \sigma_d(\theta,\varphi)\sin\theta\, d\theta\, d\varphi. \tag{1.5}$$

where $\sigma_d(\theta,\varphi)$ is the differential scattering cross-section that describes how light scatters in the direction of (θ,φ) by a particle. For example, if the particle is much smaller than the incident wavelength, the light undergoes isotropic scattering, which is called Rayleigh scattering. Rayleigh scattering [27] is strongly dependent on wavelength. Rayleigh scattering due to molecules is described by

$$I = I_0 \frac{8\pi^4 N\alpha^2}{\lambda^4 R^2}(1+\cos^2\theta) \,, \tag{1.6}$$

where I_0 is the incident light intensity, N is the number of scatterers, α is the polarizability of the

molecules, λ is the wavelength, R is the distance between the detector and the particle and θ is the scattering angle. When the particle size is much larger than the incident wavelength, anisotropic scattering occurs, with more light scattered in the forward direction [28]. $\sigma_d(\theta,\varphi)$ depends strongly on the scattering angle θ when the dimension of the particle becomes close to the incident wavelength. In this case, the scattering is described by a solution to Maxwell's equations from Lorenz-Mie theory [29], which treats electromagnetic wave scatterers as spherical particles.

When light is incident on a particle whose index of refraction is different from the surrounding, the light is deflected at an angle. The angle depends on the size and shape of the particle, incident wavelength and angle of incidence. Each particle has a scattering profile or phase function $p(\theta, \varphi)$ [4, 30, 31] which describes the probability of a photon scattering into a unit solid angle oriented at an angle (θ, φ) relative to the original direction of the photon. The anisotropic scattering of light by a particle is characterized by the anisotropy factor g, which is a measure of the extent of forward direction retained after a single scattering event. g is calculated to be the mean cosine of the scattering directions,

$$g = <\cos\theta> = \frac{\int_{4\pi} p(\theta,\varphi)\cos\theta\, d\Omega}{\int_{4\pi} p(\theta,\varphi) d\Omega}\ , \tag{1.7}$$

or

$$g = \int_0^{\pi} p(\theta)\cos\theta\, 2\pi\sin\theta\, d\theta, \text{ where } \int_0^{\pi} p(\theta) 2\pi\sin\theta d\theta = 1. \tag{1.8}$$

So g is within (-1, 1). If $g < 0$, it is backward scattering; $g > 0$, forward scattering; and $g = 0$, isotropic scattering. The scattering property of a particle can also be described by the reduced scattering coefficient μ_s' that incorporates the scattering coefficient μ_s and anisotropy factor. μ_s' is the probability that a photon is scattered isotropically per unit length.

$$\mu_s' = (1 - g)\mu_s\ . \tag{1.9}$$

Since in a biological medium, light attenuation is due to both absorption and scattering when it propagates, the total attenuation $\mu_t = \mu_a + \mu_s'$ can be used to describe the probability that a photon will either be absorbed or scattered per unit length. For a highly scattering medium, $\mu_s' >> \mu_a$, $\mu_t \approx \mu_s'$, which is called the diffusive regime, in which scattering dominates.

The inverse of μ_s' is defined to be transport mean free path (or reduced scattering length)

$$l_t = 1/\mu_s', \tag{1.10}$$

which describes the average distance after which light completely loses memory of its initial direction before it is absorbed.

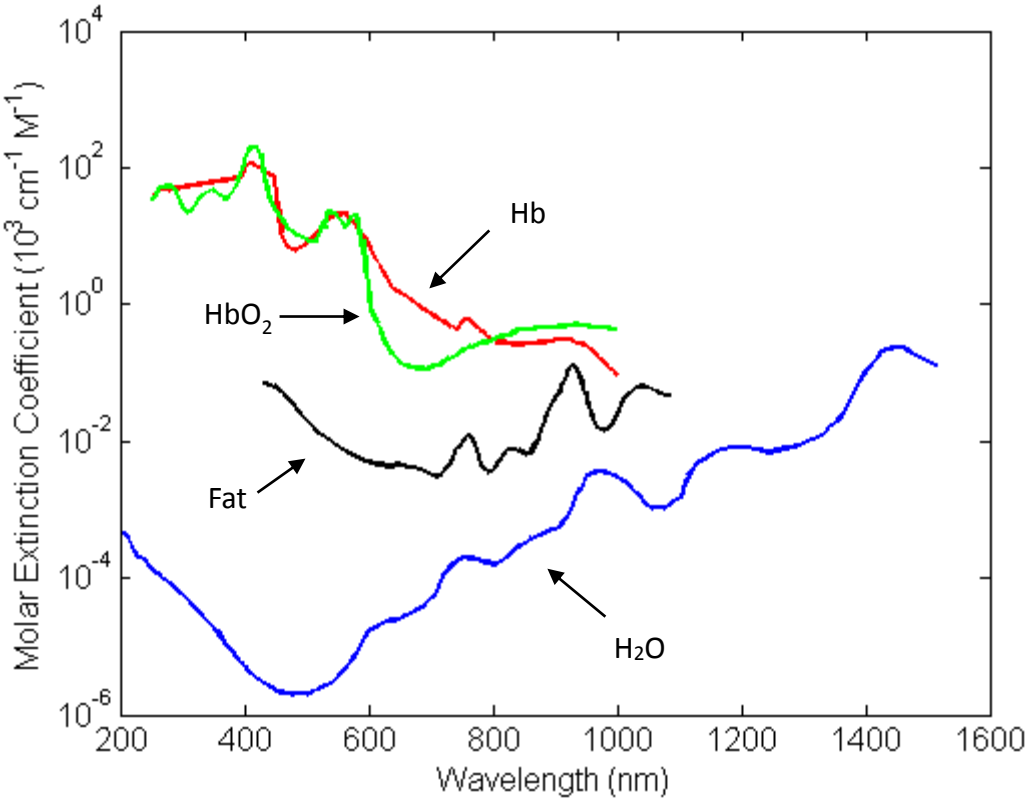

Fig. 1.1. Absorption spectra of main constituents in human breast tissue: oxy-hemoglobin (HbO_2), deoxy-hemoglobin (Hb), fat, and water (H_2O) (after Reference [33]).

In DOI, the contrast between the target and the scattering medium is based on the optical properties, such as, absorption, scattering and fluorescence of the sample. The image of a target may be generated when optical property of the target is different from the background medium.

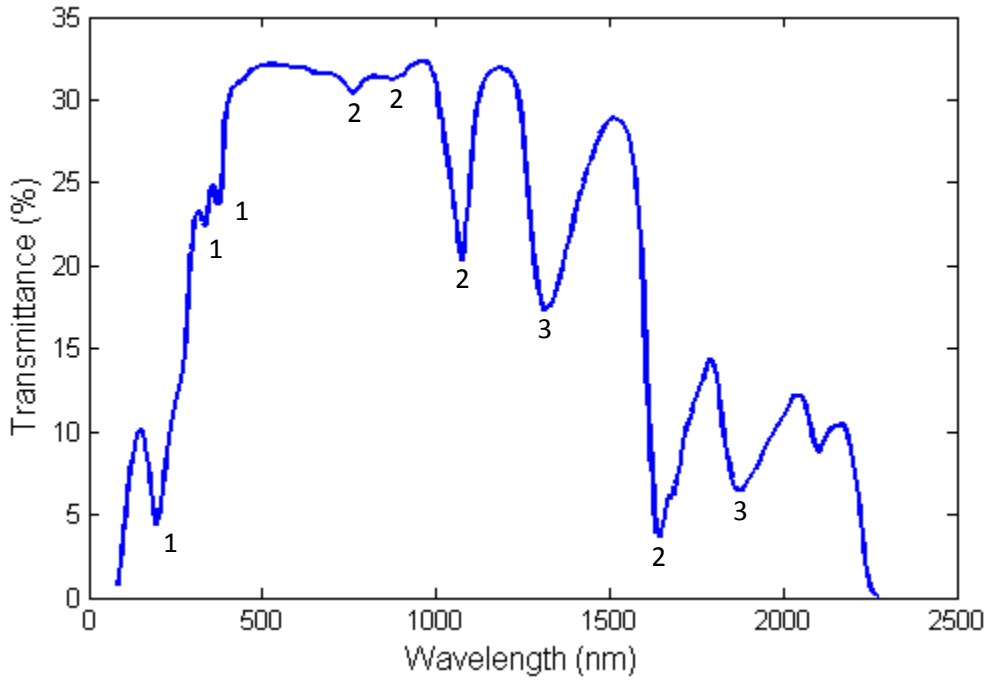

Fig. 1.2. Transmission spectrum of a 3 mm thick normal breast tissue sample showing absorption resonances of oxy-hemoglobin (1), fat (2), and water (3) superimposed on the losses due to scattering (after Reference [34]).

One main application of this work is breast cancer detection. Light may be used to measure different native parameters of tissue through which they travel, such as absorption, scattering, spectral characteristics, and fluorescence. However, due to strong absorption and scattering in biological tissue, the penetration distance of light is limited. In order to achieve good contrast and sensitivity in the optical imaging, a proper wavelength should be carefully chosen. For breast cancer detection, the illumination light with the ideal wavelength should be least absorbed or scattered by the normal breast tissue, which provides with the optimal penetration distance. Hemoglobin, proteins, water and fat are the main absorbing constituents in human breast tissue

[32]. They have their lowest absorption coefficient in the NIR region around 650 - 900 nm as shown in Fig. 1.1.

The transmission spectrum of normal breast tissue due to both absorption and scattering (Fig. 1.2) [34] also shows that the NIR window is ideally suited for *in vivo* imaging because of minimal light absorption by hemoglobin (<650 nm) and water (>900 nm).

The ideal illumination light should be absorbed or scattered at a significantly different level by the breast tumors than by the normal breast tissue for adequate contrast.

1.3.2. Optical imaging of breast cancer

Breast cancer incidence in women in the United States is 1 in 8 (about 12%). In 2013, an estimated 232,340 new cases of invasive breast cancer are expected to be diagnosed in women in the U.S., along with 64,640 new cases of non-invasive (*in situ*) breast cancer. About 39,620 women in the U.S. are expected to die in 2013 from breast cancer [35].

The female human breast is comprised of lobules, ducts and stroma as shown in Fig. 1.3 [35]. The lobules are the glands that produce milk inside the female breast. Ducts are the tiny tubes that carry the milk from the lobules to the nipple. Stroma are the fatty tissues and connective tissues surrounding the ducts and lobules, blood vessels, and the lymphatic vessels. The lymph (lymphatic) system is composed of lymph nodes that are collections of immune system cells that are connected by lymphatic vessels. The lymphatic vessels carry lymph outside the bloodstream away from the breast, which contains tissue fluid, waste products, and immune system cells.

Tumors in breast include two types, benign and malignant (cancerous). Benign breast tumors are breast tissues that undergo abnormal growths, but are not invasive, and do not spread to the surrounding normal tissue and outside the breast. Most lumps in breast turn out to be not cancerous (benign), and caused by fibrosis and/or cysts. However, malignant tumors are life

threatening. If malignant tumors are not detected and treated in time, the cancer cells may enter the lymphatic vessels, spread to and grow in the lymph nodes. These cancer cells may also spread to distant sites of the body through the lymphatic system or bloodstream system. So it is critical to detect cancer at its early growth stages, so that that treatment can be planned in time.

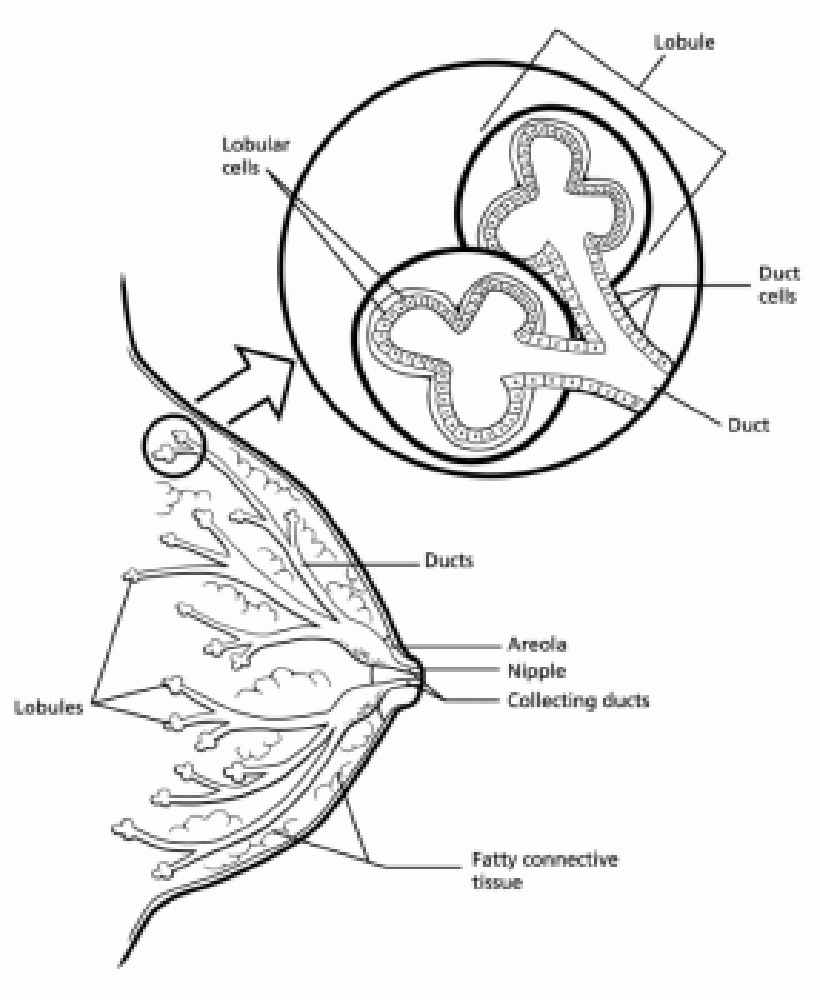

Fig. 1.3 Anatomy of a female breast (after Reference [35])

Currently used clinical techniques for detection of breast cancers include mammography, ultrasound tomography (ultrasonography), magnetic resonance imaging (MRI) etc. The drawbacks of these methods have been discussed in Section 1.1. In contrast, optical mammography as an affordable non-invasive modality could overcome these drawbacks, and has

attracted much attention over last two decades. It uses near infrared (NIR) light (wavelength range of 700 nm to 1300 nm) that is safe to human body. Optical imaging can provide functional information [36]. Optical spectroscopic information may be obtained which has potential for diagnosis, and for distinguishing normal, benign and cancerous tissues or tumors at different stages.

Cutler [37] first attempted optical mammography by transillumination of a female breast with a bright light source in a darkened room. He revealed that multiple scattering caused features below the surface to appear extremely blurred. Wist *et al.* [38] demonstrated the ability to observe 1.5-mm details through 6 mm of breast-equivalent scattering phantoms. They also demonstrated for the first time that images of internal structures such as lesions in a tissue thicker than 1cm could be obtained. This field has since been developed [3, 8, 9, 39, 40] over the last decades with the development of broadly tunable NIR lasers, highly sensitive detectors, charge coupled device (CCD) cameras, amplitude modulation schemes, and image reconstruction algorithms. Based on the techniques and algorithms that have been sufficiently developed, optical mammography systems attempt to use the diffuse light in frequency domain, time domain or steady-state continuous wave (CW) mode to obtain two-dimensional (2-*D*) projection images, or three dimensional (3-*D*) tomographic images of the breast using proper image reconstruction algorithms. Such techniques are referred to as diffuse optical tomography (DOT). A DOT method typically illuminates a boundary of a sample, such as human breast with a tumor inside using near-infrared (NIR) light. The illumination beam or fluorescence emitted by fluorescent targets propagates through the sample and is measured on the boundary of the sample. Different analytical or stochastic models have been used to describe the light propagation through a turbid medium. Then light intensity distribution measured on the sample boundary is used along with

the knowledge of the source and a proper forward model to reconstruct the image of the targets. The forward and inverse problems will be further explained in the next section.

1.3.3. Diffusion approximation and forward and inverse problems

Different ways are available to describe light scattering in turbid media including wave theory and transport theory. Wave theory starts with Maxwell's equation, while the transport theory which is also called radiative transfer theory deals directly with the transport of power through turbid media [41, 42]. In highly scattering media, such as biological media, light propagation is a stochastic random process. Both phase and amplitude of light vary randomly. Phases are considered to be uncorrelated on scales larger than the transport mean free path (l_t), *i.e.* light loses its coherence. Radiative transfer theory has been widely used to describe light scattering in random media containing particles, with a Boltzmann-type transport equation, or radiative transfer equation (RTE). RTE can be written as [5, 8, 43, 44]

$$\frac{\partial}{c_m \partial t}\Phi(\boldsymbol{r},\boldsymbol{s},t) + \hat{s}\cdot\nabla\,\Phi(\boldsymbol{r},\boldsymbol{s},t) + (\mu_a+\mu_s)\Phi(\boldsymbol{r},\boldsymbol{s},t) = S(\boldsymbol{r},\boldsymbol{s},t) + \mu_s \int p(\boldsymbol{s},\boldsymbol{s}')\Phi(\boldsymbol{r},\boldsymbol{s},t)d^2\boldsymbol{s}' \,, \tag{1.12}$$

where $\Phi(\boldsymbol{r}, \boldsymbol{s}, t)$, the specific intensity, is the photon distribution function; c_m is the light speed in the medium; μ_a and μ_s are the absorption and scattering coefficients respectively. $p(\boldsymbol{s},\boldsymbol{s}')$ is the phase function that represents the probability of scattering into a direction $\boldsymbol{s}'$ from $\boldsymbol{s}$. $S(\boldsymbol{r}, \boldsymbol{s}, t)$ is the radiation source term. The diffusion approximation (DA) of the RTE is widely used for light propagation in highly scattering media. The DA approach is based on the fact that after undergoing a large number of scatterings, the multiply scattered light has lost its phase information, and coherence, so that any interference effect in the medium can be neglected [45]. As a result, only the light intensity needs to be considered for the propagation of light [46]. The diffusion equation due to a pulse point light source is [5, 43]

$$\frac{\partial}{c_m \partial t}\Phi(\boldsymbol{r},t) - D\nabla^2\Phi(\boldsymbol{r},t) + \mu_a\,\Phi(\boldsymbol{r},t) = q_0(\boldsymbol{r},t)\,, \tag{1.13}$$

where $q_0(\boldsymbol{r}, t) = \delta(\boldsymbol{r})\delta(t)$ represents the impulse incident source at $t = 0$ and position $\boldsymbol{r} = 0$, $D = l_t/3$ is the diffusion coefficient.

When a short light pulse is scattered as it propagates, the propagating light consists of early portion (ballistic and snake-like) and diffusive portion. The diffusion equation can only describe the diffusive light, which falls in the diffusion regime, and cannot describe the early light. DA holds when the thickness of sample is at least $10l_t$ [44]. It can be an excellent approximation when z/l_t is large and the g factor is small. Analytical solutions to the DA exist only for a few simple geometries [43, 47-49], such as infinite, semi-infinite, infinite-slab, cylindrical and spherical geometries. An analytical solution to the diffusion equation when the source is a delta function is a Green's function, which may be used to derive other types of sources using convolution. The Green's function for diffusion approximation in an infinite medium is [43]

$$G(\boldsymbol{r},\boldsymbol{r}') = \frac{1}{4\pi D}\frac{\exp(-\kappa|\boldsymbol{r}-\boldsymbol{r}'|)}{|\boldsymbol{r}-\boldsymbol{r}'|}, \tag{1.14}$$

where $\boldsymbol{r}$ and $\boldsymbol{r}'$ are the positions of two points, $\kappa = [(\mu_a - i\omega/c_m)/D]^{1/2}$. The Green's function for a slab geometry is [13]

$$G(\boldsymbol{r},\boldsymbol{r}') = G(\rho,z,z') = \frac{1}{4\pi D}\sum_{k=-\infty}^{\infty}\left[\frac{\exp(-\kappa r_k^+)}{r_k^+} - \frac{\exp(-\kappa r_k^-)}{r_k^-}\right], \tag{1.15}$$

with an incident intensity-modulated illumination source of modulation frequency ω, where $r_k^{\pm} = [\rho^2 + (z \mp z' \pm 2kd)^2]^{1/2}$, $\rho = [(x-x')^2 + (y-y')^2]$ is the lateral distance between the two points $\boldsymbol{r} = (x, y, z)$ and $\boldsymbol{r}' = (x', y', z')$, $k = 0, \pm1, \pm2, \cdots$, and the extrapolated boundaries of the slab are located at $z = 0$ and $z = d = L_z + 2z_e$, respectively, where L_z is the physical thickness of the slab and the extrapolated length z_e is determined from the boundary condition of the slab.

Cai *et al.* has developed an analytical solution to the transport equation [42, 50-52] which

provides a more accurate description of photon distribution in space as well as photon velocity direction.

Since light becomes diffusive when it goes through a thick highly scattering turbid medium and, a direct shadow image cannot be formed for a target embedded in the scattering medium. Diffuse optical tomography (DOT) attempts to detect the target using the diffuse light that comes out from the boundary of the sample. Therefore, an inverse image reconstruction (IIR) technique is needed to reconstruct the image of the target. To implement an IIR method, a forward model is employed. A forward model calculates the photon density distribution when light propagates through the medium, with given sources, detectors, and the optical properties of the sample. The analytical solution to the diffusion equation may be used in the forward model if only simple geometry is involved. In this case, a perturbation approach may be used to describe the light propagation through a homogenous medium with localized small targets, and the optical properties of the targets are different from the background medium, so that the scattered light is considered to be the sum of the original unscattered light and the perturbation in the photon density distribution due to the targets. [43] However, since the analytical solution to the diffusion equation is limited to only a few simple geometries, other methods have also been used in the forward model, such as finite element method (FEM) [53, 54], finite difference method (FDM) [55-57], finite volume method (FVM) [58], and Monte Carlo methods [59-62]. These methods are not limited to the sample geometry.

DOT is an inverse image reconstruction (IIR) problem, which is ill-posed [8, 40, 63], that is, solutions obtained in the inverse problem usually lack stability with respect to small variation in the data. For IIR, it is difficult to converge to the “true solution” before it falls at a “local minimum” in the error (cost) function. Regularization is commonly employed [8] in the IIR to

improve the stability, such as Tikhonov regularization [64]. In principle, a general unique solution to the inverse problem for the Boltzmann equation or DOT does not exist [8, 40], due to the range of the unknowns, such as absorption coefficient, scattering coefficient, anisotropy, refractive index, coupling coefficients, geometry etc. But useful results may still be obtained in situations where unique solutions do not exist. Particularly, Arridge *et al.* discussed the uniqueness of diffusion equation, and showed that the absorption and scattering coefficients cannot be separated if intensity alone is acquired in continuous wave (CW) measurements, but they can be separated if it is measured in frequency domain. [8]

A variety of IIR methods have been developed to reconstruct a property map of the sample [8, 10, 40]. These include analytic methods such as direct inversion [65-67], and Fourier transform [68, 69]; or numerical image reconstruction methods including linear methods, such as, conjugate gradients, algebraic reconstruction technique (ART) and Newton methods, and non-linear methods such as Gauss-Newton method, gradient methods. Numerical methods that involve running the forward model iteratively and minimizing the difference between the calculated data using the forward model and the experimental data, are very time-consuming, particularly if Monte Carlo method is used as the forward model and billions of photons need to be simulated.

The perturbation approach is commonly used in the IIR process. In the perturbation approach, the targets are assumed to be localized weak inhomogeneities in a homogenous medium, with optical properties slightly different from the background. It is a non-linear inverse problem that uses the influence due to local perturbation in the optical properties to calculate the Jacobian of the forward model, and minimize the error norm [43]. For simplification, the problem is often linearized. Compared to the homogeneous background, the change in the

intensity due to the targets is linearized using the first order of Born approximation, or the change in the log intensity is linearized using Rytov approximation [40].

In our study, both approximations may be used. Here Born approximation is used. When illuminated by a point source of unit power, the light intensity perturbation on the detector plane (the sample surface where light exits and is collected by detector arrays such as a CCD camera) to the first order of Born Approximation can be written as [13, 43, 70]

$$\Delta\phi(\boldsymbol{r}_d, \boldsymbol{r}_s) = -\int G(\boldsymbol{r}_d, \boldsymbol{r})\delta\mu_a(\boldsymbol{r})c_m G(\boldsymbol{r}, \boldsymbol{r}_s)d\boldsymbol{r} - \int \delta D(\boldsymbol{r})c_m \nabla_{\boldsymbol{r}} G(\boldsymbol{r}_d, \boldsymbol{r}) \cdot \nabla_{\boldsymbol{r}} G(\boldsymbol{r}, \boldsymbol{r}_s)d\boldsymbol{r}, \tag{1.16}$$

where $\boldsymbol{r}_s$, $\boldsymbol{r}$, and $\boldsymbol{r}_d$ are the positions of the source, the inhomogeneity, and the detector, respectively; $\delta\mu_a = \mu_{a,obj} - \mu_a$ and $\delta D = D_{obj} - D$ are the differences in absorption coefficient and diffusion coefficient, respectively, between the inhomogeneity and the background; c_m is the speed of light in the medium; and $G(\boldsymbol{r}_d, \boldsymbol{r}_j)$ and $G(\boldsymbol{r}_j, \boldsymbol{r}_s)$ are Green's functions describing light propagation from an inhomogeneity to a detector and a source to the inhomogeneity respectively in the background turbid medium of absorption μ_a and diffusion coefficient D.

For absorptive inhomogeities, the j^{th} ($1 \le j \le J$) one contained in volume δV_j centered at $\boldsymbol{r}_j$, Eq. (1.16) can be re-written as [13]

$$-\Delta\phi(\boldsymbol{r}_d, \boldsymbol{r}_s) = \sum_{j=1}^{J} G(\boldsymbol{r}_d, \boldsymbol{r}_j)\tau_j G(\boldsymbol{r}_j, \boldsymbol{r}_s)\,, \tag{1.17}$$

where $\tau_j = \delta\mu_a(\boldsymbol{r}_j)c_m\delta V_j$, is the absorptive strength of the target.

For scattering inhomogeneities, the j'^{th} ($1 \le j' \le J'$) one contained in volume $\delta V_j'$ centered at $\boldsymbol{r}_j$, a similar form of the equation can be written [13],

$$-\Delta\phi(\boldsymbol{r}_d, \boldsymbol{r}_s) = \sum_{j=1}^{J'} g_z(\boldsymbol{r}_j, \boldsymbol{r}_d)\tau_j' g_z(\boldsymbol{r}_j, \boldsymbol{r}_s) +$$

$$\sum_{j=1}^{J'} \rho_{dj}\cos\theta_d g_\perp(\boldsymbol{r}_j, \boldsymbol{r}_d)\tau_j'\rho_{sj}\cos\theta_s\, g_\perp(\boldsymbol{r}_j, \boldsymbol{r}_s) +$$

$$\sum_{j=1}^{J'} \rho_{dj} \cos\theta_d g_\perp(\boldsymbol{r}_j, \boldsymbol{r}_d) \tau_j' \rho_{sj} \sin\theta_s \, g_\perp(\boldsymbol{r}_j, \boldsymbol{r}_s) \,, \tag{1.18}$$

where $\tau_j' = \delta D(\boldsymbol{r}_j) c_m \delta V_j'$, is the scattering strength. One small scattering inhomogeneity is a mixture of three components.

Though the ultimate goal of breast DOT is to generate images of breast cancer, with both high resolution and specificity, many applications require rather accurate determination of location of target(s) in three dimensions. For example, a recent study involving 35,319 patients underscores the influence of primary tumor location on breast cancer prognosis [71], and makes it imperative that DOT for breast cancer detection be able to obtain three-dimensional (3-*D*) location of the tumor. While two-dimensional (2-*D*) IIR approaches may provide only lateral positions, 3-*D* IIR approaches attempt to retrieve all three position coordinates of the target(s). Various frequency-domain, time-domain, and steady-state DOT approaches have addressed the target localization problem with different measures of success [8, 9, 40, 53, 63, 70, 72, 73]. Several groups have paid particular attention to retrieving target location. Kepshire *et al.* developed a subsurface DOT approach to obtain location information of absorbing and fluorescent targets, but observed the sensitivity to vary nonlinearly with depth [74]. Mohajerani *et al.* reported a fluorescent tomography method for locating fluorescent targets embedded in a heterogeneous medium using partitioning of the fluorophore distribution into an object subspace and a background subspace [75]. Godavarty *et al.* developed another fluorescent tomography approach that used a hemispherical breast phantom, near-infrared light-induced fluorescence from a contrast agent, and finite element method-based reconstruction algorithms to obtain target information up to a depth of 2 cm from breast phantom surface [76]. Zhao *et al.* introduced a layer-based sigmoid adjustment method to improve depth resolution of DOT and achieved positioning error within 3 mm for depths from 10 to 30 mm [77]. Optical tomography using

independent component analysis (OPTICA) approach developed by Xu *et al.* uses multi-source probing and multi-detector signal acquisition scheme and a numerical algorithm based on independent component analysis (ICA) of information theory to obtain 3-*D* position information of absorbing, scattering and fluorescent targets embedded in highly scattering turbid media, and "model breast" assembled using *ex vivo* human breast tissue [13-15, 78, 79]. Co-registration approaches that use another modality, such as, ultrasound, magnetic resonance imaging, and x-ray mammography for locating suspect areas and DOT for obtaining images have also been introduced [80-83]

This thesis develops two approaches for diffuse optical imaging. One approach is called time reversal optical tomography (TROT) based on time reversal symmetry and subspace-based algorithm that have been used for ultrasound and electromagnetic waves. The other approach is based on decomposition methods that use ICA, PCA and NMF algorithms of blind source separation (BBS) problem. These tomography approaches run faster than the regular model-based IIR methods. Most other model-based image reconstruction methods discretize the sample into voxels, and attempt to find the optical properties at every voxel in the sample through an iterative process that minimize the difference between the experimental measurements and calculated light intensities on the sample boundaries, which is time consuming. On the contrary, the approaches presented in this thesis mainly focus on localization of the targets, and attempt to find some characteristics about the targets.

1.3.4. Time reversal optical tomography

The multi-source illumination and multi-detector signal acquisition scheme is used. The light intensity distribution measured on the sample boundary is use to a form a data matrix. A so-called "time reversal matrix" [84, 85] is calculated which describes light propagation from the

sources through the medium and targets to the detectors and back from detectors to sources. An eigenvalue decomposition or singular value decomposition (SVD) is used to find the leading (principal) components that correspond to targets. Using a subspace-based method, multiple signal classification (MUSIC), a pseudo spectrum is calculated for all discretized voxels in the sample [85, 86]. The pseudo spectrum describes the likelihood of each voxel belonging to a target. The maxima in the pseudo spectrum are used to determine the positions of the targets. The pseudo spectrum is also used to estimate the dimension of the target. Though TROT can be used with various geometries (slab, cylindrical, semi-spherical etc.) and measurement domains (frequency domain, time domain, CW), transillumination slab geometry and CW laser are used in the study presented in this thesis.

1.3.5. Decomposition methods based diffuse optical tomography

The signal measured on the sample boundary is considered to be linear combination of component signals due to targets. The problem is treated as a blind source separation (BSS) problem. The experimental arrangement, uses multi-source probing and multi-detector signal acquisition. A decomposition method is used to analyze the data matrix and extract the component signals which directly correspond to light propagation from sources to targets or from targets to detectors. Decomposition methods including principal component analysis (PCA) and non-negative matrix factorization (NMF) and independent component analysis (ICA) are used and compared with each other. The component signals are then fitted to the Green's functions to retrieve the position and optical properties of the targets. Then the component signals are back projected to the axial (z) planes of the target to estimate the cross-section of the target.

1.4. Thesis organization

The thesis is organized as follows.

Chapter 2 introduces the Time Reversal Optical Tomography (TROT) approach, based on time reversal (TR) imaging and multiple signal classification (MUSIC) for point targets. This chapter is focused on localization of small targets, either absorptive or scattering, in turbid media. The efficacy of the approach is evaluated using both simulated and experimental data. The resolution of TROT is also examined for different source and detector arrangements using simulations.

In **Chapter 3**, TROT is further developed to retrieve optical strength and size of absorptive and scattering targets.

Chapter 4 introduces the decomposition methods that treat DOI as a blind source separation (BSS) problem. Various BSS methods (matrix decomposition methods) including independent component analysis (ICA), principal component analysis (PCA), and non-negative matrix factorization (NMF) are used to separate signals due to different targets and the background, which are then fitted to Green's functions to retrieve position, optical strength and cross sectional area of the targets.

Chapter 5 presents the results of an experimental study of a realistic model breast assembled using *ex vivo* breast tissue with two pieces of breast tumors embedded. TROT and NMF-based optical tomography (NMF-OT) approach are used for detection of the targets. Multiple datasets are acquired with source beams at different wavelengths to test if the use of multiple wavelengths can result in any improvement in the efficacy of TROT and NMF-OT.

Chapter 6 explores fluorescence optical imaging using experiments and relevant simulation. The sample consists of a highly scattering medium with two fluorescent targets embedded. Both TROT and NMF approaches are extended to detect and characterize the fluorescent targets. Transmission data are also acquired in the experiments, and analyzed for comparison.

Chapter 7 summarizes the results and outlines the future work that can build on the developments presented in this thesis.

References

1. A. Ishimaru, *Wave Propagation and Scattering in Random Media* (Academic Press, New York, 1978).
2. S. K. Gayen, and R. R. Alfano, "Emerging optical biomedical imaging techniques," Opt. Photonics News **7**, 22 (1996).
3. S. K. Gayen, and R. R. Alfano, "Sensing lesions in tissues with light," Opt. Express **4**, 475 (1999).
4. S. Chandrasekhar, *Radiative Transfer* (Clarendon, Oxford, 1950).
5. M. S. Patterson, B. Chance, and B. C. Wilson, "Time resolved reflectance and transmittance for the noninvasive measurement of tissue optical properties," Appl. Opt. **28**, 2331-2336 (1989).
6. A. Ishimaru, "Diffusion of a pulse in densely distributed scatterers," J. Opt. Soc. Am. A **68**, 1045-1050 (1978).
7. K. Furutsu, "On the diffusion equation derived from the space-time transport equation," J. Opt. Soc. Am. A **70**, 360-366 (1980).
8. S. R. Arridge, "Optical tomography in medical imaging," Inverse Probl. **15**, R41-R93 (1999).
9. S. R. Arridge, and J. C. Hebden, "Optical imaging in medicine: II. Modelling and reconstruction," Phys. Med. Biol. **42** 841-853 (1997).
10. S. R. Arridge, and J. C. Schotland, "Optical tomography: forward and inverse problems," Inverse Probl. **25**, 123010 (2009).

11. J. C. Hebden, S. R. Arridge, and D. T. Delpy, "Optical imaging in medicine: I. Experimental techniques," Phys. Med. Biol. **42** 825-840 (1997).

12. A. Hyvärinen, J. Karhunen, and E. Oja, *Independent Component Analysis* (Wiley, New York, 2001).

13. M. Xu, M. Alrubaiee, S. K. Gayen, and R. R. Alfano, "Optical imaging of turbid media using independent component analysis: theory and simulation," J. Biomed. Opt. **10**, 051705 (2005).

14. M. Xu, M. Alrubaiee, S. K. Gayen, and R. R. Alfano, "Three-dimensional localization and optical imaging of objects in turbid media using independent component analysis," Appl. Opt. **44**, 1889-1897 (2005).

15. M. Xu, M. Alrubaiee, S. K. Gayen, and R. R. Alfano, "Optical diffuse imaging of an *ex vivo* model cancerous human breast using independent component analysis," IEEE J. Sel. Top. Quantum Electron. **14**, 43-49 (2008).

16. I. T. Jolliffe, *Principal Component Analysis* (Springer, New York, 1986).

17. B. Wu, M. Alrubaiee, W. Cai, M. Xu, and S. K. Gayen, "Diffuse optical imaging using decomposition methods," Int. J. Opt. **2012**, 185435 (2012).

18. D. D. Lee, and H. S. Seung, "Learning the parts of objects by non-negative matrix factorization," Nature **401**, 788-791 (1999).

19. M. W. Berry, M. Browne, A. N. Langville, V. P. Pauca, and R. J. Plemmons, "Algorithms and applications for approximate nonnegative matrix factorization," Comp. Stat. Data Anal. **52**, 155-173 (2007).

20. A. Corlu, R. Choe, T. Durduran, M. A. Rosen, M. Schweiger, S. R. Arridge, M. D. Schnall, and A. G. Yodh, "Three-dimensional *in vivo* fluorescence diffuse optical tomography of breast cancer in humans," Opt. Express **15**, 6696-6716 (2007).

21. A. Godavarty, M. J. Eppstein, C. Zhang, S. Theru, A. B. Thompson, M. Gurfinkel, and E. M. Sevick-Muraca, "Fluorescence-enhanced optical imaging in large tissue volumes using a gain modulated ICCD camera," Phys. Med. Biol. **48**, 1701-1720 (2003).

22. A. B. Milstein, S. Oh, K. J. Webb, C. A. Bouman, Q. Zhang, D. A. Boas, and R. P. Millane, "Fluorescence optical diffusion tomography," Appl. Opt. **42**, 3081-3094 (2003).

23. M. S. Patterson, and B. W. Pogue, "Mathematical model for time-resolved and frequency-domain fluorescence spectroscopy in biological tissues," Appl. Opt. **33**, 1963-1974 (1994).

24. V. Ntziachristos, and R. Weissleder, "Experimental three-dimensional fluorescence reconstruction of diffuse media by use of a normalized Born approximation," Opt. Lett. **26**, 893-895 (2001).

25. I. D. Campbell, and R. A. Dwek, *Biological Spectroscopy* (Benjamin/Cummins Publishing Co. Inc., California, 1984).

26. R. R. Alfano, S. K. Gayen, and A. Katz, "Advances in mediphotonic imaging and biopsy," IS&T/OSA Optics & Imaging in the Information Age **299** (1997).

27. L. Rayleigh, "On the scattering of light by small particles," Phil. Mag. **41**, 447 (1871).

28. M. I. Mishchenko, L. D. Travis, and A. A. Lacis, *Scattering, Absorption, and Emission of Light by Small Particles* (Cambridge University Press, 2002).

29. G. Mie, "Beitzrâge zur optik truber Medien, speziell kolloidaler Metalolsungen," Ann. Phys. **25**, 377 (1908).

30. A. Ishimaru, "Diffusion of light in turbid material," Appl. Opt. **28**, 2210 (1989).

31. S. L. Jacques, C. A. Alter, and S. A. Prahl, "Angular dependence of HeNe laser light scattering by human dermis," Lasers Life Sci. **1**, 309-333 (1987).

32. P. Taroni, G. Danesini, A. Torricelli, A. Pifferi, L. Spinelli, and R. Cubeddu, "Clinical trial of time-resolved scanning optical mammography at 4 wavelengths between 683 and 975 nm," J. Biomed. Opt. **9**, 464-473 (2004).

33. R. Weissleder, "A clearer vision for *in vivo* imaging," Nat. Biotechnol. **19**, 316-317 (2001).

34. F. A. Marks, "Optical determination of the hemoglobin oxygenation state of breast biopsies and human breast cancer xenografts in nude mice," Proc. SPIE **1641**, 227-237 (1992).

35. http://www.cancer.org/cancer/breastcancer/detailedguide/breast-cancer-key-statistics.

36. A. G. Yodh, and D. A. Boas, "Functional imaging with diffusing light," in *Biomedical Photonics*, T. Vo-Dinh, ed. (CRC Press, Boca Raton, 2003).

37. M. Cutler, "Transillumination as an aid in the diagnosis of breast lesions," Surg. Gynecol. Obstet. **48**, 721-729 (1929).

38. A. O. Wist, P. P. Fatouros, and S. L. Herr, "Increased spatial resolution in transillumination using collimated light," IEEE Trans. Med. Imaging **12**, 751-757 (1993).

39. W. R. Hendee, and E. R. Ritenour, *Medical Imaging Physics* (Wiley-Liss, 2002).

40. A. P. Gibson, J. C. Hebden, and S. R. Arridge, "Recent advances in diffuse optical imaging," Phys. Med. Biol. **50**, R1-R43 (2005).

41. M. Lax, V. Narayanamurti, and R. C. Fulton, "Classical diffusive photon transport in a slab," in *Proc. Symp. on Laser Optics and Condensed Matter*, J. L. Birman, H. Z. Cummins, and A. A. Kaplyanskii, eds. (Plenum, New York, 1987), pp. 229-235.

42. W. Cai, M. Lax, and R. R. Alfano, "Analytical solution of the polarized photon transport equation in an infinite uniform medium using cumulant expansion," Phys. Rev. E **63**, 016606 (2000).

43. S. R. Arridge, "Photon-measurement density functions. Part I: Analytical forms," Appl. Opt. **34**, 7395-7409 (1995).

44. K. M. Yoo, F. Liu, and R. R. Alfano, "When does the diffusion approximation fail to describe photon transport in random media?," Phys. Rev. Lett. **64**, 2647 (1990).

45. J. Crank, *The Mathematics of Diffusion* (Clarendon Press, Oxford, 1956).

46. M. Xu, "Optical image reconstruction in highly scattering media," (PhD Thesis, City University of New York, 2001).

47. X. D. Li, T. Durduran, A. G. Yodh, B. Chance, and D. N. Pattanayak, "Diffraction tomography for biochemical imaging with diffuse-photon density waves," Opt. Lett. **22**, 573-575 (1997).

48. D. A. Boas, M. A. O'Leary, B. Chance, and A. G. Yodh, "Scattering of diffuse photon density waves by spherical inhomogeneities within turbid media: analytic solution and applications," Proc. Natl. Acad. Sci. USA **91** 4887-4891 (1994).

49. S. R. Arridge, M. Cope, and D. T. Delpy, "The theoretical basis for the determination of optical pathlengths in tissue: temporal and frequency analysis," Phys. Med. Biol. **37** 1531-1559 (1992).

50. W. Cai, M. Xu, and R. R. Alfano, "Analytical form of the particle distribution based on the cumulant solution of the elastic Boltzmann transport equation," Phys. Rev. E **71**, 041202 (2005).

51. W. Cai, M. Lax, and R. R. Alfano, "Cumulant solution of the elastic Boltzmann transport equation in an infinite uniform medium," Phys. Rev. E **61**, 3871-3876 (2000).

52. W. Cai, X. Ni, S. K. Gayen, and R. R. Alfano, "Analytical cumulant solution of the vector radiative transfer equation investigates backscattering of circularly polarized light from turbid media," Phys. Rev. E **74**, 056605 (2006).

53. S. R. Arridge, M. Schweiger, M. Hiraoka, and D. T. Delpy, "A finite element approach to modeling photon transport in tissue," Med. Phys. **20**, 299-309 (1993).

54. S. R. Arridge, and M. Schweiger, "Photon-measurement density functions. Part 2: finite-element-method calculations," Appl. Opt. **34**, 841-853 (1995).

55. B. W. Pogue, M. S. Patterson, H. Jiang, and K. D. Paulsen, "Initial assessment of a simple system for frequency domain diffuse optical tomography," Phys. Med. Biol. **40** 1709-1729 (1995).

56. J. P. Culver, R. Choe, M. J. Holboke, L. Zubkov, T. Durduran, A. Slemp, V. Ntziachristos, B. Chance, and A. G. Yodh, "Three-dimensional diffuse optical tomography in the parallel plane transmission geometry: evaluation of a hybrid frequency domain/continuous wave clinical system for breast imaging," Med. Phys. **30**, 235-247 (2003).

57. A. H. Hielscher, A. D. Klose, A. K. Scheel, B. Moa-Anderson, M. Backhaus, U. Netz, and J. Beuthan, "Sagittal laser optical tomography for imaging of rheumatoid finger joints," Phys. Med. Biol. **49**, 1147-1163 (2004).

58. K. Ren, G. S. Abdoulaev, G. Bal, and A. H. Hielscher, "Algorithm for solving the equation of radiative transfer in the frequency domain," Opt. Lett. **29**, 578-580 (2004).

59. S. A. Prahl, M. Keijzer, S. L. Jacques, and A. J. Welch, "A Monte Carlo model of light propagation in tissue," in *SPIE Proceedings of Dosimetry of Laser Radiation in Medicine and Biology*, G. Mueller, and D. Sliney, eds. (1989), pp. 102-111.

60. L. Wang, and S. L. Jacques, "Hybrid model of Monte Carlo simulation and diffusion theory for light reflectance by turbid media," J. Opt. Soc. Am. A **10**, 1746-1752 (1993).

61. L. Wang, and S. L. Jacques, "Optimized radial and angular positions in Monte Carlo modeling," Med. Phys. **21**, 1081-1083 (1994).

62. L. Wang, S. L. Jacques, and L. Zheng, "MCML-Monte Carlo modeling of light transport in multi-layered tissues," Comput. Methods Programs Biomed. **47**, 131-146 (1995).

63. W. Cai, S. K. Gayen, M. Xu, M. Zevallos, M. Alrubaiee, M. Lax, and R. R. Alfano, "Optical tomographic image reconstruction from ultrafast time-sliced transmission measurements," Appl. Opt. **38**, 4237-4246 (1999).

64. A. N. Tikhonov, "Solution of incorrectly formulated problems and the regularization method," Soviet Math. Dokl. **4**, 1035-1038 (1963).

65. J. C. Schotland, "Continuous-wave diffusion imaging " J. Opt. Soc. Am. A **14**, 275-279 (1997).

66. J. C. Schotland, and V. A. Markel, "Inverse scattering with diffusing waves," J. Opt. Soc. Am. A **18**, 2767-2777 (2001).

67. V. A. Markel, and J. C. Schotland, "Symmetries, inversion formulas and image reconstruction for optical tomography," Phys. Rev. E **70**, 056616 (2004).

68. S. D. Konecky, G. Y. Panasyuk, K. Lee, V. Markel, A. G. Yodh, and J. C. Schotland, "Imaging complex structures with diffuse light," Opt. Express **16**, 5048-5060 (2008).

69. M. Xu, M. Lax, and R. R. Alfano, "Time-resolved Fourier optical diffuse tomography," J. Opt. Soc. Am. A **18**, 1535-1542 (2001).

70. M. A. O'Leary, D. A. Boas, B. Chance, and A. G. Yodh, "Experimental images of heterogeneous turbid media by frequency-domain diffusing-photon tomography," Opt. Lett. **20**, 426–428 (1995).

71. N. Kroman, J. Wohlfahrt, H. T. Mouridsen, and M. Melbye, "Influence of tumor location on breast cancer prognosis," Int. J. Cancer **105**, 542-545 (2003).

72. B. A. Brooksby, H. Dehghani, B. W. Pogue, and K. D. Paulsen, "Near-infrared (NIR) tomography breast image reconstruction with *a priori* structural information from MRI: algorithm development for reconstructing heterogeneities," IEEE J. Sel. Top. Quantum Electron. **9**, 199-209 (2003).

73. Y. Tao, Y. Wang, Y. Pei, W. Zhu, and R. L. Barbour, "Frequency-domain optical imaging of absorption and scattering distributions by a Born iterative method," J. Opt. Soc. Am. A. **14**, 325-342 (1997).

74. D. S. Kepshire, S. C. Davis, H. Dehghani, K. D. Paulsen, and B. W. Pogue, "Subsurface diffuse optical tomography can localize absorber and fluorescent objects but recovered image sensitivity is nonlinear with depth," Appl. Opt. **46**, 1669-1678 (2007).

75. P. Mohajerani, A. A. Eftekhar, and A. Adibi, "Object localization in the presence of a strong heterogeneous background in fluorescent tomography," J. Opt. Soc. Am. A **25**, 1467-1479 (2008).

76. A. Godavarty, A. B. Thompson, R. Roy, M. Gurfinkel, M. J. Eppstein, C. Zhang, and E. M. Sevick-Muraca, "Diagnostic imaging of breast cancer using fluorescence-enhanced optical tomography: phantom studies," J. Biomed. Opt. **9**, 488-496 (2004).

77. Q. Zhao, L. Ji, and T. Jiang, "Improving depth resolution of diffuse optical tomography with a layer-based sigmoid adjustment method," Opt. Express **15**, 4018-4029 (2007).

78. M. Alrubaiee, M. Xu, S. K. Gayen, M. Brito, and R. R. Alfano, "Three-dimensional optical tomographic imaging of scattering objects in tissue-simulating turbid medium using independent component analysis," Appl. Phys. Lett. **87**, 191112 (2005).

79. M. Alrubaiee, M. Xu, S. K. Gayen, and R. R. Alfano, "Localization and cross section reconstruction of fluorescent targets in *ex vivo* breast tissue using independent component analysis," Appl. Phys. Lett. **89**, 133902 (2006).

80. A. Poellinger, J. C. Martin, S. L. Ponder, T. Freund, B. Hamm, U. Bick, and F. Diekmann, "Near-infrared laser computed tomography of the breast: first clinical experience," Acad. Radiol. **15** (2008).

81. V. Ntziachristos, A. G. Yodh, M. Schnall, and B. Chance, "Concurrent MRI and diffuse optical tomography of breast after indocyanine green enhancement," Proc. Natl. Acad. Sci. **97**, 2767-2772 (2000).

82. Q. Zhu, M. Huang, N. G. Chen, K. Zarfos, B. Jagjivan, M. Kane, P. Hedge, and S. H. Kurtzman, "Ultrasound-guided optical tomographic imaging of malignant and benign breast lesions - initial clinical results of 19 cases," Neoplasia **5**, 379-388 (2003).

83. A. Li, E. L. Miller, M. E. Kilmer, T. J. Brukilacchio, T. Chaves, J. Stott, Q. Zhang, T. Wu, M. Chorlton, R. H. Moore, D. B. Kopans, and D. A. Boas, "Tomographic optical breast imaging guided by three-dimensional mammography," Appl. Opt. **42**, 5181-5190 (2003).

84. C. Prada, J.-L. Thomas, and M. Fink, "The iterative time reversal process: analysis of the convergence," J. Acoust. Soc. Am. **97** (1995).

85. A. J. Devaney, "Time reversal imaging of obscured targets from multistatic data," IEEE Trans. Antenn. Propag. **53**, 1600-1610 (2005).

86. B. Wu, W. Cai, M. Alrubaiee, M. Xu, and S. K. Gayen, "Time reversal optical tomography: locating targets in a highly scattering turbid medium," Opt. Express **19**, 21956-21976 (2011).

Chapter 2

Time reversal optical tomography: locating small absorptive and scattering targets

2.1. Introduction

Optical imaging of targets in a highly scattering turbid medium for biomedical applications is an active area of research where the thrust is on developing fast and accurate methods for detecting and characterizing targets, and as outlined in Chapter 1, several approaches have evolved over the years. In this chapter we report on the development of an alternative approach, time reversal optical tomography (TROT) [1-3] for NIR optical imaging of target(s) in a turbid medium, and present initial results of its efficacy using both simulated and experimental data.

Time reversal (TR) invariance, the basic symmetry that commonly holds in microscopic physics, forms the basis for macroscopic TR imaging. TR imaging using the so-called "time-reversal mirrors" (TRMs) has been used as an experimental tool in acoustics with practical applications in medicine, underwater imaging, and nondestructive testing [4-7]. The theoretical and numerical techniques involved in time reversal have been used for applications involving both acoustic waves and electromagnetic waves (radar) [7-12].

Devaney and associates developed a theoretical framework for a TR imaging method with Multiple Signal Classification (MUSIC) for finding the location of scattering targets whose size is smaller than the wavelength of acoustic waves or electromagnetic waves (radar) used for probing the homogeneous or inhomogeneous background medium in which the targets were embedded [13, 14]. While their initial focus was on *back-propagation geometry* that used coincident acoustic or electromagnetic transceiver array for collecting the back-scattered signal

from the targets, they later extended the formalism to *transmission geometry* where sources and detectors were distinct and separated [15]. They also generalized the theory which was based on distorted wave Born approximation (DWBA) to account for multiple scattering between the targets [16]. In its basic form TR-MUSIC found target location from knowledge of the response matrix *K*, which was constructed from multi-static data collected by the transceiver array [13, 14]. TR-MUSIC provided higher spatial resolution than the conventional TR imaging, especially in the case where targets were not well resolved [13, 14, 17].

We are adapting and extending the TR-MUSIC approach to the optical domain, *i.e.* to diffusive optical imaging for detecting and locating targets embedded in a turbid medium. In this chapter, TROT is studied in details using both simulated data and data from transillumination NIR imaging experiments in slab geometry. A TR matrix is obtained by multiplying the response matrix formed using experimental or simulated data to its conjugate matrix. The leading non-zero eigenvalues of the Hermitian TR matrix determine the signal subspace due to presence of the targets. The signal subspace is separated from the noise subspace using an *L*-curve method [18-20]. The vector subspace method, MUSIC, along with Green's functions calculated from an appropriate forward model for light propagation through the turbid medium is then used to determine the locations of the targets. The MUSIC algorithm judges if the calculated Green's function vector corresponding to a location in the sample is mapped into the signal subspace or the noise subspace.

Several salient features make TROT attractive and potentially more promising than other IIR methods. First, the size of the TR matrix is much smaller than those used in other IIR approaches, which makes solution of the eigenvalue problem easier and faster. Second, to determine locations of targets, TR-MUSIC approach runs the program over all voxels only once,

and there is no need to carry out an iterative procedure done by other inverse approaches. Other IIR approaches seek to determine the absorption and scattering parameters at all voxels into which the sample is divided. The process is iterative, computationally intensive, and leads to a solution of the inverse problem that is not unique because the problem is ill-posed, even when there is no noise. In contrast, TROT seeks to determine the locations of the targets first and thereafter retrieve other information, such as, the size and optical properties of the limited number of targets in the medium, which requires significantly less computation time. The focus of this chapter is on finding the locations of targets.

Our result using simulated data shows that without the presence of noise TROT determines the locations of the embedded targets accurately with high resolution. TROT exhibits promise to locate targets both in simulations and experiments even when substantial noise is present. Images of small targets obtained by this approach are sharper than that obtained by other IIR approaches.

This remainder of this chapter is organized as follows. In Section 2.2, the formalism of the TROT approach is presented. In Section 2.3, the numerical algorithm of TROT is described. In Section 2.4, the efficacy of the formalism is tested using simulated data. Section 2.5 presents the results when the formalism is applied to experimental data using Intralipid-20% suspension in water as the highly scattering turbid medium. Section 2.6 discusses the results.

2.2. Theoretical formalism

2.2.1. Diffusion approximation, perturbation method and response matrix

The starting point for the TROT formalism is the diffusion approximation [21-23] of the radiative transfer equation (RTE) [24, 25]. The perturbation in the light intensity distribution due to small inhomogeneities (targets) embedded in a homogeneous medium, to the first order Born approximation, can be written as [26, 27]

$$\Delta\phi(\boldsymbol{r}_d,\boldsymbol{r}_s) = -\int G(\boldsymbol{r}_d,\boldsymbol{r})\delta\mu_a(\boldsymbol{r})cG(\boldsymbol{r},\boldsymbol{r}_s)d^3\boldsymbol{r} - \int \delta D(\boldsymbol{r})c\nabla_{\boldsymbol{r}}G(\boldsymbol{r}_d,\boldsymbol{r})\cdot\nabla_{\boldsymbol{r}}G(\boldsymbol{r},\boldsymbol{r}_s)d^3\boldsymbol{r}, \quad (2.1)$$

where $\boldsymbol{r}_s$, $\boldsymbol{r}_d$, and $\boldsymbol{r}$ are the positions of a point-like source of unit power, detector and target, respectively; $G(\boldsymbol{r}, \boldsymbol{r}_s)$ and $G(\boldsymbol{r}_d, \boldsymbol{r})$ are the Green's functions that describe light propagations from the source to the target and from the target to the detector, respectively; $\delta\mu_a$ is the difference in absorption coefficient and δD is the difference in diffusion coefficient between the targets and the background medium; and c is the light speed in the medium.

A multi-source interrogation and multi-detector signal acquisition scheme is used to acquire transillumination data, from which the difference in the light intensity distribution due to the targets, $\Delta\phi = \phi - \phi_0$, is found, where ϕ is the light intensity distribution measured on the sample boundary with targets embedded in the scattering medium, and ϕ_0 is ideally the light intensity distribution without the targets, which in practice is approximated by an "average" over all the multi-source measurements. A response matrix K is constructed with $-\Delta\phi$, to describe the transport of light from different sources through the embedded objects to the array of detectors [1, 15].

For small, point-like absorptive targets, the matrix elements can be rewritten in a discrete form as:

$$K_{ij} = \sum_{m=1}^{M} G^d(\boldsymbol{r}_i, \boldsymbol{X}_m)\tau_m G^s(\boldsymbol{X}_m, \boldsymbol{r}_j), i = 1,2,\ldots,N_d;\ j = 1,2,\ldots,N_s, \quad (2.2)$$

where $\tau_m = \delta\mu_a(\underline{\boldsymbol{X}}_m)c_m\delta V_m$ is the optical absorption strength of the m^{th} target, δV_m is the volume of m^{th} target, $\boldsymbol{r}_i$, $\boldsymbol{r}_j$ and $\boldsymbol{X}_m$ are locations of the i^{th} detector, j^{th} source and m^{th} target, respectively. Due to the reciprocity of light propagation in the medium, $G(\boldsymbol{r}, \boldsymbol{r}') = G(\boldsymbol{r}', \boldsymbol{r})$. Thus,

$$K_{ij} = \sum_{m=1}^{M} G^d\left(\boldsymbol{X}_m, \boldsymbol{r}_i\right)\tau_m G^s\left(\boldsymbol{X}_m, \boldsymbol{r}_j\right), \tag{2.3}$$

and

$$K = \left\{K_{ij}\right\} = \sum_{m=1}^{M} g_d\left(\boldsymbol{X}_m\right)\tau_m {g_s}^T\left(\boldsymbol{X}_m\right), \tag{2.4}$$

where $g_s(\boldsymbol{r})$ and $g_d(\boldsymbol{r})$ are Green's function vectors (GFVs) defined as

$$g_s\left(\boldsymbol{r}\right) = [G^s\left(\boldsymbol{r}_1, \boldsymbol{r}\right), G^s\left(\boldsymbol{r}_2, \boldsymbol{r}\right), ; G^s\left(\boldsymbol{r}_{N_s}, \boldsymbol{r}\right)]^T, \tag{2.5a}$$

$$g_d\left(\boldsymbol{r}\right) = [G^d\left(\boldsymbol{r}_1, \boldsymbol{r}\right), G^d\left(\boldsymbol{r}_2, \boldsymbol{r}\right), ; G^d\left(\boldsymbol{r}_{N_d}, \boldsymbol{r}\right)]^T, \tag{2.5b}$$

associated with the source array and detector array, respectively, where the superscript T denotes transpose; and N_s, N_d and M are the numbers of sources, detectors and targets, respectively. It is assumed the number of targets is less than the number of sources and detectors, $M < \min(N_d, N_s)$. $K^T = \{K_{ji}\}$ describes light propagation from the positions of detectors through the medium and targets to sources.

For a homogeneous background medium, the rank R of matrix K, is equal to the dimension of the source array vector space $\mathcal{G}_s$ spanned by $g_s(\boldsymbol{r}_m)$, and also equal to the dimension of the detector array vector space $\mathcal{G}_d$ spanned by $g_d(\boldsymbol{r}_m)$, where $\mathcal{G}_s \subseteq C^{N_s}$ and $\mathcal{G}_d \subseteq C^{N_d}$. For absorptive targets, R is equal to the number of targets M.

Similar forms of the response matrix and GFVs can be obtained for scattering targets. As the dot product in the second term of Eq. (2.1) implies, each scattering target is represented by three components coexisting at one location. The elements of the K matrix for L scattering target may be written as

$$K_{ij} = \sum_{l=1}^{L} \tau_l \nabla_{\boldsymbol{r}} G^d\left(\boldsymbol{r}_i, \boldsymbol{X}_l\right) \cdot \nabla_{\boldsymbol{r}} G^s\left(\boldsymbol{X}_l, \boldsymbol{r}_j\right)$$
$$= \sum_{l=1}^{L} \tau_l \sum_{\alpha=\{x,y,z\}} \partial_\alpha G^d\left(\boldsymbol{r}_i, \boldsymbol{X}_l\right) \partial_\alpha G^s\left(\boldsymbol{X}_l, \boldsymbol{r}_j\right), \tag{2.6}$$

where $\tau_l = \delta D(\boldsymbol{X}_l) c_m \delta V_l$ is the optical scattering strength of the l^{th} target. The K matrix for scattering targets can be written in a manner similar to that for absorptive targets:

$$K = \sum_{l=1}^{L} \sum_{\alpha=\{x,y,z\}} \partial_\alpha g_d\left(\boldsymbol{X}_l\right) \tau_l \partial_\alpha g_s{}^T\left(\boldsymbol{X}_l\right). \tag{2.7}$$

The Green's function for a slab geometry is [27, 28]

$$G\left(\boldsymbol{r}, \boldsymbol{r}'\right) = G\left(\boldsymbol{r}', \boldsymbol{r}\right) = \frac{1}{4\pi D} \sum_{k=-\infty}^{\infty} \left(\frac{e^{-\kappa r_k^+}}{r_k^+} - \frac{e^{-\kappa r_k^-}}{r_k^-} \right), \tag{2.8a}$$

$$r_k^{\pm} = \left[(x-x')^2 + (y-y')^2 + (z \mp z' + 2kd)^2 \right]^{1/2}, \tag{2.8b}$$

where $\kappa = \left[\left(\mu_a - i\omega / c \right) / D \right]^{1/2}$ in frequency domain with amplitude modulation frequency ω. The extrapolated boundaries of the slab are located at $z = 0$ and $z = d = L + 2z_e$, respectively, where L is the physical thickness of the slab and the extrapolation length z_e is determined from the boundary condition of the slab [29, 30].

Under ideal conditions, when all three scattering components of each of the L scattering targets are well-resolved, the rank of K contributed by L scattering targets is $3L$. In practice, four components (one for absorption and three for scattering) are calculated for each target, since the targets may have both scattering and absorptive characteristics, or the exact nature may not be known *a priori*. The dominant characteristic is used to label the target as absorptive or scattering in nature.

2.2.2. Point spread functions

If light emitted by a source of unit power at target position $\boldsymbol{X}$ propagates in the sample medium, the signal measured by the detector array at the sample boundary is $G_d(\boldsymbol{r}_i, \boldsymbol{X})$. The signal is then "time-reversed" and back-propagated with the Green's function of the background medium. TR operation is phase conjugation in Fourier domain [7, 31]. So the signal evaluated at $\boldsymbol{r}$ is [13]

$$H_d(\boldsymbol{r},\boldsymbol{X}) = \sum_{i=1}^{N_d} G^d(\boldsymbol{r},\boldsymbol{r}_i) G^{d*}(\boldsymbol{r}_i,\boldsymbol{X}) = {g_d}^T(\boldsymbol{r})\,{g_d}^*(\boldsymbol{X}) = {g_d}^\dagger(\boldsymbol{X})\,g_d(\boldsymbol{r}) = \langle g_d(\boldsymbol{X}), g_d(\boldsymbol{r})\rangle, \tag{2.9}$$

where * denotes complex conjugate, † denotes adjoint, and $\langle \rangle$ denotes inner product. $H_d(\boldsymbol{r}, \boldsymbol{X})$ is the detector array point spread function (PSF). A source array PSF can be similarly formed as

$$H_s(\boldsymbol{r},\boldsymbol{X}) = g_s(\boldsymbol{X})^\dagger\, g_s(\boldsymbol{r}) = \langle g_s(\boldsymbol{X}), g_s(\boldsymbol{r})\rangle. \tag{2.10}$$

Due to the time reversal assumption, $H_d(\boldsymbol{r}, \boldsymbol{X})$ peaks at $\boldsymbol{r} = \boldsymbol{X}$, so it can be considered as an image of the source at $\boldsymbol{X}$ formed by the TR detector array. PSF vanishes when $\boldsymbol{r}$ is far away from $\boldsymbol{X}$. A similar interpretation can be used for $H_s(\boldsymbol{r}, \boldsymbol{X})$.

2.2.3. Time reversal and MUSIC

The TR matrix may be constructed to represent light propagation from sources to detectors and back denoted by T_{SDDS}, or to represent light propagation from detector positions to source positions and back denoted by T_{DSSD}, a consequence of the reciprocity of light propagation [8, 13, 17, 31, 32]. For frequency domain, $T_{SDDS} = K^\dagger K$, and $T_{DSSD} = (K^T)^\dagger K^T = K^* K^T$, where response data matrix K is formed using modulated intensities, instead of the field with phase information used in the conventional TR. For CW measurements $T_{SDDS} = K^T K$, and $T_{DSSD} = K K^T$ (K is real and only includes intensity values).

Since T_{SDDS} and T_{DSSD} are Hermitian ($T^\dagger = T$), they have complete sets of orthonormal eigenvectors v_j (j = 1, …, N_s) and u_i (i = 1, …, N_d), with a common set of non-negative real

eigenvalues. For $M < \min(N_s, N_d)$ absorptive targets without the presence of noise, the rank of T_{SDDS} and T_{DSSD} is M. The eigenvalues $\lambda_j > 0$, when $j = 1, \ldots, M$, and $\lambda_j \approx 0$, when $j = M + 1, \ldots, N_s$ for T_{SDDS} and $j = M + 1, \ldots, N_d$ for T_{DSSD}. The eigen system $\{v_j, u_j, \lambda_j > 0\}$, $j = 1, \ldots, M$, is related to the targets. The TR matrix T_{SDDS} can be written as [1, 13]

$$T_{SDDS} = \sum_{m=1}^{M}\sum_{m'=1}^{M} \tau_m{}^{*}\tau_{m'} \left\langle g_d\left(\boldsymbol{X}_m\right), g_d\left(\boldsymbol{X}_{m'}\right)\right\rangle g_s{}^{*}\left(\boldsymbol{X}_m\right) g_s{}^{T}\left(\boldsymbol{X}_{m'}\right). \tag{2.11}$$

Subsequent formalism may be different depending on whether the targets are "well resolved" or "poorly resolved."

2.2.3.1. *Well-resolved targets*

If the m^{th} and m'^{th} targets ($m \neq m'$) are well resolved, defined by the conditions: $H_s(\boldsymbol{X}_m, \boldsymbol{X}_{m'}) \approx 0$ and $H_d(\boldsymbol{X}_m, \boldsymbol{X}_{m'}) \approx 0$, *i.e.* the GFVs at $\boldsymbol{X}_m$ and $\boldsymbol{X}_{m'}$ are orthogonal, $\langle g_d(\boldsymbol{X}_m), g_d(\boldsymbol{X}_{m'})\rangle = H_d(\boldsymbol{X}_{m'}, \boldsymbol{X}_m) = \|g_d(\boldsymbol{X}_m)\|^2 \delta_{mm'}$. So we have

$$T_{SDDS} = \sum_{m=1}^{M} |\tau_m|^2 \left\|g_d\left(\boldsymbol{X}_m\right)\right\|^2 g_s{}^{*}\left(\boldsymbol{X}_m\right) g_s{}^{T}\left(\boldsymbol{X}_m\right), \tag{2.12}$$

where $\|\cdot\|$ denotes $L2$ norm [33]. The eigenvectors of T_{SDDS} are proportional to the complex conjugate of the GFVs associated with the M targets [1, 13], *i.e.*

$$T_{SDDS}\, g_s{}^{*}\left(\boldsymbol{X}_m\right) = |\tau_m|^2 \left\|g_d\left(\boldsymbol{X}_m\right)\right\|^2 \left\|g_s\left(\boldsymbol{X}_m\right)\right\|^2 g_s{}^{*}\left(\boldsymbol{X}_m\right). \tag{2.13}$$

The eigenvectors are

$$v_j = \frac{g_s{}^{*}\left(\boldsymbol{X}_j\right)}{\left\|g_s\left(\boldsymbol{X}_j\right)\right\|}, \tag{2.14}$$

with eigenvalues $\lambda_j = |\tau_j|^2 \|g_d(\boldsymbol{X}_j)\|^2 \|g_s(\boldsymbol{X}_j)\|^2$, $j = 1, \ldots, M$. Thus T_{SDDS} is a projection operator that projects a vector onto the conjugate of the source array vector space $\mathcal{G}_S$. The j^{th} non-zero eigenvalue λ_j is directly related to the optical strength τ_j of the j^{th} target. Similar equations can be

derived for T_{DSSD}, which is a projection operator for the conjugate of the detector array vector space $\mathcal{G}_d$. The eigenvectors of T_{DSSD} are

$$u_j = \frac{g_d^{*}\left(\boldsymbol{X}_j\right)}{\left\|g_d\left(\boldsymbol{X}_j\right)\right\|}, \tag{2.15}$$

$j = 1, \ldots, M$, with the same eigenvalues as T_{SDDS}.

Therefore, for well-resolved targets, the target locations can be determined by the inner product [1, 13, 15, 32]

$$\begin{aligned}\psi_j{}^{s} &= \left\langle v_j{}^{*}, g_s\left(\boldsymbol{X}_p\right)\right\rangle = v_j{}^{T} g_s\left(\boldsymbol{X}_p\right) = \frac{g_s{}^{\dagger}\left(\boldsymbol{X}_j\right)}{\left\|g_s\left(\boldsymbol{X}_j\right)\right\|} g_s\left(\boldsymbol{X}_p\right) \\ &= \frac{1}{\left\|g_s\left(\boldsymbol{X}_j\right)\right\|} H_s\left(\boldsymbol{X}_p, \boldsymbol{X}_j\right),\end{aligned} \tag{2.16a}$$

or

$$\begin{aligned}\psi_j{}^{d} &= \left\langle u_j{}^{*}, g_d\left(\boldsymbol{X}_p\right)\right\rangle = u_j{}^{T} g_d\left(\boldsymbol{X}_p\right) = \frac{g_d{}^{\dagger}\left(\boldsymbol{X}_j\right)}{\left\|g_d\left(\boldsymbol{X}_j\right)\right\|} g_d\left(\boldsymbol{X}_p\right) \\ &= \frac{1}{\left\|g_d\left(\boldsymbol{X}_j\right)\right\|} H_d\left(\boldsymbol{X}_p, \boldsymbol{X}_j\right),\end{aligned} \tag{2.16b}$$

where $\boldsymbol{X}_p$ is a test target position, which is the position of any voxel in the sample space. $\psi_j{}^{s}$ and $\psi_j{}^{d}$ peak when $\boldsymbol{X}_p$ happens to be the position of the j^{th} target. In the classical TR imaging [4, 8, 17, 31] for ideally resolved targets, each eigenvector of the TR operator can be used to focus on one particular target. Here $\psi_j{}^{s}$ and $\psi_j{}^{d}$ represent focusing of signals from the source and detector planes on to the target position, respectively. Use of the eigenvectors v_j and u_j, $j = 1, \ldots, M$, ensures that the j^{th} target is sorted out. When T_{SDDS} and source array vector space (T_{DSSD} and detector array vector space) are used, we call the scheme SDDS (DSSD). Both source and detector arrays can be considered simultaneously to locate the target by calculating

$$\psi_j = \psi_j{}^d \psi_j{}^{s\dagger} = \frac{1}{\left\| g_s\left(\boldsymbol{X}_j\right)\right\| \cdot \left\| g_d\left(\boldsymbol{X}_j\right)\right\|} H_d\left(\boldsymbol{X}_p, \boldsymbol{X}_j\right) H_s{}^*\left(\boldsymbol{X}_j, \boldsymbol{X}_p\right), \tag{2.17}$$

j = 1, …, M, which is computationally equivalent to a process that light emitted from a virtual source of unit power at a test target position $\boldsymbol{X}_p$, propagates to the TR source array and back to a true target position $\boldsymbol{X}_j$; then it is re-emitted and further propagates to the TR detector array and back to the original position $\boldsymbol{X}_p$. ψ_j peaks when the test target position $\boldsymbol{X}_p$ coincides with the true target position $\boldsymbol{X}_j$ associated with the j^{th} eigenvector.

2.2.3.2. ***Poorly-resolved targets and MUSIC***

When the targets are too close to each other or the sources and/or detectors are significantly sparse, the targets are considered to be poorly resolved and the GFVs at $\boldsymbol{X}_m$ and $\boldsymbol{X}_{m'}$ are not orthogonal. In such cases, the eigenvectors v_j and u_j do not correspond one-to-one with the GFVs associated with target positions $\boldsymbol{X}_m$ (m = 1, …, M). The image resolution degrades because of contributions from multiple targets. To solve this problem, the subspace-based method, MUSIC was implemented with TR [13, 15, 32]. MUSIC algorithm is based on the idea that although the vectors characterizing the targets are no longer orthogonal with each other, they are all located in the signal subspace, which is orthogonal to the noise subspace.

The orthonormal sets $\{v_j^*\}$ (j = 1, …, N_s) and $\{u_j^*\}$ (j = 1, … N_d) span the spaces C^{N_s} and C^{N_d} associated with the source and detector arrays, respectively. While $\{v_j^*\}$ and $\{u_j^*\}$, with $\lambda_j >$ 0, form the signal subspaces on the source and detector arrays, $\mathcal{S}^s = \{v_j{}^*\}$ and $\mathcal{S}^d = \{u_j{}^*\}$ (j = 1, …, M), respectively; $\{v_j^*\}$ and $\{u_j^*\}$, with $\lambda_j \approx 0$, form the noise subspaces, $\mathcal{N}^s = \{v_j{}^*\}$ (j = M + 1, …, N_s) and $\mathcal{N}^d = \left\{u_j{}^*\right\}$ (j = M + 1, …, N_d), respectively. Thus $C^{N_s} = \mathcal{S}^s \oplus \mathcal{N}^s$ and $C^{N_d} = \mathcal{S}^d \oplus \mathcal{N}^d$ [15, 32]. Since the dimensions of the signal subspaces $\mathcal{S}^s$ and $\mathcal{S}^d$ and of the

GFV spaces $\mathcal{G}_s$ and $\mathcal{G}_d$ are all equal to M, $\mathcal{G}_s \equiv \mathcal{S}^s$ and $\mathcal{G}_d \equiv \mathcal{S}^d$ [32]. The GFVs, $g_s(\boldsymbol{X}_m)$ and $g_d(X_m)$, $m = 1, \ldots, M$, are linear combinations of v_j^* and u_j^*, $j = 1, \ldots, M$, respectively. Therefore, $g_s(\boldsymbol{X}_m) \in \mathcal{S}^s$ and $g_d(\boldsymbol{X}_m) \in \mathcal{S}^d$, $m = 1, \ldots, M$, associated with m^{th} target are orthogonal to $v_j^* \in \mathcal{N}^s$ ($j = M + 1, \ldots, N_s$) and $u_j^* \in \mathcal{N}^d$ ($j = M + 1, \ldots, N_d$), respectively:

$$\left\langle v_j^*, g_s(\boldsymbol{X}_m) \right\rangle = v_j^T g_s(\boldsymbol{X}_m) \approx 0, \; j = M+1, \ldots, N_s, \tag{2.18a}$$

$$\left\langle u_j^*, g_d(\boldsymbol{X}_m) \right\rangle = u_j^T g_d(\boldsymbol{X}_m) \approx 0, \; j = M+1, \ldots, N_d. \tag{2.18b}$$

The locations of targets can be determined by calculating the following squared sum of inner products:

$$Q_s(\boldsymbol{X}_p) = \sum_{j=M+1}^{N_s} \left| v_j^T g_s(\boldsymbol{X}_p) \right|^2, \tag{2.19a}$$

$$Q_d(\boldsymbol{X}_p) = \sum_{j=M+1}^{N_d} \left| u_j^T g_d(\boldsymbol{X}_p) \right|^2. \tag{2.19b}$$

$Q_s(\boldsymbol{X}_p)$ and $Q_d(\boldsymbol{X}_p)$ vanish when the test target position $\boldsymbol{X}_p$ is a true target position. Similar to Eq. (2.17), $Q = Q_s Q_d$ can be calculated with both source and detector arrays considered simultaneously. An alternative approach to accentuate a target position is to plot a pseudo spectrum defined as

$$P_s(\boldsymbol{X}_p) = \left\| g_s(\boldsymbol{X}_p) \right\|^2 \Big/ \left| Q_s(\boldsymbol{X}_p) \right| \tag{2.20a}$$

associated with the source array, or

$$P_d(\boldsymbol{X}_p) = \left\| g_d(\boldsymbol{X}_p) \right\|^2 \Big/ \left| Q_d(\boldsymbol{X}_p) \right| \tag{2.20b}$$

associated with the detector array, or

$$P(\boldsymbol{X}_p) = P_s(\boldsymbol{X}_p) P_d(\boldsymbol{X}_p) \tag{2.20c}$$

associated with both source and detector arrays [1, 13, 15, 32], where $\|g_s(\boldsymbol{X}_p)\|^2$ and $\|g_d(\boldsymbol{X}_p)\|^2$ are used for normalization. The poles of the pseudo spectrum correspond to target locations. These MUSIC pseudo spectra can also be used to locate well-resolved targets.

Since the dimension of the signal subspace is generally much smaller than that of the noise subspace, it is preferred that in Eq. (2.19) and Eq. (2.20), the signal subspace is used rather than the noise subspace for ease of computation. Using the properties of the projection operators associated with the source and detector arrays [1, 13, 15, 32], $Q_s(\boldsymbol{X}_p)$ and $Q_d(\boldsymbol{X}_p)$ can be calculated as

$$Q_s\left(\boldsymbol{X}_p\right)=\left\|g_s\left(\boldsymbol{X}_p\right)\right\|^2-\sum_{j=1}^{M}\left|v_j{}^T g_s\left(\boldsymbol{X}_p\right)\right|^2, \tag{2.21a}$$

$$Q_d\left(\boldsymbol{X}_p\right)=\left\|g_d\left(\boldsymbol{X}_p\right)\right\|^2-\sum_{j=1}^{M}\left|u_j{}^T g_d\left(\boldsymbol{X}_p\right)\right|^2. \tag{2.21b}$$

When the targets are embedded in a non-uniform medium, or when there is significant noise present, the noise or false targets contribute significantly to the eigenvalues. The near-zero and non-zero eigenvalues are not as well separated as when there are no noise. In this case, the rank of the TR matrix is larger than the number of targets *M*. The TR matrix may even be full rank. However, as long as *M* is less than min (N_s, N_d) and eigenvalues contributed by the noise and false targets are smaller than those contributed by the real targets with a threshold ϵ, the target positions can be obtained using a pseudo spectrum [15, 32] associated with the source array,

$$P_s\left(\boldsymbol{X}_p\right)=\left\|g_s\left(\boldsymbol{X}_p\right)\right\|^2\Big/\left|Q_s\left(\boldsymbol{X}_p\right)_{\lambda_j\le\epsilon}\right|, \tag{2.22}$$

where $Q_s\left(\boldsymbol{X}_p\right)_{\lambda_j\le\epsilon}=\left\|g_s\left(\boldsymbol{X}_p\right)\right\|^2-\sum_{\lambda_j>\epsilon}\left|v_j{}^T g_s\left(\boldsymbol{X}_p\right)\right|^2$. Pseudo spectra associated with the detector array or with both source and detector arrays can also be obtained similarly. In practice, the

threshold is selected to separate the signal and noise subspaces using a method similar to *L*-curve regularization [18].

When scattering targets are concerned, the GFVs $\partial_\alpha g$ ($\alpha = x, y, z$), associated with the test target position $\boldsymbol{X}_p$ will be used to calculate the pseudo spectrum. For a target with both absorption and scattering properties at the wavelength of probing light, one GFV corresponding to absorption constructed as g and three GFVs corresponding to scattering target constructed with $\partial_\alpha g$ ($\alpha = x, y, z$), are used to calculate the pseudo spectrum over every voxel. Ideally, for an absorptive and scattering target four pseudo-values will be obtained for every target position. If the dominant value corresponds to the absorptive (any of the scattering) GFV the target will be identified as absorptive (scattering) in nature.

2.3. Algorithm

Implementation of TROT to locate targets embedded in a highly scattering turbid medium involves the steps outlined below. For simplicity, the sizes of source array and detector array are assumed to be the same, *i.e.*, $N_d = N_s = N$.

(a) A response matrix K with size $N \times N$ is constructed using experimental data (or estimated data in simulation). Data consist of the perturbations in the light intensity distribution due to the targets, $\Delta\phi = \phi - \phi_0$, where ϕ is the light intensity distribution measured on the sample boundary with targets embedded in the scattering medium and ϕ_0 is ideally the light intensity distribution without the targets. In practice, ϕ_0 is approximated by an "average" over all the multi-source measurements, while in simulation it can be estimated without such approximation.

(b) A detector array TR matrix, $T_{DSSD} = KK^T$ with size $N \times N$ for CW measurements is constructed. All the eigenvalues and the eigenvectors of the T_{DSSD} matrix are computed. The eigenvectors are orthogonal to each other. It is to be noted that in this procedure we only deal with a matrix of dimension N, not a matrix of dimension of $N \times N$ as done in traditional inverse procedures.

(c) The non-zero eigenvalues of T_{DSSD} belonging to the signal subspace are separated from the near-zero eigenvalues belonging to the noise subspace using the L-curve method [18-20].

(d) MUSIC approach [13, 15, 32] is next used to determine the locations of the targets as follows. (i) The 3-D medium is divided into a certain number of voxels. A detector array GFV, $g_d(\boldsymbol{X}_p)$, associated with an absorptive test target position $\boldsymbol{X}_p$ at p^{th} voxel is calculated using Diffusion Approximation of RTE. Other proper forward models could be used as well. In order to check if $g_d(\boldsymbol{X}_p)$ is located in the signal subspace or in the noise subspace, a pseudo spectrum associated with the detector array is computed using Eq. (2.20b), where M is the dimension of the signal subspace found in step (c). If $g_d(\boldsymbol{X}_p)$ is located in the signal subspace, the corresponding pseudo value $P(\boldsymbol{X}_p)$ in Eq. (2.20b) will become a maximum. (ii) Pseudo spectra are also calculated using the other three GFVs, $\partial_\alpha g_d(\boldsymbol{X}_p)$, ($\alpha = x, y, z$) for scattering property. (iii) All pseudo values are put together and sorted in a descending order. Since the leading pseudo values at $\boldsymbol{X}_p$ are associated with targets and specific GFVs, the positions of the embedded targets and their nature (absorptive or scattering) are determined. The pseudo spectrum in the whole sample space can be used to plot pseudo tomographic images.

In this approach, only a single run is needed for calculating the pseudo spectrum and no iterative procedure is involved, which makes it faster and computationally less intensive than the

traditional IIR approaches. Similar procedure can be used for application of TROT when $N_d \neq N_s$. The pseudo spectrum associated with either the source array, or the detector array, or both source and detector arrays, as outlined in Eq. (2.20) can be used to obtain target positions.

It is instructive to compare the computational complexity of TROT formalism with that of typical iterative methods. For a typical iterative method, an equation $b = Wx$ is solved to find the inhomogeneities (targets), where W is a weight matrix with size $N_dN_s \times N$, N is the number of voxels, b is an $N_dN_s \times 1$ vector describing the perturbation in the detected light intensity due to the presence of inhomogeneities, and x is the perturbation or variation in the optical properties from the background values with dimension of $N \times 1$. The computational complexity is typically $O(N_dN_sN^2)$ for a single iteration. The computational complexity of TROT is much smaller than that for even one iteration of an iterative method. For the SDDS scheme, the complexity for TROT is $O(N_dN_s^2)$ if $N_dN_s > NN_k$, and $O(N_sNN_k)$ otherwise, where N_k is the dimension of the signal subspace. In the DSSD scheme, the complexity is $O(N_sN_d^2)$ if $N_dN_s > NN_k$, and $O(N_dNN_k)$ otherwise. TROT does not involve any iteration.

In the following sections, TROT will be tested using simulation and experimental data.

2.4. Testing TROT with simulated data

To test the efficacy of the TROT approach, we first consider a rather challenging task of detecting and locating six targets embedded in a simulated sample which is a 40-mm thick uniform scattering slab. Its absorption and diffusion coefficients are μ_a = 1/300 mm^{-1} and D = 1/3 mm, respectively. The incident CW beam was step-scanned in an x-y array of 41 × 41 grid points with a step size of 2 mm on the input plane covering an 80 mm × 80 mm area. Light transmitted from the opposite side (output plane) was recorded at 41 × 41 grid points covering the same area. No random noise was added.

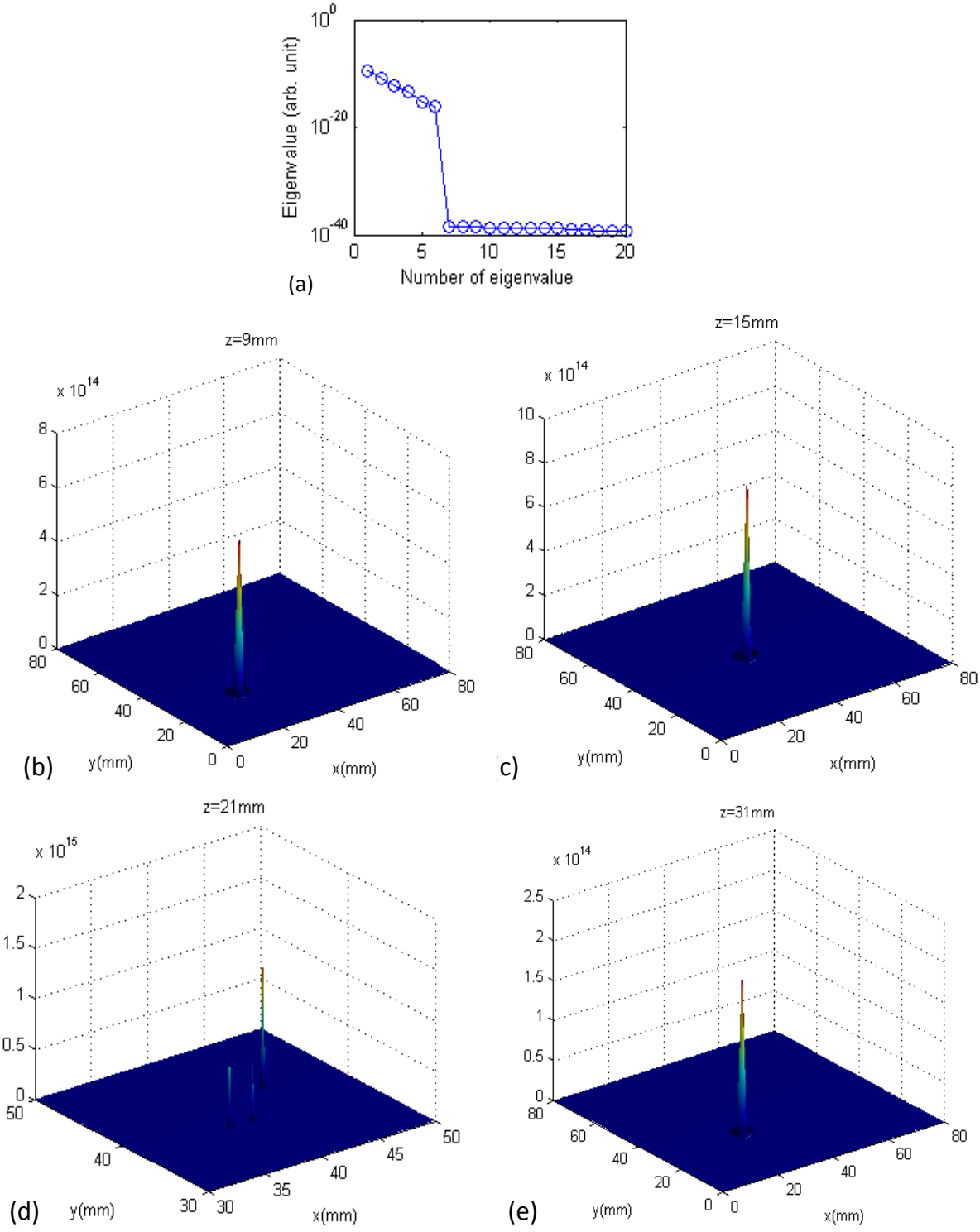

Fig. 2.1. (a) A plot of first twenty (20) eigenvalues on logarithmic scale. (b-e) 2-*D* slices of the pseudo spectrum on *z* = 9 mm, 15 mm, 21 mm, and 31 mm planes, respectively, showing the location of the six targets, where *z* = 21 mm shows a zoomed-in image of the three difficult targets described in the text.

The six (M = 6) point-like absorptive targets, with absorption coefficient difference of $\Delta\mu_a$ = 0.01 mm^{-1} from the background, were placed at A (24 mm, 26 mm, 9 mm), B (38 mm, 38 mm, 15 mm), C (38 mm, 38 mm, 21 mm), D (40 mm, 38 mm, 21 mm), E (44 mm, 42 mm, 21 mm) and F (30mm, 30mm, 31 mm), respectively. The origin (0 mm, 0 mm, 0 mm) was located at the upper-left corner of the input boundary (source plane) of the sample. The medium was divided into $40 \times 40 \times 20$ voxels, with each voxel of size 2 mm $\times$ 2 mm $\times$ 2 mm. As can be seen from the assigned coordinates, targets C and D are located at two adjacent voxels, and are close to target E, and these three targets are located in the same z layer. Consequently, targets C and D are expected to be very difficult to resolve, and hard to distinguish from target E. Target B and C have the same lateral position x and y, and different depths. Target A is close to the source plane, while F is close to the detector plane.

Using the Diffusion Approximation of the RTE as the model for light propagation in slab geometry, signals arising from light propagation from the source array to the detector array through medium *with* and *without* the targets were calculated. The difference between the two sets, which is the perturbation due to the targets, was used as the "simulated data". The size of the K matrix is $N \times N = 1681 \times 1681$. The TR matrix $T = KK^T$ was constructed. Then, 1681 eigenvalues and 1681 eigenvectors of T were found.

The first seven (7) computed eigenvalues in a descending order of magnitude are listed in the first column of Table 2.1. The leading twenty eigenvalues are plotted in Fig. 2.1(a) on a logarithmic scale. The first six (6) eigenvalues are at least 10 orders-of-magnitude higher than the 7-th and other smaller eigenvalues. Hence, the dimension of the signal subspace and the number of targets are determined to be six. The pseudo spectrum (consisting of $40 \times 40 \times 20 \times 4$ elements) was calculated using the M eigenvectors in the signal subspace. The values of

elements in the pseudo spectrum were sorted in a descending order. The seven leading pseudo values are listed in Table 2.1 with the corresponding positions of voxels. The six peaks are found to be associated with the GFVs for absorptive targets, and consequently, the six targets are identified to be absorptive targets.

Table 2.1. Eigenvalues, pseudo spectrum and the corresponding positions

Leading Eigenvalues	Poles of Pseudo Spectrum	Retrieved Position (x, y, z) mm	Know Position (x, y, z) mm
2.6697E-010	1.5911E+015	(44, 42, 21)	(44, 42, 21)
1.1722E-011	8.6376E+014	(38, 38, 15)	(38, 38, 15)
4.0081E-013	7.9559E+014	(38, 38, 21)	(38, 38, 21)
3.6676E-014	7.2328E+014	(40, 38, 21)	(40, 38, 21)
5.2629E-016	6.3010E+014	(24, 26, 9)	(24, 26, 9)
6.4837E-017	2.1159E+014	(30, 30, 31)	(30, 30, 31)
2.8337E-039	2.4353E+005	(38, 38, 19)	
…	…		

All six large pseudo-values are located at the exact known target locations and their values are approximately 9 orders-of-magnitude larger than those at their neighborhood locations. A 2-*D* slice of the pseudo spectrum on z = 21 mm plane is shown in Fig. 2.1(b), showing the locations of the three difficult targets.

With the highly encouraging result from simulation even for a considerably challenging task, we proceeded to test the approach for the realistic situation of detecting and locating targets from experimental data.

2.5. Testing TROT with experimental data

2.5.1. Experimental materials and methods

Three different experiments with three different samples were carried out to test the efficacy of the TROT approach in detecting and locating targets in a turbid medium. All three samples used a 250 mm × 250 mm × 60 mm transparent plastic container filled with Intralipid-20% suspension in water as the background medium. The concentration of Intralipid-20% was adjusted to provide an estimated [34, 35] absorption coefficient μ_a ~0.003 mm^{-1} at 790 nm, and a transport mean free path l_t ~1 mm, which were similar to the average values of those parameters for human breast tissue, while the cell thickness of 60 mm was comparable to thickness of a typical compressed breast.

Intralipid is an FDA-approved safe fat emulsion for human use. It is mixture of multiple types of fatty acid that can be used clinically as an intravenously administered nutrient. Since Intralipid is a highly scattering suspension with low absorption, it has also been widely used as the basis of biological tissue phantom for investigation of properties of biological tissues, light propagation in tissue and methods applied in imaging through biological tissues. The optical properties of Intralipid suspension have been well studied [34-36]. The scattering coefficient μ_s and the anisotropy factor g of 1L aqueous Intralipid suspension prepared by diluting 1mL Intralipid-10% with distilled water can be calculated [34] to be $\mu_s(\lambda) = 0.016\lambda^{-2.4}$ and $g(\lambda) = 1.1 - 0.58\lambda$, respectively for $0.4\mu_m < \lambda < 1.1\mu_m$, where the unit of μ_s is mL^{-1} L mm^{-1}.

In the first experiment, the depth (position along z-axis) of an absorptive target was varied to explore how the accuracy of position estimate depended on depth. The target was a glass sphere of

diameter ~9 mm filled with ink dissolved in Intralipid-20% suspension in water (μ_s was adjusted to be the same as that of the background medium, while $\mu_a \approx 0.013$ mm^{-1} was about 3 times higher than that of background medium).

In the second experiment, the separation between two absorptive targets was varied to test how close those could be and yet be resolved as separate objects. Both the targets were similar to the target in the first experiment.

In the third experiment, the depth of a scattering target was varied to explore the efficacy of TROT in locating and characterizing a scattering target. The target was a glass sphere of diameter 10 mm filled with Intralipid-20% suspension in water to provide a transport mean free path l_t of 0.25 mm, and a scattering coefficient $\mu_s \approx 11$ mm^{-1}.

A multi-source interrogation and multi-detector signal acquisition scheme, shown in Fig. 2.2, was used to acquire data. A 100-mW 790-nm diode laser beam was used to illuminate the samples. A 1024 × 1024 pixels charge coupled device (CCD) camera equipped with a 60-mm focal-length camera lens was used on the opposite side of the sample to detect the transmitted light on the boundaries of the slab samples (detector plane). The pixel size was 24 μm. The multi-source illumination scheme was realized by scanning the sample across the laser beam in a two-dimensional *x*-*y* array of grid points using a computer-controlled translation stage. The first and third samples were scanned across the laser beam in an array of 9 × 9 grid points, and the second sample was scanned in an array of 15 × 11 grid points, with a step size of 5 mm in all cases. The scanning and data acquisition processes were controlled by a personal computer (PC). Raw transillumination images of the sample were recorded by the PC for each scan position, and stored for subsequent analysis. A typical image, which is a 2-*D* intensity distribution, is shown in the right side of Fig. 2.2.

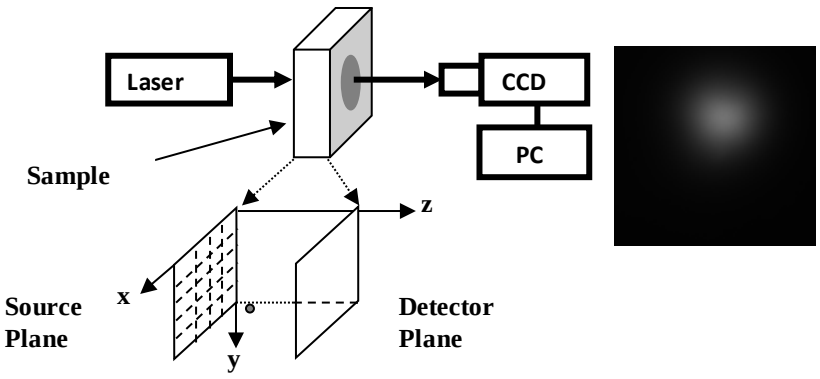

Fig.2.2. A schematic diagram of the experimental arrangement for imaging objects embedded in a turbid medium. (Key: CCD = charge coupled device, PC = personal computer) Inset (below) shows the 2-*D* array in the input plane that was scanned across the incident laser beam, and inset (right) shows a typical raw image.

While we have scanned the sample and kept the source fixed in the experiments reported here, a more clinically relevant approach would be to scan the source and fix the sample. In the experimental arrangement, the source scanning may be accomplished by: (a) delivering the beam using an optical fiber, and translating the delivery end of the fiber in an *x*-*y* array using a computer-controlled translation stage; or (b) raster scanning the laser beam using two orthogonal (*x*-*y*) galvanometers. The main change in the processing of data would involve alignment of the images so that laser beam positions are overlapped before averaging to generate the background image.

2.5.2. Data Processing and Analysis

From each image, a region of interest was cropped out and then every 5×5 pixels in the cropped image were binned to one pixel to enhance the signal-to-noise ratio. The background image was generated by taking an average of the original images for all scan positions, which is a reasonable approximation since for most of the scan positions the target(s) is (are) not along the direction of the incident beam. Then the background image was also cropped and binned corresponding to the

region of interest for each scan position. Perturbation in the light intensity distribution $\Delta\phi$ due to targets in each image was found by subtracting the background image from each individual image. The response matrix was constructed using the light intensity perturbations, $-\Delta\phi$. The TR matrix was generated by multiplying the response matrix by its transpose for our continuous-wave (CW) probing scheme. The eigenvalue equation was solved and the signal subspace was selected and separated from the noise subspace. MUSIC was then used to calculate the pseudo spectrum for all voxels in the 3-*D* space of the sample. For each voxel, four pseudo values, one for absorption and three for scattering as described in Algorithm step (d), were calculated. The voxel size was 0.77 mm $\times$ 0.77 mm $\times$ 1 mm. By sorting the pseudo spectrum in a descending order, the target(s) were located.

The voxel size to be used in reconstruction and its relation to the target size is an important consideration. In general, smaller voxels provide reconstruction of higher resolution at the cost of increased computational time. Finer details of an extended target may be obtained using smaller voxels. Decreasing the voxel size indefinitely may not improve resolution because of the diffusive nature of light propagation in the turbid medium. However, the computation time increases dramatically, which has been observed by other researchers [37]. The optimal voxel size for a given reconstruction problem will depend on factors, such as, target size, experimental geometry, and noise level.

Since the signal used in image reconstruction is taken to be the difference between the image recorded for a scan position and the background image, estimation of the background image is an important issue. This is a common problem for every diffuse optical imaging modality using perturbation method, and needs further elaboration. We accumulated data in the transillumination slab geometry, and generated the background image by averaging images for

all scan positions after proper alignment with respect to the incident source position. This averaging method for generating background image worked well for small targets that we used in our experiments, as the ratio of sample volume to target volume was quite high (~500:1). This volume ratio for breast and a tumor in early stages of growth will also be substantially high for the averaging method to be applicable. Assuming a scenario where the volume ratio is substantially smaller than in above examples, a modified approach would be to select recorded images which were minimally affected by embedded targets for averaging [38]. As long as the targets only occupy a limited volume within the host medium, a clean background image can be generated in this fashion. It should also be noted that while estimation of target optical properties, such as absorption coefficient and scattering coefficient, are sensitively dependent on background image estimation, estimation of target positions are not so sensitive.

Several alternative ways of generating background image are suggested in the literature. One experimental approach is to record image using a phantom that has the same average optical properties as the sample, such as human breast [39]. Along the same line, image of the healthy contralateral breast taken under the same experimental conditions as that of the suspect breast may be used as background image for breast imaging [40]. Some authors have suggested acquiring data at a wavelength for which the target(s) and the background have identical optical properties for assessing the background, *e.g.,* measurement using 805-nm light for which hemoglobin and oxy-hemoglobin have the same absorption coefficient may serve as background to image hemoglobin oxygenation[41]. Still another approach is to compute the background using an appropriate forward model [42]. Any of these approaches may be employed for generating the background image for use with the TROT formalism presented here.

The geometries commonly used in DOT include slab, cylindrical, hemispherical, and semi-infinite; and different source-detector combinations have been used to record images in these geometries. As long as multiple source-detector combinations provide multiple angular views of the sample the TROT formalism can be adapted to obtain target location for these geometries. TR imaging and TR-MUSIC was originally developed for reflection (backscattering) geometry that used coincident transceiver array to detect the return signal [7-9, 13, 14]. With requisite modification in the experimental arrangement TROT would be suited for use in the reflection geometry.

2.5.3. Results

2.5.3.1. *Single absorptive target at different depths*

In the first experiment, only one target was used, the lateral (x, y) position of the target was kept the same at (25.5 mm, 24.7 mm), while seven different depths (position along z-axis) of 15 mm, 20 mm, 25 mm, 30 mm, 35 mm, 40 mm and 45 mm were used. The eigenvalue spectrum plotted on logarithmic scale for the target at z = 30 mm is shown in Fig. 2.3. Similar eigenvalue spectra were obtained for other cases.

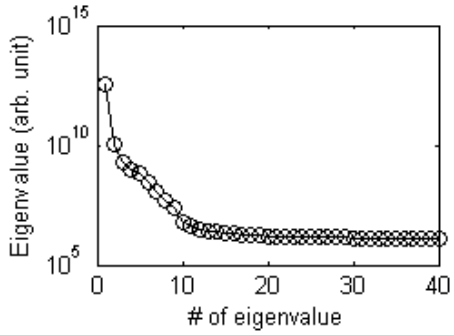

Fig. 2.3. A semi-log plot of eigenvalue spectrum with first 40 leading eigenvalues for the target at z = 30 mm

Both SDDS and DSSD pseudo spectra were calculated using Eq. (2.20). The target was identified as an absorptive target. In the DSSD pseudo spectrum, the absorptive pseudo value at

the peak position is ~41 times of the scattering pseudo value associated with $\partial_z g_d$, and even larger than those associated with $\partial_x g_d$, and $\partial_y g_d$, as shown in Table 2.2. Similarly in the SDDS scheme, the absorptive pseudo value at the peak position is ~33 times of the scattering pseudo value with $\partial_z g_d$, and much larger than the other two.

Table 2.2. Pseudo values associated with absorptive and scattering components at the peak position

Scheme with GFV (g)	Absorptive pseudo value	Scattering pseudo value		
		$\partial_x g$	$\partial_y g$	$\partial_z g$
DSSD (g_d)	1305.0	1.0	1.0	31.7
SDDS (g_s)	2729.3	14.0	1.1	81.6

Three-dimensional tomographic images were generated using the whole absorption pseudo spectrum for all voxel positions in the sample. The left pane of Fig. 2.4(a) shows a tomographic image for the target at z = 30 mm. The spatial profiles in the x, y and z directions, shown in the right pane of Fig. 2.4(a) were used to assess the target location. Similar images were generated for other depths. The retrieved target positions are compared with known positions in Table 2.3.

As is evident from Table 2.3, when DSSD scheme was used, the TROT-assessed lateral positions (x, y) were within 0.6 mm of the known values, which is an excellent agreement. The accuracy of the z-position was found to be optimal when the target was located in the middle plane of the sample, and deteriorated when the target was closer to the source plane or the detection plane. When using SDDS scheme, the TROT-assessed lateral positions were also within 0.6 mm of the known positions, except for z = 40 mm and 45 mm, where the error in y direction was 1.2 mm and 2 mm, respectively. However, remarkable improvement in the accuracy of the z-position

estimation was observed, the error Δz being within 0.5 mm for all cases except for z = 35 mm, where the error was 1.5 mm. We ascribe the superior performance of the scheme using T_{SDDS}, to the much larger size of the detector array (1024 × 1024) than that of the source array (9 × 9) used in the experimental arrangement.

Table 2.3. Positions of one absorptive target located at different depths

Known Positions x, y, z (mm)	DSSD Scheme		SDDS Scheme	
	Retrieved Positions x, y, z (mm)	Error $\Delta x, \Delta y, \Delta z$ (mm)	Retrieved Positions x, y, z (mm)	Error $\Delta x, \Delta y, \Delta z$ (mm)
25.5, 24.7, 15	24.9, 24.4, 17.5	0.6, 0.3, 2.5	24.9, 25.2, 15.5	0.6, 0.5, 0.5
25.5, 24.7, 20	25.7, 24.4, 21.5	0.2, 0.3, 1.5	24.9, 25.2, 20.5	0.6, 0.5, 0.5
25.5, 24.7, 25	25.7, 24.4, 26.5	0.2, 0.3, 1.5	25.7, 24.4, 24.5	0.2, 0.3, 0.5
25.5, 24.7, 30	25.7, 24.4, 30.5	0.2, 0.3, 0.5	25.7, 25.2, 29.5	0.2, 0.5, 0.5
25.5, 24.7, 35	25.7, 25.2, 33.5	0.2, 0.5, 1.5	24.9, 24.4, 36.5	0.6, 0.3, 1.5
25.5, 24.7, 40	24.9, 25.2, 36.5	0.6, 0.5, 3.5	24.9, 25.9, 40.5	0.6, 1.2, 0.5
25.5, 24.7, 45	24.9, 25.2, 39.5	0.6, 0.5, 5.5	24.9, 26.7, 45.5	0.6, 2.0, 0.5

It should be noted that the choice of either DSSD or SDDS scheme depends on experimental parameters, such as, the number and density of sources and detectors, and does not depend on the characteristics of the background medium. When more detectors than sources are used and inter-detector spacing is small, SDDS would provide better resolution than DSSD, and vice versa. However, due to the diffusive nature of light propagation in the turbid medium, increasing the

numbers and decreasing the spacing of the sources/detectors beyond a limit may not always improve the results.

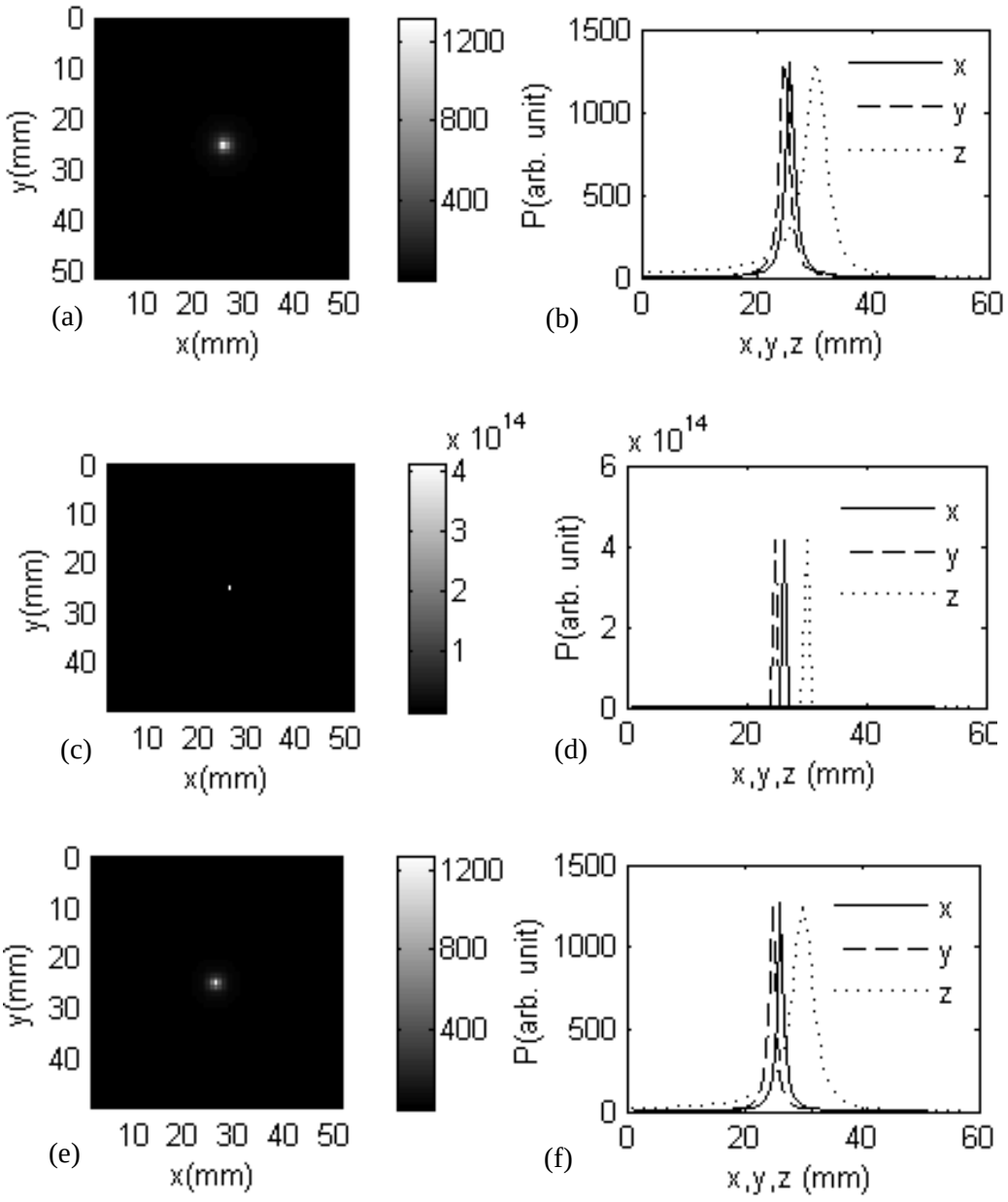

Fig. 2.4. Pseudo image of the target (left pane) and corresponding spatial intensity profiles (right pane) when the target is located at z = 30 mm: (a) and (b) experimental data; (c) and (d) simulation without any added noise; and (e) and (f) simulation with 20% Gaussian noise added. The pseudo values are calculated using Eq. (2.20).

While the target position could be obtained from the experimental data, it was observed that the difference between the smaller eigenvalues in the signal subspace and the larger eigenvalues in the noise subspace were not as pronounced as observed in the simulation in Section 4. To assess the effect of noise and to what extent noise may be present in the experimental data, we generated simulated data mimicking the experimental conditions, and added different noise levels. The lateral positions were (25.5 mm, 24.7 mm) and all seven *z*-positions (depth) of 15 mm, 20 mm, 25 mm, 30 mm, 35 mm, 40 mm, and 45 mm were tested. Typical pseudo images generated for z = 30 mm without and with 20% Gaussian multiplicative noise to compare with the experimental result are shown in Fig. 2.4(b) and Fig. 2.4(c), respectively. Simulated data provided the known position coordinates.

The simulated spatial profiles with zero added noise are much sharper than the profiles obtained from experimental data, or from simulated data with 20% added Gaussian noise. Broadening of spatial profile is an indication of the uncertainty in determination of position coordinates. Results from simulation show that uncertainty in position determination increases with added noise, and that experimental data behave in a way similar to simulated data with added noise.

2.5.3.2. ***Resolving two absorptive targets***

In the second experiment using two targets the depth (z) and height (y) were kept same (z = 30 mm, y = 26.0 mm), while three different center-to-center separations, Δx of ~12.6 mm, 17.6 mm, and 27.6 mm, between them along the x-axis were considered. A cross-sectional pseudo image of the targets when separated by a center-to-center distance of 27.6 mm, generated using the pseudo spectrum is shown in the left pane of Fig. 2.5 (a). Fig. 2.5(b) and 2.5(c) show similar images for the separation 17.6 mm and 12.6 mm (separation between nearest edges ~4 mm). The profiles in the x, y and z directions through the right target are shown in the right panes of Fig. 2.5(a) – Fig.

2.5(d). These profiles were used to assess locations of the targets, and the separation between the two targets. In all cases, the targets were determined to be absorptive, because peaks occurred in the pseudo spectrum with the GFVs corresponding to absorption property.

The known and retrieved positions from the experiments and separations Δx between the two targets appear in Table 2.4. In all the cases, the two targets were resolved, even when their center-to-center separation was 12.6 mm, nearest sides separated by only ~4 mm. For all retrieved positions, the maximum error in the lateral positions is 3.0 mm, and the maximum error in the axial positions is 1.5 mm. The errors in the lateral positions increase as the targets get closer. We ascribe this increase in error in the lateral position to the crosstalk between the two targets, the peak due to one target being affected by the other. The shift in the peaks is also affected by noise. When the two targets are very close or significant noise is present, the two peaks merge, so that the two targets are not resolved. This behavior was confirmed in simulations.

The results were compared with simulated data using similar conditions. For the more challenging case of two targets located at z = 30 mm and separated by 12.6 mm, exact target locations were found when no noise was added. With 10% noise present, the positions of the two targets were found to be (39.0 mm, 24.8 mm, 29.0 mm) and (30.0 mm, 24.8 mm, 29.0 mm) with target separation 9.0 mm, compared to 12.6 mm (known) and 6.9 mm retrieved from experiment. The pseudo image and the corresponding profiles through the right target are shown in Fig. 2.5(d). Similar images were also obtained for the left target. The retrieved separation between the two targets in simulation with 10% noise was smaller than the actual separation. But the error was less than the experimental result. However, when 20% noise was added, the two peaks merged (not shown here).

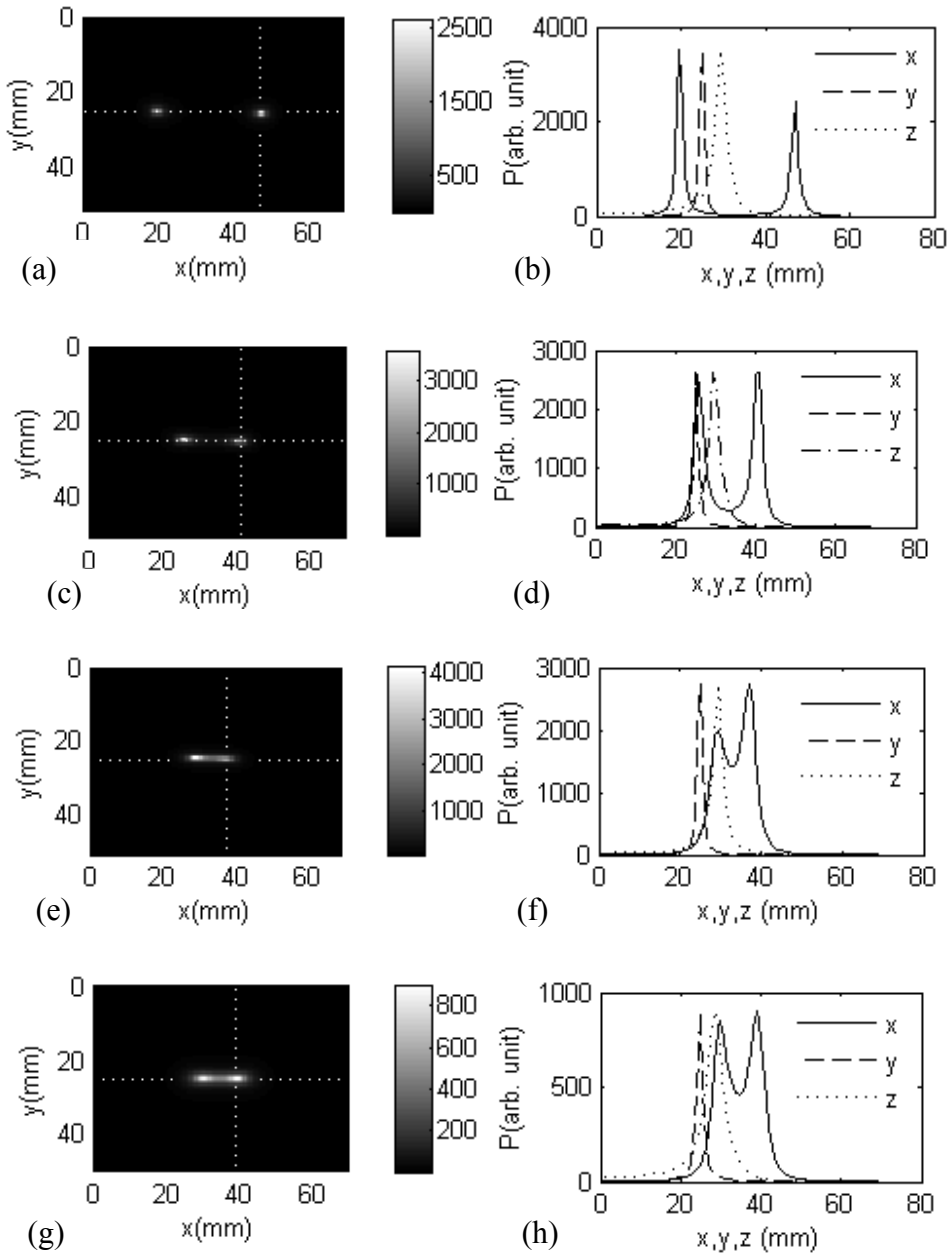

Fig. 2.5. (Experiment): TROT generated cross-section pseudo images when the targets are separated by 27.6 mm, 17.6 mm, and 12.6 mm are shown in (a), (c) and (e), respectively; and pseudo-value profiles through the right target along *x*, *y* and *z* directions are shown in (b), (d) and (f), respectively. (Simulation): TROT generated cross-section pseudo image when two targets are separated by 12.6 mm is shown in (g) and the corresponding pseudo-value profiles are plotted in (h). In simulation 10% Gaussian noise is added for comparison with the experimental results. *P* is pseudo value calculated using Eq. (2.20).

Table 2.4. Positions of two targets separated by different distances

Known Separation [Δx (mm)]	Target #	Known Position [x, y, z (mm)]	Retrieved Position [x, y, z (mm)]	Error (mm)	Retrieved Separation [Δx (mm)]
12.6	1	27.6, 26.0, 30	30.3, 24.4, 28.5	2.7, 1.6, 1.5	6.9
	2	40.2, 26.0, 30	37.2, 25.2, 29.5	3.0, 0.8, 0.5	
17.6	1	25.1, 26.0, 30	26.4, 24.4, 28.5	1.3, 1.6, 1.5	14.6
	2	42.7, 26.0, 30	41.0, 25.2, 29.5	1.7, 0.8, 0.5	
27.6	1	20.1, 26.0, 30	19.5, 25.2, 29.5	0.6, 0.8, 0.5	27.6
	2	47.7, 26.0, 30	47.1, 25.2, 30.5	0.6, 0.8, 0.5	

The limits on the size of targets, separation between the targets, and the target-to-background contrast ratio that are needed to detect and locate the targets depend on noise level, experimental parameters (such as, number and concentration of sources and detectors), and ultimately on the diffuse nature of light propagation in the turbid medium.

2.5.3.3. ***Single scattering target at different depths***

The experiment involving the third sample is the same as the first one except that the target was scattering in nature. The scattering target was a 10-mm diameter glass sphere filled with Intralipid-20% suspension in water, whose concentration was adjusted to provide l_t = ~0.25 mm, μ_s = 11.3 mm^{-1}. The same scanning and data acquisition scheme was used as for the absorptive targets and the following z-positions of the target were used: 15 mm, 20 mm, 25 mm, 30 mm, 35 mm, 40 mm, and 45 mm. DSSD scheme was used to calculate the pseudo spectrum. A cross-section pseudo image and the corresponding spatial profiles are displayed in Fig. 2.6(a) when z =

30 mm. It is compared to the simulation results with 20% Gaussian noise (Fig. 2.6(b)). The lateral (x, y) spatial profiles of the pseudo image generated using simulated data are considerably wider, while the axial (z) spatial profile is narrower than those obtained using experimental data, and the peak values from the two cases are of the same order. The retrieved target positions are listed in Table 2.5. SDDS scheme was also used and provided with similar results.

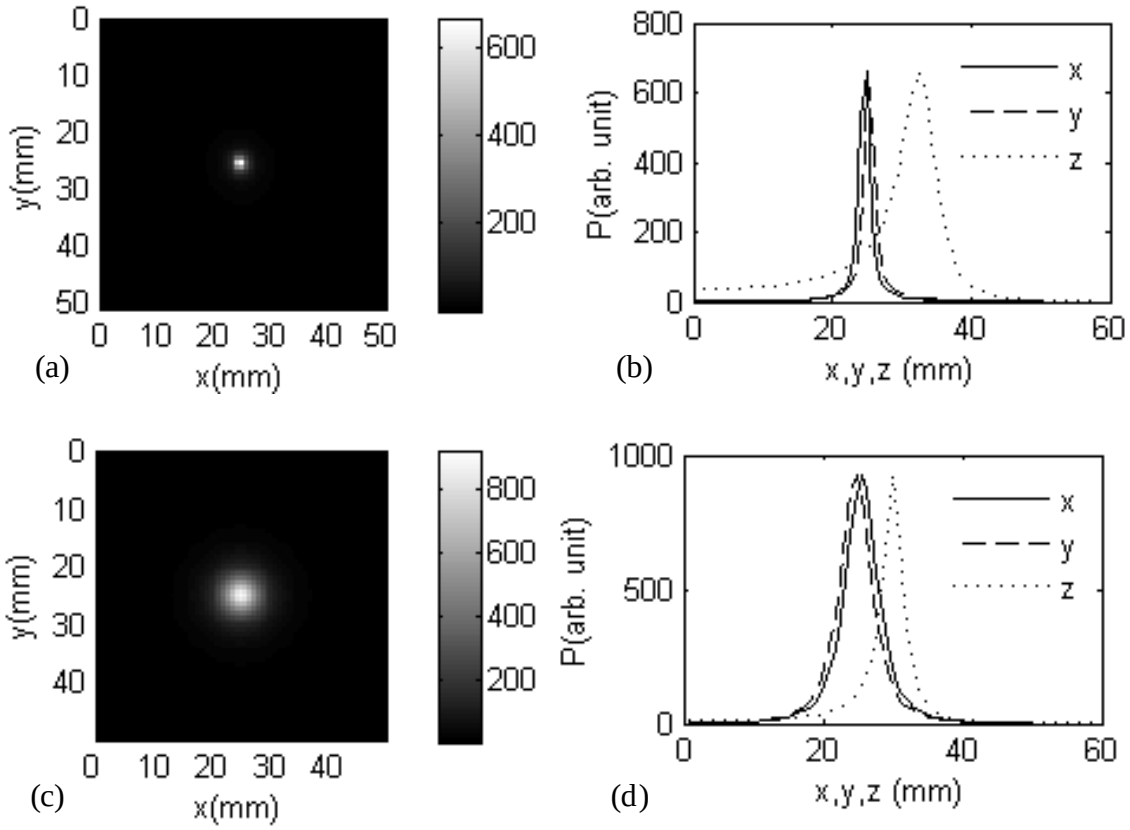

Fig. 2.6. Pseudo image of the target (a) and corresponding spatial intensity profiles (b) when the target is located at z = 30 mm: (a) and (b) experimental data; (c) and (d) simulation with 20% Gaussian noise added. *P* is pseudo value calculated using Eq. (2.20).

In Fig. 2.5, and more prominently in Fig. 2.6, the image resolution seems better for experimental data than simulated data. Since the peak values and bandwidth of lines (the poles)

in the pseudo spectrum depend strongly on the noise, this difference in image resolution is presumably due to lower noise level in the experiments than that used in simulations.

Table 2.5. Positions of one scattering target located at different depths

Known Positions [x, y, z (mm)]	Retrieved Positions [x, y, z (mm)]	Error (mm)
25.7, 24.5, 15	24.9, 25.9, 18.5	0.8, 1.4, 3.5
25.7, 24.5, 20	27.2, 26.7, 20.5	1.5, 2.2, 0.5
25.7, 24.5, 25	25.7, 26.7, 23.5	0.0, 2.2, 1.5
25.7, 24.5, 30	24.9, 25.2, 32.5	0.8, 0.7, 2.5
25.7, 24.5, 35	24.9, 25.2, 36.5	0.8, 0.7, 1.5
25.7, 24.5, 40	24.9, 25.9, 41.5	0.8, 1.4, 1.5
25.7, 24.5, 45	24.9, 25.9, 45.5	0.8, 1.4, 0.5

A comparison of experimental results for scattering and absorptive targets validate the common notion that it is more challenging to locate and image scattering targets than absorptive targets in a highly scattering medium. Also the lateral (x, y) positions are determined with higher accuracy than the axial (z) position. Overall the TROT-retrieved target positions are in good agreement with the known positions.

2.6. Illumination and detection schemes

In this section we will evaluate how the resolution of TROT depends on the scanning (source) and acquisition (detector) arrangements, and the difference in the resolution between SDDS and DSSD, using simulation. A 40-mm thick uniform scattering slab was used as the background

medium. Its absorption and diffusion coefficients were taken to be μ_a = 0.003 mm^{-1} and D = 1/3 mm (transport mean free path, l_t = 1 mm), respectively. Two absorptive point targets were embedded and placed at (30, 40, 20) mm and (50, 40, 20) mm. 50% additive Gaussian noise was added. Sources and detectors were placed on the opposite sides of the slab. The positions and numbers of sources and detector were varied to generate different data for subsequent analysis. Two peaks in the pseudo spectrum were generated corresponding to the two targets. The results (resolution) were evaluated by comparing the retrieved positions (separation and the z position) of the two targets and the contrast, which is defined to be (I_{max} - I_{min}) / (I_{max} + I_{min}), I_{max} is the average of the two peaks corresponding to the two targets, and I_{min} is the valley between the two peaks.

2.6.1. Noise

In simulated data, either additive or multiplicative noise could be added. Additive Gaussian noise is expressed as $X(\boldsymbol{r}) = X_0(\boldsymbol{r}) + \delta(\boldsymbol{r})$, where $X_0(\boldsymbol{r})$ is the pure signal at $\boldsymbol{r}$, δ is the random noise, the statistics of which follows Gaussian distribution; while multiplicative Gaussian noise is expressed as $X(\boldsymbol{r}) = X_0(\boldsymbol{r})\,(1 + \delta(\boldsymbol{r}))$, where the ratio $\delta(\boldsymbol{r})$ is the random variable and $X_0(\boldsymbol{r})\delta(\boldsymbol{r})$ is the noise added at $\boldsymbol{r}$. To check the difference between the additive and multiplicative noise, 50% additive or multiplicative Gaussian noise was added, and singular value decomposition (SVD) was used to decompose the data. The first three components retrieved by SVD are shown in Fig. 2.7 and Fig. 2.8 for additive and multiplicative Gaussian noise, respectively. The corresponding singular values are shown in Fig. 2.9. When multiplicative noise was added, the third component carried some signal and showed some "pattern" in the 2D distribution. The higher order singular values (SV) in the SV spectrum with multiplicative noise are higher, and approaching the 2nd singular value, compared to the case with additive noise.

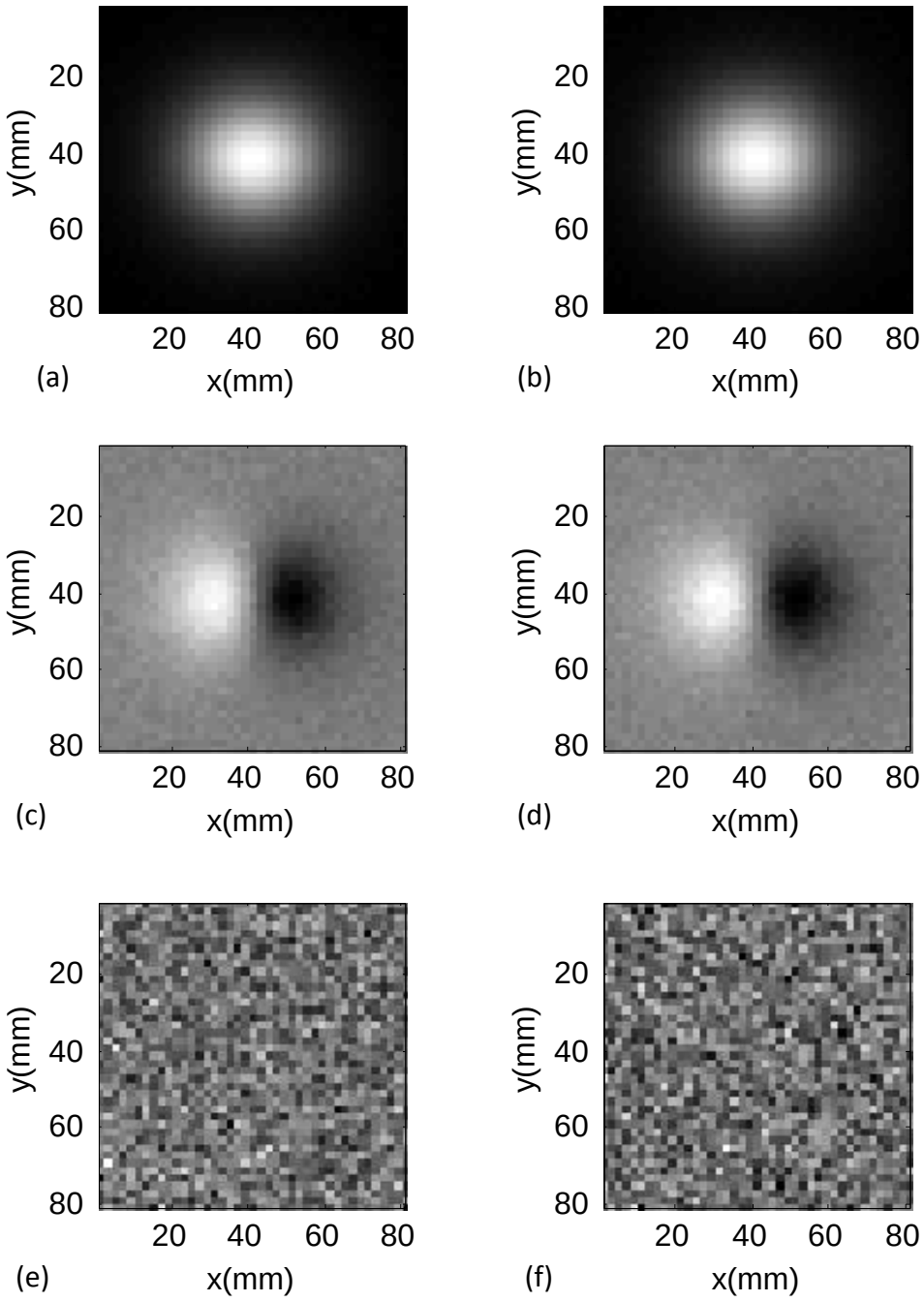

Fig. 2.7. (a), (c) and (e) are the three singular components on the detector plane retrieved by SVD from simulated data with additive noise; (b), (d) and (f) are the corresponding components on the source plane.

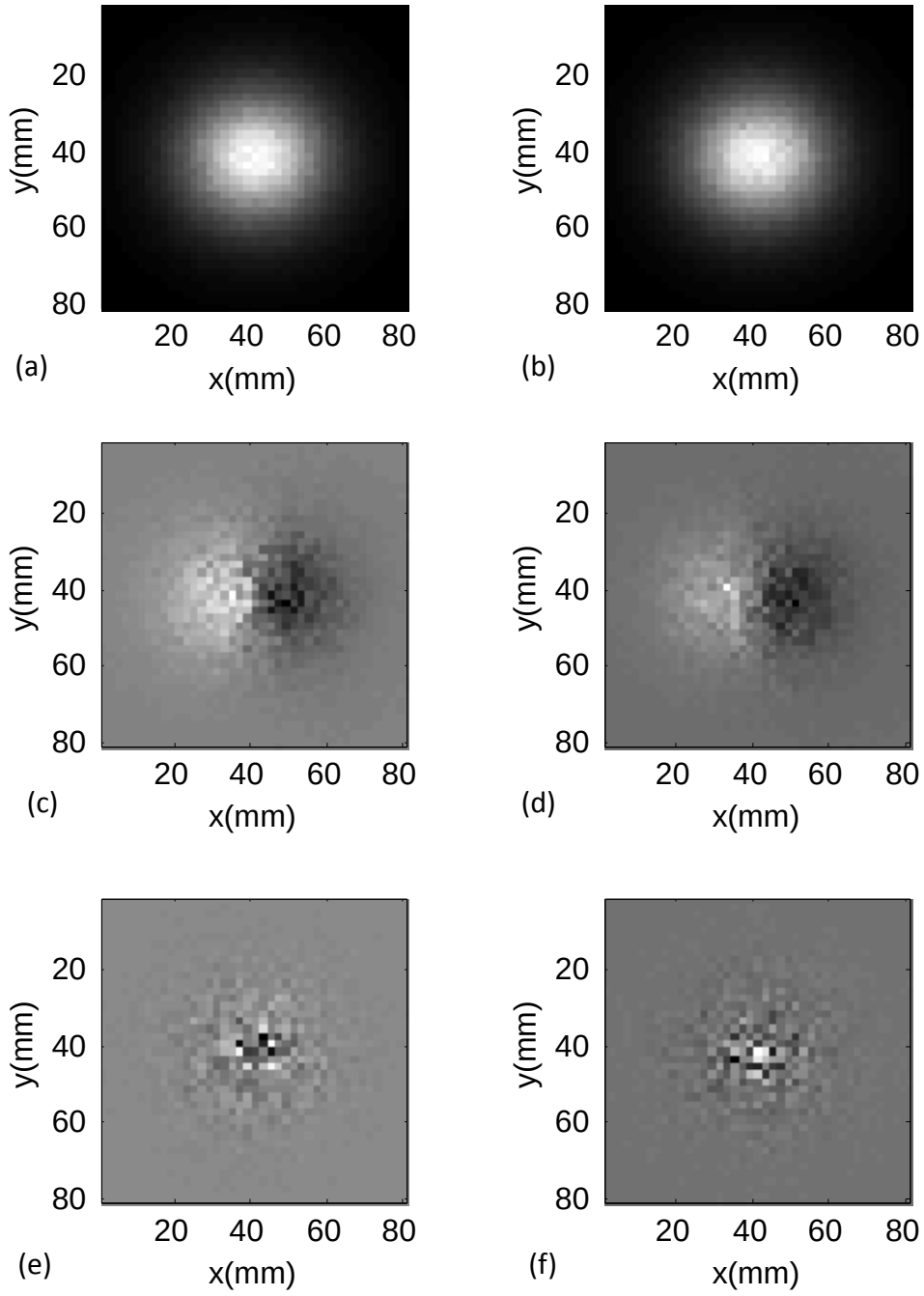

Fig. 2.8. (a), (c) and (e) are the three components on the detector plane with multiplicative noise; (b), (d) and (f) are the corresponding components on the source plane.

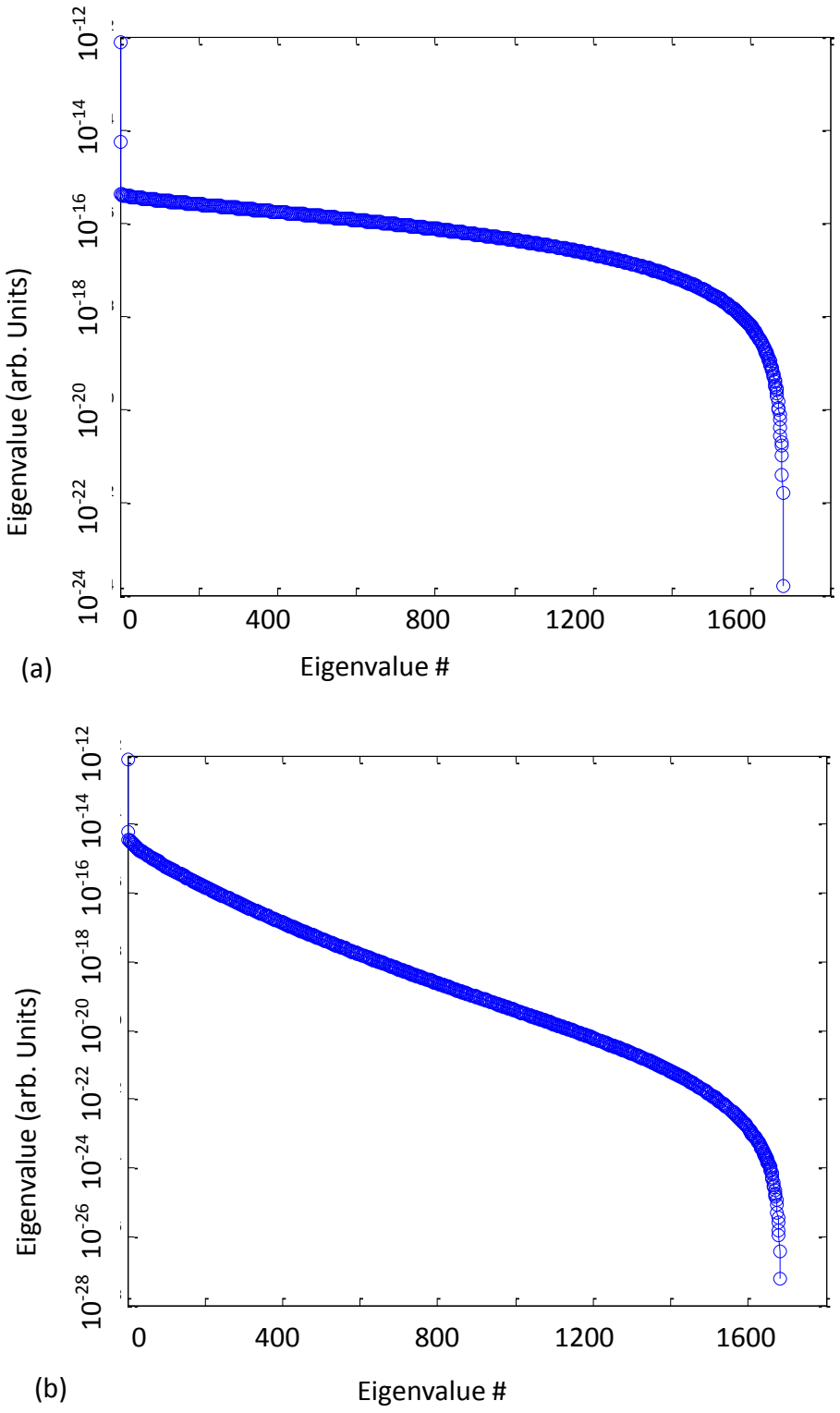

Fig. 2.9. The singular values retrieved by SVD from simulative data with the presence of (a) additive and (b) multiplicative noise, respectively.

Since in the experimental condition the random noise was expected to be a uniformly distributed Gaussian white noise, the additive noise model was used in this study.

2.6.2. Results

Different number and spacing of sources and detectors were used to generate simulative data. Both the areas covered by the grid points where the sources and detectors are located, are centered. Both SDDS and DSSD were used to analyze for each source/detector configuration, and the results are shown in Table 2.6 and 2.7, respectively.

Table 2.6. SDDS TROT retrieved target information

Sources;Spacing (mm)	Detectors;Spacing (mm)	Left Target (x, y, z) (mm)	Right Target (x, y, z) (mm)	Separation (mm)	Contrast
41×41;2	33×33;2.5	18, 21, 22	24, 21, 22	6	0.1812
51×51;1.6	33×33;2.5	17, 21, 22	25, 21, 22	8	0.2070
17×17;1.25	41×41;2	N/A	N/A	Not resolved	N/A
17×17;5	41×41;2	17, 21, 22	25, 21, 22	8	0.2718
33×33;2.5	41×41;2	17, 21, 22	25,21, 22	8	0.3182
41×41;1	41×41;2	17, 21, 22	25, 21, 22	8	0.3397
41×41;2	41×41;2	17, 21, 22	25, 21, 22	8	0.3407
41×41;3	41×41;2	17, 21, 22	25, 21, 22	8	0.3237
51×51;1.6	41×41;2	17, 21, 22	25, 21, 22	8	0.3478
41×41;2	41×41;1	17, 21, 22	25, 21, 22	8	0.3852
41×41;2	41×41;3	17, 21, 22	25, 21, 22	8	0.3234

41×41;1	41×41;1	16, 21, 21	26, 21, 21	10	0.6805
41×41;3	41×41;3	17, 21, 22	25, 21, 22	8	0.3182
17×17;5	51×51;1.6	17, 21, 22	26, 21, 21	9	0.4312
33×33;1.25	51×51;1.6	16, 21, 21	25, 21, 22	9	0.4645
33×33;2.5	51×51;1.6	16, 21, 21	26, 21, 21	10	0.6416
41×41;2	51×51;1.6	16, 21, 21	25, 21, 22	9	0.4689
33×33;5	51×51;1.6	16, 21, 21	26, 21, 21	10	0.6207
33×33;2.5	51×51;0.8	16, 21, 21	26, 21, 21	10	0.6978
33×33;2.5	51×51;3.2	16, 21, 21	25, 21, 22	9	0.6089
17×17;1.25	101×101;2	17, 21, 22	25, 21, 22	8	0.4732
17×17;1.25	101×101;0.8	16, 21, 21	26, 21, 21	10	0.6843
17×17;1.25	101×101;0.4	16, 21, 21	26, 21, 21	10	0.8827
17×17;1.25	101×101;0.2	16, 21, 21	26, 21, 21	10	0.9508
17×17;1.25	101×101;0.1	16, 21, 21	26, 21, 21	10	0.9323
17×17;1.25	51×51;0.2	16, 21, 21	26, 21, 21	10	0.7444
17×17;1.25	101×101;0.05	16, 21, 21	26, 21, 21	10	0.7759
17×17;5	101×101;0.4	16, 21, 21	26, 21, 21	10	0.8799
101×101;0.4	17×17;2.5	N/A	N/A	Not resolved	N/A

Table 2.7. DSSD TROT retrieved target information

Sources;Spacing (mm)	Detectors;Spacing (mm)	Left Target (x, y, z) (mm)	Right Target (x, y, z) (mm)	Separation (mm)	Contrast
17×17;2.5	101×101;2	N/A	N/A	Not resolved	N/A
17×17;2.5	101×101;0.8	N/A	N/A	Not resolved	N/A
17×17;2.5	101×101;0.4	N/A	N/A	Not resolved	N/A
17×17;2.5	101×101;0.2	N/A	N/A	Not resolved	N/A
17×17;2.5	101×101;0.1	N/A	N/A	Not resolved	N/A
17×17;5	101×101;0.4	N/A	N/A	Not resolved	N/A
17×17;1.25	101×101;0.4	N/A	N/A	Not resolved	N/A
33×33;5	51×51;1.6	18, 21, 20	24, 21, 20	6	0.1791
33×33;2.5	41×41;2	24, 21, 20	18, 21, 20	6	0.1819
33×33;2.5	51×51;3.2	18, 21, 20	24, 21, 20	6	0.1806
33×33;2.5	51×51;1.6	18, 21, 20	25, 21, 20	7	0.1943
33×33;2.5	51×51;0.8	17, 21, 20	25, 21, 20	8	0.2276
33×33;1.25	51×51;1.6	17, 21, 20	25, 21, 20	8	0.2381
41×41;3	41×41;3	17, 21, 20	25, 21, 20	8	0.2992
41×41;3	41×41;2	17, 21, 20	25, 21, 20	8	0.3177
41×41;2	51×51;1.6	17, 21, 20	25, 21, 20	8	0.3341
41×41;2	41×41;3	17, 21, 20	25, 21, 20	8	0.3174
41×41;2	41×41;2	17, 21, 20	25, 21, 20	8	0.3391
41×41;2	41×41;1	17, 21, 20	25, 21, 20	8	0.3466

41×41;2	33×33;2.5	17, 21, 20	25, 21, 20	8	0.3429
41×41;1	41×41;2	17, 21, 20	25, 21, 20	8	0.3670
41×41;1	41×41;1	16, 21, 20	26, 21, 20	10	0.6795
51×51;1.6	17×17;5	16, 21, 21	25, 21, 20	9	0.4148
51×51;1.6	33×33;2.5	16, 21, 20	26, 21, 20	10	0.6385
51×51;1.6	41×41;2	16, 21, 20	26, 21, 20	10	0.6359
101×101;0.4	17×17;2.5	16, 21, 21	26, 21, 21	10	0.9323

In general, for both the source and detector sides, the following two cases provide more information and therefore may result in better resolution: (a) the spacing between sources (detectors) stays the same, while the number of sources (detectors) increases therefore a larger source (detector) plane is covered; (b) the area of the source (detector) plane stays the same, while the spacing between sources (detectors) decreases therefore the number of sources (detectors) increases. However, due to the diffusive nature of light propagation, increase in the area of the source (detector) plane or decrease in the source (detector) spacing may not always result in improvement in the resolution. For SDDS, if the number of sources is fixed, there is a trade-off between the area covered by the detectors and the spacing between them; and it is also the case for DSSD. For example, for SDDS, when the (17×17;1.25) (17 rows 17 columns with 1.25-mm spacing, covering 20mm×20mm area) source configuration is used, compared to the detector configuration (51×51;0.2) (covering 10mm×10mm), both (101×101;0.2) (covering 20mm×20mm) and (101×101;0.1) (covering 10mm×10mm) detector configurations, which have larger area with same spacing and same area with smaller spacing, respectively, showed better results. If the number of detector is fixed to be 101×101, compared to 0.2mm spacing, both configurations with spacing of 0.05mm and 2mm, which provide smaller spacing with smaller

area and larger spacing with larger area respectively, showed worse results. Tables 2.6 and 2.7 indicate that SDDS scheme strongly depends on the number and arrangement of detectors, while DSSD depends strongly on the number and arrangement of sources. If the detector side has more information than source side, SDDS has better results than DSSD, and *vice versa*. If source and detector sides have similar configuration, SDDS and DSSD provide similar results.

In general, sources and detectors that are located closer to the targets should provide signal that carries more target information. If the targets are close to each other, smaller spacing of sources (detectors) could provide with more detailed information of the region where targets are located. The target information is mainly recorded by the sources (detectors) nearby the target(s), while the sources (detectors) that are further away carry less target information, since the diffusive light decays over distance. In this case, the results may not benefit much from a larger source (detector) plane covered by more sources (detectors) with same spacing.

In a realistic experiment, if the number of sources (detectors) is given, larger area of source (detector) plane or smaller spacing of sources (detectors), which provides better resolution, varies from one case to another.

2.7. Discussion

This chapter presents the development of time reversal imaging approach with subspace classification, MUSIC in the optical domain. The results from experiment and simulation show that TROT is a faster and less computation intensive approach for detecting small targets in highly scattering turbid media and determining their locations in 3-*D* than other inverse image reconstruction techniques. While the dominant features in the pseudo spectrum are related to the square of the difference between the absorption (scattering) coefficient of the targets and that of the background, the approach does not directly determine these parameters. It is common for IIR

approaches to estimate the optical properties of every voxel in the sample and identify target(s) from differences of these properties between the sample and the target(s), which is a considerably computation intensive undertaking. On the contrary, TROT identifies the targets as poles of the pseudo spectrum and focuses on determining their positions, which do not require as much computation time. Other IIR approaches involve iteration, while TROT is non-iterative. In TROT the dimension of the involved matrices is lower compared to other IIR approaches, which enables analysis and utilization of very large datasets. These two features together make TROT faster. Fast image reconstruction algorithms are of particular interest.

It was observed that lateral (x, y) positions are better determined than the depth (z). Also the spatial profile is more spread out along z compared to that along x, y. We ascribe this difference to fewer data along z-direction compared to those along x-y planes. Addition of another set of data with light incident and signal collected perpendicular to the z-direction is expected to further improve resolution in this dimension. Even without that addition, TROT determines the target position well.

While we have used slab geometry and CW illumination, the TROT approach may be used for other geometries (such as, cylindrical, and spherical), different types of illumination (e.g. frequency domain and pulsed) and different models for light propagation through the medium. Application and adaption of the TROT formalism to inhomogeneous media and extended targets may require careful consideration of several factors. In a non-uniform, inhomogeneous medium, structures other than the desired targets may appear as "false targets" and may interfere with identification of "real targets". However, as long as the contributions to the signal by any false target is smaller than that made by real targets, TROT with MUSIC will be useful in detecting and locating targets, by choosing a proper threshold to separate the signal and noise subspaces.

What is even more important, expected wavelengths dependence of the target spectroscopic properties could be used to assess the difference between the real and false targets in experiments using multi-wavelength interrogation of the sample.

The TROT formalism presented in this chapter is particularly suited for point-like targets requiring fewer eigenvectors in the signal subspace to construct a pseudo spectrum. However, for extended finite-size targets, the formalism needs to be modified and much more eigenvectors may be needed to calculate the pseudo spectrum [19, 43, 44]. These interesting problems for further study are currently being pursued.

References

1. W. Cai, M. Alrubaiee, S. K. Gayen, M. Xu, and R. R. Alfano, "Three-dimensional optical tomography of objects in turbid media using the round-trip matrix," Proc. SPIE **5693**, 4-9 (2005).
2. Binlin Wu, M. Alrubaiee, W. Cai, M. Xu, and S. K. Gayen, "Optical imaging of objects in turbid media using principal component analysis and time reversal matrix methods," in *Computational Optical Sensing and Imaging, OSA Technical Digest (CD) (Optical Society of America, 2009), paper JTuC10* (San Jose, California, 2009).
3. Binlin Wu, W. Cai, M. Alrubaiee, M. Xu, and S. K. Gayen, "Three dimensional time reversal optical tomography," Proc. SPIE **7892**, 78920G (2011).
4. C. Prada, F. Wu, and M. Fink, "The iterative time reversal mirror: a solution to self-focusing in the pulse echo mode," J. Acoust. Soc. Am. **90**, 1119-1129 (1991).
5. M. Fink, C. Prada, F. Wu, and D. Cassereau, "Self-focusing in inhomogeneous media with time-reversal acoustic mirrors," Proc. IEEE Ultrason. Symp. **2**, 681-686 (1989).

6. M. Fink, "Time reversal of ultrasonic fields -- part I: basic principles," IEEE Trans. Ultrason. Ferroelec. Freq. Control **39**, 555-556 (1992).

7. M. Fink, "Time reversal mirrors," J. Phys. D: Appl. Phys. **26**, 1333-1350 (1993).

8. C. Prada, J.-L. Thomas, and M. Fink, "The iterative time reversal process: analysis of the convergence," J. Acoust. Soc. Am. **97**, 62-71 (1995).

9. F. K. Gruber, E. A. Marengo, and A. J. Devaney, "Time-reversal-based imaging and inverse scattering of multiply scattering point targets," J. Acoust. Soc. Am. **118**, 3129-3138 (2005).

10. M. Fink, D. Cassereau, A. Derode, C. Prada, P. Roux, M. Tanter, J.-L. Thomas, and F. Wu, "Time-reversed acoustics," Rep. Prog. Phys. **63**, 1933-1995 (2000).

11. W. A. Kuperman, W. S. Hodgkiss, H. C. Song, T. Akal, C. Ferla, and D. R. Jackson, "Phase conjugation in the ocean: experimental demonstration of an acoustic time reversal mirror," J. Acoust. Soc. Am. **103**, 25-40 (1998).

12. G. Lerosey, J. de Rosny, A. Tourin, and M. Fink, "Focusing beyond the diffraction limit with far-field time reversal," Science **315**, 1120-1122 (2007).

13. A. J. Devaney, "Super-resolution processing of multi-static data using time reversal and MUSIC," (available online: http://www.ece.neu.edu/faculty/devaney/) (2000).

14. H. Lev-Ari, and A. J. Devaney, "The time reversal techniques re-interpreted: subspace-based signal processing for multi-static target location," in *Proc. IEEE sensor array and multichannel signal processing workshop*(2000), pp. 509-513.

15. S. K. Lehman, and A. J. Devaney, "Transmission mode time-reversal super-resolution imaging," J. Acoust. Soc. Am. **113**, 2742-2753 (2003).

16. F. K. Gruber, E. A. Marengo, and A. J. Devaney, "Time-reversal imaging with multiple signal classification considering multiple scattering between the targets," J. Acoust. Soc. Am. **115**, 3042-3047 (2004).

17. C. Prada, and J. Thomas, "Experimental subwavelength localization of scatterers by decomposition of the time reversal operator interpreted as a covariance matrix," J. Acoust. Soc. Amer. **114**, 235-243 (2003).

18. P. C. Hansen, "Analysis of discrete ill-posed problems by means of the *L*-curve," SIAM Rev. **34**, 561-580 (1992).

19. E. A. Marengo, F. K. Gruber, and F. Simonetti, "Time reversal MUSIC imaging of extended targets," IEEE Trans. Image Process. **16**, 1967-1984 (2007).

20. W. Cai, S. K. Gayen, M. Xu, M. Zevallos, M. Alrubaiee, M. Lax, and R. R. Alfano, "Optical tomographic image reconstruction from ultrafast time-sliced transmission measurements," Appl. Opt. **38**, 4237-4246 (1999).

21. A. Ishimaru, "Diffusion of a pulse in densely distributed scatterers," J. Opt. Soc. Am. **68**, 1045-1050 (1978).

22. K. Furutsu, "Diffusion equation derived from the space-time transport equation," J. Opt. Soc. Am. **70**, 360-366 (1980).

23. M. S. Patterson, B. Chance, and B. C. Wilson, "Time resolved reflectance and transmittance for the non-invasive measurement of tissue optical properties," Appl. Opt. **28**, 2331-2336 (1989).

24. S. Chandrasekhar, *Radiative Transfer* (Clarendon Press, Oxford, 1950).

25. A. Ishimaru, *Wave Propagation and Scattering in Random Media, Volume 1: Single Scattering and Transport Theory* (Academic, New York, 1978).

26. S. R. Arridge, and J. C. Schotland, "Optical tomography: forward and inverse problems," Inverse Probl. **25**, 123010 (2009).

27. S. R. Arridge, "Photon-measurement density functions. part I: analytical forms," Appl. Opt. **34**, 7395-7409 (1995).

28. M. Xu, M. Alrubaiee, S. K. Gayen, and R. R. Alfano, "Three-dimensional localization and optical imaging of objects in turbid media using independent component analysis," Appl. Opt. **44**, 1889-1897 (2005).

29. R. C. Haskell, L. O. Svaasand, T.-T. Tsay, T.-C. Feng, M. S. McAdams, and B. J. Tromberg, "Boundary conditions for the diffusion equation in radiative transfer," J. Opt. Soc. Am. A **11**, 2727-2741 (1994).

30. M. Lax, V. Nayaramamurti, and R. C. Fulton, "Classical diffusion photon transport in a slab," in *Laser Optics of Condensed Matter*, J. L. Birman, H. Z. Cummins, and A. A. Kaplyanskii, ed. (Plenum, NewYork, 1987), pp. 229-237.

31. C. Prada, S. Manneville, D. Spoliansky, and M. Fink, "Decomposition of the time reversal operator: detection and selective focusing on two scatterers," J. Acoust. Soc. Am. **99**, 2067-2076 (1996).

32. A. J. Devaney, "Time reversal imaging of obscured targets from multistatic data," IEEE Trans. Antenn. Propag. **53**, 1600-1610 (2005).

33. N. Bourbaki, *Topological Vector Spaces: Chapters 1-5* (Springer-Verlag, Berlin-Heidelberg-New York, 1987).

34. H. J. v. Staveren, C. J. M. Moes, J. v. Marle, S. A. Prahl, and M. J. C. v. Gemert, "Light scattering in Intralipid-10% in the wavelength range of 400--1100 nm," Appl. Opt. **31**, 4507-4514 (1991).

35. C. Bordier, C. Andraud, J. Lafait, E. Charron, M Anastasiadou, and A. de Martino, "Illustration of a bimodal system in Intralipid 20% by polarized light scattering: experiments and modelling," Appl. Phys. A **94**, 347-355 (2008).

36. I. Driver, J. W. Feather, P. R. King, and J. B. Dawson, "The optical properties of aqueous suspensions of Intralipid, a fat emulsion," Phys. Med. Biol. **34**, 1927-1930 (1989).

37. S. D. Konecky, G. Y. Panasyuk, K. Lee, V. Markel, A. G. Yodh, and J. C. Shotland, "Imaging complex structures with diffuse light," Opt. Express **16**, 5048-5060 (2008).

38. M. Xu, Y. Pu, and W. Wang, "Clean image synthesis and target numerical marching for optical imaging with backscattering light," Biomed. Opt. Express **2**, 850-857 (2011).

39. T. Nielsen, B. Brendel, R. Ziegler, M. van Beek, F. Uhlemann, C. Bontus, and T. Koehler, "Linear image reconstruction for a diffuse optical mammography system in a noncompressed geometry using scattering fluid," Appl. Opt. **48**, D1-D13 (2009).

40. Y. Ardeshirpour, N. Biswal, A. Aguirre, and Q. Zhu, "Artifact reduction method in ultrasound-guided diffuse optical tomography using exogenous contrast agents," J. Biomed. Opt. **16**, 046015 (2011).

41. B. W. Pogue, M. S. Patterson, H. Jiang, and K. D. Paulsen, "Initial assessment of a simple system for frequency domain diffuse optical tomography," Phys. Med. Biol. **40**, 1709-1729 (1995).

42. A. Poellinger, J. C. Martin, S. L. Ponder, T. Freund, B. Hamm, U. Bick, and F. Diekmann, "Near-infrared laser computed tomography of the breast: first clinical experience," Acad. Radiol. **15**, 1545-1553 (2008).

43. S. Hou, K. Solna, and H. Zhao, "Imaging of location and geometry for extended targets using the response matrix," J. Comput. Phys. **199**, 317-338 (2004).

44. F. K. Gruber, and E. Marengo, "Reinterpretation and enhancement of signal-subspace-based imaging methods for extended scatterers," SIAM J. Imaging Sciences **3**, 434-461 (2010).

Chapter 3

Time reversal optical tomography: retrieval of properties of targets in turbid media

3.1. Introduction

Time Reversal Optical Tomography (TROT) has been developed [1] to detect and locate small absorptive and scattering targets embedded in an optically thick highly scattering turbid medium , as detailed in Chapter 2. The method was based on Diffusion Approximation of the Radiative Transfer Equation (RTE) to describe light propagation in a highly scattering turbid medium, and a Time Reversal (TR) Multiple-Signal-Classification (MUSIC) algorithm developed by other groups in acoustics and radar applications [2-7]. In this chapter, we extend the TROT approach further to estimate size and optical properties of targets including point-like and finite-size small targets.

When an extended target is present, the dimension of the signal subspace spanned by the eigenvectors of the TR matrix is expected to be higher than one for a point target. Hou *et al.* developed algorithms with TR-MUSIC approach to detect and find the shape of an extended target using a sonar or a radar system for remote sensing applications. In one approach [4], a proper threshold was determined to separate the eigenvectors of the TR matrix in the signal subspace from the noise subspace. Then the pseudo spectrum was calculated to generate the image of the extended target. Another approach [5] used the first eigenvector of the TR matrix to calculate the MUSIC pseudo spectrum, the maximum of which provided an estimate of the position of the extended target. This approach used a level set method (LSM) [8-10] which is a numerical method for following evolution of interfaces (contours). A prescribed appropriate

continuous level set function $\varphi(\boldsymbol{r}, t)$, such as a signed-distance function, was used to describe the domain Ω or surface $\partial\Omega$ (shape of the target), where $\boldsymbol{r}$ is the position of any point in the space and t is (pseudo-) time: $\varphi(\boldsymbol{r}, t) = 0$ for the points on $\partial\Omega$, $\varphi(\boldsymbol{r}, t) < 0$ and $\varphi(\boldsymbol{r}, t) > 0$ for the interior and exterior points of $\partial\Omega$, respectively. The surface was updated by solving an advection level set equation (Hamilton-Jacobi equation), $\partial\varphi/\partial t + v_n|\nabla\varphi| = 0$, where v_n is the velocity function defined in the outward normal direction according to the gradient descent. Using retrieved target position as *a priori* information to initialize the level set function φ. a surface is repeatedly generated as an estimate of the boundary of the target to calculate the data matrix using the forward model. The surface was optimized by minimizing the difference (residue) between the calculated data matrix and actual data matrix which was either obtained from experiment or simulation.

Marengo and Gruber *et al.* introduced a TR-MUSIC approach using angles and distances between subspaces to find the size and shape of an extended target for radar and acoustic remote sensing [6, 7]. In one of the approaches, the target position was first determined using the maximum in the pseudo spectrum. Then contours in the pseudo spectrum were used as test boundaries of the target which corresponds to "test spaces". The optimal surface was determined by maximizing the orthogonality between the "test spaces" and the noise subspace of the TR matrix. In another similar approach [6, 7], instead of using the contours in the pseudo spectrum, a level set method was used to generate the test surfaces.

The main difference between the approaches developed by the two groups is that different ways were used to evaluate and optimize the surfaces (contours). The shape and detailed structure of the targets were reconstructed by the groups. The problem they studied was

considered relatively easier, since there was much less scattering of the ultrasonic or electromagnetic waves used and phase information of the wave was available.

In this chapter, we report on our work to extend above-mentioned approaches to the optical domain to retrieve the size and optical properties of targets. The efficacy of the formalism was tested using simulated and experimental data. This chapter is organized as follows. Section 2 outlines the extended TROT formalism for retrieval of optical property and size of targets. Section 3, and Section 4 test the formalism using simulated data and experimental data, respectively. Section 5 provides a discussion of results and summarizes key findings.

3.2. Theoretical formalism

Similar to what we have shown in Chapter 2, in the first order Born approximation, the perturbation in the light intensity distribution due to the presence of the finite-size targets (inhomogeneities in optical properties) may be expressed using a data matrix [1] of the form:

$$K \approx \left\{ \sum_{m=1}^{M} \sum_{l}^{L_m} G^d\left(\boldsymbol{r}_i, \boldsymbol{X}_{ml}\right) \tau_{ml} G^s\left(\boldsymbol{X}_{ml}, \boldsymbol{r}_j,\right) \right\} = \sum_{m=1}^{M} \sum_{l}^{L_m} g_d\left(\boldsymbol{X}_{ml}\right) \tau_{ml} g_s{}^T\left(\boldsymbol{X}_{ml}\right), \tag{3.1a}$$

for *absorptive* targets, and

$$K \approx \sum_{m=1}^{M} \sum_{l}^{L_m} \sum_{\alpha=\{x,y,z\}} \partial_\alpha g_d\left(\boldsymbol{X}_{ml}\right) \tau_{ml} \partial_\alpha g_s{}^T\left(\boldsymbol{X}_{ml}\right), \tag{3.1b}$$

for *scattering* targets, where N_s, N_d and M are the numbers of sources, detectors and targets, respectively; L_m is the number of voxels the m^{th} target is divided into ($M < \min(N_d, N_s)$); $g_s(\boldsymbol{r}) = \{G^s(\boldsymbol{r}, \boldsymbol{r}_j),\ j = 1, \ldots, N_s\}$ and $g_d(\boldsymbol{r}) = \{G^d(\boldsymbol{r}_i, \boldsymbol{r}),\ i = 1, \ldots, N_d\}$ are the Green's function vectors (GFVs) associated with the source and detector planes, respectively; the superscript T denotes transpose; $G^s(\boldsymbol{r}, \boldsymbol{r}_s)$ and $G^d(\boldsymbol{r}_d, \boldsymbol{r})$ are the Green's functions that describe light propagations in the background medium from a source at $\boldsymbol{r}_s$ to a voxel (inhomogeneity) at $\boldsymbol{r}$ and from the voxel to a

detector at $\boldsymbol{r}_d$, respectively; and τ_{ml} is the *optical strength* of the l^{th} voxel in the m^{th} target. Our focus in this section is on developing a method for estimation of $\tau_m = \sum_l^{L_m} \tau_{ml}$.

Assuming the m^{th} target is homogenous, and localized within a volume ΔV_m; the centroid position of the target is $\boldsymbol{X}_m$; the optical strength τ_m is,

$$\tau_m = \sum_l^{L_m} \tau_{ml} = \sum_l^{L_m} \delta\mu_a(\boldsymbol{X}_{ml}) c\delta V_{ml} \approx \delta\mu_a(\boldsymbol{X}_m) c\Delta V_m, \tag{3.2a}$$

for an *absorptive* target and

$$\tau_m = \sum_l^{L_m} \tau_{ml} = \sum_l^{L_m} \delta D(\boldsymbol{X}_{ml}) c\delta V_{ml} \approx \delta D(\boldsymbol{X}_m) c\Delta V_m, \tag{3.2b}$$

for a *scattering* target, where c_m is the light speed in the medium, δV_{ml} is the volume of the l^{th} voxel in the m^{th} target, and $\delta\mu_a$ (δD) is the difference in the absorption coefficient (diffusion coefficient) between the m^{th} target and the background medium assuming the target property is homogenous.

If the target is very small, and the Green's functions for different voxels in a target may be assumed to be the same, then Eqs. (3.1a) and (3.1b) become the same as Eq. (2.4) and Eq. (2.7), respectively. As shown in Chapter 2, for a small target that can be approximated to be point-like, when the eigenvalue equation of the TR matrix is solved, ideally, one absorptive target corresponds to one eigen component (eigenvalue and eigenvector), and one scattering target corresponds to three eigen components.

As shown in Eq. (3.1), an extended target with volume ΔV_m is considered consisting of a cluster of tiny pieces (e.g. voxels) with volume δV_{ml} located next to each other, and every piece may be considered as an individual small target as discussed in Chapter 2.

Similar to the formalism developed for point target in Chapter 2, a TR matrix is then constructed using the data matrix as $T_{SDDS} = K^{\dagger}K$ [$T_{DSSD} = (K^T)^{\dagger}K^T = K^*K^T$] in frequency domain,

and $T_{SDDS} = K^T K$ ($T_{DSSD} = KK^T$) in the continuous wave (CW) illumination mode. T_{DSSD} and T_{SDDS} have a common set of eigenvalues $\{\lambda_j, j = 1, \ldots, \min(N_s, N_d)\}$, and different sets of eigenvectors $\{u_i, i = 1, \ldots, N_d\}$ and $\{v_j, j = 1, \ldots, N_s\}$, respectively. The eigenvectors are separated into signal and noise subspaces using an *L*-curve method [11] with an eigenvalue threshold ε.

Since the eigenvalues and eigenvectors of T_{SDDS} and T_{DSSD} can be connected using singular value decomposition (SVD) [2, 12], *i.e.*

$$K = \sum_{j=1}^{\min(N_s, N_d)} u_j \sigma_j v_j^T \approx U \Sigma V^T, \tag{3.3}$$

where $V = \{v_j\}$ and $U = \{u_j\}$, corresponding to $\Sigma = \text{diag}\{\sigma_j > \varepsilon\}$, are matrices of the signal subspaces; u_j and v_j are left and right singular vectors of K, with singular values $\sigma_j = \sqrt{\lambda_j}$. $K^T K = (U\Sigma V^T)^T U\Sigma V^T = V\Sigma^T U^T U\Sigma V^T = V\Sigma^2 V^T$ where Σ is diagonal, i.e. $K^T K\, v_j = \lambda v_j$. Similarly, $KK^T u_j = \lambda u_j$. Therefore, u_i and v_j are the eigenvectors of $T_{DSSD} = KK^T$ and $T_{SDDS} = K^T K$, respectively, with a common set of eigenvalues λ_j. The singular values (eigenvalues of T_{SDDS} and T_{DSSD}) follow an L-shaped curve, with the first value accounting for the most of the variance in the signal. The singular value spectrum [7] works similarly to the L-curve method [11] used in Tikhonov regularization [13]. Hence, the singular value (eigenvalue) spectrum will also be called L-curve in this context. The "corner" of the L-curve is used to separate the signal and noise subspaces.

Once the signal subspace is determined, the MUSIC pseudo spectrum is calculated the same way as for a point target shown in Chapter 2. For absorptive targets, the locations are estimated using the maximum in the pseudo spectrum [1]

$$P_s(\boldsymbol{X}_p) = \left\| g_s(\boldsymbol{X}_p) \right\|^2 \Bigg/ \left| \left\| g_s(\boldsymbol{X}_p) \right\|^2 - \sum_{\lambda_j > \varepsilon} \left| v_j^T g_s(\boldsymbol{X}_p) \right|^2 \right|, \tag{3.4a}$$

associated with the source plane, or a similar form for the detector plan

$$P_d\left(\boldsymbol{X}_p\right)=\left\|g_d\left(\boldsymbol{X}_p\right)\right\|^2\Bigg/\left|\left\|g_d(\boldsymbol{X}_p)\right\|^2-\sum_{\lambda_j>\varepsilon}\left|u_j{}^T g_d(\boldsymbol{X}_p)\right|^2\right|, \tag{3.4b}$$

or the product of these two,

$$P\left(\boldsymbol{X}_p\right)=P_s\left(\boldsymbol{X}_p\right)P_d\left(\boldsymbol{X}_p\right), \tag{3.4c}$$

where $\boldsymbol{X}_p$ is a test target position in the sample volume.

Since the tiny pieces in an extended target are considered as non-well-resolved targets, in the signal subspace, the eigenvectors (singular vectors) are linear combinations of the GFVs associated with the tiny pieces (targets). The optical signal due to an extended target is mainly contributed by the leading eigen components, with the light intensity distribution determined by the orthonormal eigenvectors and magnitude determined by the eigenvalues (singular values). The leading eigenvalues account for the most of the optical strength of a target. So the optical strengths of targets can be estimated using the leading eigen components. However, to reconstruct the shape of a target in the pseudo image accurately, high-order components that carry details of the spatial structure are needed. In an ideal case, if all components are available, every voxel in the target acting as a tiny target will produce one large value in the pseudo spectrum, while a voxel outside the target produces a small value. In this case, a sharp pseudo image is generated. However, in a simulation with the presence of noise or under experimental conditions, the high-order components are easily buried in the noise. In this case, the tiny pieces in an extended target cannot be individually detected, *i.e.* the detailed spatial structure of the target cannot be reconstructed. The edge of the target in the pseudo image is also blurred and cannot be identified, *i.e.*, the shape of the target cannot be obtained. But with the leading components still available, the optical property (strength) of the targets may be obtained. The low-order leading components may also be used to estimate the approximate size of the target.

By comparing Eq. (3.3) with Eq. (3.1) and assuming the Green's functions at different voxels in the extended target are all the same, the optical property of the target can be retrieved by transforming the singular value matrix Σ via

$$\Gamma \approx (\mathbb{G}^d)^{-1} U \Sigma V^T ((\mathbb{G}^s)^T)^{-1}, \tag{3.5}$$

where $\Gamma = \text{diag}\{\tau_m,\ m = 1, \ldots, M\}$; $\mathbb{G}^s = \{g_s(\boldsymbol{r}_m)\}$, $\mathbb{G}^d = \{g_d(\boldsymbol{r}_m)\}$ are matrices including GFVs associated with the retrieved target positions (centroid positions). Since $\mathbb{G}^s$ and $\mathbb{G}^d$ are usually not square matrices, pseudo inverse is calculated. For scattering targets, the GFVs g_d and g_s in Eqs. (3.4) and (3.5) are replaced by $\partial_\alpha g_d$ and $\partial_\alpha g_s$, $\alpha = x, y, z$, respectively. Since the optical strength is carried by every term ($\alpha = x, y, z$), in principle, it will be retrieved three times for one target. Therefore, $\Gamma = \text{diag}\{\tau_m,\ \tau_m,\ \tau_m,\ m = 1, \ldots, M\}$; $\mathbb{G}^s = \{\partial_x g_s(\boldsymbol{r}_m),\ \partial_y g_s(\boldsymbol{r}_m),\ \partial_z g_s(\boldsymbol{r}_m)\}$; $\mathbb{G}^d = \{\partial_x g_d(\boldsymbol{r}_m),\ \partial_y g_d(\boldsymbol{r}_m),\ \partial_z g_d(\boldsymbol{r}_m)\}$. Each term of ∂_α results in an estimate of τ_m. Since the ∂_x and ∂_y terms in the optical signal are usually much weaker than ∂_z term under realistic conditions [14], the optical strength retrieved from the ∂_z term is mainly considered with the other two terms ignored, *i.e.* $\Gamma = \text{diag}\{\tau_m, m = 1, \ldots, M\}$; $\mathbb{G}^s = \{\partial_z g_s(\boldsymbol{r}_m)\}$, $\mathbb{G}^d = \{\partial_z g_d(\boldsymbol{r}_m)\}$.

Usually if the extended target is not too big, the first eigen component involves optical strength that is approximately the superposition of all tiny pieces in the target and the distribution that is approximately the GFV associated with the centroid position of the extended target, as shown in Eqs. (3.1) and (3.2). In this case, the location and optical strength of the target can be estimated by using the first eigen component. The retrieved location of the target using the pseudo spectrum will be at the weighted center of the optical strength of the target or geometrical center if the target is homogenous, as if all the tiny pieces are co-located at one position. If higher-order components are available and used to calculate the pseudo spectrum, the full-width-at-half-maximum (FWHM) may be used to estimate the size of the target.

The size of the target may be quantitatively estimated. The target surface may be approximated to be one of the contours (an isosurface Ω when it is plotted in 3D) in the pseudo spectrum, or the pseudo spectrum in logarithmic scale. The optimal contour in the pseudo spectrum is selected to be the boundary of the target(s), via [6]

$$\Omega = \arg\min_{\Omega} \left\| K - K_{cal}(\Omega) \right\|^2, \tag{3.6}$$

where K is the measured data matrix and $K_{cal}(\Omega)$ is a calculated data matrix. K is either measured in experiments or obtained in simulations using a forward model with known target information. $K_{cal}(\Omega)$ is the data matrix calculated using a forward model assuming a contour of the pseudo spectrum to be the target boundary. A contour in pseudo spectrum is a surface plotted in 3D. Any appropriate forward model could be used such as the analytical forward model in Eq. (3.1), or a finite-element-method-based forward model to calculate $K_{cal}(\Omega)$. The Green's functions used in the calculation are those for the intervening medium. In order to search for the contour gradually, the pseudo spectrum in logarithmic scale $\log(P(\boldsymbol{X}_p))$ is used instead of linear scale.

When searching for the optimal contour, starting from the maximum of the pseudo spectrum, successive contour levels are selected. When a contour Ω is selected, the volume V enclosed inside is assumed to be the target volume, and then the data matrix is calculated and compared with the measured (simulated or experimental) data. To save computation time, when the next larger volume $V + dV$ is selected, only the signal generated for the extra volume dV is calculated, and added to the signal generated for the volume V. Applying this "local contour" method [5], the optimal contour is found using Eq. (3.6).

In summary, the framework of TROT for extended targets is as follows: a) data matrix is constructed using "experimental data" (or forward model data in simulations), and TR matrix is calculated; b) SVD is performed on the TR matrix; c) the signal subspace of the TR matrix is

determined with a proper threshold in the singular values; d) the MUSIC pseudo spectrum is calculated based on the signal subspace; e) the positions of targets are determined using the maxima in the pseudo images; f) the optical strengths of targets are retrieved by unmixing the rank-reduced data matrix using the pseudo inverse of the matrices constructed with Green's functions associated with the retrieved target positions; g) the target size/shape is estimated using contours of pseudo spectrum through an optimization process which minimizes the difference between the calculated and the actual data matrix; h) the absorption or scattering coefficient is estimated using the optical strength and the volume of a target. Unlike other inverse image reconstruction (IIR) techniques, TROT does not attempt to retrieve the optical property of every voxel. Instead, it uses Born approximation and perturbation approach, considers a target as a localized inhomogeneity in the background medium, and locate the target and retrieve size and property of the target separately. It does not consider the heterogeneity inside a target. If a target is heterogeneous, it may be considered as multiple inhomogeneities, whose locations may be determined using the same algorithm if they can be resolved in the pseudo image.

In the following sections, simulated and experimental data are used to examine the efficacy of TROT in retrieving the property and size of small targets. Localization of targets is also re-evaluated using the whole signal subspace determined in the logarithmic scale.

3.3. Simulations

The background medium was taken to be a 40-mm thick uniform scattering slab. Its absorption and diffusion coefficients were $\mu_a = 0.003$ mm^{-1} and $D = 1/3$ mm (transport mean free path, $l_t = 1$ mm), respectively, which are similar to the average value of those parameters for human breast tissue. The index of refraction n of the medium was taken to be 1.33. The speed of light c is 2.998×10^8 m/s, or 299.8 mm/ns in vacuum, and $c_m \approx 225.4$ mm/ns in the medium. Single or

multiple finite-size absorptive or scattering targets were embedded. The extended target was simulated with a cluster of voxels whose size was $1mm^3$. The simulated data were generated using analytical forward model (Eq. (3.1)) for subsequent TROT analysis. The retrieved optical strength has a unit of mm^3/ns and mm^5/ns for absorptive and scattering strength, respectively.

3.3.1. Singular value decomposition and determination of signal subspace

To demonstrate the relationship between the singular value (eigenvalue) spectrum and pseudo spectrum and the target size for the case of an extended target with different noise levels, a two-dimensional (2-*D*) absorptive target (21 mm × 21 mm) was embedded in the above scattering medium to generate simulated forward model data. The 2-*D* target is used for simplicity since the transillumination slab geometry has lower resolution in the axial direction. The thickness of the target is one voxel (1 mm). 41 × 41 sources and 41 × 41 detectors were placed on the source and detector planes with 2-mm spacing covering an area of 80 mm × 80 mm. The target was placed in the center of the medium, with its center position located at (40, 40, 20) mm. For simplicity, when the reconstruction result is displayed, a smaller volume of 41 mm × 41 mm × 40 mm around the center is selected. In the display coordinates, the center of the target is located at (21, 21, 20) mm.

The absorption coefficient of the targets was set to be higher than the background with $\Delta\mu_a$ = 0.01 mm^{-1}. The volume of the targets was 441 mm^3, and the sample volume was discretized into 1 mm × 1 mm × 1 mm voxels in the forward model. The optical strength of the absorptive targets was $\Delta\mu_a c\Delta V$ = 994.0 mm^3/ns.

The forward model data were generated. The TR matrix was calculated and the SVD of the TR matrix was performed. When no noise was added into the forward model data, the singular value spectrum including 1681 singular values was plotted in linear and logarithmic scales. Fig.

3.1(a) shows the first 20 values of the singular value spectrum, while Fig. 3.1(b) shows the singular value spectrum in logarithmic scale. As shown in Fig. 3.1(a), the singular value spectrum is similar to the L-curve in Tikhonov regularization. Following the first singular value, the rest singular values dropped dramatically. The As explained above, even though the target includes 1681 voxels, since they are non-well-resolved, the eigen components are not one-to-one related to the voxles or equivalent to each other. Instead, the eigen vectors are linear combinations of the GFVs associated with individual voxels. According to Eq. (3.3), the first component contributes to the signal with the first singular value as the strength of the component. The first eigen component accounts for 97.74% variance of the signal (ratio between the first eigenvalue and the sum of all eigenvalues). The second and third components are about 10 times weaker than the first component. The higher-order components are even weaker. The first three eigen components account for 99.97% variance of the signal.

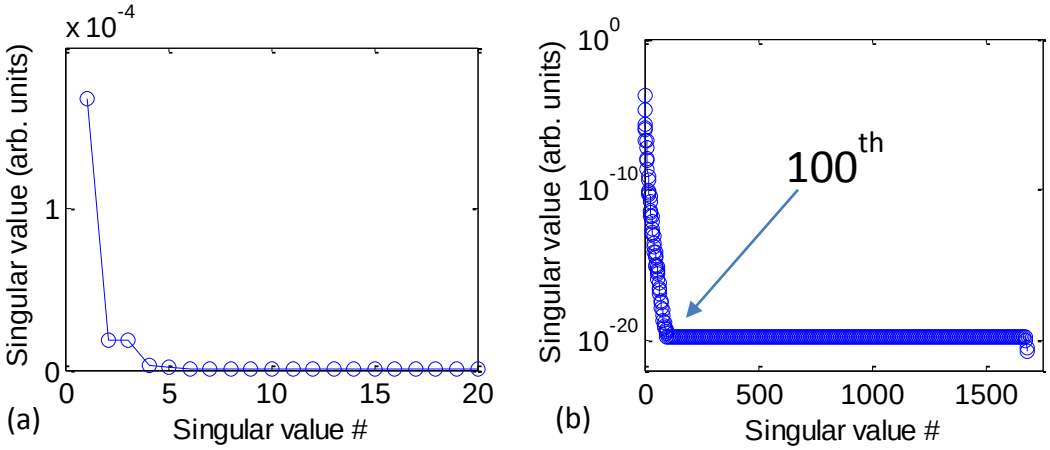

Fig. 3.1. (a) and (b) are singular value spectra plotted in linear and logarithmic scales.

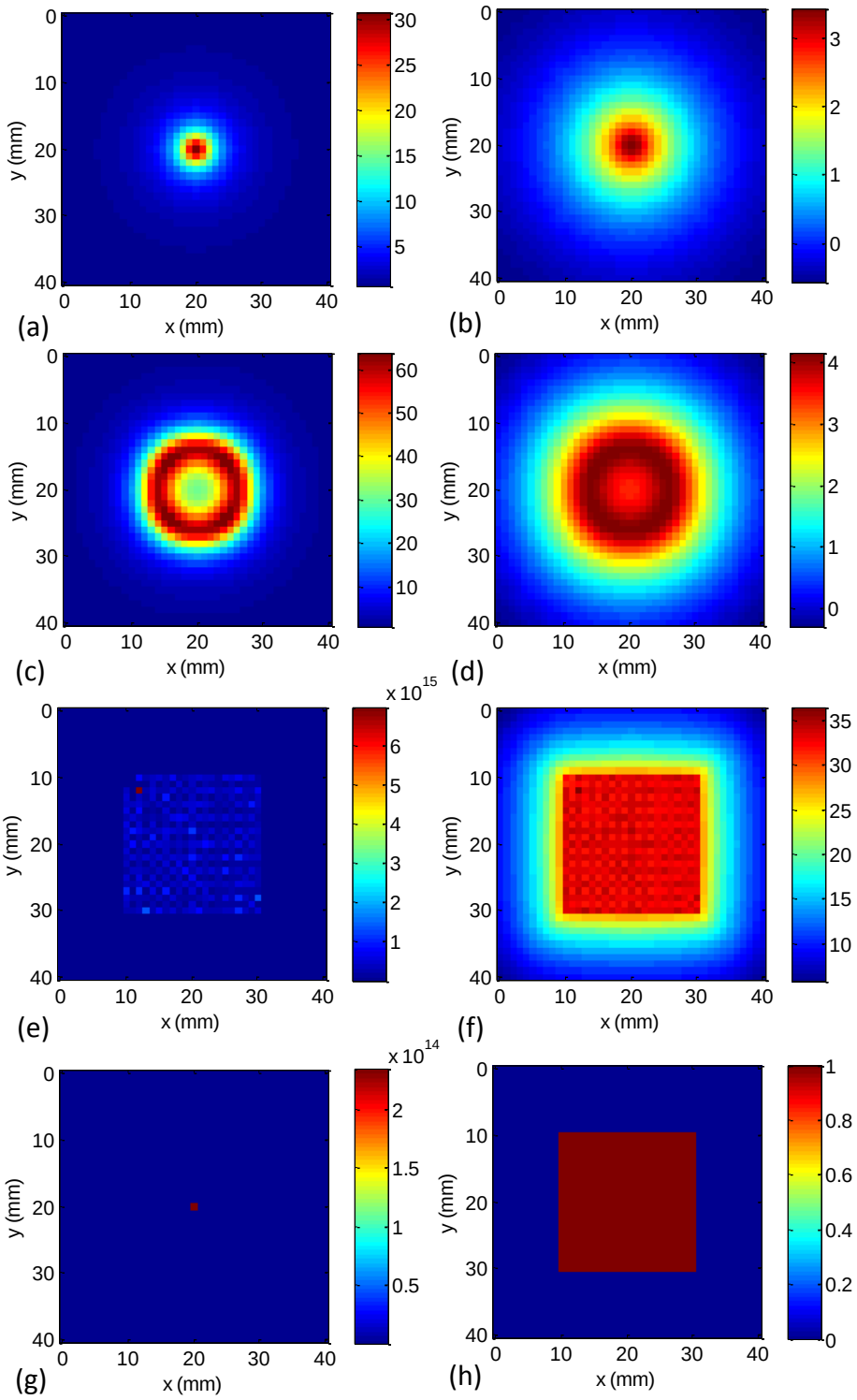

Fig. 3.2. The pseudo images of the target generated using pseudo spectrum with 1, 3 and 100 eigen components shown in linear scale in (a), (c) and (e), respectively; and in logarithmic scale in (b), (d) and (f), respectively. (g) and (h) are the actual images of the point target and 20 mm × 20 mm target, respectively, for comparison.

Since the high-order components carry shape information of the target, the singular value spectrum is plotted in logarithmic scale to help select more higher-order components. The Semi-log plot of the singular value spectrum is also an *L*-shaped curve. So the "corner" of the "*L*-curve" is used. Therefore, the first 100 eigen components are used to calculate the pseudo spectrum, and compared to 3 and 1. The pseudo spectrum calculated using 1 eigen component, 3 eigen components and 100 eigen components are shown in linear scale in Fig. 3.2(a), 3.2(c) and 3.2(e), respectively; and in logarithmic scale in Fig. 3.2(b), 3.2(d) and 3.2(f), respectively.

As shown in Fig. 3.2, when 1 eigen component was used, one sharp peak was generated in the pseudo image, using which the target was found to be located to be at (21, 21, 20) mm in the reconstruction coordinates. However, no size information of the target was obtained. The reconstructed image for a point target located at (21, 21, 20) mm is show in Fig. 3.2(g) for comparison. When 3 eigen components were used, the image of the target was extended. But the shape of the image is round instead of square. The full-width-at-half-maximum (FWHM) in the pseudo image of logarithmic scale was measured to be 24.4 mm in both *x* and *y* directions, which was used to estimate the size of the target. When 100 eigen components were used, all details in the image, including the edges and corners were detected. Therefore, the exact square shape was detected, as shown in Fig. 3.2(e). Due to the large range in the pseudo values, the image is re-plotted in logarithmic scale in Fig. 3.2(f) to enhance the contrast. The actual image of the target is shown in Fig. 3.2(h) for comparison. In all cases, the pseudo image of the target is centered at (21, 21, 20) mm.

The optical strength of the target was estimated using Eq. (3.5) where the GFV was calculated using the center position of the retrieved target image. The retrieved optical strengths are shown in Table 3.1, and compared to the known value.

Table 3.1. Retrieved optical absorption strength and FWHM of the pseudo spectrum with 0 noise

		Optical strength (mm^3/ns)	Error (%)	FWHM (mm)
Known value		994.0	-	20
Retrieved value using	1 eigen component	786.5	20.9	3.2
	3 eigen components	786.5	20.9	15.6
	100 eigen components	786.6	20.9	~ 20
	1681 eigen components (original data matrix)	786.6	20.9	~ 20

As shown in Table 3.1, when calculating the optical absorption strength, increase in the number of eigen components does not significantly improve the retrieved strength. There is 20.9% error in the retrieved value no matter 1 eigen component was used or the whole original data matrix was used. We ascribe the error to the assumption that all GFVs related to different positions in the target are the same and correspond to the centroid position of the target. For small target, smaller error is expected. However, the FWHM of the pseudo spectrum increases as the number of components increases. When 100 components (corresponding to the "corner" of the singular value spectrum in logarithmic scale) are used, the pseudo spectrum becomes stable. The dimension of the plateau on the top of the pseudo spectrum instead of the FWHM is shown in the Table, which is almost equal to the known dimension of the target.

Next the effect of noise was explored. 20% additive Gaussian random noise was added to the data to evaluate the efficacy of the method again. When the noise is added, the data matrix is X =

X_0+N, where X_0 is the simulated raw data without noise added, and N is the Gaussian random noise with 0 mean and standard deviation of 20% of the mean value of the raw data without noise.

The singular value spectrum constructed using SVD of the TR matrix is shown in Fig. 3.3.

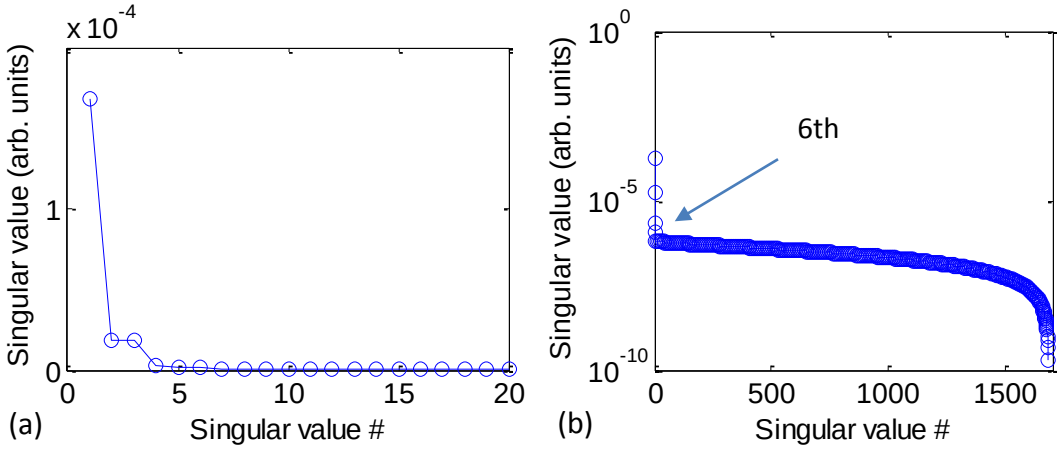

Fig. 3.3. Singular value spectrum in (a) linear scale and (b) logarithmic scale.

With noise added, the first three singular values were still prominent. But as shown in the semi-log plot, most of higher-order components were then buried in the noise. The "corner" of the *L*-curve occurred at 6th singular value. The first 1, 3, 6, and 100 singular components are used to calculate pseudo spectrum, as shown in Fig. 3.4, for comparison.

As Fig. 3.4 shows, when 1 and 3 eigen components are used, the pseudo images shown in Fig. 3.4(a), 3.4(b), 3.4(c) and 3.4(d) are almost identical to those generated without noise. When 6 eigen components are used, the image is shown in linear scale in Fig. 3.4(e) and in logarithmic scale in Fig. 3.4(f). The size of the pseudo image of the target estimated using the FWHM is still comparable to the actual size. However, the shape of the image is not as accurate as that in the no-noise case with 100 eigen components used. Even if 100 eigen components are used to calculate the pseudo spectrum, as shown in Fig. 3.4(g) (linear) and 3.4(h) (logarithmic), the

pseudo image cannot be improved. This is because the higher-components which carry more detailed information of the target shape are buried in the noise and not available any more.

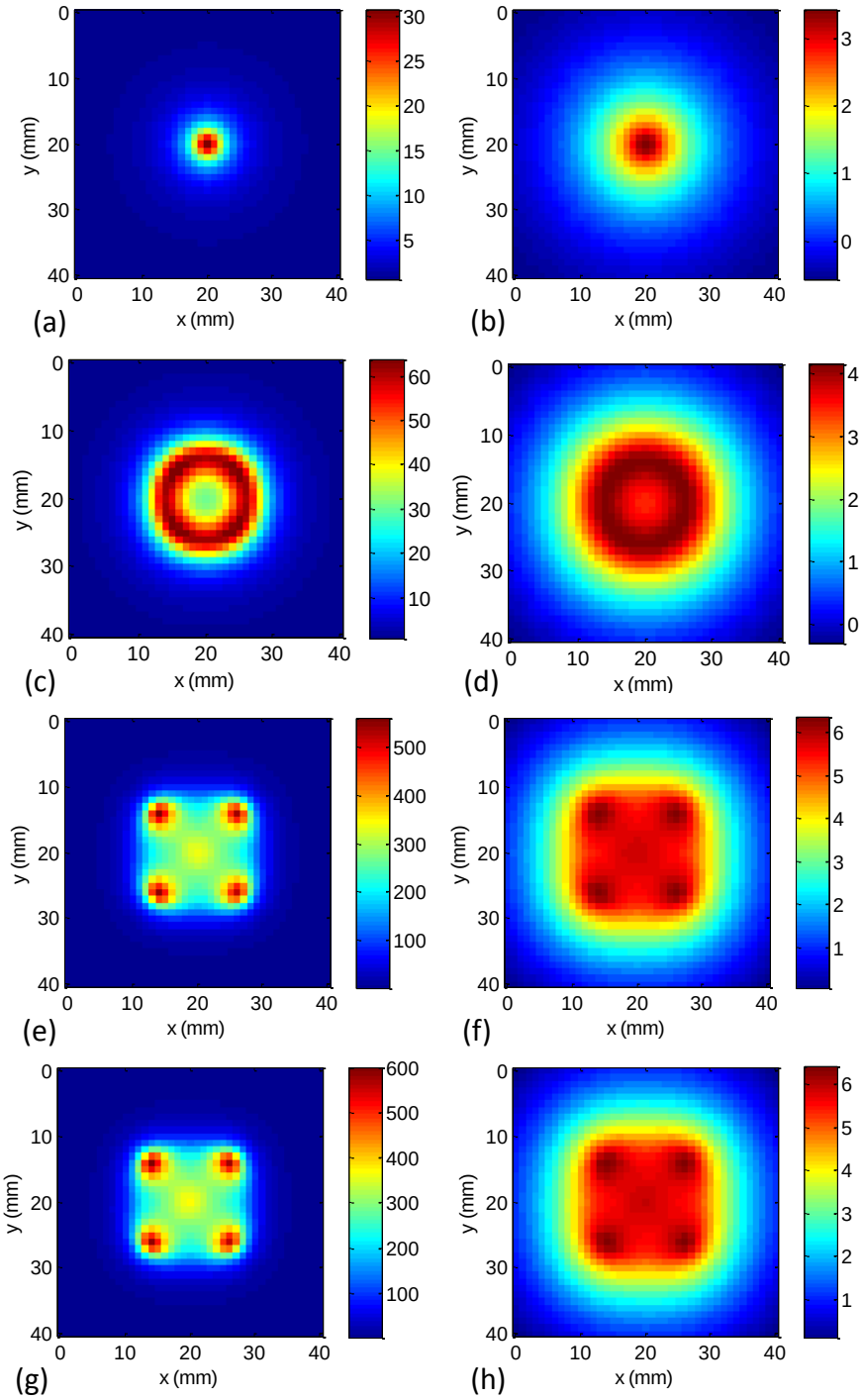

Fig. 3.4. The pseudo images of the target generated using 1, 3, 6 and 100 eigen components shown in linear scale in (a), (c), (e) and (g), respectively; and in logarithmic scale in (b), (d), (f) and (h), respectively.

The optical strength of the target is calculated using different number of eigen components and shown in Table 3.2.

Table 3.2. Retrieved optical absorption strength and FWHM of the pseudo spectrum with 20% additive Gaussian noise

		Optical strength (mm^3/ns)	Error (%)	FWHM (mm)
Known value		994.0	-	20
Retrieved value using	1 eigen component	786.5	20.9	3.2
	3 eigen components	786.5	20.9	15.6
	100 eigen components	786.6	20.9	~ 20
	1681 eigen components (original data matrix)	786.6	20.9	~ 20

The retrieved optical strength of the target is identical to those obtained in the non-noise case. In all cases of using different numbers of eigen components, the optical strength is found to be ~ 786.6 mm^3/ns with 20.9% error.

3.3.2. Localization, property and size retrieval using simulated data

In this section, we use a set of simulated datasets to evaluate the efficacy of the TROT algorithm we have developed in Section 3.2 in locating and retrieving optical strength and size of finite-size targets. Two approaches that use FWHM in the pseudo spectrum and "local contour" will be used to estimate the target size. 3-*D* targets will be used. Even though the targets used in the simulations are not big, they are simulated using Eq. (3.1) and treated as extended targets,

instead of point targets used in Chapter 2. Therefore, after SVD, each target contributes more than one eigen component (eigenvalue and eigenvector).

In these simulations, the same medium and source (detector) configurations were used as above simulation in Section 3.3.1. Three datasets were simulated. In the first simulation, one 10-mm-diameter absorptive target was centered at (40, 40, 20) mm. In the second simulation one 10-mm-diameter scattering target was centered at (40, 40, 20) mm. In the third simulation, one 10-mm-diameter and one 6-mm-diameter absorptive targets were located at (10, 10, 20) mm and (30, 30, 20) mm, respectively. The absorption coefficient of all the absorptive targets was set to be higher than the background with $\delta\mu_a$ = 0.001 mm^{-1}, while the diffusion coefficient was taken to be the same as that of background. The diffusion coefficient of the scattering target was set to be lower than the background (higher scattering coefficient) with δD = -0.1 mm (l_t = 0.7 mm), while the absorption coefficient was taken to be the same as that of the background. The volume of the 10-mm-diameter target was 515 mm^3 when the sample volume is discretized into 1 mm × 1 mm × 1 mm voxels in the forward model. The volume of the 6-mm-diameter target was 123 mm^3. The optical strength of the 10-mm-diameter absorptive targets was $\delta\mu_a c\Delta V$ = 116.08 mm^3/ns, of the 6-mm-diameter target 27.72 mm^3/ns; while the optical strengths of the scattering target was $\delta D c\Delta V$ = -11608.1 mm^5/ns. The incident CW beam step scanned the sample at 41 × 41 grid points covering an 80 × 80 mm^2 area, with a step size of 2 mm. Light on the opposite side was recorded at 41 × 41 grid points covering the same area. Additive Gaussian noise of different noise levels was added to the simulated data and compared to no-noise case. The simulated data matrix K was calculated using Eq. (3.1) directly, and then analyzed using TROT. The results are shown below. For simplicity, when the reconstruction result for one target is displayed, a smaller volume of 40 mm × 40 mm × 40 mm around the center is selected.

3.3.2.1. *Single absorptive target*

The first 20 singular values of the TR matrix with 0 noise added are plotted in Fig. 3.5(a) and Fig. 3.5(b) for linear scale and logarithmic scale, respectively. In the linear plot, only one eigen component is prominent. In the semi-log plot, the "corner" is right after 78th component. So the dimension of the signal subspace was determined to be 78. Using Eq. (3.4), the pseudo spectrum was calculated. Both of axial and sagittal views of the target using the pseudo spectrum are plotted in logarithmic scale in Fig. 3.5(c) and 3.5(d). A "plateau" is found in the center of the image and used to estimate the size of the target. The isosurface of the "plateau" is plotted in Fig. 3.5(e). The dimension of the target image is similar to that of the target. The image is not exactly spherical, due to the lower resolution in the *z* direction for the transillumination slab geometry. Since 0 noise is an ideal case and there is a discontinuity in the derivative of the pseudo spectrum due to the plateau, target size will not be estimated using the proposed approaches. The retrieved target volumes are shown in Table 3.3 and compared with the known volume.

The target position is described by the centroid position of the pseudo image, which is found to be exactly (20, 20, 20) mm. Using Eq. (3.5), the optical strength was found to be 112.4 mm^3/ns when all eigen components in the signal subspace were used. If only the first eigen component in the signal subspace was used, the optical strength was found to be the same, which confirms the single prominent eigen component in the linear plot of singular value spectrum contributes the most to the optical strength. The retrieved optical strength and size of the target are shown in Table 3.3.

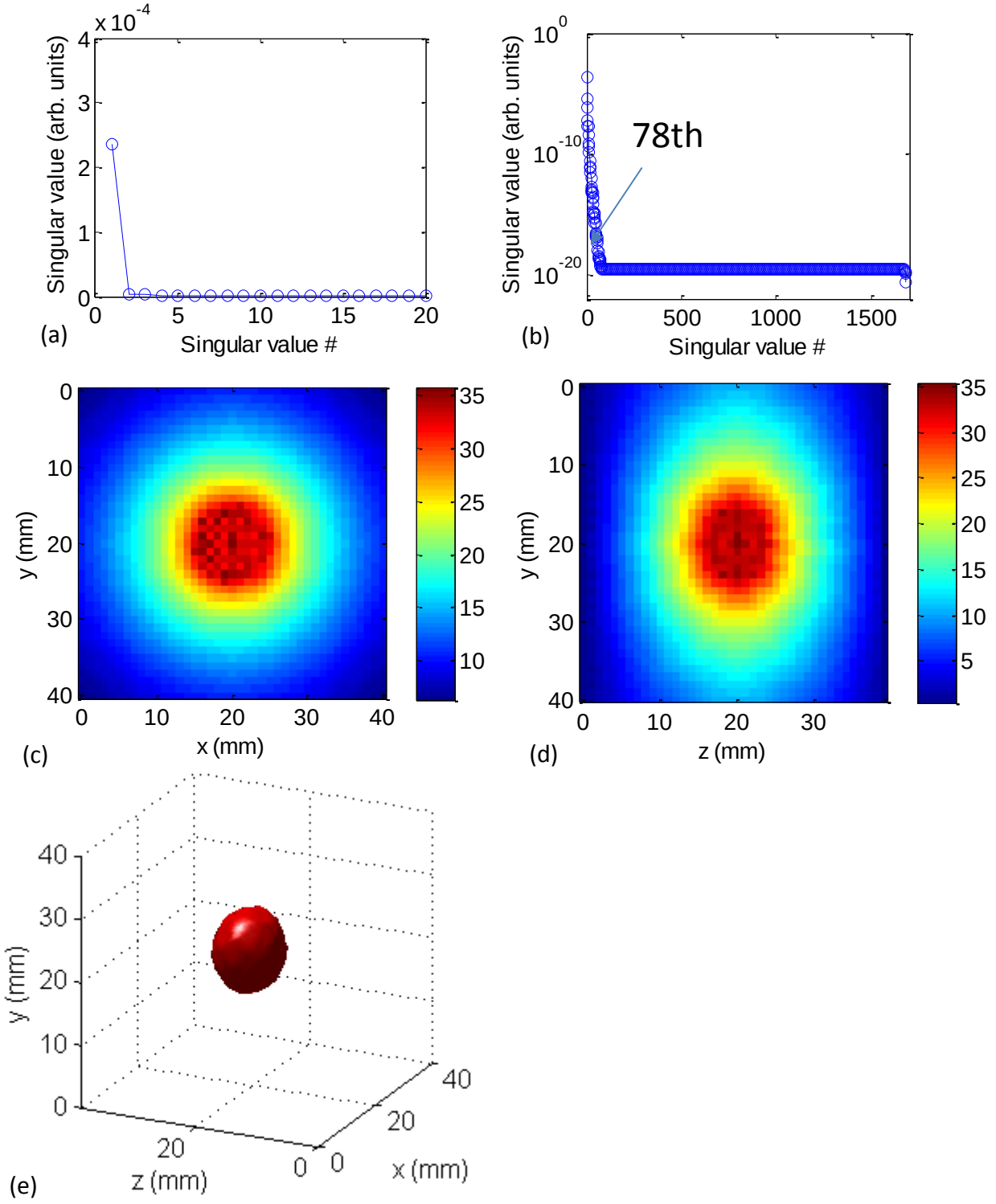

Fig. 3.5. (a) and (b) are singular value spectrum in linear and logarithmic scales respectively. (c) and (d) are axial and sagittal pseudo images of the absorptive target in logarithmic scale. (e) shows the isosurface for the "plateau" in the pseudo image (logarithmic scale). No noise was added to the simulated data.

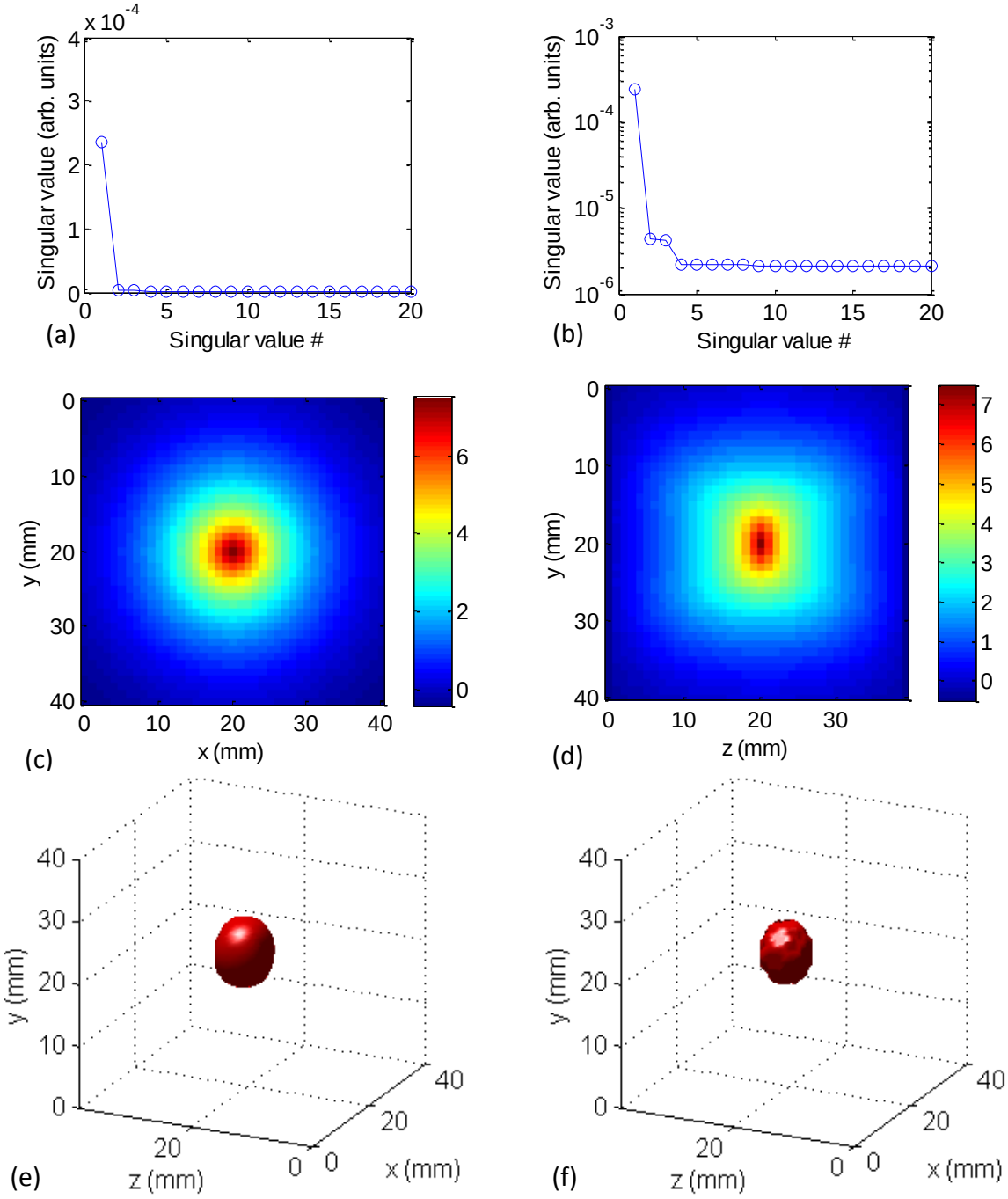

Fig. 3.6. (a) and (b) are singular value spectrum in linear and logarithmic scales respectively. (c) and (d) are axial and sagittal pseudo images of the absorptive target in logarithmic scale. (e) shows the isosurface for the FWHM in the pseudo image (logarithmic scale). (f) is the isosurface found using the local contour method in Eq. (3.6). 20% noise was added to the simulated data.

With 20% additive Gaussian noise added, the first 20 singular values were plotted in Figs. 3.6(a) and 3.6(b) for linear and logarithmic scales, respectively. The first singular value was still approximately the same as the one in no-noise case. In the semi-log plot, still 3 singular values are prominent. So the dimension of the signal subspace was then determined to be 3. The pseudo spectrum was calculated. Both of axial and sagittal views of the target using the pseudo spectrum are plotted in logarithmic scale in Figs. 3.6(c) and 3.6(d). The isosurface of the FWHM in the pseudo image is shown in Fig. 3.6(e), whose volume is 571 mm^3. If the volume is approximated to be spherical, the estimated diameter is 10.3 mm. The isosurface found using Eq. (3.6) is shown in Fig. 3.6(f), whose volume is 385 mm^3, which is corresponding to 9.0 mm spherical diameter. The target position is obtained to be at exactly (20, 20, 20) mm. The absorption strength is determined to be 112.4 mm^3/ns, which is the same as that in the non-noise case.

Table 3.3. Optical strength and size of an absorptive target

Noise Level (%)	Optical Strength		Retrieved Size					
	Retrieved (mm^3/ns)	Error (%)	Contour (mm^3)	Diameter (mm)	Error (%)	FWHM (mm^3)	Diameter (mm)	Error (%)
0	112.4	3.2	-	-	-	-	-	-
5	112.4	3.2	480	9.7	3	806	11.5	15
10	112.4	3.2	243	7.7	23	784	11.4	14
20	112.4	3.2	385	9.0	10	571	10.3	13

* Known values: volume: 515 mm^3, absorptive optical strength: 116.08 mm^3/ns.

Similar simulated results are obtained for 5% and 10% noise. In all cases, the target is accurately located. The retrieved optical strength and size of the target are shown in Table 3.3. The retrieved optical strength is the same as that retrieved in the case of 0 and 20% noise.

Further simulations show the optical strength can be accurately retrieved if the noise level is even higher or the target size and location are varied. The retrieved target size (diameter) using both methods is within 25% uncertainty. However, for a larger target, the error in the retrieved target size may increase significantly. The accuracy in the retrieved target size and optical property seems not to well correlate with the noise level.

3.3.2.2. *Single scattering target*

Similar simulations were carried out when one scattering target was embedded in the medium. Simulated data was generated and the subsequent analysis was conducted with no noise and with 5% noise, 10% noise and 20% noise added separately.

The first 20 eigenvalues of the TR matrix for one absorptive target 0 noise and with 20% noise are plotted in and shown in Fig. 3.7 and Fig. 3.8. With 0 noise added, three eigen components are prominent in the linear plot of the singular value spectrum for one single scattering. In the semi-log plot, 103 eigen components are prominent, which are chosen to form the signal subspace. When 20% noise was added, the singular value spectrum in linear scale is almost identical to that for no-noise case. However, in the logarithmic scale, there are only 6 prominent singular values. So the dimension of the signal subspace is chosen to be 6. The pseudo spectrum was calculated using Eq. (3.4). The axial and sagittal views of the target using the pseudo spectrum for 0 noise are plotted in Figs. 3.7(c) and 3.7(d) for linear and logarithmic scales, respectively. The axial and sagittal views of the target with 20% noise added are plotted in Figs. 3.8(c) and 3.8(d) for linear and logarithmic scales, respectively.

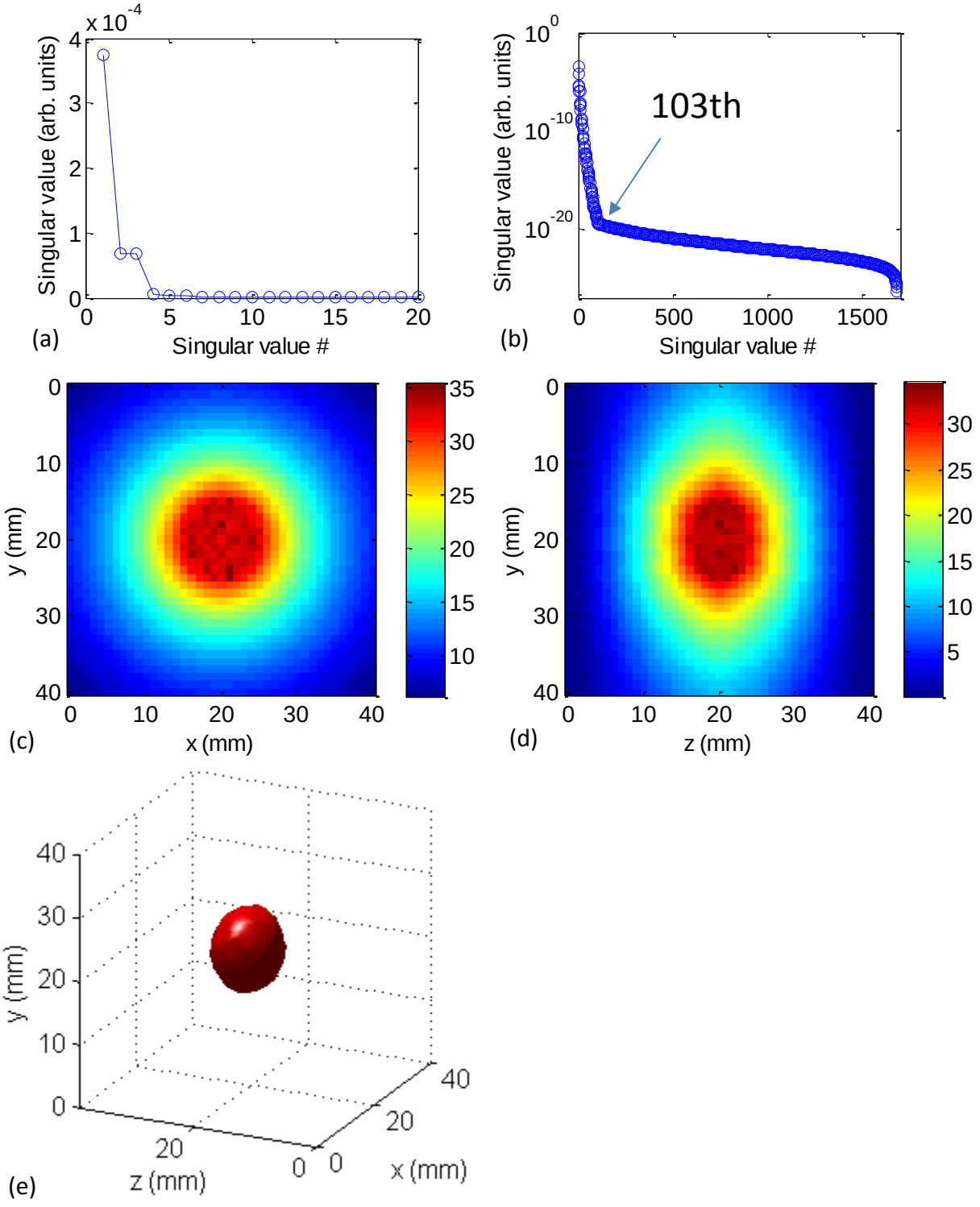

Fig. 3.7. (a) and (b) are singular value spectrum in linear and logarithmic scales respectively. (c) and (d) are axial and sagittal pseudo images of the scattering target in logarithmic scale. (e) shows the isosurface for the FWHM in the pseudo image (logarithmic scale). No noise was added to the simulated data.

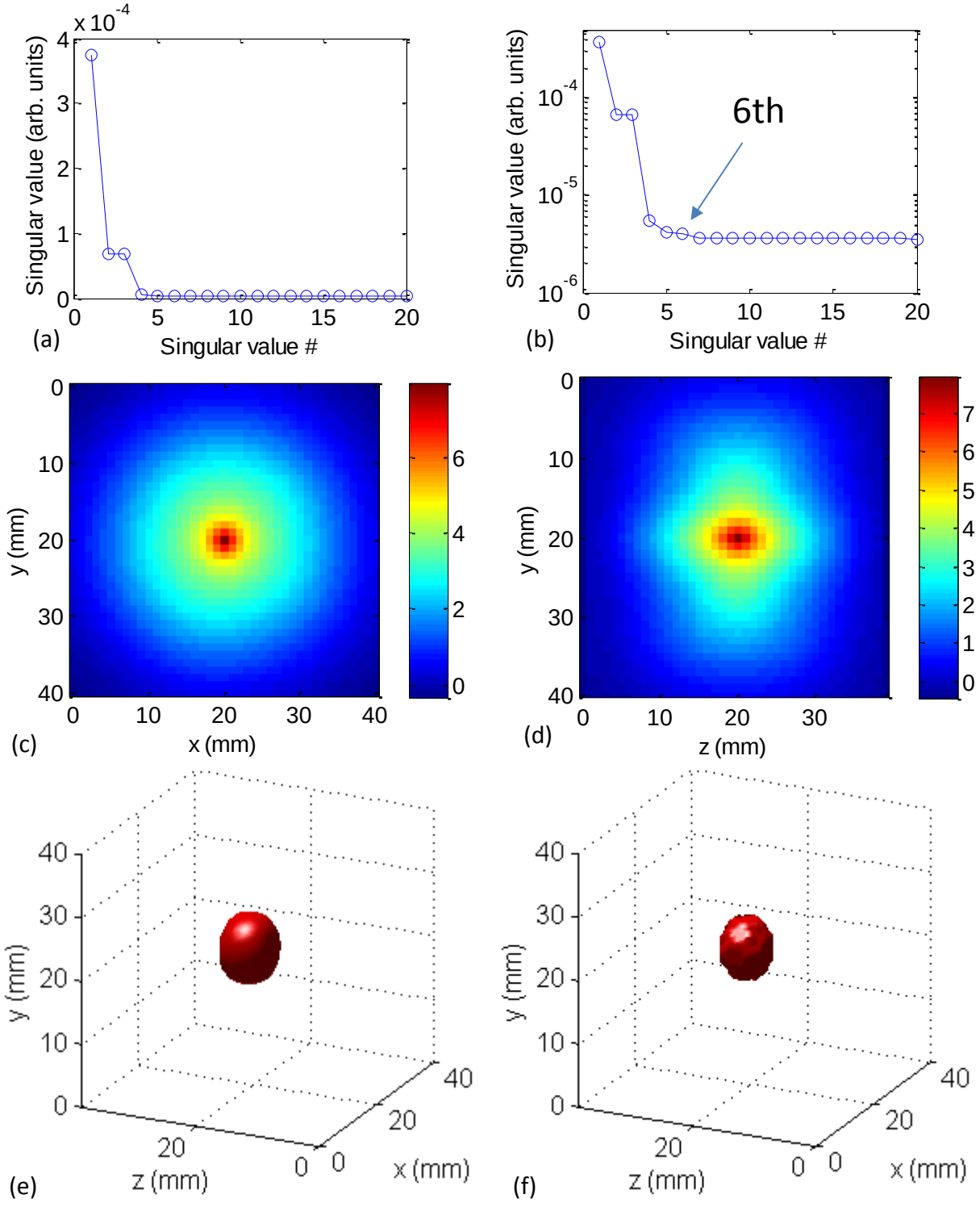

Fig. 3.8. (a) and (b) are singular value spectrum in linear and logarithmic scales respectively. (c) and (d) are axial and sagittal pseudo images of the scattering target in logarithmic scale. (e) shows the isosurface for the FWHM in the pseudo image (logarithmic scale). (f) is the isosurface found using Eq. (3.6). 20% noise was added to the simulated data.

Similar to the absorptive target, with 0 noise, there is a "plateau" shown in pseudo image. The isosurface was obtained using the "plateau" in the pseudo spectrum and plotted in Fig. 3.7(e). The size of the "plateau" is similar to the actual value of the target. When 20% noise was added, the two isosurfaces appeared as plotted in Figs. 3.8(e) and 3.8(f), respectively. The size of the target is estimated to be 576 mm^3 (10.3 mm diameter) using FWHM of the pseudo spectrum and 438 mm^3 (9.4 mm diameter) using the "local contour" method (Eq. (3.6)).

Similar images were obtained for 5% and 10% noise levels. The target location and optical strength of the target was accurately retrieved in all cases. The size in all cases was retrieved using FWHM of the pseudo spectrum (logarithmic scale) and the "local contour" method (Eq. (3.6)). The retrieved target optical strength and size are all shown in Table 3.3, and compared to the known values.

Table 3.4. Optical strength and size of a scattering target

Noise Level (%)	Optical Strength		Retrieved Size using					
			Local Contour			FWHM		
	Retrieved (mm^5/ns)	Error (%)	Volume (mm^3)	Error (%)	Diameter (mm)	Volume (mm^3)	Error (%)	Diameter (mm)
0	-10985.4	5.4	-	-	-	-	-	-
5	-10985.8	5.4	539	4.7	10.1	423	17.9	9.3
10	-10985.2	5.4	665	29.1	10.8	231	55.2	7.6
20	-10987.2	5.3	576	11.8	10.3	438	15.0	9.4

* Known values: volume: 515 mm^3, scattering optical strength: -11608.1 mm^5/ns

The target location was accurately found to be (20, 20, 20) mm for all noise levels (0%, 5%, 10% and 20%). The scattering optical strength of the target was retrieved within 5.4% error and the size of targets was found within 25% error for all noise levels.

3.3.2.3. *Two absorptive targets*

Next we consider the case of two spherical absorptive targets with different size (one with diameter 10 mm, the other with diameter 6 mm) embedded in the medium, with a center-to-center separation of 14.1 mm. Simulated data are generated with different additive noise levels: 5%, 10%, 20%, and compared to 0-noise case. The singular value spectrum of the TR matrix with 0 noise is shown in Fig. 3.9(a) (linear scale) and in Fig. 3.9(b) (logarithmic scale).

In linear scale, the "corner" of the "*L*-curve" is after 2th singular value, corresponding to the two targets. In logarithmic scale, the "corner" is after 115th singular value, where the high-order components carry more details of the shape. The pseudo spectrum was calculated. The centroid positions of the two targets were determined to be exactly the same as the known positions (10, 10, 20) mm and (30, 30, 20) mm, respectively. The sagittal pseudo images of the two targets at x = 10 mm and x = 30 mm are shown in Figs. 3.9(c) and 3.9(d), respectively. The axial pseudo image of the two targets at z = 20 mm is shown in Fig. 3.9(e). There are two "plateaus" in the pseudo image corresponding to the two targets, whose sizes are approximately the same as the known values. The optical strengths of the two targets are estimated using Eq. (3.5). The retrieved optical strengths using 115 eigen components are shown in Table 3.5. When 2 eigen components are used, the retrieved strengths are about the same as those retrieved using 115 eigen components. This confirms that the leading two eigen components contribute the most to the optical strengths.

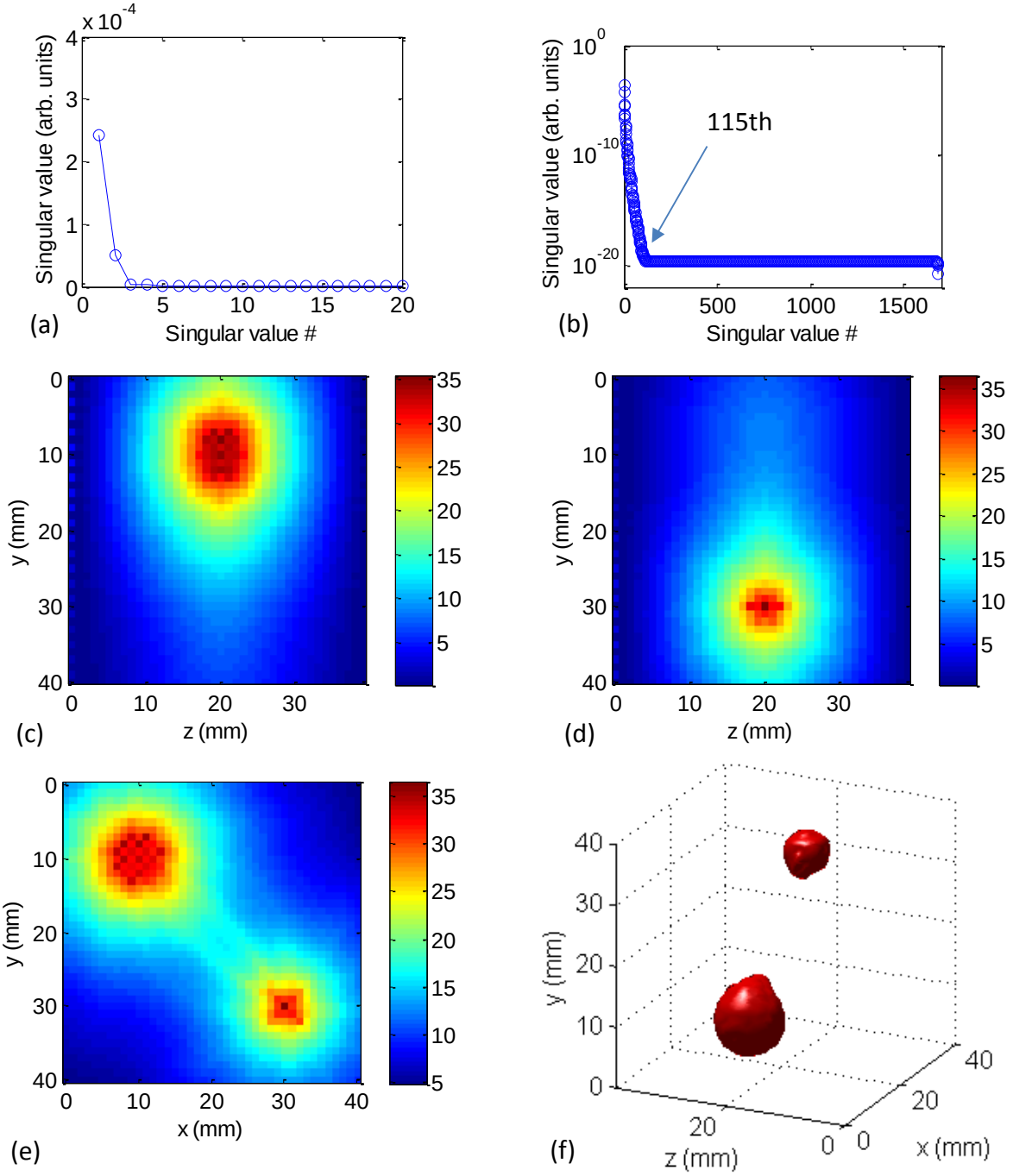

Fig. 3.9. (a) and (b) are singular value spectrum in linear and logarithmic scales respectively. (c) and (d) are sagittal pseudo images (logarithmic scale) of the two targets, respectively. (e) is the axial pseudo image (logarithmic scale) of the two targets at z = 20 mm. (f) shows the isosurface generated using the FWHM in the pseudo image.

Table 3.5. Optical strength and size of two absorptive targets

Noise Level (%)	Target	Optical Strength		Retrieved Size using			
				Local contour		FWHM	
		Retrieved (mm^3/ns)	Error (%)	Volume (mm^3)	Diameter (mm)	Volume (mm^3)	Diameter (mm)
0	Left	110.61	4.7	-	-	-	-
	Right	27.73	0.04	-	-	-	-
5	Left	110.61	4.7	3280	18.4	775	11.4
	Right	27.73	0.04	654	10.8	131	6.3
10	Left	110.61	4.7	3751	19.3	931	12.1
	Right	27.73	0.04	370	8.9	52	4.6
20	Left	110.61	4.7	3819	19.4	937	12.1
	Right	27.72	0	438	9.4	55	4.7

* Known values: for left target, volume = 515 mm^3, optical strength = 116.08 mm^3/ns; for right target, volume = 123 mm^3, optical strength = 27.72 mm^3/ns.

The singular value spectrum when 20% noise was added is shown in Fig. 3.10(a) (linear scale) and 10(b) (logarithmic scale). In linear scale, the singular value spectrum appear to be similar to that in the 0 noise case. When 20% noise is added, 5 eigen components are separated to be the signal subspace. The pseudo spectrum is calculated using 5 eigen components. The centroid locations of the two targets are exactly retrieved. The sagittal pseudo images of the two targets at x = 10 mm and x = 30 mm are shown in Figs. 3.10(c) and 3.10(d), respectively. The axial pseudo image of the two targets at z = 20 mm is shown in Fig. 3.10(e).

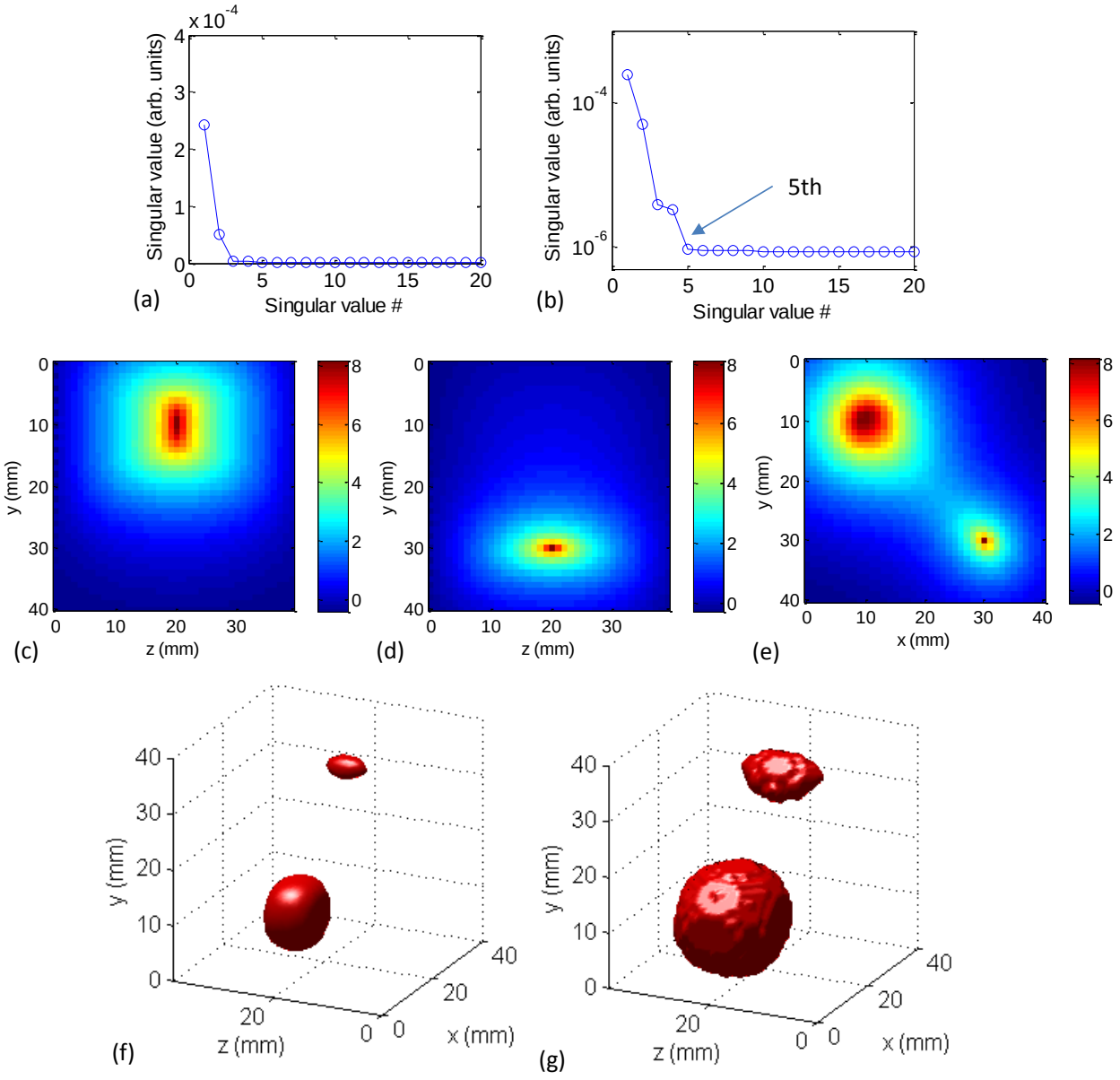

Fig. 3.10. (a) and (b) are singular value spectra in linear and logarithmic scales, respectively. (c) and (d) are sagittal pseudo images (logarithmic scale) of the two targets, respectively. (e) is the axial pseudo image (logarithmic scale) of the two targets at z = 20 mm. (f) shows the isosurface generated using the FWHM in the pseudo image. (g) is the isosurface generated using the "local contour" method.

The isosurfaces are generated using the FWHM in the pseudo image and the "local contour" method to estimate the size of the targets. The estimated sizes of the two targets are shown in Table 3.5. The volumes of the two targets estimated using the "local contour" method are 7.4 and

3.6 times of the actual values. Assuming these are spherical volumes, the corresponding diameters are about 2 and 1.6 times of the actual values. The diameters estimated using the FWHM in the pseudo spectrum have approximately 21% error.

When 5% and 10% noises were added, similar images were obtained. The estimated sizes of the two targets are also shown in Table 3.5. The sizes of the two targets estimated using the optimal "local contour" method are similar for different noise levels, and are not as accurate as those estimated using the FWHM method. The estimated size of a target when two targets were present is not as accurate as that when only one target was present. The sizes estimated using the FWHM in the pseudo spectrum with 5% noise are the most accurate among different noise levels. The main reasons why the accuracy of size retrieval using the "local contour" method degrades may be: 1) The contours are not good estimates of the shape of the target and the actual target boundary is not available in the pseudo spectrum. In particular when the targets are not far from each other, the pseudo images of different targets are not well separated. 2) Due to the diffusive nature of light transmission, the signal is not sensitive to the shape (size) of the small target. In simulations with noise added or in experiments, when the forward model is used with the estimated target shape, the "optimal" contour may easily be a wrong contour with a "local minimum" in Eq. (3.6).

The retrieved optical strength for all noise levels is approximately the same, since the optical strength is mainly determined by the leading (low order) singular components which are little affected by the noise. The retrieved strength of the left target (larger) has 4.7% error, and of right target almost retrieved exactly. The error may be due to the approximation of the GFVs for extended targets by using one single GFV corresponding to the centroid position. Therefore, a larger target leads to larger error in the retrieved strength.

3.4. Experiments

3.4.1. Absorptive targets

The first experiment is the same as that introduced in Section 2.5.3.2 of Chapter 2, except that the concentration of the ink in targets was adjusted to provide absorption coefficient μ_a = 0.5 mm^{-1}, instead of 0.013 mm^{-1}. The two targets were ~ 9 mm diameter, embedded in 60-mm transparent plastic container filled with Intralipid-20% suspension in water. The absorption coefficient of the background medium is 0.003 mm^{-1}, and the transport mean free path l_t, 1 mm. The separation of the two targets varied to be 19.3 mm, 29.3 mm, and 39.3 mm. The sample was scanned by a 100-mW 790-nm diode laser at 15 × 11 grid points with 5 mm step size. The images were acquired using a water-cooled CCD camera. The experimental setup and other details are the same as those in Chapter 2.

When the two targets are ~ 2 cm apart, the eigenvalue spectrum and the pseudo spectrum were plotted in Figs. 3.11(a) and 3.11(b) in linear and logarithmic scales, respectively. In linear scale, two singular values are prominent and correspond to two targets. In logarithmic scale, the "corner" is determined to be after the 13th singular value. To test the sensitivity of localization with respect to the dimension of signal subspace, the pseudo spectrum is calculated using two eigen component and 13 eigen components, and shown in Figs. 3.11(c) and 3.11(d), respectively. The locations of the targets are determined using the maxima in the pseudo spectra, and shown in Table 3.6 and 3.7 for comparison with known results. The separation between the two targets is retrieved to be 18.4 mm. The FWHM in the pseudo spectrum calculated using 13 eigen components is used to generate an isosurface and shown in Fig. 3.11(e). The same pseudo spectrum is used to generate the isosurface using the "local contour" method (Eq. (3.6)), as

shown in Fig. 3.11(f). The FWHM isosurface is not available in logarithmic scale, so it is generated using pseudo spectrum in linear scale.

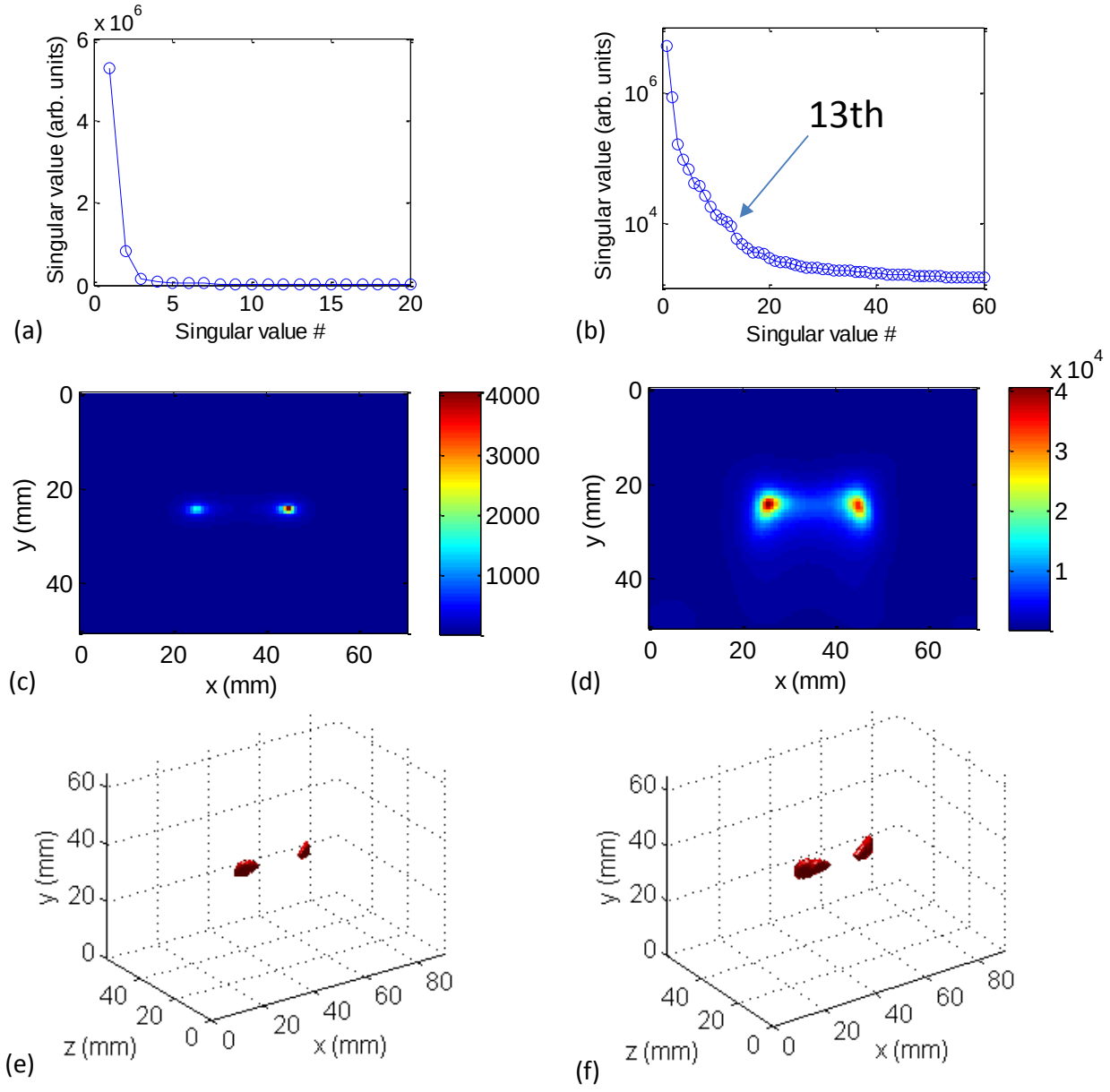

Fig. 3.11. (a) and (b) are singular value spectrum in linear and logarithmic scales respectively. (c) and (d) are pseudo images of the two targets generated using 2 eigen components and 13 eigen components, respectively. (e) shows the isosurface generated using the FWHM in the pseudo image. (f) is the isosurface generated using the "local contour" method.

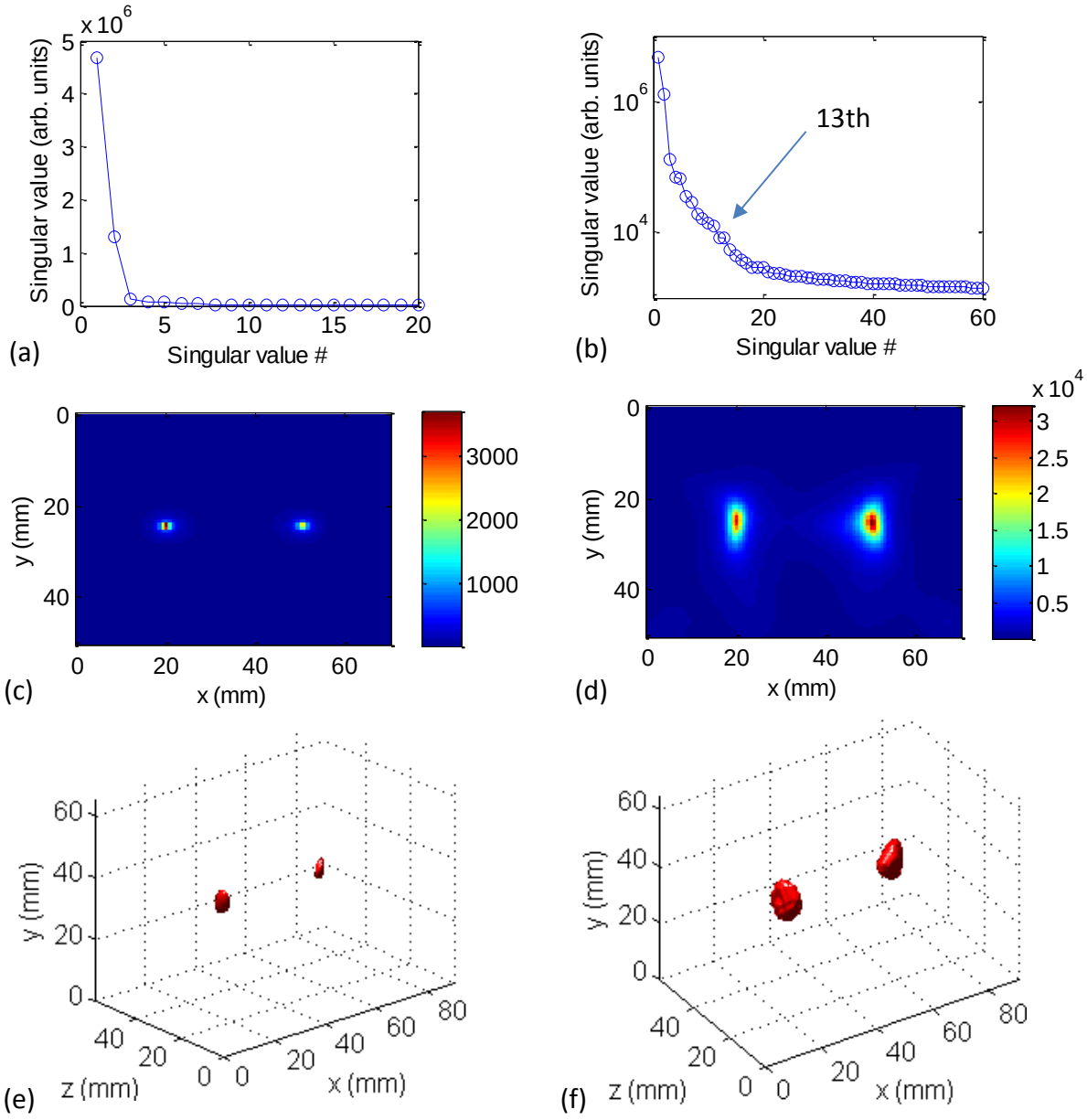

Fig. 3.12. (a) and (b) are singular value spectrum in linear and logarithmic scales respectively. (c) and (d) are pseudo images of the two targets generated using 2 eigen components and 13 eigen components, respectively. (e) shows the isosurface generated using the FWHM in the pseudo image. (f) is the isosurface generated using the "local contour" method.

The strengths of the targets are retrieved using 2 eigen components, 13 eigen components and the original data matrix, and shown in Table 3.8 with comparison to the known value (Eq.

(3.5)). The sizes of the targets are estimated using the FWHM in the pseudo spectrum and the "local contour" method, and shown in Table 3.9.

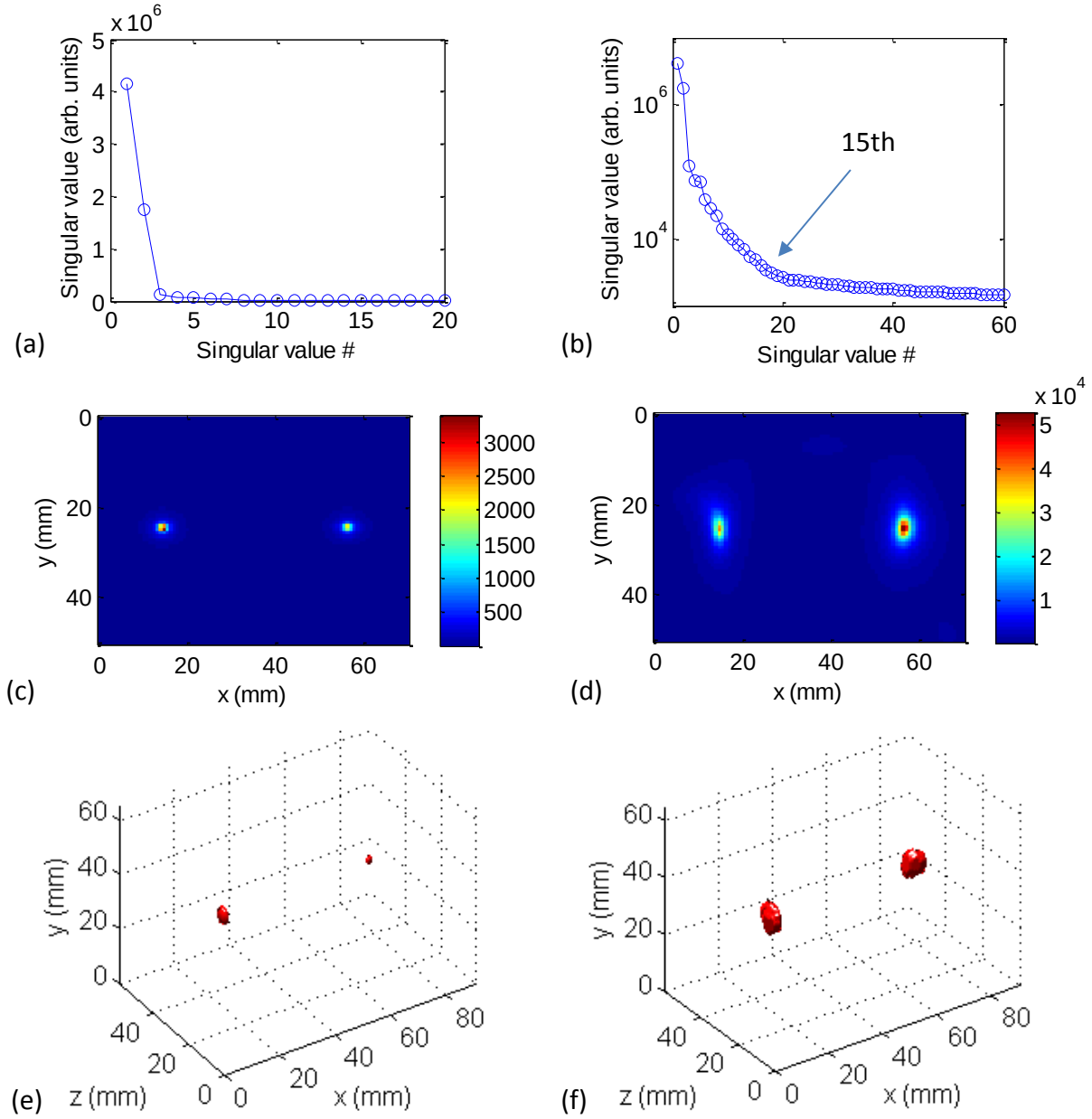

Fig. 3.13. (a) and (b) are singular value spectrum in linear and logarithmic scales respectively. (c) and (d) are pseudo images of the two targets generated using 2 eigen components and 13 eigen components, respectively. (e) shows the isosurface generated using the FWHM in the pseudo image. (f) is the isosurface generated using the "local contour" method.

Table 3.6. Retrieved target locations using 13* eigenvectors

Separation	Target	Known Positions [x, y, z (mm)]	Retrieved Positions [x, y, z (mm)]	Error (mm)
2cm	Left	25.1, 25.1, 30	26.4, 25.2, 30.5	1.3, 0.1, 0.5
	Right	44.4, 25.1, 30	44.8, 25.2, 31.5	0.4, 0.1, 1.5
3cm	Left	20.1, 25.1, 30	20.3, 25.2, 31.5	0.2, 0.1, 1.5
	Right	49.4, 25.1, 30	51.0, 25.2, 32.5	1.6, 0.1, 2.5
4cm	Left	15.1, 25.1, 30	14.9, 26.7, 31.5	0.2, 1.6, 1.5
	Right	54.4, 25.1, 30	56.3, 25.2, 32.5	1.9, 0.1, 2.5

* 15 eigen components for 4-cm separation

Table 3.7. Retrieved target locations using 2 eigenvectors

Separation	Target	Known Positions [x, y, z (mm)]	Retrieved Positions [x, y, z (mm)]	Error (mm)
2cm	Left	25.1, 25.1, 30	25.7, 24.4, 31.5	0.6, 0.7, 1.5
	Right	44.4, 25.1, 30	44.8, 24.4, 29.5	0.4, 0.7, 0.5
3cm	Left	20.1, 25.1, 30	20.3, 24.4, 30.5	0.2, 0.7, 0.5
	Right	49.4, 25.1, 30	51.0, 24.4, 28.5	1.6, 0.7, 1.5
4cm	Left	15.1, 25.1, 30	14.9, 25.2, 30.5	0.2, 0.1, 0.5
	Right	54.4, 25.1, 30	56.3, 24.4, 29.5	1.9, 0.7, 0.5

Similar analysis is also performed when the two target are ~ 3 cm and 4 cm apart. The singular value spectra (linear and logarithmic scale), pseudo images (using 2 and 13 eigen components for 3-cm separation, and 2 and 15 eigen components for 4-cm separation), and isosurfaces generated using FWHM in the pseudo images and "local contour" method are shown in Figs. 3.12 and 3.13 respectively. The retrieved target locations using 2 and 13(15) eigen components are shown in Table 3.6 and 3.7 for comparison. For the 3-cm and 4-cm separations, the retrieved separation between the targets is 30.7 mm and 41.4 mm, respectively. The strengths of the targets with 3-cm (4-cm) separation are estimated using 2 eigen components and 13(15) eigen components for comparison, and shown in Table 3.8. The sizes of the targets are estimated using the FWHM in the pseudo spectrum (linear scale) and the "local contour" method and shown in Table 3.9.

Table 3.8. Retrieved optical strengths of the two targets

Separation	Retrieved τ (using 2 comps) ($\times 10^4$ mm^3/ns)		Retrieved τ (using 13* comps) ($\times 10^4$ mm^3/ns)		Retrieved τ (using the whole data matrix) ($\times 10^4$ mm^3/ns)		Known τ ($\times 10^4$ mm^3/ns)	
	Left	Right	Left	Right	Left	Right	Left	Right
2cm	2.85	2.76	2.90	2.81	2.90	2.81	4.19	4.19
3cm	3.46	3.32	3.53	3.41	3.53	3.41		
4cm	3.93	3.74	4.03	3.87	4.03	3.89		

* 15 eigen components for 4-cm separation

Table 3.9. Estimated size and absorption coefficient of the targets

Separation (cm)	Retrieved size using FWHM (mm^3)		Retrieved size using "local contour" (mm^3)		Retrieved absorption coefficient (μ_a) (mm^{-1})		Known absorption coefficient (μ_a) (mm^{-1})	
	Left	Right	Left	Right	Left	Right	Left	Right
2	97	131	211	171	0.61	0.73	0.5	0.5
3	78	48	548	589	0.29	0.26		
4	60	9	253	271	0.71	0.63		

* Known target size (9-mm-diameter sphere): 381.7 mm^3

The target locations retrieved using 2 eigen components (prominent in singular value spectrum in linear scale) and more eigen components (prominent in singular value spectrum in logarithmic scale) are both accurate.

Compared with the actual optical strengths of the targets ~ 4.19×10^4 (mm^3/ns), the retrieved values are within 32.9%, 18.6% and 7.6% for 2-cm, 3-cm and 4-cm separation between the samples, respectively. The further the two targets, the more accurate results are obtained. Using the dimension of the signal subspace determined using the singular value spectrum in logarithmic scale only slightly improves the retrieved optical strengths of the targets. Further increasing the number of eigen components in Eq. (3.5) does not lead to improved accuracy in the retrieved optical strengths. So the estimate of location and optical strength of a target using TROT is not sensitive to the determination of the dimension of the signal subspace. In other words it is not critical to find the optimal threshold around the "corner" of the "*L*-curve" to separate the signal subspace from noise subspace so as to retrieve the location and optical

strength of the targets accurately. If there are M absorptive targets present, it is mainly the leading M eigen components that determine the locations and optical strengths of the targets. For the experiments presented above, the target locations and strengths are mainly determined by the first two eigen components. The dimension of the signal subspace determined using the singular value spectrum in logarithmic scale may be used to retrieve slightly more accurate optical strength, since more higher-order components that belong to the signal subspace will be separated from the noise subspace. This also helps in retrieving more accurate size or shape of the targets, since higher-order components carry more size information of the targets.

As shown in Table 3.9, the sizes of targets estimated using the FWHM of the pseudo spectrum in linear scale are all much smaller than the actual values. The estimated sizes using the "local contour" method are more accurate and further used to estimate the absorption coefficient of the m^{th} target using $\delta\mu_a = \tau_m/c\Delta V_m$. Compared to the known target size 381.7 mm^3, there is up to ~ 55% error in the retrieved sizes. Among the separations considered, the size is the most accurate for the target separation of 4-cm between the targets. The error in the estimated absorption coefficient is within 48% for the targets in all cases of separations, as shown in Table 3.9. The forward model used in the presented work is the linearized analytical model of Eq. (3.1), which only considers the first order of Born approximation. A forward model, such as, finite element method (FEM) – based forward model, which considers the non-linear effect in the diffusion process (higher orders of Born approximation) may be used to improve the estimate of target size. Since the forward model will only be run for a limited times, and there is no need to calculate the Jacobian matrix, it is different from other model-based inverse image reconstruction (IIR) methods which are very time-consuming.

3.4.2. Scattering target

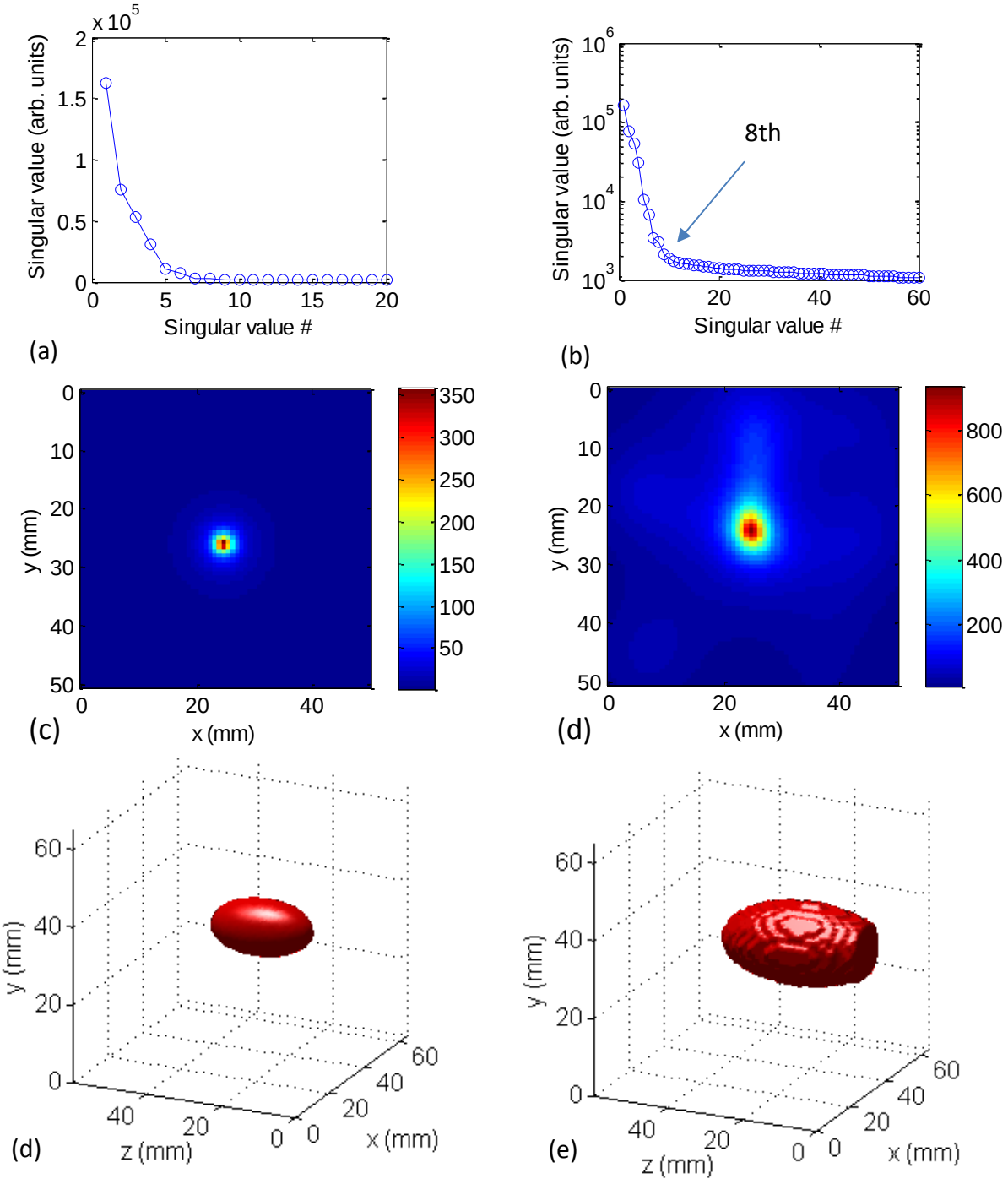

Fig. 3.14. (a) and (b) are singular value spectrum in linear and logarithmic scales respectively. (c) and (d) are pseudo images of the two targets generated using 1 eigen component and 8 eigen components, respectively. (e) shows the isosurface generated using the FWHM in the pseudo image (logarithmic scale). (f) is the isosurface generated using the "local contour" method.

The second experiment is the same as that presented in Section 2.5.3.3 of Chapter 2, where a scattering target was embedded in the mid-plane (z = 30 mm) of the scattering medium. The scattering coefficient of the target was 4 times of that of the background. All other experimental parameters are the same as in the experiments presented above. The sample was scanned by the 100-mW 790-nm diode laser at 9×9 grid points with 5 mm step size. The images were acquired for TROT analysis.

The singular value spectrum of the TR matrix is shown in Figs. 3.14(a) (linear) and 3.14(b) (logarithmic).

The pseudo images generated using 1 and 8 eigen components are shown in Figs. 3.14(c) and 3.14(d), respectively. When 8 eigen components are used, the target image is more extended. The location of the target is accurately retrieved using the maximum in both images. However, the isosurfaces cannot be generated using either the FWHM of the pseudo spectrum in logarithmic scale or the "local contour" approach. Simulations show the pseudo images for scattering targets have lower resolution and contrast than absorptive targets. Using the pseudo spectrum calculated with high order components included to estimate shape of scattering targets is more difficult. FWHM of the pseudo spectrum in logarithmic scale significantly overestimated the target size. The "local contour" approach also lead to a wrong contour. So instead of including higher-order components, the isosurfaces are generated using the 1-eigen-component pseudo spectrum for both approaches, as shown in Figs. 3.14(e) and 3.14(f). The volumes are determined to be 2921 mm^3 and 9301 mm^3 using the two approaches, FWHM of pseudo spectrum and "local contour", respectively. The actual volume is 523.6 mm^3. Both estimated volumes are much larger than the actual value. The optical scattering strength of the targets are also estimated using Eq. (3.5). When one eigen component is used, the optical strength is

estimated to be -1.06×10^4 mm^5/ns. When 8 eigen components are used, the strength is estimated to be -1.00×10^4 mm^5/ns, and stays the same even if the original data matrix is used. The known value of the strength is -2.95×10^4 mm^5/ns. As expected, it is more difficult to retrieve the optical strength and size of a scattering target than an absorptive target.

3.5. Discussion

Time reversal optical tomography (TROT) was further developed to deal with finite size targets. The center position of the target(s) is determined rather accurately for both absorptive and scattering targets. Optical strengths of targets can be calculated with acceptable accuracy by unmixing the rank-reduced data matrix for small targets. For absorptive targets, it was retrieved with < 8% error when two targets were involved with 4-cm separation, and deteriorated with less separation. However, for scattering targets, the error was ~ 66% even when only one target was present. Simulation showed that the optical strength (absorption or scattering) can be retrieved for different target size, target location and noise level. However, the accuracy in the retrieved optical strength is lower for larger targets, due to the approximation of the target location being at the centroid. The retrieved location and optical strength of a target are not sensitive to the dimension of the signal subspace. The target location and optical strength are mainly determined by the prominent eigen components shown in the linear plot of the eigenvalue (singular value) spectrum. Using more eigen components, such as the prominent ones in the semi-log plot of the eigenvalue (singular value) spectrum, may slightly improve the estimate in the locations and strengths of the targets. Further increasing the number the components does not continue to improve the results.

It is much more challenging to retrieve target size. The size of targets may be estimated by using the isosurface of the FWHM in the pseudo spectrum or using an optimal contour in the

pseudo spectrum which can minimize the difference between the experimental data and calculated data using a proper forward model. Simulation shows there is no well-defined correlation between the noise level and the estimated optical strength and size of a target. Since both optical property and target shape are unknown in the forward-model, the data must be normalized before comparison without considering the absolute value of the magnitude. So only the shape of the light intensity distribution is considered. As a result, the diffuse light signal is not sensitive to target size. Due to the diffuse nature of light propagation in the medium, the exact shape of the target is not available in the contours of the pseudo spectrum. It is very difficult to find an accurate solution that matches the actual dimension of the target. In summary, both location and optical strengths of extended targets can be retrieved with confidence; while there is low confidence in the estimated target size. It may be improved if the target boundary is optimized using the orthogonality between the noise subspace and test target space generated using a level set method [5, 6, 15].

References

1. Binlin Wu, W. Cai, M. Alrubaiee, M. Xu, and S. K. Gayen, "Time reversal optical tomography: locating targets in a highly scattering turbid medium," Opt. Express **19**, 21956-21976 (2011).
2. A. J. Devaney, "Time reversal imaging of obscured targets from multistatic data," IEEE Trans. Antenn. Propag. **53**, 1600-1610 (2005).
3. M. Fink, D. Cassereau, A. Derode, C. Prada, P. Roux, M. Tanter, J. L. Thomas, and F. Wu, "Time-reversed acoustics," Rep. Prog. Phys. **63**, 1933-1995 (2000).
4. S. Hou, K. Solna, and H. Zhao, "A Direct Imaging Algorithm For Extended Targets," Inverse Probl. **22**, 1151-1178 (2006).

5. S. Hou, K. Solna and H. Zhao, "Imaging of location and geometry for extended targets using the response matrix," J. Comput. Phys. **199**, 317-338 (2004).
6. F. K. Gruber, and E. Marengo, "Reinterpretation and enhancement of signal-subspace-based imaging methods for extended scatterers," SIAM J. Imaging Sci. **3**, 434-461 (2010).
7. E. A. Marengo, F. K. Gruber, and F. Simonetti, "Time reversal MUSIC imaging of extended targets," IEEE Trans. Image Process. **16**, 1967-1984 (2007).
8. C. Ramananjaona, M. Lambert, D. Lesselier, and J.-P. Zolesio, "Shape reconstruction of buried obstacles by controlled evolution of a level set: from a min-max formulation to numerical experimentation," Inverse Prob. **17**, 1087-1111 (2001).
9. M. Burger, "A level set method for inverse problems," Inverse Prob. **17**, 1327-1355 (2001).
10. O. Dorn, and D. Lesselier, "Level set methods for inverse scattering," Inverse Problems **22**, R67-R131 (2006).
11. P. C. Hansen, "Analysis of discrete ill-posed problems by means of the L-curve," Soc. Ind. Appl. Math. Rev. **34**, 561-580 (1992).
12. S. K. Lehman, and A. J. Devaney, "Transmission mode time-reversal super-resolution imaging," J. Acoust. Soc. Am. **113**, 2742-2753 (2003).
13. A. N. Tikhonov, "Solution of incorrectly formulated problems and the regularization method," Soviet Math. Dokl. **4**, 1035-1038 (1963).
14. M. Xu, M. Alrubaiee, S. K. Gayen, and R. R. Alfano, "Three-dimensional localization and optical imaging of objects in turbid media with independent component analysis," Appl. Opt. **44**, 1889-1897 (2005).
15. S. J. Osher, and R. P. Fedkiw, *Level Set Methods and Dynamic Implicit Surfaces* (Springer-Verlag, New York, 2002).

Chapter 4

Diffuse optical imaging using matrix decomposition methods

4.1. Introduction

Diffuse optical imaging (DOI) for detection and retrieval of location information of targets in a highly scattering turbid medium may be treated as a blind source separation (BSS) problem [1, 2]. BSS problem refer to the general class of problems involving retrieval of individual signals that constitute the measured mixed signal. Various matrix decomposition methods, such as, Independent Component Analysis (ICA) [3], Principal Component Analysis (PCA) [4] and Non-negative Matrix Factorization (NMF) [5, 6] have been developed for solving the BSS problem and retrieving desired information.

Min Xu *et al.* adapted ICA of information theory to develop Optical Tomography using Independent Component Analysis (OPTICA) and demonstrated its application for diffuse imaging of absorptive, scattering and fluorescent targets [7-11]. ICA assumes the signals from different targets to be *independent* of each other, and optimizes a relevant measure of independence to obtain the ICs associated with different targets. The position co-ordinates of targets in three dimensions are determined from the individual components separately.

PCA assumes that the PCs contributing to the signal are *uncorrelated* and explain the most variance in the signal. PCA has been widely used in various applications, such as spectroscopy [12], face recognition [13] and neuroimaging [14]. NMF seeks to factorize a matrix into two non-negative matrices (component signals and weights) and requires the contributions to signal and the weights of the components to be *non-negative*. It does not imply any relationship between the components. NMF has also been widely used in biological analysis [15], and spectral analysis [16].

The objective of the study presented in this chapter is to test and compare the efficacy of these algorithms when used to solve the DOI problem. We present results of investigations on absorptive and scattering targets embedded in model scattering media using both simulative and experimental data.

The remainder of the chapter is organized as follows. In Section 4.2, the formalisms of the three methods are introduced. Section 4.3 evaluates the resulting imaging approaches using simulated data. The approaches are further examined in Section 4.4 for experimental data acquired using absorptive and scattering targets embedded in model scattering media. Section 4.5 discusses and summarizes the results.

4.2. Theoretical Formalism

4.2.1. Blind Source Separation problem

Blind source separation (BSS), also known as blind signal separation is a general problem in information theory that seeks to separate different individual signals from the measured signals, which are weighted mixtures of those individual signals. Assuming M individual signals, $s_m(t)$; $m = 1, \ldots, M$, are linearly mixed instantaneously, the BSS problem is modeled as following. The dimension of $s_m(t)$ is N_s, the number of sampling times. In this study, t will be replaced by spatial positions of the excitation light sources. A total of N_d detectors sense N_d different mixtures of $s_m(t)$; $m = 1, \ldots, M$. The mixture measured by the i^{th} detector can be represented as $x_i(t) = \sum_{m=1}^{M} a_{im} s_m(t)$, or $X = AS$, in a matrix notation, where $A \in R^{N_d \times M}$ is a mixing or weighting matrix, $S \in R^{M \times N_s}$, $X \in R^{N_d \times N_s}$, and $M < \min(N_s, N_d)$. The objective of BSS is to retrieve the signals $s_m(t)$ and their weights, a_{im}. ICA, PCA and NMF are statistical analysis methods, used to solve the BSS problem.

4.2.2. Diffuse optical imaging problem for absorptive and scattering targets

In DOI one measures the signal at the sample boundary, which includes a weighted mixture of contributions from embedded targets. One uses the diffusion approximation [17-19] of the radiative transfer equation [20, 21] as the forward model to describe light propagation in a highly scattering turbid medium. The perturbation in the light intensity distribution measured on the boundary of the sample due to the presence of the targets (which are considered to be localized inhomogeneities in the optical properties within the sample volume) may be written, in the first order Born approximation, as [22, 23]

$$\Delta\phi(\boldsymbol{r}_d,\boldsymbol{r}_s) = -\int G(\boldsymbol{r}_d,\boldsymbol{r})\delta\mu_a(\boldsymbol{r})c_m G(\boldsymbol{r},\boldsymbol{r}_s)d^3\boldsymbol{r} - \int \delta D(\boldsymbol{r})c_m \nabla_r G(\boldsymbol{r}_d,\boldsymbol{r})\cdot\nabla_r G(\boldsymbol{r},\boldsymbol{r}_s)d^3\boldsymbol{r}, \quad (4.1)$$

where $\boldsymbol{r}_s$, $\boldsymbol{r}_d$, and $\boldsymbol{r}$ are the positions of a source of unit power, detector and target, respectively; $G(\boldsymbol{r},\boldsymbol{r}_s)$ and $G(\boldsymbol{r}_d,\boldsymbol{r})$ are the Green's functions that describe light propagation from the source to the target and from the target to the detector, respectively; $\delta\mu_a$ and δD are the differences in absorption coefficient and diffusion coefficient between the targets and the background medium, respectively; and c_m is the light speed in the medium.

A multi-source illumination and multi-detector signal acquisition scheme is used to acquire light transmitted through a scattering medium. For small absorptive targets, a perturbation data matrix is constructed using $-\Delta\phi$ for all sources. The elements of the data matrix pertaining to absorptive targets represented by the first term in Eq. (4.1) may be written in a discrete form as:

$$X_{ij} = \sum_{m=1}^{M} G^d(\boldsymbol{r}_i,\boldsymbol{r}_m)\tau_m G^s(\boldsymbol{r}_m,\boldsymbol{r}_j), \ (i = 1, 2, \ldots, N_d;\ j = 1, 2, \ldots, N_s), \quad (4.2)$$

where $\boldsymbol{r}_i$, $\boldsymbol{r}_j$ and $\boldsymbol{r}_m$ are the locations of the i^{th} detector, j^{th} source and m^{th} target, respectively; N_s, N_d and M are the numbers of sources, detectors and targets, respectively; $\tau_m = \delta\mu_a(\boldsymbol{r}_m)c_m\delta V_m$ is the *optical absorption strength* of the m^{th} target, δV_m is the volume of the target; $G^s(\boldsymbol{r}_m, \boldsymbol{r}_j)$ and $G^d(\boldsymbol{r}_i,$

$\boldsymbol{r}_m$) are the Green's functions that describe light propagation from j^{th} source to m^{th} target and from m^{th} target to i^{th} detector, respectively. The number of targets is assumed to be less than that of sources and detectors, $M < \min(N_d, N_s)$.

The m^{th} target may be considered to be a virtual source of strength $\tau_m G^s(\boldsymbol{r}_m, \boldsymbol{r}_j)$ excited by the real light source located at $\boldsymbol{r}_j$. The data matrix $X = \{X_{ij}\}$, may be considered to be a set of combinations of light signals from all virtual sources mixed by a mixing matrix $\{G^d(\boldsymbol{r}_i, \boldsymbol{r}_m)\}$. Therefore, this problem can be treated as a BSS problem.

As the second term in Eq. (4.1) suggests, each scattering target is represented by three co-located virtual sources of strength: $\tau_m \partial_p G^s(\boldsymbol{r}_m, \boldsymbol{r}_j)$, where $\partial_p = \partial/\partial p$, $(p = x, y, z)$, and $\tau_m = \delta D(\boldsymbol{r}_m) c_m \delta V_m$, is the *optical scattering strength* of the m^{th} target [8]. The mixing matrices become $\{\partial_p G^d(\boldsymbol{r}_i, \boldsymbol{r}_m)\}$, $(p = x, y, z)$, for the three virtual sources generated by the m^{th} target. The elements of the data matrix for scattering targets may be written as

$$X_{ij} = \sum_{m=1}^{M} \sum_{p=\{x,y,z\}} \partial_p G^d(\boldsymbol{r}_i, \boldsymbol{r}_m) \tau_m \partial_p G^s(\boldsymbol{r}_m, \boldsymbol{r}_j). \tag{4.3}$$

Since one absorptive target is represented by one centrosymmetric virtual source, while three virtual sources (one centrosymmetric and two dumb-bell shaped) represent one scattering target [7, 8], the number and patterns of virtual sources may be used, in favorable situations, to identify the target as absorptive or scattering in nature. In this chapter, only small targets are considered since all three algorithms are suited for small targets, and early detection, when the tumors are more amenable to treatment.

4.2.3. DOI as a BSS problem

The data matrix for the DOI problem may be written as

$$X = AS = \sum_{m=1}^{M} A_{im} S_{mj}, \tag{4.4}$$

where $A \in R^{N_d \times M}$, $S \in R^{M \times N_s}$, and $X \in R^{N_d \times N_s}$. For a*bsorptive* targets,

$$A_{im} = \beta_m G^d\left(\boldsymbol{r}_i, \boldsymbol{r}_m\right), \text{ and } S_{mj} = \alpha_m G^s\left(\boldsymbol{r}_m, \boldsymbol{r}_j\right), \tag{4.5a}$$

while for s*cattering* targets,

$$A_{im} = \beta_m \partial_p G^d\left(\boldsymbol{r}_i, \boldsymbol{r}_m\right), \text{ and } S_{mj} = \alpha_m \partial_p G^s\left(\boldsymbol{r}_m, \boldsymbol{r}_j\right). \tag{4.5b}$$

$\{S_{mj}\}$ (j = 1, 2, …, N_s) and $\{A_{im}\}$ (i = 1, 2, …, N_d) are two-dimensional intensity distributions on the source and detector planes, respectively. Source and detector planes are the boundaries of the sample through which light enters and exits the sample volume, respectively. The scaling factors β_m and α_m are related to the target optical strength, $\tau_m = \alpha_m \beta_m$. The location of the target and the scaling factors can be retrieved using a least squares fitting via

$$\underset{\alpha_m, \beta_m, r_m}{\arg\min} \left\{ \sum_j \left[\alpha_m{}^{-1} S_{mj} - G^s\left(\boldsymbol{r}_m, \boldsymbol{r}_j\right) \right]^2 + \sum_i \left[\beta_m{}^{-1} A_{im} - G^d\left(\boldsymbol{r}_i, \boldsymbol{r}_m\right) \right]^2 \right\}, \tag{4.6a}$$

or,

$$\underset{\alpha_m, \beta_m, r_m}{\arg\min} \left\{ \sum_p \left\{ \sum_j \left[\alpha_m{}^{-1} S_{mj} - \partial_p G^s\left(\boldsymbol{r}_m, \boldsymbol{r}_j\right) \right]^2 + \sum_i \left[\beta_m{}^{-1} A_{im} - \partial_p G^d\left(\boldsymbol{r}_i, \boldsymbol{r}_m\right) \right]^2 \right\} \right\}, \tag{4.6b}$$

for absorptive and scattering targets, respectively. However, when a scattering target is embedded deep in a turbid medium, only the $\tau_m \partial_z G^s(\boldsymbol{r}_m, \boldsymbol{r}_j)$ virtual source remains significant. So only $p = z$ may be used for fitting in Eq. (4.6b) [8].

4.2.4. Decomposition Methods

We now provide a brief overview of three matrix decomposition methods that are commonly used in BSS problems.

4.2.4.1. *Independent Component Analysis (ICA)*

OPTICA assume that the virtual sources are *independent* of each other [8]. So they can be retrieved through an iterative process which seeks to maximize the independence among the components. In practice, the independent components are found by maximizing some measure of independence, such as kurtosis (the fourth-order cumulant), of the unmixed components. A Matlab program for ICA was adopted from http://sccn.ucsd.edu/eeglab/. The location of the target can be retrieved by fitting the independent component intensity distributions (ICIDs) to Green's functions or derivatives of Green's functions using Eq. (4.6a) and Eq. (4.6b).

4.2.4.2. *Principal Component Analysis (PCA)*

PCA assumes that the virtual sources are uncorrelated so that the correlation (covariance) between them is ideally zero, and minimal in practice. The covariance matrix of S, $cov(S)$ should be diagonal. The general process of PCA is as follows. The data matrix $X = AS + N$, where N is random noise added to the data, and A and S are the same as defined in Eq. (4.4). When S is mean centered, elements of the mean-centered matrix S' are defined as

$$S'_{mj} = S_{mj} - \frac{1}{N_s}\sum_{j=1}^{N_s} S_{mj} \,. \tag{4.7a}$$

Similarly

$$X'_{ij} = X_{ij} - \frac{1}{N_s}\sum_{j=1}^{N_s} X_{ij} \,. \tag{4.7b}$$

PCA looks for a matrix P that decomposes X into virtual sources, $S = PX$. It also holds that $S' = PX'$, since P is just a rotation matrix which does not change the center of the data.

$$cov(S) = S'S'^{T} = (PX')(PX')^{T} = PX'X'^{T}P^{T} = \Lambda \,, \tag{4.8}$$

where $\Lambda = \text{diag}\{\lambda_1, \lambda_2, \ldots\}$. The eigenvalues λ_m are variances in the covariance matrix. Therefore, $X'X'^TP^T = P^T\Lambda$, where P^T is orthonormal. PCA is realized by eigenvalue decomposition (EVD) of the covariance matrix of X. The eigenvectors with leading eigenvalues (largest variances) are selected to be the PCs using the L-curve [24].

Since, $X = P^TS \approx AS$, A is determined as a matrix including only PCs. S is calculated as $S \approx (A^TA)^{-1}A^TX$. Rows of S and columns of A represent principal component intensity distributions (PCIDs) on the source plane and detector plane, respectively, and are proportional to the images of the virtual sources projected on the source and detector planes. The target positions are determined using Eq. (4.6).

4.2.4.3. *Nonnegative Matrix Factorization (NMF)*

NMF is a group of multivariate analysis algorithms that factorize a matrix X into A and S: $X = AS$, A and S are non-negative [6]. Unlike ICA and PCA, NMF does not imply any relationship between the retrieved components; instead, it just enforces non-negativity constraints on A and S. There are various algorithms developed to solve NMF, such as the multiplicative update method [5] and alternating least squares method [25, 26].

In the multiplicative update implementation of NMF, A and S can be found by minimizing the square of Euclidean distance $||X - AS||^2$ as the cost function, where $A \geq 0$ and $S \geq 0$, using the multiplicative update rule

$$A_{ik} \leftarrow A_{ik} \frac{\left(XS^T\right)_{ik}}{\left(ASS^T\right)_{ik}}, \tag{4.9a}$$

$$S_{kj} \leftarrow S_{kj} \frac{\left(A^TX\right)_{kj}}{\left(A^TAS\right)_{kj}} . \tag{4.9b}$$

The alternating least squares (ALS) implementation of NMF uses alternate least squares steps to estimate *A* (or *S*), and use that estimate to optimize *S* (or *A*), and keep repeating the alternative steps until the desired optimization is obtained. Non-negativity is ensured by setting any negative element of *A* or *S* equal to 0.

An NMF toolbox was obtained [27] to carry out NMF computation. A built-in command *nnmf* is also available in Matlab (R2011a).

NMF algorithm requires that the non-negativity assumption must hold in the problem. In particular, for absorptive targets, when *X* is constructed with $-\Delta\phi$, τ_m should be positive, i.*e.* the targets should be more absorbing than the background. If the targets have weaker attenuation properties than the background, *X* needs to be constructed with $+\Delta\phi$ instead. For scattering targets, *X* should be treated similarly to keep its elements positive.

When NMF is applied to a scattering target, only the centrosymmetric component shows up properly, since the other two components have dumb-bell shape which includes negative values [8]. So without any prior knowledge or some other experimental means to assess if the target is absorptive or scattering, NMF may not distinguish between the two possibilities.

The decomposition methods can be applied with different sample geometries such as slab and cydrindrical geometries, and different measurement domains such as time-resolved domain, frequency domain and continuous wave (CW). In this chapter, Green's functions for slab geometry [23] with CW measurement were used for simulation and experiments.

4.2.5. Backprojection

With the location of target(s) retrieved, the size of the target(s) may be estimated using a back-projection Fourier transform approach [11]. A back projection of $X_j(\boldsymbol{r}_d, \boldsymbol{r}_s)$ from the detection plane onto the "target plane" ($z = z_j$ plane) provides an estimate of the target dimension in the lateral

directions. However, the dimension in axial direction is collapsed with target property integrated. The perturbation signal in the light intensity distribution on the detector plane for CW illumination can be approximated by

$$X_j(\boldsymbol{r}_d,\boldsymbol{r}_s)=\int_{z=z_j} G^d(\boldsymbol{\rho}_d-\boldsymbol{\rho})\chi_j(\boldsymbol{\rho})G^s(\boldsymbol{\rho}-\boldsymbol{\rho}_s)d\boldsymbol{\rho}, \tag{4.10a}$$

due to the j^{th} absorptive target, or

$$X_j(\boldsymbol{r}_d,\boldsymbol{r}_s)=\int_{z=z_j} \partial_z G^d(\boldsymbol{\rho}_d-\boldsymbol{\rho})\chi_j(\boldsymbol{\rho})\partial_z G^s(\boldsymbol{\rho}-\boldsymbol{\rho}_s)d\boldsymbol{\rho}, \tag{4.10b}$$

which is the ($p = z$) component due to the j^{th} scattering target, where $\boldsymbol{\rho}_s$ and $\boldsymbol{\rho}_d$ are the lateral coordinates of the source and the detector, and the integration is over the $z = z_j$ plane. In the Fourier space $\chi_j(\boldsymbol{q})$ follows from Eq. (4.10) as,

$$\chi_j(\boldsymbol{q})=\frac{X_j(\boldsymbol{q}-\boldsymbol{q}_s,\boldsymbol{q}_s)}{G^d(\boldsymbol{q}-\boldsymbol{q}_s)G^s(\boldsymbol{q}_s)}, \tag{4.11a}$$

for the absorptive target, and

$$\chi_j(\boldsymbol{q})=\frac{X_j(\boldsymbol{q}-\boldsymbol{q}_s,\boldsymbol{q}_s)}{\partial_z G^d(\boldsymbol{q}-\boldsymbol{q}_s)\partial_z G^s(\boldsymbol{q}_s)}, \tag{4.11b}$$

for the scattering target, where $\boldsymbol{q}$ and $\boldsymbol{q}_s$ are the spatial frequencies on the x-y plane. The inverse Fourier transform of $\chi_j(\boldsymbol{q})$ provides the cross-section image of the j^{th} target at the $z = z_j$ plane.

The calculation of $\chi_j(\boldsymbol{q})$ using Eq. (4.11) employed Tikhonov regularization [28], with a modified *L*-curve method [24] to determine the optimal regularization parameter. This optimization is a tradeoff between obtaining a closer estimate of target cross section and fewer artifacts in the back-projection image. Since the positions of the targets were obtained from the previous steps, any artifacts cropping up in the back-projection process could be readily identified from their positions. So, instead of using the "corner" of the *L*-curve to find the optimal

regularization parameter, we settled for a lower regularization using the criterion that the highest artifact peak reaches ~50% of the target peak to improve the size estimate of the cross-section images. The full width at half maximum (FWHM) of the spatial profile of the cross-section image was used as an estimate of the target size.

4.3. Simulative Study of Decomposition Methods

First we test the efficacy of the three matrix decomposition methods using simulated data.

4.3.1. One absorptive target and one scattering target with ~ 4-cm separation

The sample was considered to be a 40-mm thick uniform scattering slab with lateral dimension of 80 mm × 80 mm, as shown in Fig. 4.1. Its absorption and diffusion coefficients were taken to be μ_a = 0.003 mm^{-1} and D = 1/3 mm (transport mean free path, l_t = 1 mm), respectively, which are similar to the average value of those parameters for female human breast tissue. The index of refraction n of the medium was taken to be 1.33. The speed of light is 2.998 × 10^8 m/s, or 299.8 mm/ns in vacuum, and 225.4 mm/ns in the medium. An absorptive and a scattering point targets were placed at (50, 60, 15) mm and (30, 30, 25) mm, respectively. The absorption coefficient of the absorptive target was set to be higher than the background by $\delta\mu_a$ = 0.008δ(**r**, **r**') mm^{-1}, where δ(**r**) is the Dirac delta function, while the diffusion coefficient was taken to be the same as that of background. The diffusion coefficient of the scattering target was set to be lower than the background (higher scattering coefficient) with δD = -0.8δ(**r**, **r**') mm (l_t = 0.7 mm), while the absorption coefficient was taken to be the same as the background. The optical strengths of the absorptive and scattering targets were $\tau = \int \delta\mu_a c_m d\boldsymbol{r}$ = 1.8032 mm^3/ns, and $\tau = \int \delta D c \delta \boldsymbol{r}$ = -180.32 mm^5/ns, respectively. The incident CW beam step scanned the sample at 21 × 21 grid points covering an 80 × 80 mm^2 area, with a step size of 4 mm. Light on the opposite side was recorded

at 41 × 41 grid points covering the same area. The simulated data matrix X was generated using Eq. (4.2). Additive Gaussian noise of 5% was added to X, *i.e.* $X = X_0 + N$, where N is Gaussian noise with mean value 0, and standard deviation 5% of average of X_0. Then the data matrix X was analyzed using the three different algorithms.

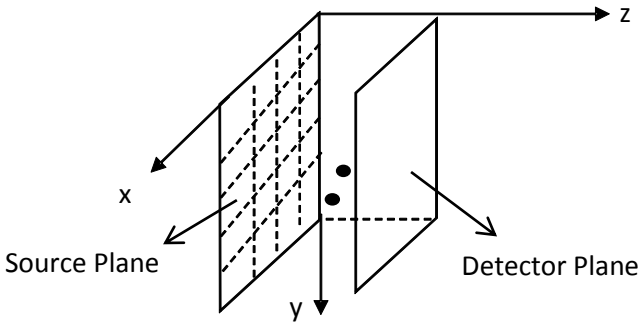

Fig. 4.1. Light intensity distribution on the detector plane is recorded when a point source scans on the source plane.

4.3.1.1. *ICA Analysis*

One independent component for the absorptive target and three independent components for the scattering target were retrieved by ICA. The independent component intensity distributions (ICIDs) on the detector plane are shown in Figs. 4.2(a), 4.2(c), 4.2(d), and 4.2(e). Similar ICIDs were obtained on the source plane. Fig. 4.2(g) shows the centrosymmetric ICID for the scattering target, and Fig. 4.2(i) shows the ICID for the absorbing target. Since there are more detectors than sources, the components on the detector plane have higher resolution.

The components in either the detector plane or the source plane can, in principle, be used to extract position and optical strength of the target(s). However, in our experimental arrangement signal is collected by a 1024 × 1024 pixels CCD camera, while the source plane is scanned in an *x-y* array of points, which is much smaller than the number of pixels in the CCD camera. Consequently, the resolution in the detector plane is much better, and the data set more robust than the source side. So, we used the images on the detector plane for retrieving target information

using experimental data. While it would not matter in simulation, to be consistent with experimental situations, we employed detector plane images when using simulated data as well for all three algorithms.

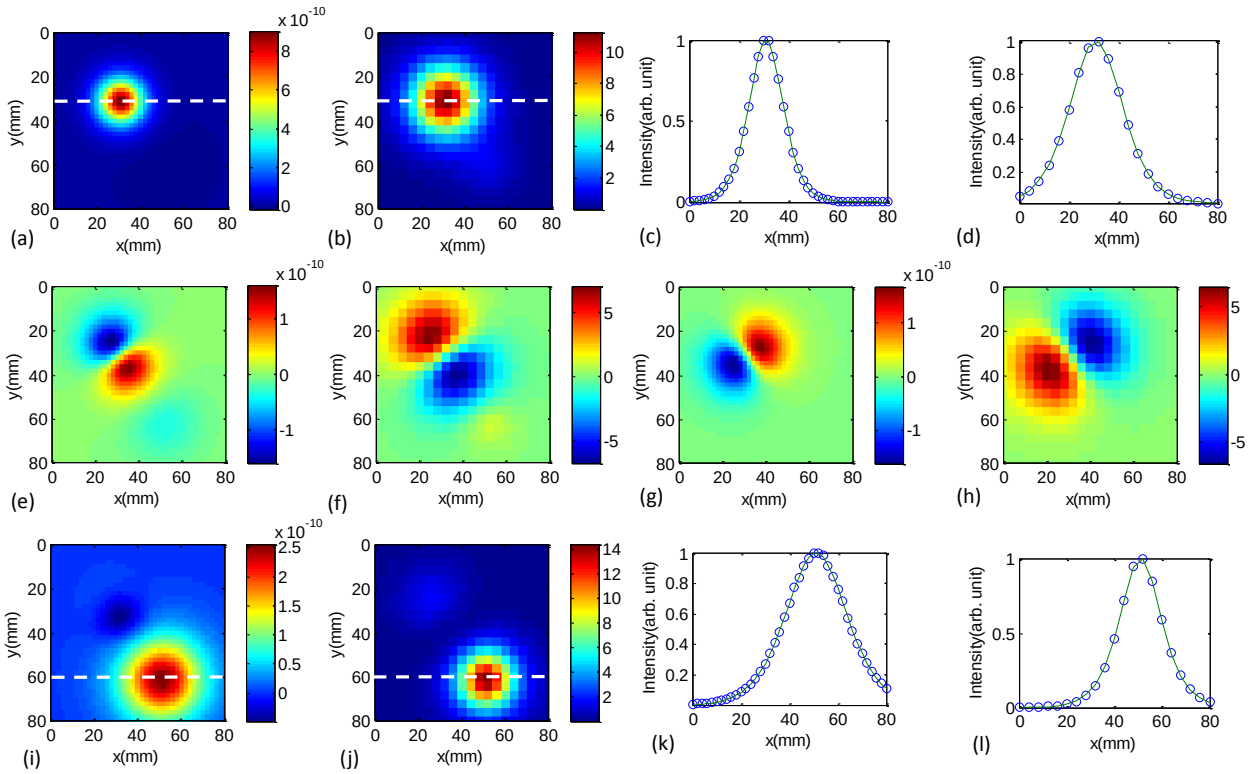

Fig. 4.2. ICA-based imaging of one absorbing and one scattering target ~4-cm apart: ICA extracted two-dimensional intensity distribution on the detector plane of: (a) the centrosymmetric component, (e) and (g) dumb-bell shaped components of the scattering target; and (i) the absorptive target. Similar intensity distribution on the source plane of: (b) the centrosymmetric, (f) and (h) dumb-bell shaped components of the scattering target, and (j) the absorptive target for comparison. Fits to the spatial intensity profiles on the detector plane along the white dashed line (shown in figures) of the centrosymmetric components of the scattering target are shown in (c), and that of the absorptive target is shown in (k). Corresponding fits to spatial profiles on the source plane are displayed in (d) and (l), respectively.

Table 4.1 lists the locations and strengths of the absorptive and scattering targets retrieved by fitting the spatial intensity profile of the centrosymmetric components on the detector plane to Green's functions and derivatives of Green's functions using Eq. 4.6(a) and Eq. 4.6(b),

respectively, as shown in Fig. 4.2(c) and Fig. 4.2(k). Fig. 4.2(d) and Fig. 4.2(l) show the corresponding fits to the profiles on the source plane.

4.3.1.2. *PCA Analysis*

Eigenvalue equation of the covariance matrix of X was solved. The eigenvalues found by PCA were sorted in descending order. Fig. 4.3 shows a plot of leading 20 eigenvalues on a logarithmic scale.

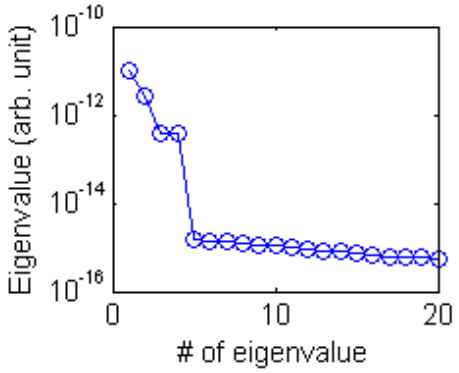

Fig.4.3. A logarithmic plot of the first 20 PCA eigenvalues

First four leading eigenvalues were selected as PCs. The corresponding principal component intensity distributions (PCIDs) were calculated. The PCIDs on the detector plane are shown in Fig. 4.4. Similar images for PCIDs on the source plane were obtained. The scattering target has one centrosymmetric (Figs. 4.4(a) and 4.4(b)) component and two dumb-bell shaped (Figs. 4.4(e) – 4.4(h)) components, while the absorptive target has only one component (Figs. 4(i) and 4(j)).

Figs. 4.4(c) and 4.4(k) show fits to the spatial intensity profile of the centrosymmetric component of the scattering target and that of the absorptive target on the detector plane, respectively. Figs. 4.4(d) and 4.4(l) show fits to the corresponding spatial intensity profiles on the source planes. The locations and optical strengths of the targets retrieved from the fit are also shown in Table 4.1.

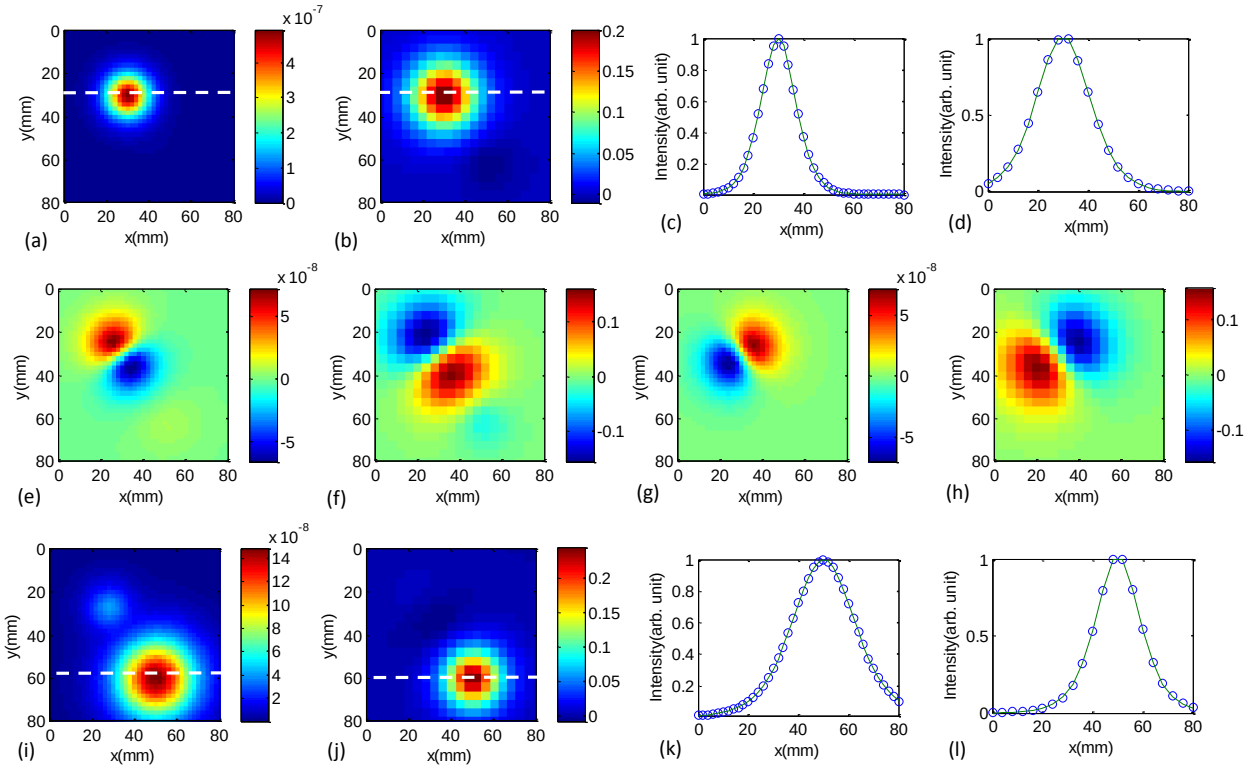

Fig. 4.4. PCA-based imaging of one absorbing and one scattering target ~4-cm apart: PCA-extracted two-dimensional intensity distribution on the detector plane of: (a) the centrosymmetric component, (e) and (g) dumb-bell shaped components of the scattering target; and (i) the absorptive target. Similar intensity distribution on the source plane of: (b) the centrosymmetric, (f) and (h) dumb-bell shaped components of the scattering target, and (j) the absorptive target for comparison. Fits to the spatial intensity profiles on the detector plane along the white dashed line (shown in figures) of the centrosymmetric components of the scattering target are shown in (c), and that of the absorptive target is shown in (k). Corresponding fits to spatial profiles on the source plane are displayed in (d) and (l), respectively.

4.3.1.3. *NMF Analysis*

The mixing matrix and virtual sources were retrieved from the data matrix X using NMF as explained in Section 4.2.3.3. As in the other two approaches, only one component is extracted for the absorptive target. Since NMF has a non-negativity constraint, only the centrosymmetric component for the scattering target is obtained. Non-negative component intensity distributions (NCIDs) on detector planes are shown in Figs. 4.5(a) and 4.5(e). Similar images for NCIDs on

source plane were also obtained using the virtual sources in *S* and shown in Figs. 4.5(b) and 4.5(f). The results are also shown and compared with those obtained using the other two methods in Table 4.1.

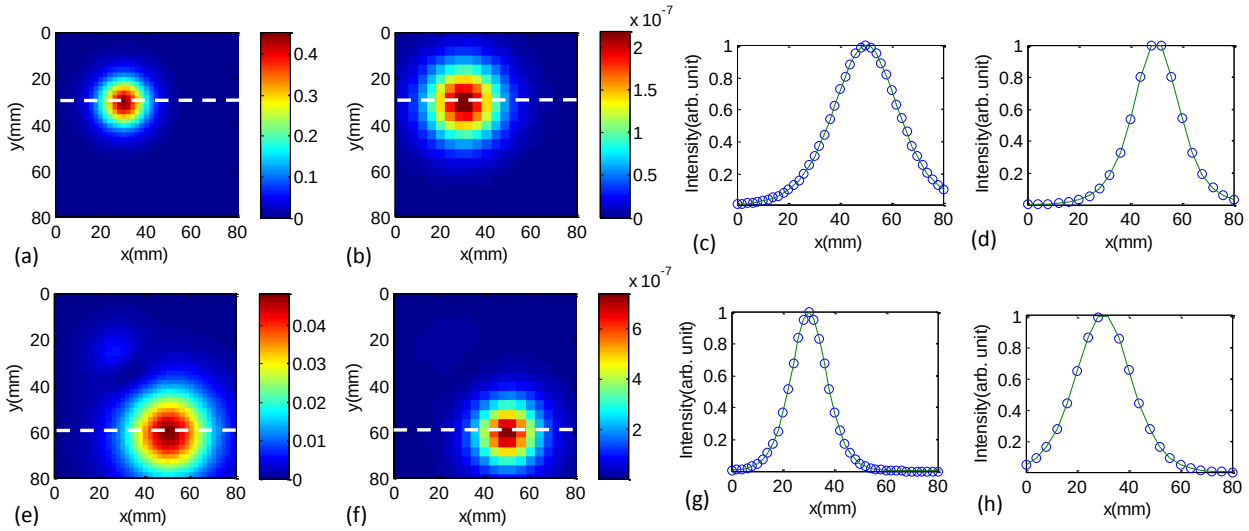

Fig. 4.5. NMF-based imaging of one absorbing and one scattering target ~4-cm apart: NMF-extracted two-dimensional intensity distribution on the detector plane of: (a) the centrosymmetric component of the scattering target; (e) the absorptive target; and the corresponding distribution on the source plane of: (b) the centrosymmetric component of the scattering target; (f) the absorptive target. Fits to the corresponding spatial intensity profiles along the dashed line (shown in figures) are shown in (c), (d), (g) and (h), respectively.

4.3.1.4. *Results and discussions*

The positions and optical strengths of the targets retrieved by ICA, PCA and NMF algorithms are shown in Table 4.1, and compared to the known values. The retrieved results using all three algorithms from this simulated data are in excellent agreement with the known values. This simulation showed that all three methods could be used to accurately locate point-like targets under the conditions set in the example. PCA and ICA can detect the dumb-bell-shaped components, which could, in principle be used to characterize targets as absorptive or scattering in nature. NMF cannot detect the dumb-bell shape component due to the nonnegativity constraint. However, in

realistic experimental condition, the dumb-bell-shaped components of scattering targets may not be detectable [8], particularly when the targets are embedded deep within the turbid medium. The above simulation did not show much difference between these decomposition methods in the efficacy of separating multiple targets and accuracy in target localization.

Table 4.1. Positions and optical strengths retrieved using ICA, PCA and NMF algorithms

Target	Known position (mm)	Algorithm	Fitted position (mm)	Error (mm)	Known* strength	Fitted* strength	Error (%)
Sca.	(30, 30, 25)	ICA	(30.0, 30.0, 25.0)	(0, 0, 0)	-180.32	-180.98	0.37
		PCA	(30.0, 30.0, 25.0)	(0, 0, 0)	-180.32	-181.50	0.65
		NMF	(30.0, 30.0, 25.0)	(0, 0, 0)	-180.32	-180.28	0.02
Abs.	(50, 60, 15)	ICA	(50.1, 60.2, 14.8)	(0.1, 0.2, 0.2)	1.8032	1.8264	1.29
		PCA	(50.0, 60.0, 15.0)	(0, 0, 0)	1.8032	1.8003	0.16
		NMF	(50.0, 60.1, 15.0)	(0, 0.1, 0)	1.8032	1.8150	0.65

* The unit for absorption strength of the target is mm^3/ns and for scattering strength is mm^5/ns.

4.3.2. One absorptive target and one scattering target with 2-cm separation

In order to further compare the three methods and evaluate the efficacy of decomposition for different targets, another two simulations were used with smaller separation between the two targets. In one simulation, the same two point-like targets as used in the first simulation were 20 mm apart, the absorptive target on the left and the scattering target on the right. All other parameters are the same as used in the above first simulation. The two point targets with optical strengths $1.8032mm^3/ns$ and $180.32mm^5/ns$ were located at (30, 40, 20) mm and (50, 40, 20) mm, respectively. 5% additive Gaussian noise was added to the data. The ICIDs, PCIDs and NCIDs are

shown in Fig. 4.6 – 4.8.

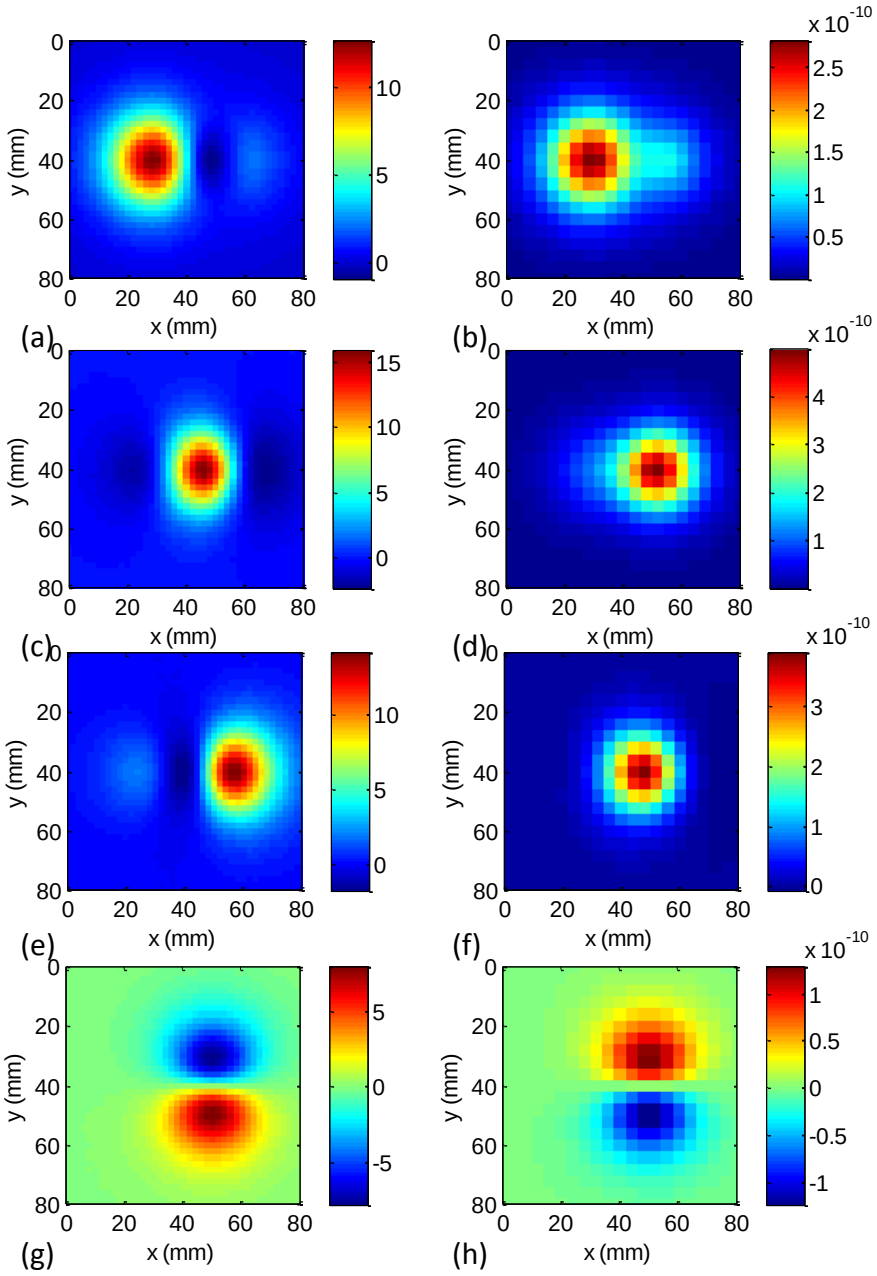

Fig. 4.6. ICA-based imaging of one absorbing and one scattering target 2-cm apart: ICIDs on the detector plane of: (a) the absorptive target; (c) the centrosymmetric component; (e) and (g) dumb-bell shaped components of the scattering target; and the corresponding ICIDs on the source plane of: (b) the absorptive target; (d) the centrosymmetric component; (f) and (h) dumb-bell shaped components of the scattering target.

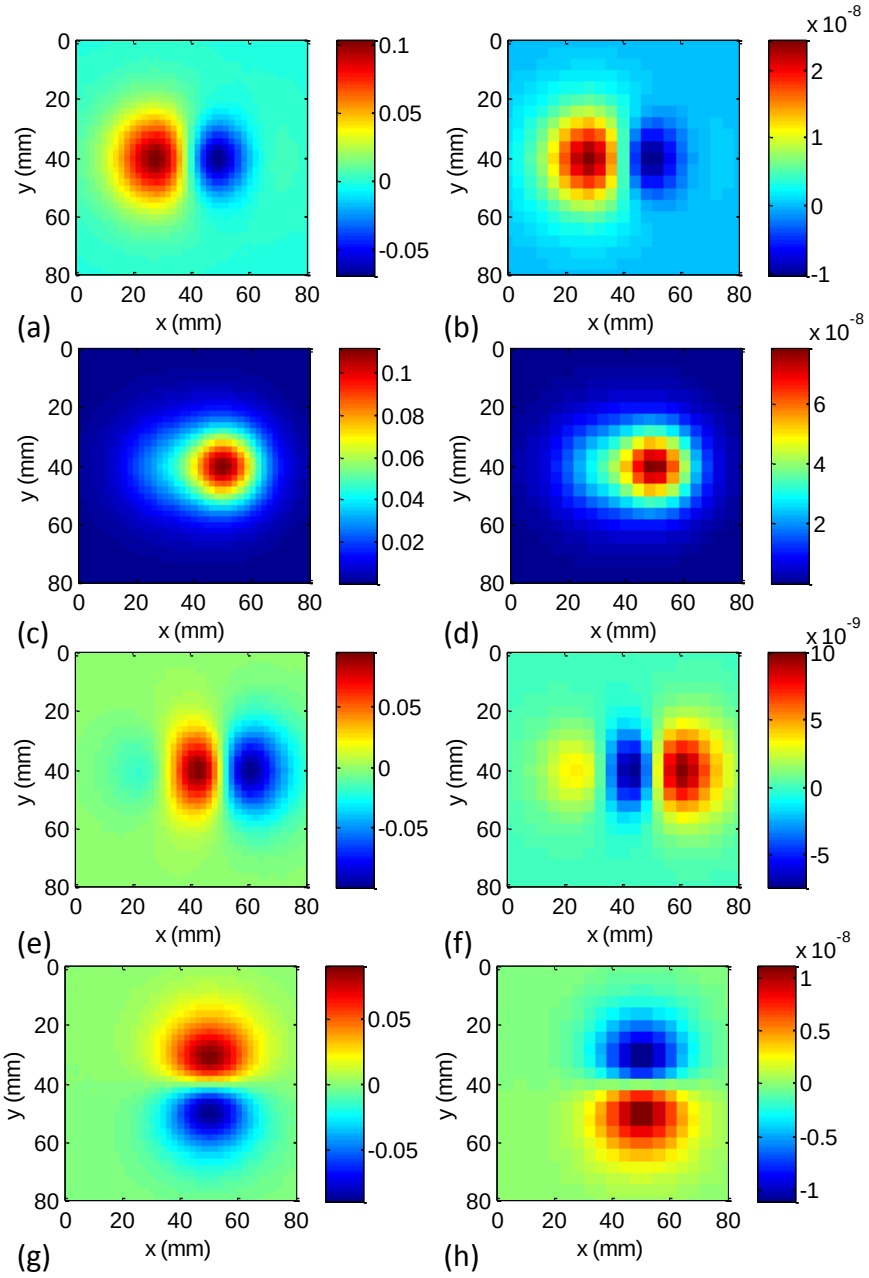

Fig. 4.7. PCA-based imaging of one absorbing and one scattering target 2-cm apart: and PCIDs on the detector plane of: (a) the absorptive target; (c) the centrosymmetric component; (e) and (g) dumb-bell shaped components of the scattering target; and the corresponding PCIDs on the source plane of: (b) the absorptive target; (d) the centrosymmetric component; (f) and (h) dumb-bell shaped components of the scattering target.

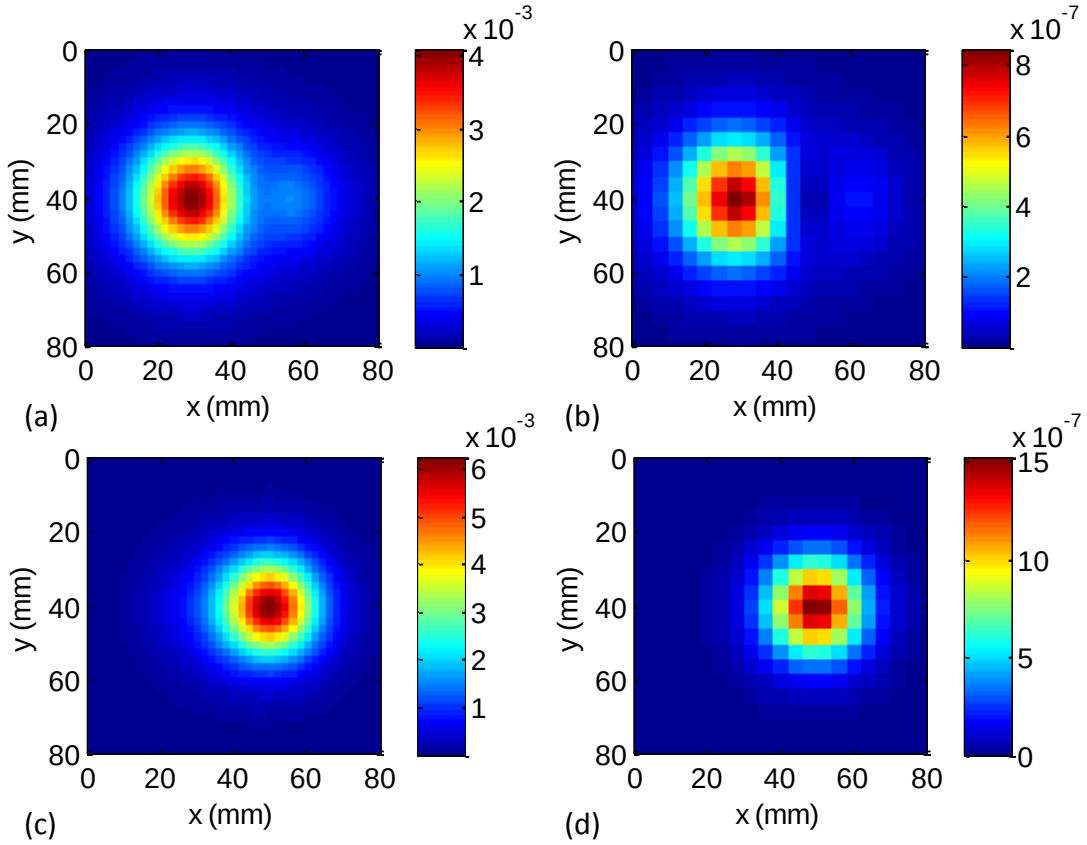

Fig. 4.8. NMF-based imaging of one absorbing and one scattering target 2-cm apart: NCIDs on the detector plane of: (a) the absorptive target; (c) the centrosymmetric component of the scattering target; and the corresponding NCIDs on the source plane of: (b) the absorptive target; (d) the centrosymmetric component.

Fig. 4.6 shows the four ICIDs corresponding to targets. The first ICID corresponds to the left absorptive target, which has a little residue due to the right scattering target. The other three ICIDs correspond to the right scattering target. Due to the cross-talk between the two targets, the components for the scattering target are also affected due to cross-talk, and the centrosymmetric component is identified by comparing the center position in all components.

Fig. 4.7 shows the PCIDs corresponding to the targets. The first PCID corresponds to the absorptive target. Compared to the ICID, this PCID has more residue due to the scattering target. The other three PCIDs correspond to the scattering target, with the centrosymmetric component

more clearly recognized than that in ICIDs.

Fig. 4.8 shows the two NCIDs corresponding to the two targets, respectively. Even though there is also a little cross-talk between the targets, the retrieved components are much "cleaner" than those obtained by the other two methods. Similar to the previous simulated case, only one component was detected for each of the absorptive and scattering targets. No dumb-bell-shaped components were detected for the scattering target.

Table 4.2. Positions and optical strengths retrieved using simulated data and ICA, PCA and NMF algorithms for one absorptive and one scattering point targets

Target	Known position (mm)	Algorithm	Fitted position (mm)	Error (mm)	Known* Strength	Fitted* strength	Error (%)
Abs.	(30, 40, 20)	ICA	(28.3, 40.0, 23.4)	1.7, 0, 3.4	1.8032	1.44	20.1
		PCA	(24.9, 40.0, 20.9)	5.1, 0, 0.9	1.8032	1.40	22.4
		NMF	(28.3, 40.0, 19.1)	1.7, 0, 0.9	1.8032	1.48	17.9
Sca.	(50, 40, 20)	ICA	(47.4, 40.0, 23.3)	2.6, 0, 3.3	-180.32	-146.9	18.5
		PCA	(48.4, 40.0, 20.2)	1.6, 0, 0.2	-180.32	-158.0	12.4
		NMF	(49.4, 40.0, 19.8)	0.6, 0, 0.2	-180.32	-182.5	1.2

* The unit for absorption strength of the target is mm^3/ns and for scattering strength is mm^5/ns.

All the centrosymmetric components were used to fit the positions and strengths of targets. The two dumb-bell-shaped components were used to help identify the scattering target. The retrieved positions and optical strengths of the targets are shown in Table 4.2. As expected, in these methods, NMF-retrieved values are more accurate than those retrieved using ICA and PCA, since the components were better resolved using NMF. But the difference between PCA and ICA is not

significant in this particular case.

4.3.3. Two absorptive targets with 2-cm separation

A similar simulation is tested using two absorptive point targets with other parameters the same as used in the above simulations. The two absorptive targets with both optical strengths 1.8032mm^3/ns, were located at (30, 40, 20) mm and (50, 40, 20) mm, respectively. The two ICIDs, PCIDs and NCIDs corresponding to the two targets are shown in Figs. 4.9 – 4.11, respectively.

It is shown in Figs. 4.9 – 4.11 that PCA and ICA could not separate the two targets, while NMF clearly separated them. The positions and absorption strengths of the two targets were fitted for NCIDs only. The retrieved positions and absorption strengths of the two targets are shown in Table 4.3. The lateral positions of the two targets were perfectly retrieved, while the axial positions have only 0.5 mm error. The strengths of the two targets are retrieved within 1% uncertainty.

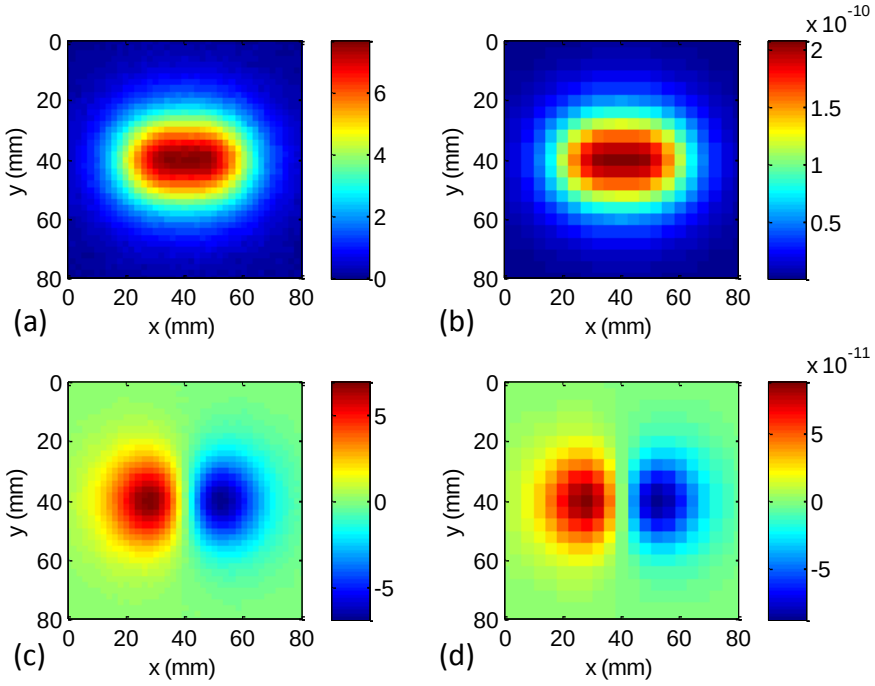

Fig. 4.9. ICA-based imaging of two absorbing target 2-cm apart: (a) and (c) are the two ICIDs on the detector plane for the two targets. (b) and (d) are the two corresponding ICIDs on the source plane for the two targets.

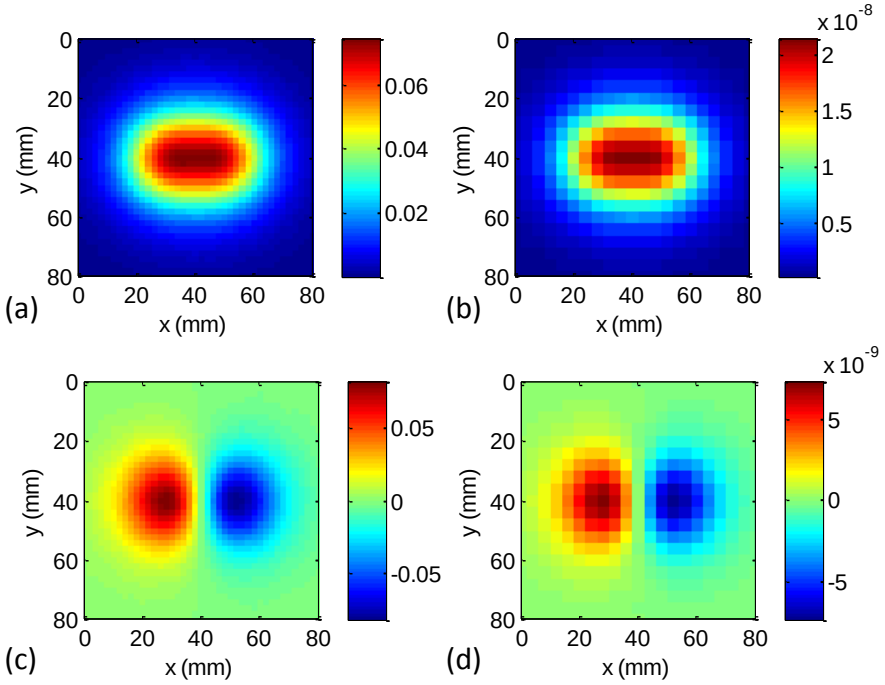

Fig. 4.10. PCA-based imaging of two absorbing target with 2-cm separation: (a) and (c) are the two PCIDs on the detector plane for the two targets. (b) and (d) are the two corresponding PCIDs on the source plane for the two targets.

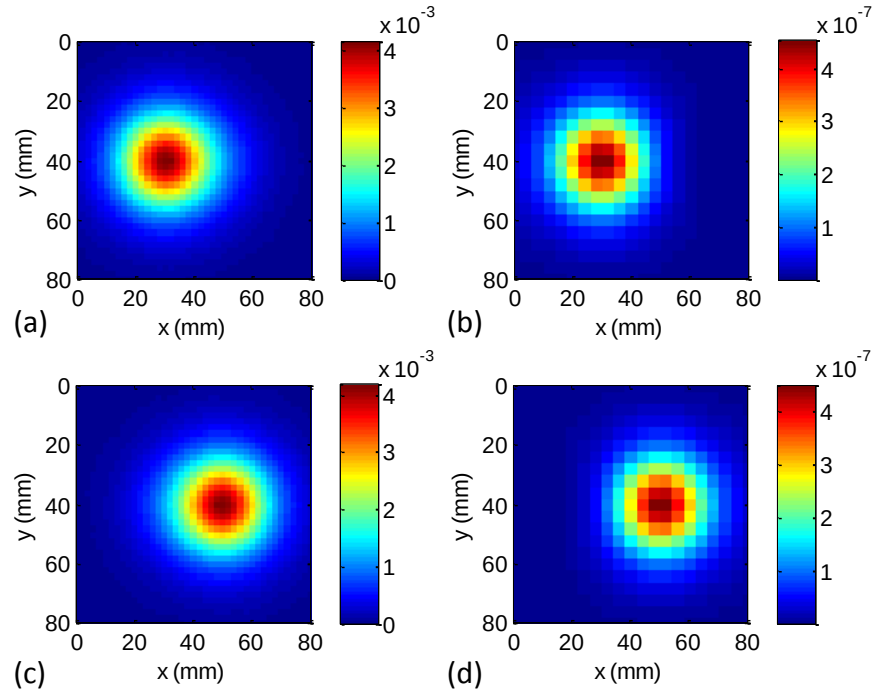

Fig. 4.11. NMF-based imaging of two absorbing target 2-cm apart: (a) and (c) are the two NCIDs on the detector plane for the two targets. (b) and (d) are the two corresponding NCIDs on the source plane for the two targets.

Table 4.3. Positions and optical strengths retrieved using simulated data and ICA, PCA and NMF algorithms for two absorptive point targets

Target	Known position (mm)	Fitted position (mm)	Error (mm)	Known strength (mm^3/ns)	Fitted strength (mm^3/ns)	Error (%)
Left	30, 40, 20	30.0, 40.0, 19.5	0, 0, 0.5	1.8032	1.8133	0.56
Right	50, 40, 20	50.0, 40.0, 19.5	0, 0, 0.5	1.8032	1.8110	0.43

4.3.4. Imaging extended targets

The imaging approaches using decomposition methods were developed for point-like targets in Section 4.2. However, in realistic condition, there is no point-like target. Any target has some finite size, either small or big. In this section, we evaluate the effect of the size of the targets, and efficacy of detecting realistic targets using the decomposition methods. Simulated data was generated using the same condition as in the previous section, except that an extended target was embedded. The centroid position of the target was used to describe the position of the target. A $2 \times 2 \times 2$-mm^3 target, a $10 \times 10 \times 10$-mm^3 (1 cm^3) target, and a $20 \times 20 \times 20$-mm^3 (8 cm^3) target with $\delta\mu_a$ = 0.001 mm^{-1}, were embedded at (40, 40, 20) mm in two separate simulations, respectively. 5% additive Gaussian random noise was added. For the small target, three components were retrieved by ICA and PCA and shown in Fig. 4.12 and Fig. 4.13, respectively. NMF does not retrieve negative signal, so only one component was obtained and shown in Fig. 4.14. For the larger targets, ICA and PCA also retrieved three components. For the $10 \times 10 \times 10$-mm^3 target, the ICIDs and PCIDs are shown in Fig. 4.15 and Fig. 4.16, respectively. NMF retrieved one component as shown in Fig. 17. The components for the $20 \times 20 \times 20$-mm^3 target were also obtained, which were similar to those of the $10 \times 10 \times 10$-mm^3 target, and not shown here.

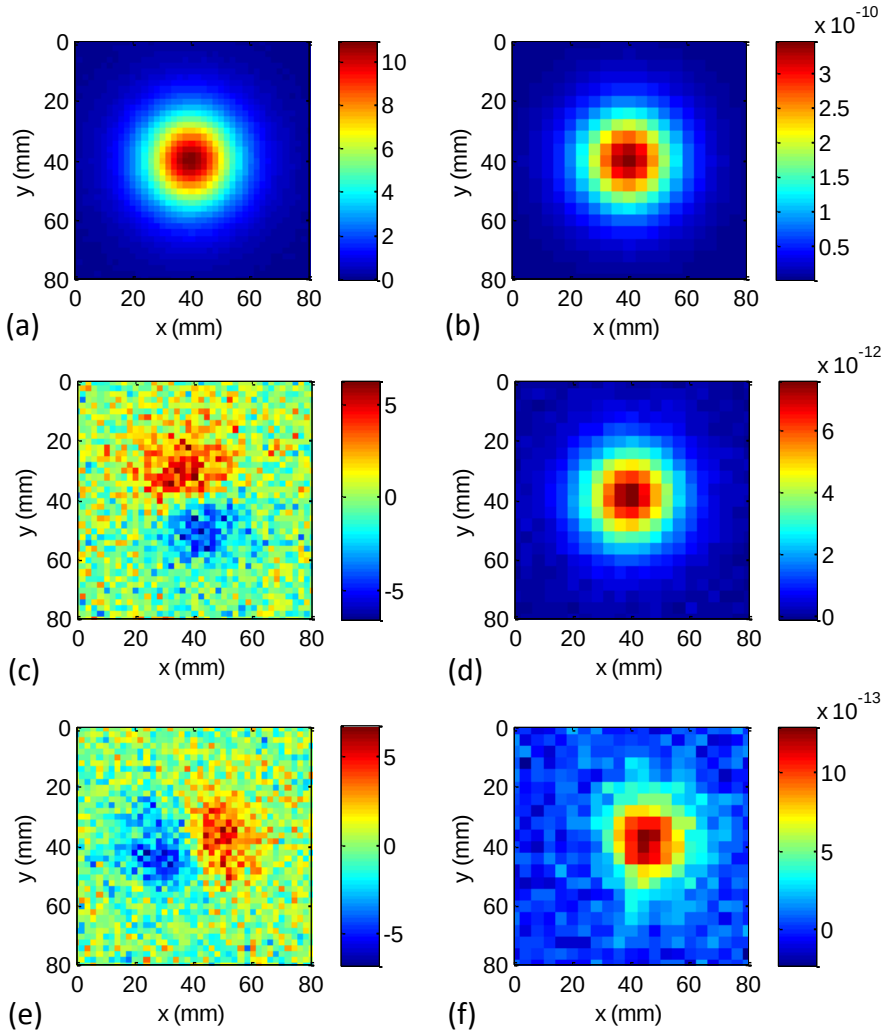

Fig. 4.12. ICA-based imaging of one 2 × 2 × 2 mm^3 absorptive target: (a), (c) and (e) are the three ICIDs on the detector plane for the target. (b), (d) and (f) are the three corresponding ICIDs on the source plane for the target.

The components in the left and right columns in the Figs. 4.12 – 4.17 are on the detector and source planes, respectively. As seen in the figures, ICA and PCA retrieved three components for a single finite-size absorptive target, including one centrosymmetric and two dumb-bell-shaped. This is similar to a point scattering target. When the target was small, with size 2 × 2 × 2 mm^3, the centrosymmetric component dominated and the dumb-bell-shaped components were much weaker. When the size of the target was 10 × 10 × 10 mm^3, the dumb-bell-shaped components became more significant. When the light distribution due to a finite-size object is decomposed, the first

component corresponds to light from a point source at the "optical center" of the object, the higher-order components are due to the spatial distribution, which are analogous to the multi-pole expansion for a complex structure. The centrosymmetric components were used to fit the locations and absorption strengths of the targets, as shown in Table 4.4, 4.5 and 4.6 for the three targets, respectively.

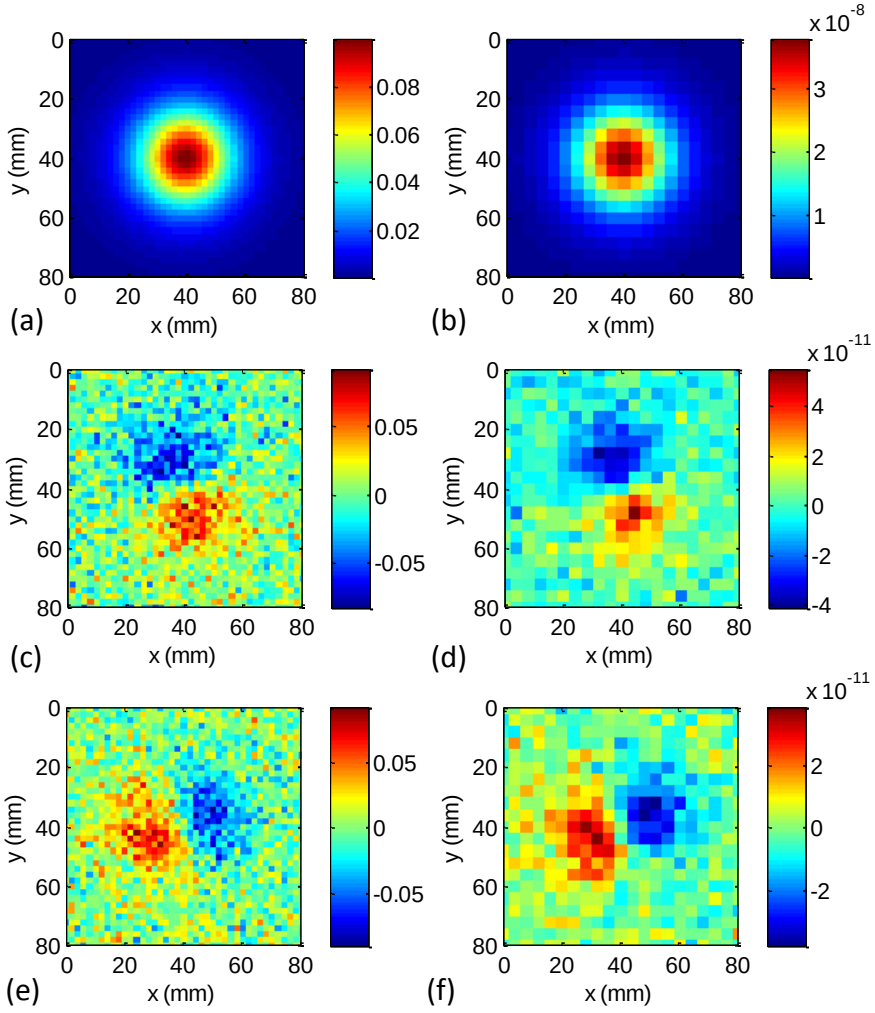

Fig. 4.13. PCA-based imaging of one 2 × 2 × 2 mm^3 absorptive target: (a), (c) and (e) are the three PCIDs on the detector plane for the target. (b), (d) and (f) are the three corresponding PCIDs on the source plane for the target.

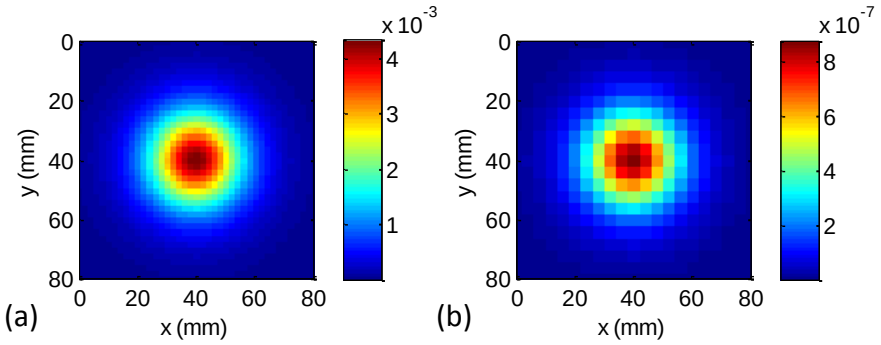

Fig. 4.14. NMF-based imaging of one $2 \times 2 \times 2$ mm^3 absorptive target: (a) and (b) are the NCIDs for the target on the detector plane and source plane, respectively.

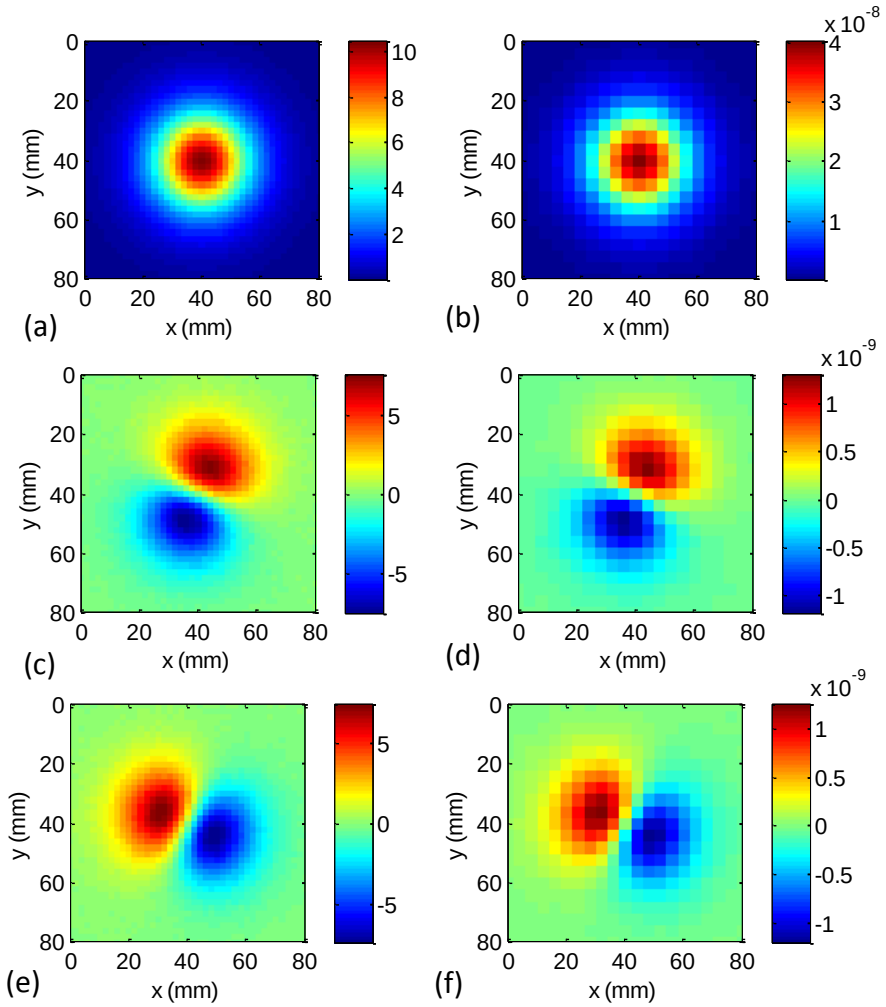

Fig. 4.15. ICA-based imaging of one $10 \times 10 \times 10$ mm^3 absorptive target: (a), (c) and (e) are the three ICIDs on the detector plane for the target. (b), (d) and (f) are the three corresponding ICIDs on the source plane for the target.

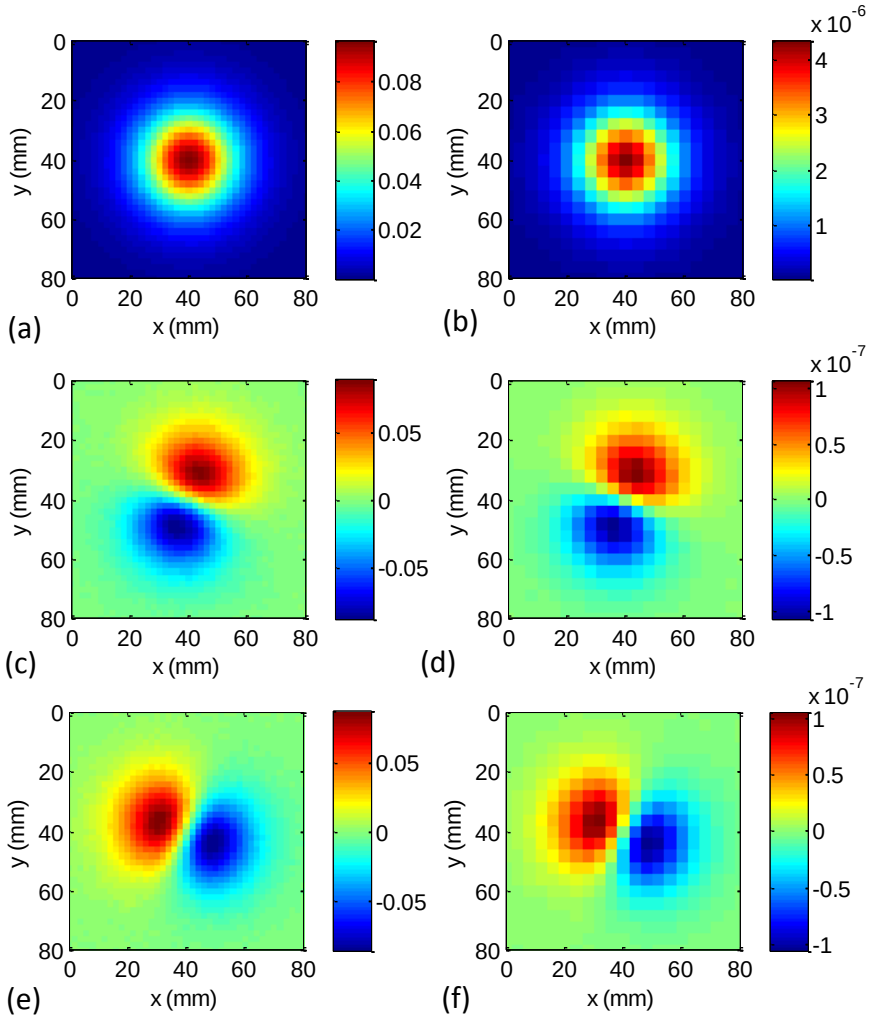

Fig. 4.16. PCA-based imaging of one 10 × 10 × 10 mm^3 absorptive target: (a), (c) and (e) are the three PCIDs on the detector plane for the target. (b), (d) and (f) are the three corresponding PCIDs on the source plane for the target.

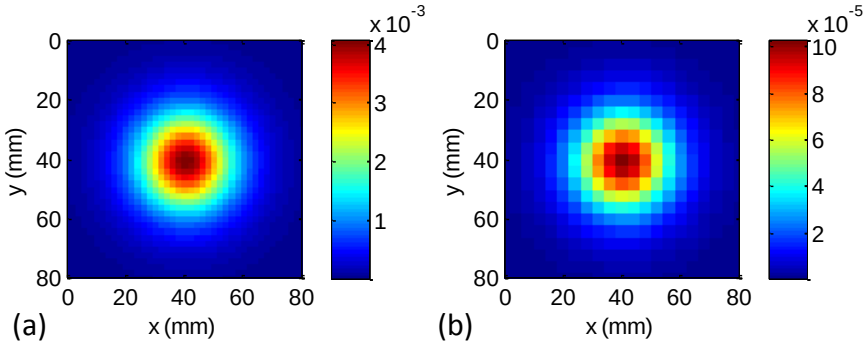

Fig. 4.17. NMF-based imaging of one 10 × 10 × 10 mm^3 absorptive target: (a) and (b) are the NCIDs for the target on the detector plane and source plane, respectively.

Table 4.4. Retrieved and known positions and absorption strength of the $2 \times 2 \times 2$ mm^3 target

	Target position [x, y, z (mm)]	Error [Δx, Δy, Δz (mm)]	Absorption Strength (mm^3/ns)	Error (%)
Known	40.0, 40.0, 20.0	-	1.8032	-
PCA	40.0, 40.0, 20.0	0, 0, 0	1.7968	0.35
ICA	40.5, 40.1, 20.0	0.5, 0.1, 0	1.7959	0.40
NMF	40.0, 40.0, 20.0	0, 0, 0	1.7969	0.35

Table 4.5. Retrieved and known positions and absorption strength of the $10 \times 10 \times 10$ mm^3 target

	Target position [x, y, z (mm)]	Error [Δx, Δy, Δz (mm)]	Absorption Strength (mm^3/ns)	Error (%)
Known	40.0, 40.0, 20.0	-	225.4	-
PCA	40.0, 40.0, 20.0	0, 0, 0	199.8	11.4
ICA	40.0, 40.0, 20.0	0, 0, 0	199.8	11.4
NMF	40.0, 40.0, 20.0	0, 0, 0	200.3	11.1

Table 4.6. Retrieved and known positions and absorption strength of the $20 \times 20 \times 20$ mm^3 target

	Target position [x, y, z (mm)]	Error [Δx, Δy, Δz (mm)]	Absorption Strength (mm^3/ns)	Error (%)
Known	40.0, 40.0, 20.0	-	1803.2	-
PCA	40.0, 40.0, 20.0	0, 0, 0	1120.5	37.9
ICA	40.0, 40.0, 20.0	0, 0, 0	1120.5	37.9
NMF	40.0, 40.0, 20.0	0, 0, 0	1126.4	37.5

The target positions were perfectly retrieved in all these cases using the centrosymmetric components, except the case when ICA was used for the 2 × 2 × 2-mm^3 target, where the uncertainty was within 0.5 mm. Therefore the decomposition methods can be used to detect and locate an extended target. The position of the target is the "center of optical strength", which is the geometric center of a target if the target is homogenous in property and symmetric in geometry. However, the dumb-bell-shaped components cannot be used to characterize a finite-size target as scattering in nature in a realistic experiment.

Since only the first component was used to retrieve the optical strength of a target, the larger the target, the higher the uncertainty in the retrieved optical strength. For the 8-mm^3 target, the errors in the retrieved optical strength using all three decomposition are within 0.4%. However, for the 10 × 10 × 10-mm^3 target, the errors are about ~ 11%, and for the 20 × 20 × 20-mm^3 target, the errors are ~ 38%.

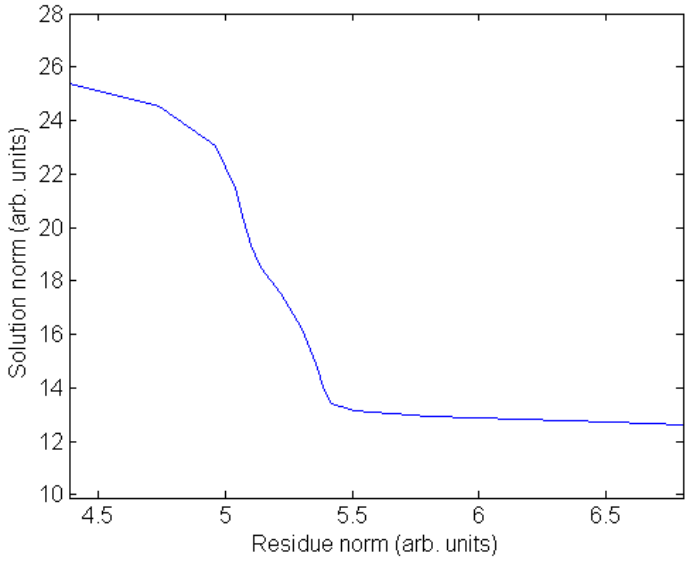

Fig. 4.18. *L*-curve for back-projection of ICID, where *x* axis is the residue norm $\|X_j(\boldsymbol{q}-\boldsymbol{q}_s, \boldsymbol{q}_s) - G_d(\boldsymbol{q}-\boldsymbol{q}_s)\,\chi_j(\boldsymbol{q})\,G^*(\boldsymbol{q}_s)\|$ derived from Eq. (4.11a), and *y* axis is the solution norm $\|\chi_j(\boldsymbol{q})\|$.

A cross section image through the *z*-position of the target was then generated by using

backprojection of ICID, PCID and NCID to estimate the dimension of the target. For the 2 × 2 × 2-mm^3 target, when calculating $\chi(\boldsymbol{q})$ using ICID in Eq. (4.11), the *L*-curve was generated as shown in Fig. 4.18.

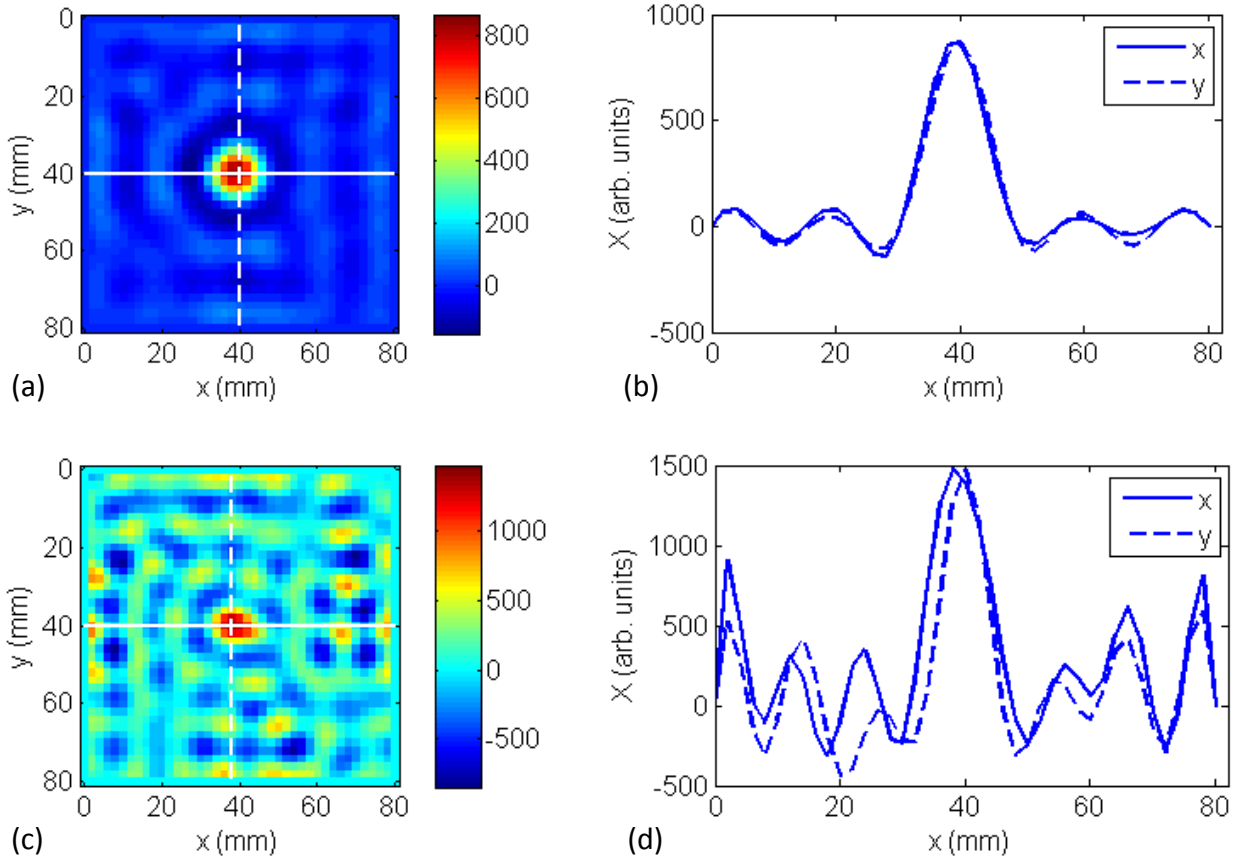

Fig. 4.19. (a) and (c) are cross-section images through the target, generated using the regularization parameter corresponding to the "corner" of the *L*-curve, and an optimized regularization parameter, respectively. (c) and (d) are the corresponding profiles through the maxima in the cross-section images.

When the corner of the *L*-curve was used, the cross-section image through the *z*-position of the target was generated and shown in Fig. 4.19(a). The profiles through maximum are plotted and shown in Fig. 4.19(b). The full-width-at-half-maximum (FWHM) is used to estimate the dimension of the target. The FWHMs in the *x* and *y* direction were found to be 10.5 mm and 10.4 mm, respectively. The FWHMs in the cross-section image are much larger than the actual

dimension of the target (2 mm), which is due to the diffusive nature of light propagation. The back-projection was then optimized using lower regularization. The cross-section image using optimized regularization is shown in Fig. 4.19(c), and the profiles through the maximum are shown in Fig. 4.9(d). The FWHMs were found to be 10.1 mm and 7.3 mm in the *x* and *y* directions, respectively.

Similarly, optimized cross-section images were also generated using PCID and NCID for back-projection, and shown in Fig. 4.20.

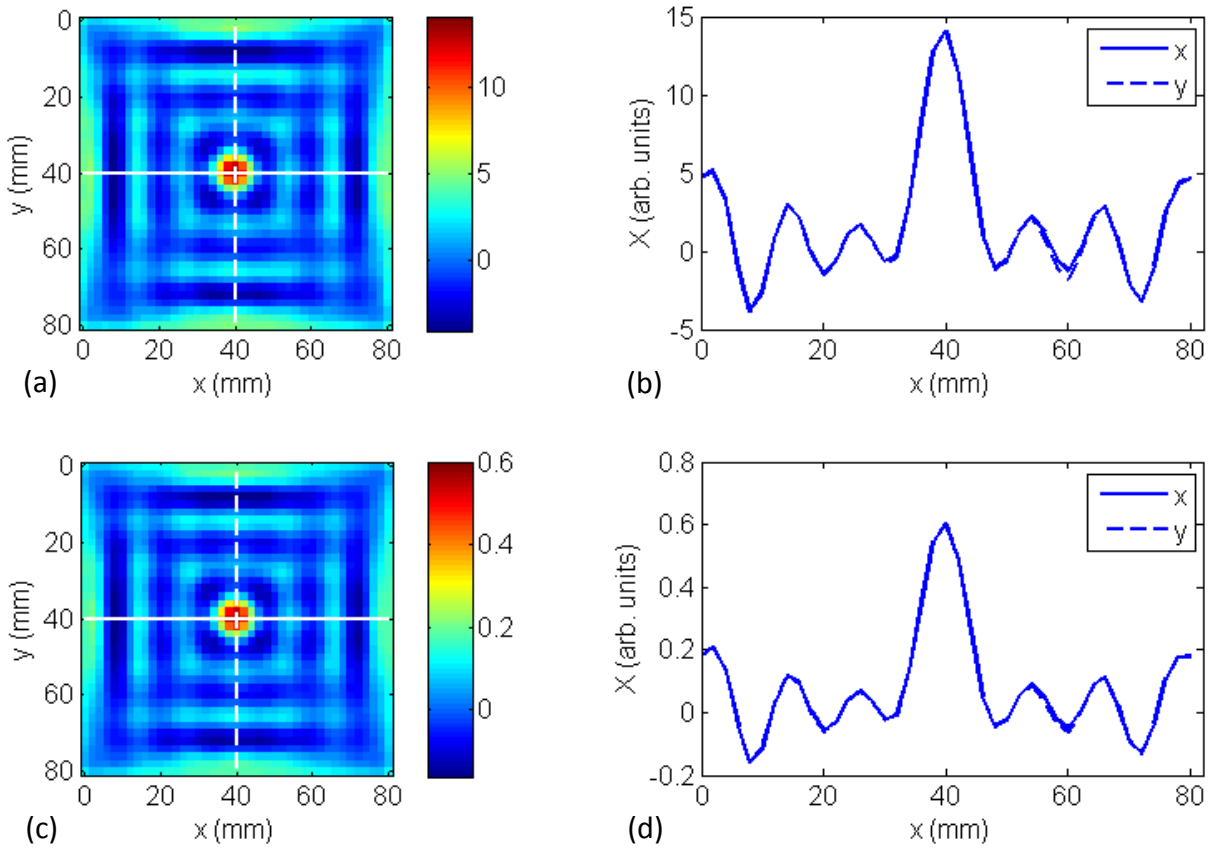

Fig. 4.20. (a) and (c) are cross-section images through the target, generated using the PCID and NCID. (c) and (d) are the corresponding profiles through the maxima in the cross-section images.

The FWHMs were also obtained from the cross-section images corresponding to PCID and NCID. All the FWHMs were put in Table 4.7 for comparison. The FWHMs obtained using all

three decomposition methods were approximately 4 times of the actual dimension of the target.

For the 10 × 10 × 10-mm^3 target, similar cross-section images generated using ICID, PCID and NCID are shown in Figs. 4.21(a), 4.21(c) and 4.21(e). The profiles through the maxima of the three cross-section images are shown in Figs. 4.21(b), 4.21(d) and 4.21(f), respectively.

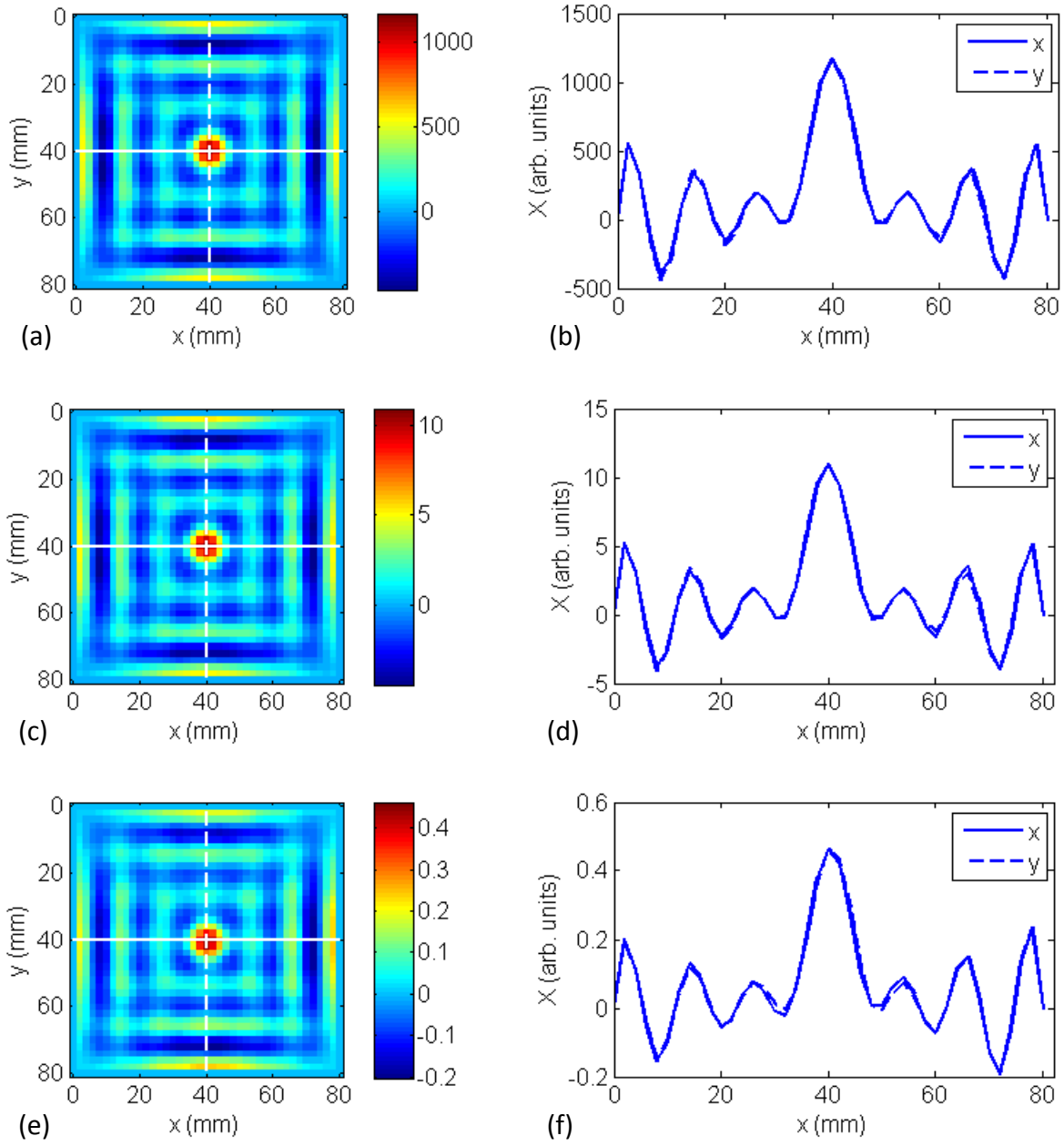

Fig. 4.21. (a), (c) and (e) are cross-section images through the target generated using ICID, PCID, and NCID. (b), (d) and (f) are the corresponding profiles through the maxima in the cross-section images.

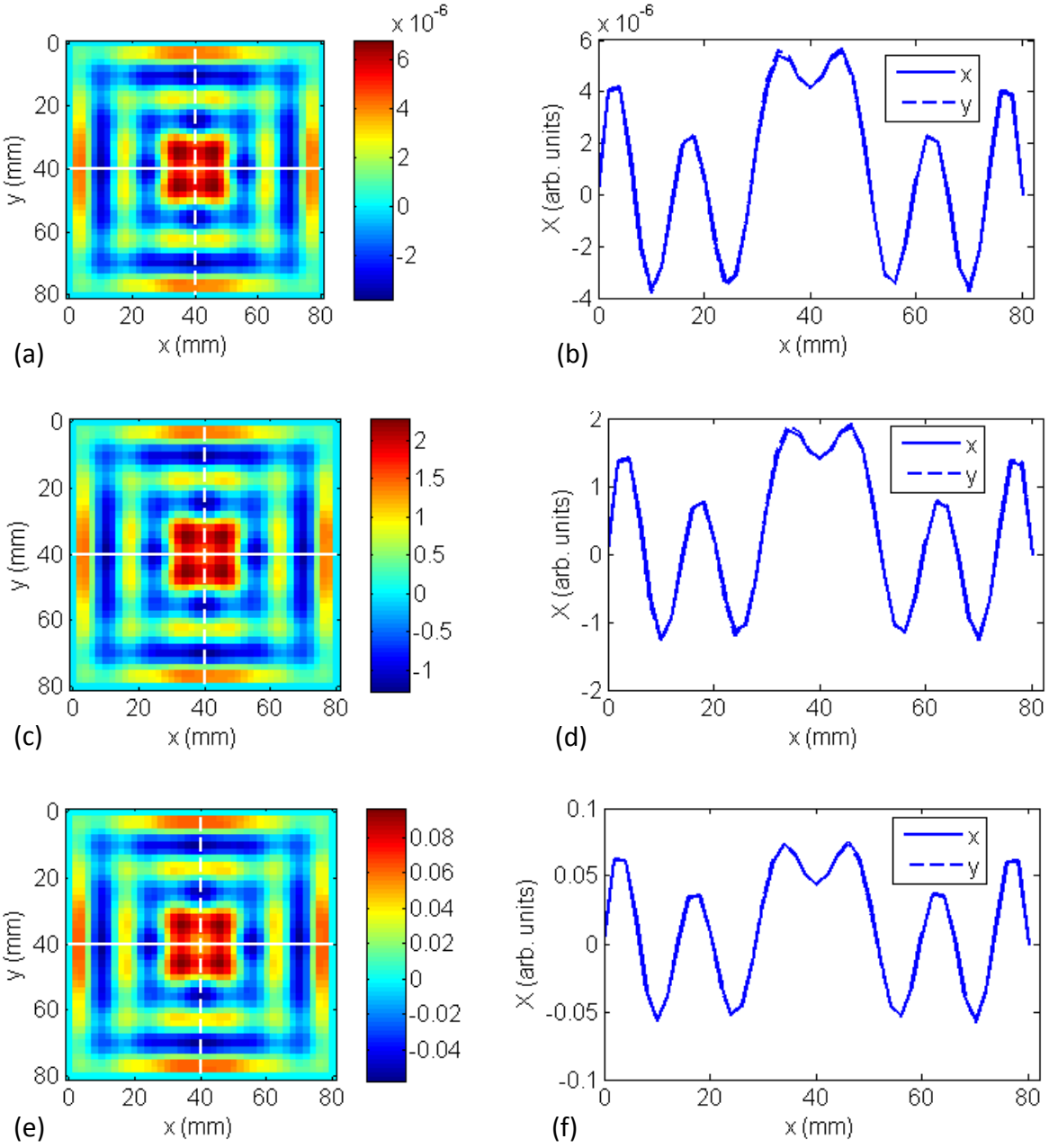

Fig. 4.22. (a), (c) and (e) are cross-section images through the target generated using ICID, PCID, and NCID. (b), (d) and (f) are the corresponding profiles through the maxima in the cross-section images.

The FWHMs obtained from the cross-section images generated using ICID, PCID and NCID are shown in Table 4.7.

For the 20 × 20 × 20-mm^3 target, similar cross-section images generated using ICID, PCID and NCID are shown in Figs. 4.22(a), 4.22(c) and 4.22(e). The profiles through the maxima of the

three cross-section images are shown in Figs. 4.22(b), 4.22(d) and 4.22(f), respectively.

The FWHMs obtained from the cross-section images generated using ICID, PCID and NCID are shown in Table 4.7.

Table 4.7. FWHMs retrieved from the cross section images using ICA, PCA and NMF

Target Size (mm^3)	FWHM [Δx, Δy (mm)]		
	ICA	PCA	NMF
$2 \times 2 \times 2$	10.1, 7.3	8.1, 8.1	8.1, 8.1
$10 \times 10 \times 10$	8.9, 8.7	8.4, 8.5	8.3, 8.5
$20 \times 20 \times 20$	19.3, 19.9	19.3, 19.9	20.8, 20.8

The FWHMs retrieved for the $10 \times 10 \times 10$-mm^3 and $20 \times 20 \times 20$-mm^3 targets are close to the actual dimensions of the targets, with less than 2-mm uncertainty for the $10 \times 10 \times 10$-mm^3 target, and less than 1-mm uncertainty for the $20 \times 20 \times 20$-mm^3 target. However, due to the diffusive nature of light propagation, the cross-section image and its FWHM due to the $2 \times 2 \times 2$-mm^3 and the $10 \times 10 \times 10$-mm^3 targets are approximately the same. For one single finite-size target, ICID, PCID and NCID gives rise to similar cross-section image, therefore similar estimate of target dimension. Further simulations showed that as noise increases high resolution cross-section image with low regularization may be buried in noise and cannot be obtained any more. The cross-section image obtained using the regularization at the "corner" of the *L*-curve is more robust with respectively to the noise level. For the $20 \times 20 \times 20$-mm^3 target in the above simulation with 5% additive Gaussian noise, the target size estimated from the cross-section image is ~ 16 mm if the regularization at the "corner" of the *L*-curve is used. If 100% noise is added, the estimated size remains approximately the same.

4.4. Experiments

4.4.1. Experimental materials and methods

In this Section, the algorithms are evaluated using experimental data for absorptive and scattering targets embedded in model scattering media whose absorption and scattering properties are adjusted to mimic the average values of those parameters for human breast tissues. Two different experiments were carried out with two different samples. The sample used in the first experiment was a 250 mm $\times$ 250 mm $\times$ 50 mm transparent plastic container filled with Intralipid-10% suspension in water as the background medium. The concentration of Intralipid-10% was adjusted to provide [29, 30] an absorption coefficient of $\mu_a \sim 0.003$ mm^{-1}, and a transport mean free path $l_t \sim 1.43$ mm at 785 nm. Two absorptive targets were embedded in the medium. The targets were ~ 10-mm diameter glass spheres filled Indocyanine green (ICG) dye dissolved in Intralipid-20% suspension in water to obtain an absorption coefficient $\mu_a = 1.15$ mm^{-1} at 785 nm, and to match the background scattering coefficient of 2.11 mm^{-1}. Target 1 and target 2 were placed at (57.2, 18.1, 20.0) mm and (19.9, 48.1, 25.0) mm, respectively.

The second experiment used a similar container with dimension of 250 mm $\times$ 250 mm $\times$ 60 mm filled with Intralipid-20% suspension in water. The concentration of Intralipid-20% was adjusted to provide [29, 30] $\mu_a \sim 0.003$ mm^{-1}, and $l_t \sim 1$ mm at 785 nm. These optical parameters of the medium were selected to be similar to the average values of those parameters for human breast tissue. The thickness of the samples was also comparable to that of a typical compressed female human breast. Two scattering targets were embedded, which were also ~ 10 mm diameter glass spheres, filled with Intralipid-20% suspension in water. The transport mean free path, l_t was adjusted to be 0.25 mm, with scattering coefficient $\mu_s \approx 11$ mm^{-1}, and absorption coefficient μ_a same as the background

medium. The targets were placed in the middle plane (z = 30 mm) in the container with a lateral distance of 40 mm from each other (center to center).

The experimental setup is schematically shown in Fig. 4.23. A 10-mW 785-nm diode laser beam was used to illuminate the first sample, while a 100-mW 790-nm diode laser beam was used for the second sample. The input surface (source plane) of the samples was scanned across the laser beam in an *x*-*y* array of grid points to realize the multi-source interrogation of the samples. The transmitted light from the exit surface (detector plane) was recorded by a 1024 pixel ×1024 pixel (pixel size = 24 μm) CCD camera (Photometrics CH350) equipped with a 60-mm focal-length camera lens. Each pixel of the CCD camera can be considered to be a detector implementing the multi-detector signal acquisition arrangement. The two samples were scanned in an array of 11×12 and 11×15 grid points, respectively, with a step size of 5 mm in both cases. The processes of scanning and data acquisition were controlled by a personal computer. At all scan positions, raw transillumination images of the samples were recorded by the computer for further analysis.

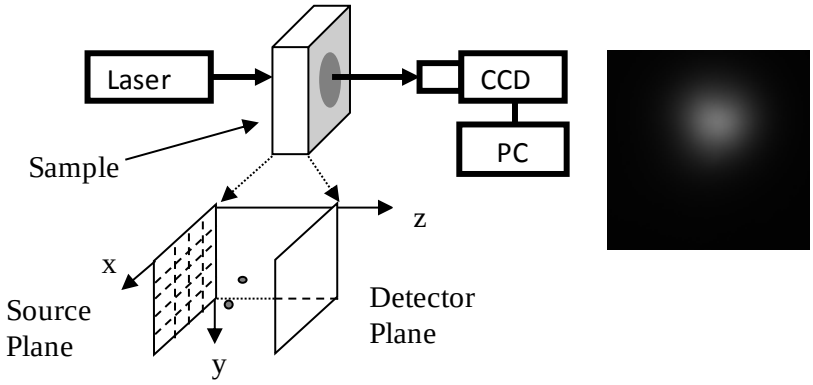

Fig. 4.23. A schematic diagram of the experimental arrangement used for imaging objects embedded in a turbid medium. The inset at the bottom shows the 2D array in the input plane that was scanned across the incident laser beam; and the inset to the right shows a typical raw image recorded by the CCD. (CCD = charge coupled device, PC = personal computer)

A region of interest (ROI) was cropped out from each image. Then every 5×5 pixels in each

cropped image were binned to one pixel to enhance signal-to-noise ratio. A background image was generated by calculating an average image for all scan positions to approximate the transillumination image without target(s) embedded.

This averaging method for generating background image is suitable for small targets used in our experiments, as the ratio of the volume of the sample to that of the target was quite high (~500:1). For *in vivo* imaging of tumors in early stages of growth, the breast-to-tumor volume ratio will be similarly high and the averaging method will be applicable. Alternative approaches for generating a background image include using image of (a) a phantom that has the same average optical properties as the sample [31]; (b) the healthy contralateral breast for breast imaging [32]; and (c) the sample obtained using light of wavelength for which the target(s) and the background have identical optical properties [33]. Still another approach is to compute the background using an appropriate forward model [34]. A more detailed discussion of this important issue appears in one of our earlier publications [35].

The background image was also cropped and binned corresponding to the ROI for each scan position. Perturbation in the light intensity distribution, $\Delta\phi$ due to targets in each image was found by subtracting the background image from the image. The data matrix X was then constructed using the light intensity perturbations at all scan positions. ICA, PCA, and NMF decomposition algorithms were performed on the data matrix separately. Results are shown and discussed below.

4.4.2. Experimental Results

4.4.2.1. *Absorptive targets*

The images on the detector plane obtained using the ICA, PCA, and NMF algorithms are shown in Fig. 4.24, Fig. 4.25, and Fig. 4.26, respectively. Similar images on the source plane were also obtained using all three algorithms.

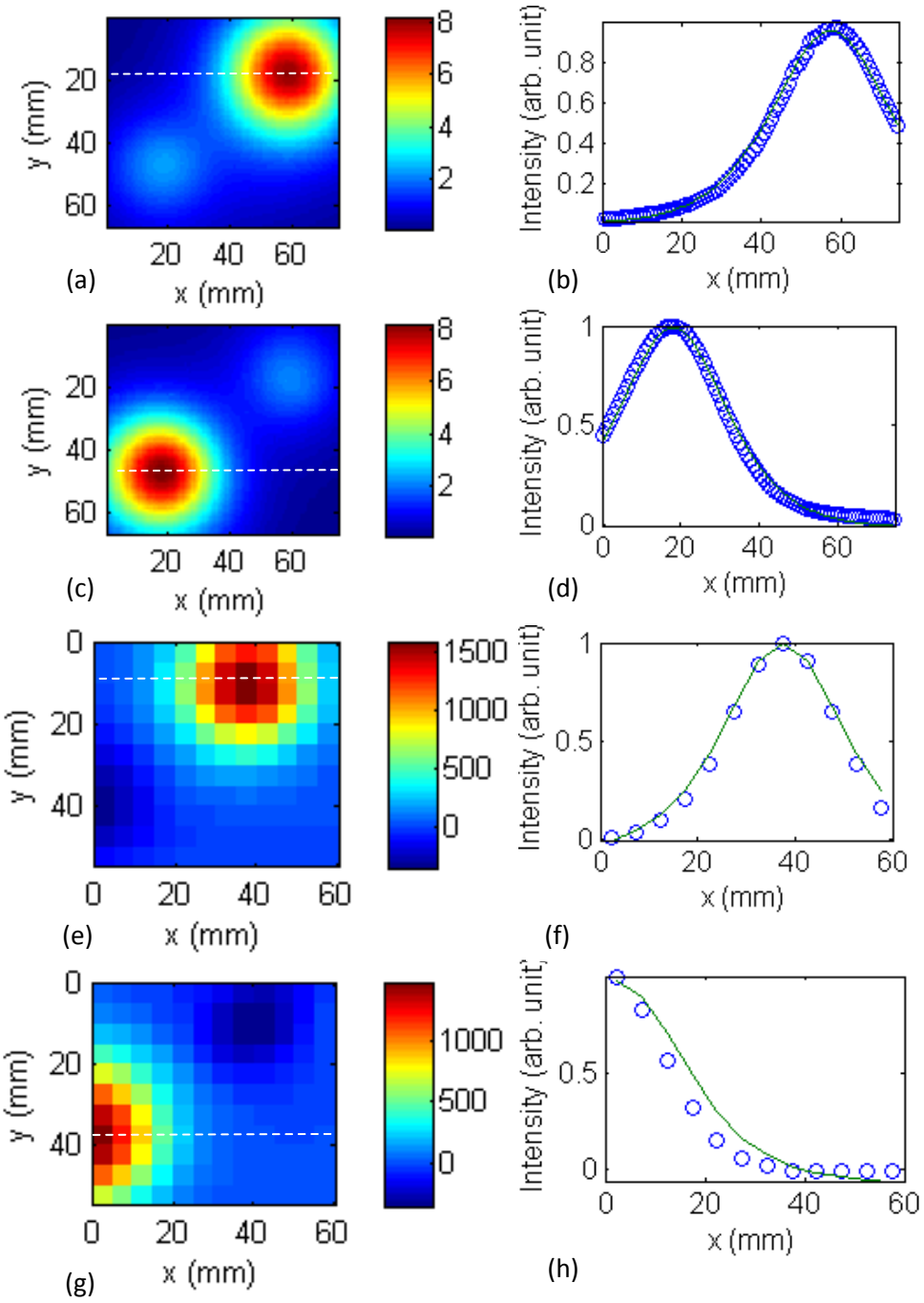

Fig. 4.24. ICA-based imaging of two absorptive targets ~5-cm apart: ICA-generated ICIDs on the detector plane are shown in (a) and (c) for target 1 and 2, respectively; corresponding Green's function fits to the horizontal spatial profiles through the dashed lines are shown in (b) and (d) for target 1 and 2, respectively. ICIDs on the source plane are shown in (e) and (g) for target 1 and 2, respectively; corresponding Green's function fits to the horizontal spatial profiles through the dashed line are shown in (f) and (h) for target 1 and 2, respectively.

The right side of each figure shows the corresponding spatial intensity profile. Locations of the targets are extracted from fits to these spatial intensity profiles, as described in Section 4.2.2 using Eq. (4.6). The results are presented in Table 4.8. In Fig. 4.24, images on the source plane are shown in (e) and (g), and Green's function fits to their spatial profiles are shown in (f) and (h) for comparison.

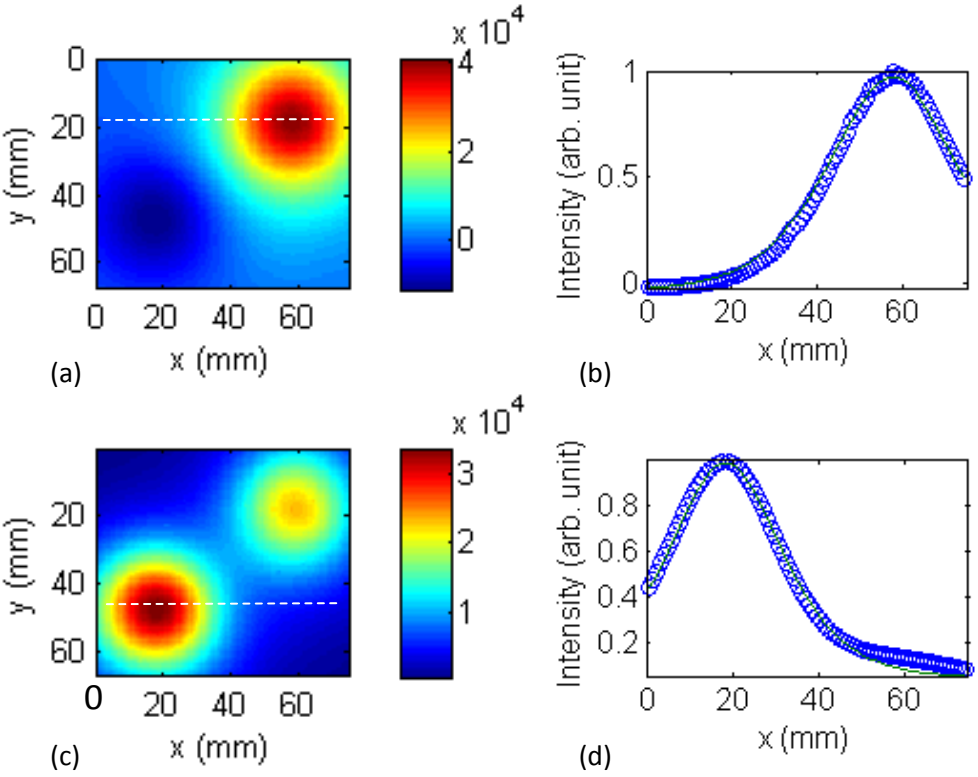

Fig. 4.25. PCA-based imaging of two absorptive targets ~5-cm apart: PCIDs on the detector plane are shown in (a) and (c) for target 1 and 2, respectively; and corresponding Green's function fits to the horizontal spatial profiles through the dashed line are shown in (b) and (d) for target 1 and 2, respectively.

It follows from the comparison of in Table 4.8 that the positions retrieved by all three algorithms are in good agreement with the known positions. The errors in the retrieved locations (x, y, z) of the two targets were within 1.7 mm. The PCIDs were not totally separated. Some "residue" was observed in one PCID from the other. ICA and NMF separated two components from this dataset more clearly.

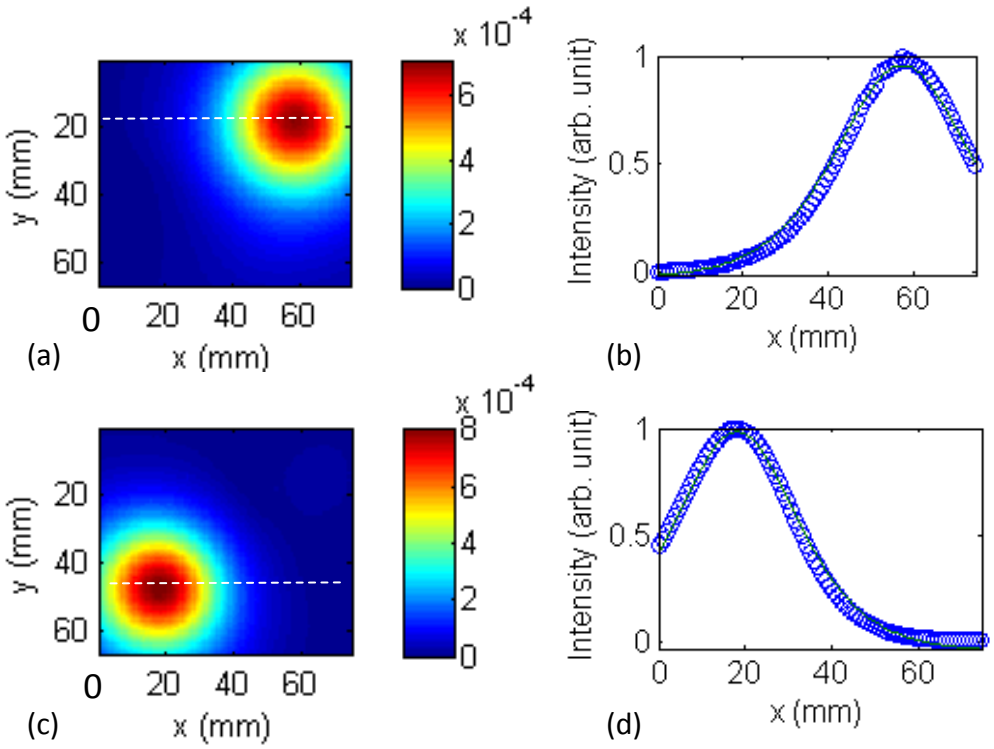

Fig. 4.26. NMF-based imaging of two absorptive targets ~5-cm apart: NCIDs on the detector plane are shown in (a) and (c) for target 1 and 2, respectively; corresponding Green's function fits to the horizontal spatial profiles through the dashed line are shown in (b) and (d) for target 1 and 2, respectively.

Table 4.8. Retrieved positions of the absorptive targets using ICA, PCA and NMF algorithms

Target	Known position (mm)	Algorithm	Fitted position (mm)	Error (mm)
1	(57.2, 18.1, 20)	ICA	(57.4, 18.2, 21.5)	(0.2, 0.1, 1.5)
		PCA	(57.4, 18.2, 20.6)	(0.2, 0.1, 0.6)
		NMF	(57.4, 18.2, 19.5)	(0.2, 0.1, 0.5)
2	(19.9, 48.1, 25)	ICA	(18.2, 46.7, 24.7)	(1.7, 1.4, 0.3)
		PCA	(18.2, 47.6, 25.9)	(1.7, 0.5, 0.9)
		NMF	(18.2, 47.6, 23.3)	(1.7, 0.5, 1.7)

The cross-section images of the targets were generated to estimate the size of the targets, using backcprojection of the component intensity distributions, and shown in Figs. 4.27 – 4.29.

The cross-section images were generated using the optimized *L*-curve method to achieve higher resolution. The FWHMs of the profiles in the cross sections are used to estimate the sizes of targets. The retrieved FWHMs using three methods are shown in Table 4.9. It is shown that the retrieved sizes are all close to the actual size of the targets (~ 10 mm diameter). However, there are some artifacts around the target peak whose values are close to the target peak. Since most values in the other parts of the images are much weaker than the target peak, we still use these images. In the second cross-section image for the bottom-left target, the top-right target also shows up, since there was residue in the PCID due to the other target.

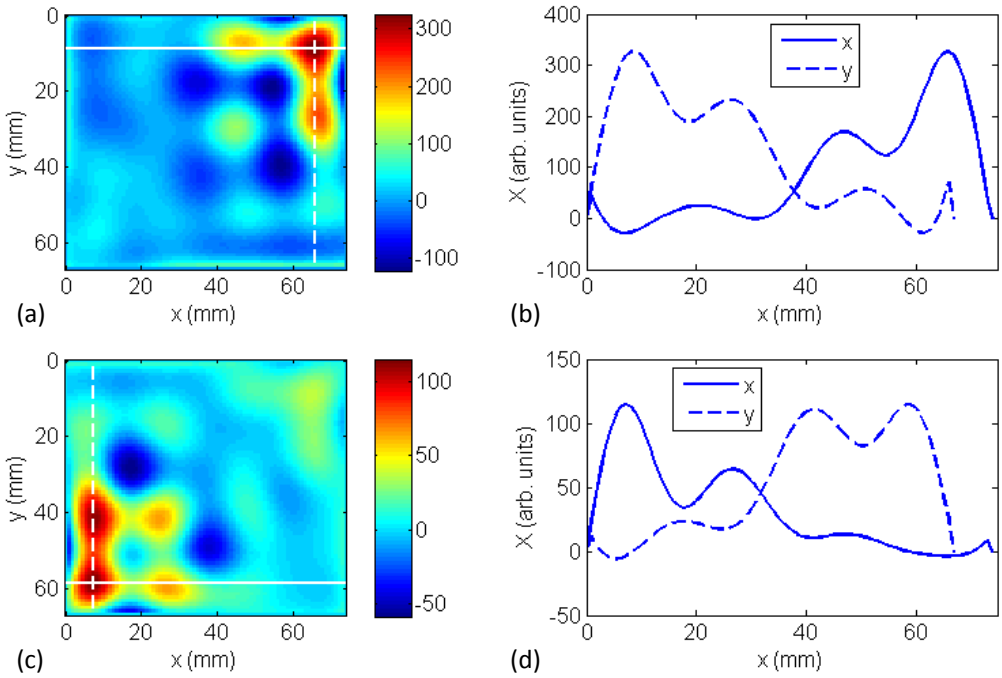

Fig. 4.27. (a) and (c) are cross-section images of the two targets, respectively, generated using back-projection of ICIDs. (b) and (d) are the profiles through the maxima in the cross-section images, respectively.

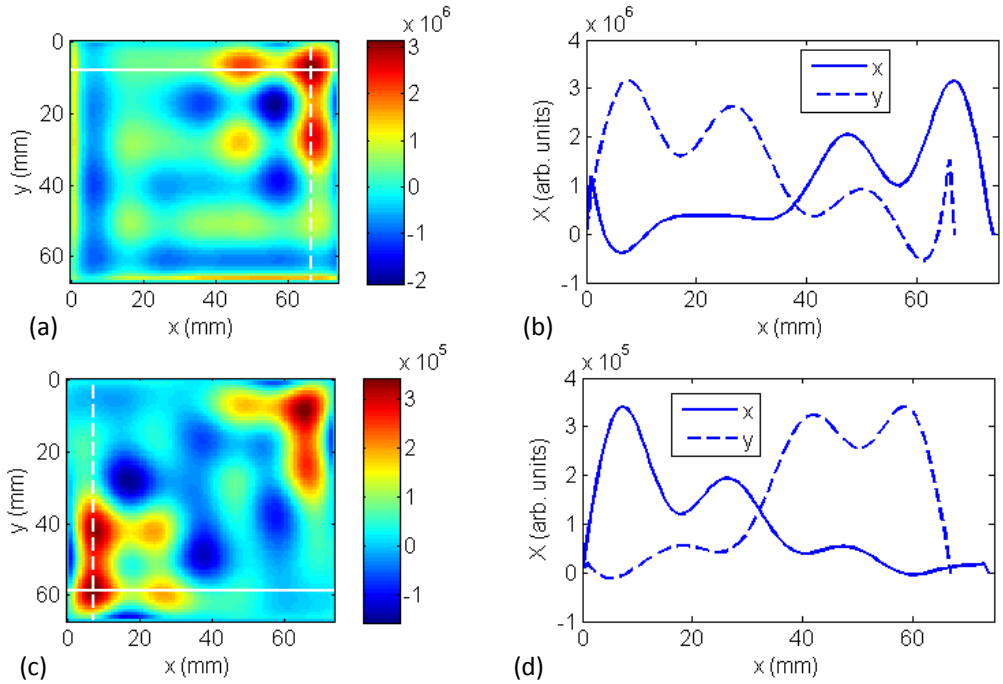

Fig. 4.28. (a) and (c) are cross-section images of the two targets, respectively, generated using back-projection of PCIDs. (b) and (d) are the profiles through the maxima in the cross-section images, respectively.

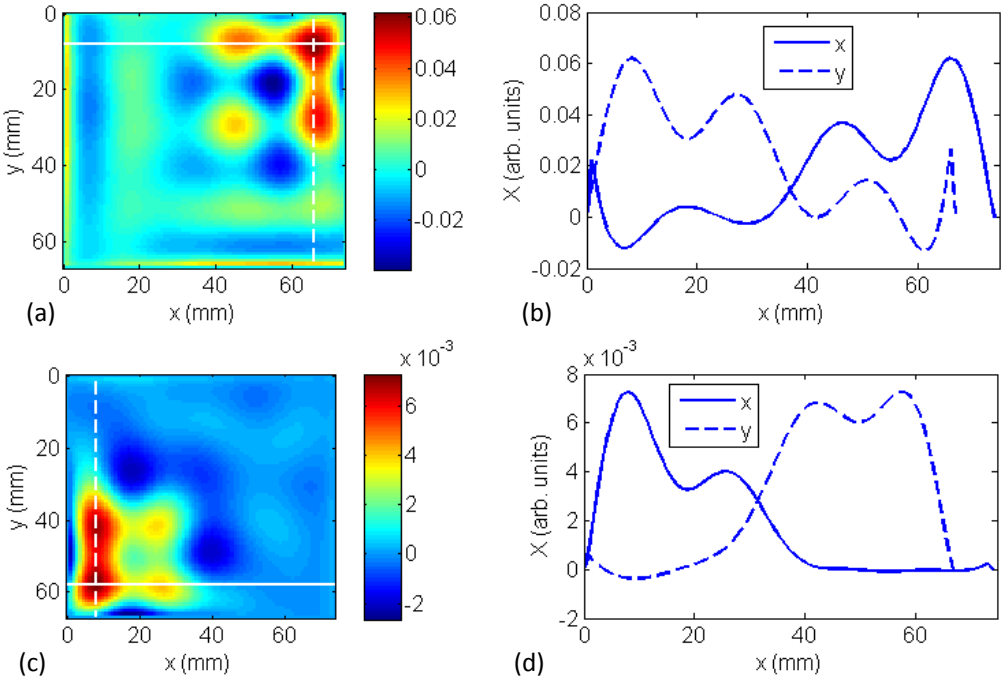

Fig. 4.29. (a) and (c) are cross-section images of the two targets, respectively, generated using back-projection of NCIDs. (b) and (d) are the profiles through the maxima in the cross-section images, respectively.

Even though the "quality" of decomposition of NMF is slightly better than ICA, and much better than PCA, the retrieved locations of targets from this experiment do not clearly show the difference among these three methods.

Table 4.9. FWHMs retrieved from the cross section images using ICA, PCA and NMF

Target	FWHM [Δx, Δy (mm)]		
	ICA	PCA	NMF
1	10.3, 10.4	11.4, 11.6	9.9, 9.7
2	9.7, 9.5	9.8, 9.6	10.2, 10.2

To further compare the three approaches, we test them with the experimental data that was used in Chapter 2, where two 9-mm diameter spherical absorptive targets were embedded in the 60-mm thick medium, l_t of the medium is 1 mm, and the two targets were separated by ~ 40mm. The components retrieved by the three methods are shown in Figs. 4.30, 4.31 and 4.32, respectively. The two targets are still entangled in the PCIDs. ICA separates two targets better than PCA. Figs. 4.30(a), 4.30(c), 4.31(a), 4.31(c), 4.32(a), and 4.32(c) are the components on the detector plane, and correspond to the two targets retrieved by the three methods. Similarly, Figs. 4.30(b), 4.30(d), 4.31(b), 4.31(d), 4.32(b) and 4.32(d) are the corresponding components on the source plane. However, in each component, the residue due to the other target is still present. The fitted positions are shown in Table 4.10. Even though the axial (z) position of the targets retrieved by PCA are more accurate than that retrieved by ICA, the lateral positions are significantly less accurate. Normalized mean squared error (NMSE) was used to evaluate the quality of the fitting. As shown in Table 4.10, the NMSE for PCA and ICA are significantly larger than that for NMF. The NMSE for the right target retrieved by PCA is comparable to that retrieved by ICA, however, NMSE for the left target retrieved by PCA is significantly larger than that retrieved by ICA.

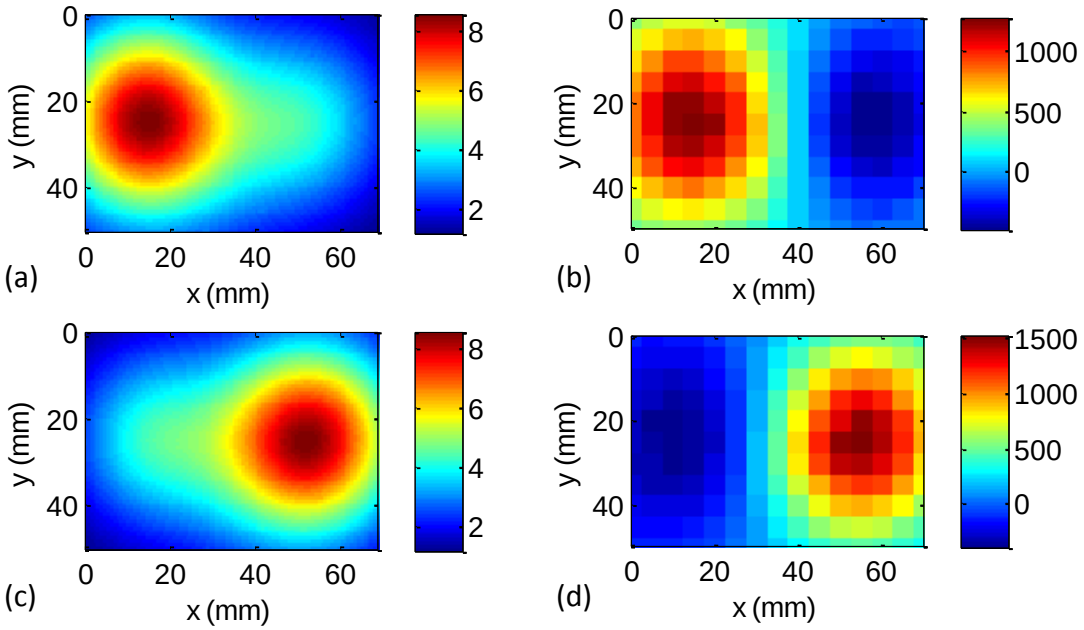

Fig. 4.30. ICA-based imaging of two absorptive targets 4-cm apart: (a) and (c) are the two ICIDs on the detector plane; (b) and (d) are the two ICIDs on the source plane.

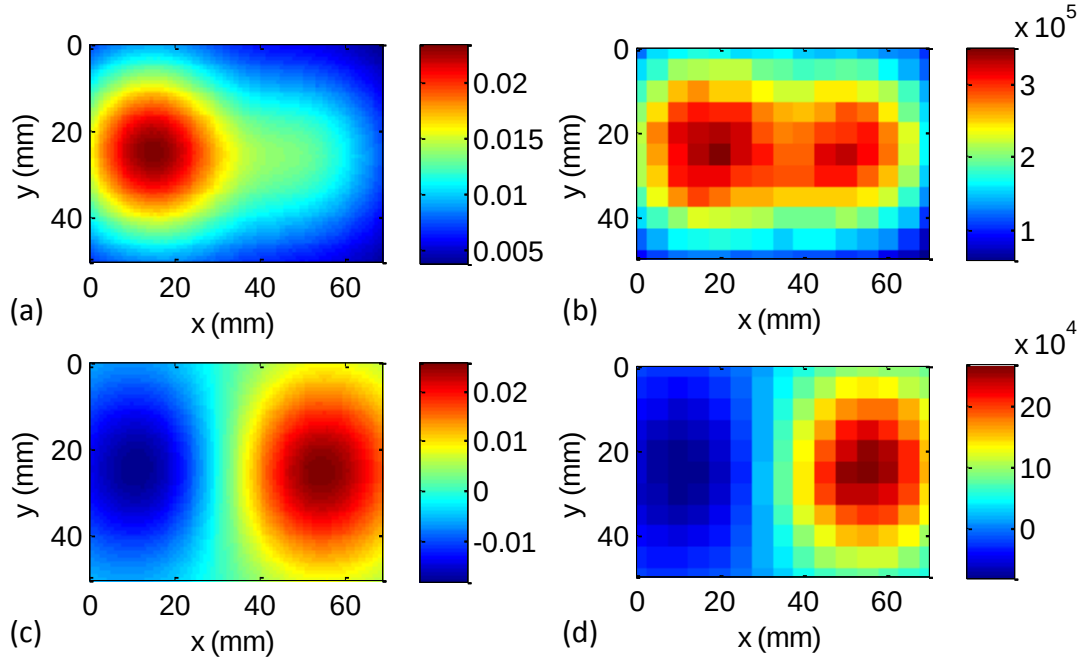

Fig. 4.31. PCA-based imaging of two absorptive targets 4-cm apart: (a) and (c) are the two PCIDs on the detector plane; (b) and (d) are the two PCIDs on the source plane.

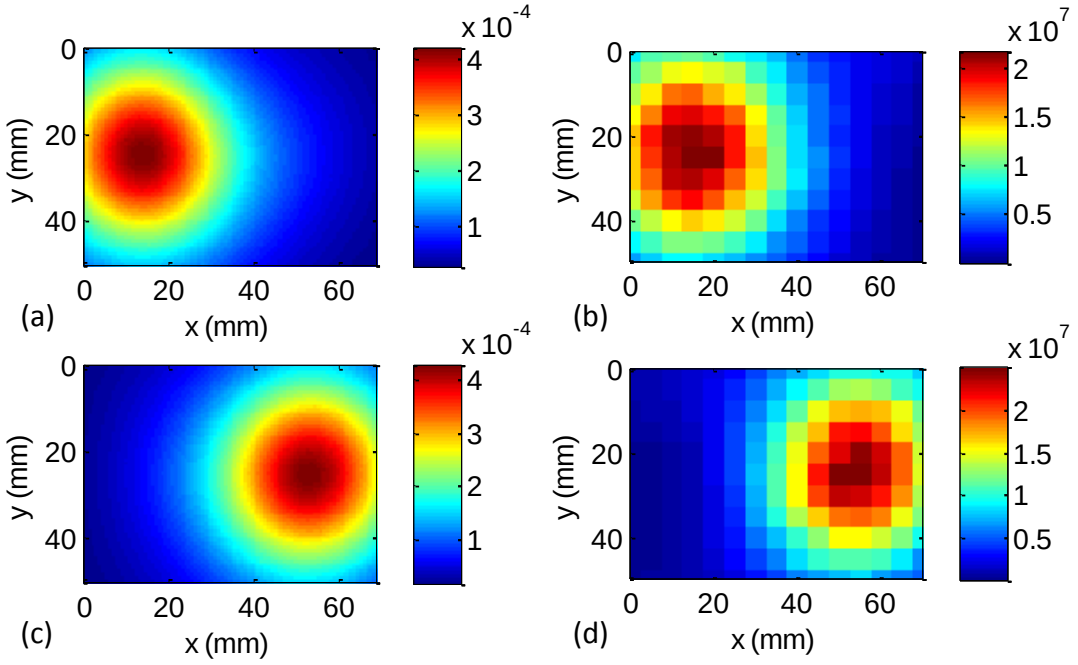

Fig. 4.32. NMF-based imaging of two absorptive targets 4-cm apart: (a) and (c) are the two NCIDs on the detector plane; (b) and (d) are the two NCIDs on the source plane.

Table 4.10. Retrieved positions of the absorptive targets using ICA, PCA and NMF

Target	Algorithm	Position (mm)	Error (mm)	NMSE
1	Known	15.1, 26.0, 30	-	-
	PCA	20.1, 24.2, 33.8	5.0, 1.8, 3.8	0.67
	ICA	14.0, 24.7, 36.3	1.1, 1.3, 6.3	0.19
	NMF	13.6, 24.4, 32.4	1.5, 1.6, 2.4	0.0108
2	Known	52.7, 26.0, 30	-	-
	PCA	55.6, 25.1, 28.5	2.9, 0.9, 1.5	0.14
	ICA	52.4, 25.1, 35.9	0.3, 0.9, 5.9	0.19
	NMF	53.1, 24.8, 29.5	0.4, 1.2, 0.5	0.0074

4.4.2.2. *Scattering targets*

The "images" corresponding to the centrosymmetric components of the virtual sources (targets) on the detector plane obtained using the ICA, PCA, and NMF algorithms are shown in Figs. 4.33, 4.34, and 4.35, respectively. Similar images on the source plane were also obtained. The right side of each figure shows the corresponding spatial intensity profile. Locations of the targets are extracted from fits to these spatial intensity profiles, as described in Section 4.2.2 using Eq. (4.6). The results are presented in Table 4.11.

Both targets were detected by all three algorithms. The target locations retrieved by three algorithms are shown in Table 4.11, and compared with known locations. Overall, all three algorithms detect and locate the scattering and the absorptive targets with good accuracy, the maximum deviation of any one coordinate from the known value being ~3 mm.

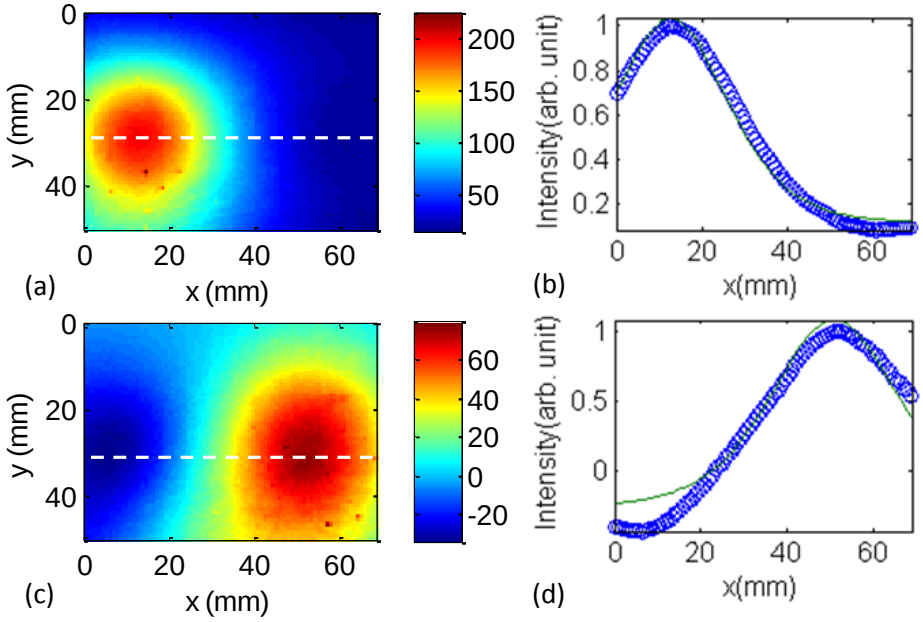

Fig. 4.33. ICA-based imaging of two scattering targets 4-cm apart: ICA-generated ICIDs on the detector plane are shown in (a) and (c); corresponding Green's function fits to the horizontal spatial profiles through the dashed line are shown in (b) and (d).

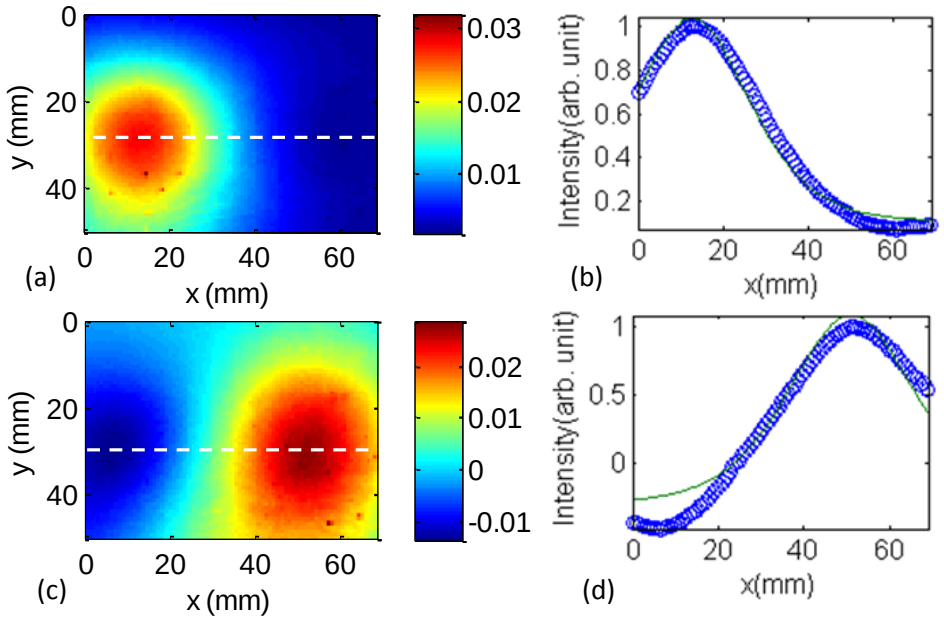

Fig. 4.34. NMF-based imaging of two scattering targets 4-cm apart: PCIDs on the detector plane are shown in (a) and (c); corresponding Green's function fits to the horizontal spatial profiles through the dashed line are shown in (b) and (d).

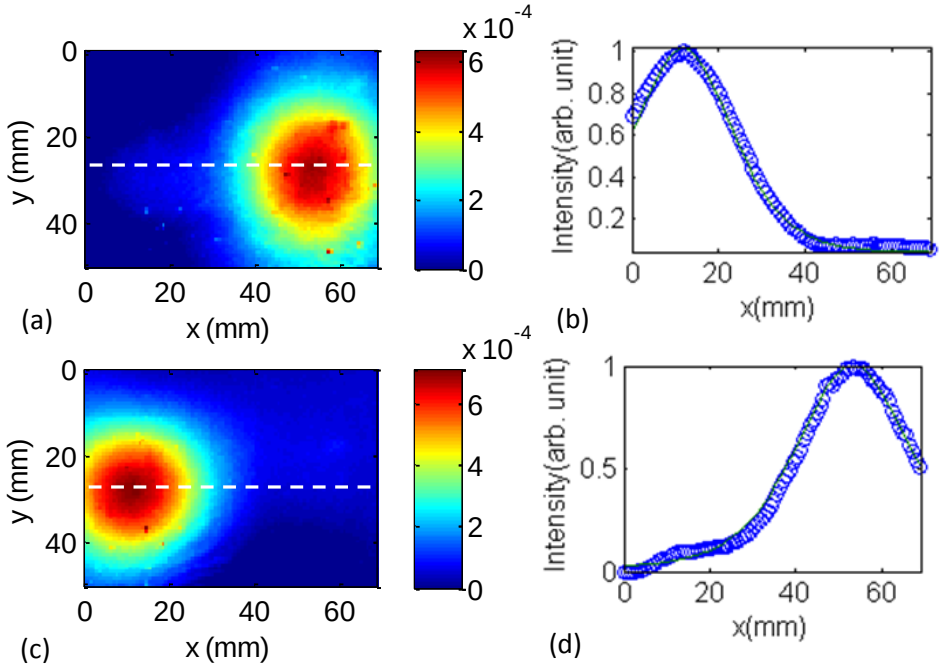

Fig. 4.35: NCIDs on the detector plane are shown in (a) and (c); corresponding Green's function fits to the horizontal spatial profiles through the dashed line are shown in (b) and (d).

Table 4.11. Retrieved positions of the scattering targets using ICA, PCA and NMF algorithms

Target #	Known position (mm)	Algorithm	Retrieved position (mm)	Error (mm)
1	(13.0, 28.0, 30.0)	ICA	(12.6, 28.7, 29.1)	(0.4, 0.7, 0.9)
		PCA	(12.6, 28.7, 28.6)	(0.4, 0.7, 1.4)
		NMF	(12.0, 28.5, 33.0)	(1.0, 0.5, 3.0)
2	(53.3, 28.5, 30.0)	ICA	(51.0, 31.8, 26.8)	(2.3, 3.3, 3.2)
		PCA	(50.9, 31.8, 26.7)	(2.4, 3.3, 3.3)
		NMF	(53.3, 28.0, 30.3)	(0.0, 0.5, 0.3)

Since the maximum difference between the known and retrieved position coordinates was larger for the scattering targets, we calculated the squared correlation coefficient γ to assess the fitting quality. NMF retrieves the position coordinates better (within 0.5 mm) for the scattering target #2 than done by ICA and PCA (deviation from known values being between 2-3 mm). NMF retrieved the position coordinates for target #1 with 3.0 mm error in *z* direction, which is not as good as that done by ICA and PCA. But γ is 0.783 and 0.778 in the fittings for ICA and PCA, respectively, as compared to 0.993 for NMF, indicating that the quality of the fitting is better for NMF. The quality of fitting is presumably affected by the efficacy of decomposition. The decomposed NCIDs by NMF were more "clean" than those decomposed by ICA and PCA. We ascribe the observed higher errors in ICA and PCA estimates of the position coordinates of the scattering target #2 than the NMF estimates to the interference from the other virtual source (corresponding to target #1) in ICA (Fig. 4.33(c)) and PCA (Fig. 4.34(c)) images. It is commonly believed that errors in locating a scattering target are higher than that for locating an absorptive target, and the results of this study conform to that notion.

Since the three decomposition methods can also be used for fluorescent targets, they will be further tested and compared in Chapter 6.

4.5. Discussion

Diffusive optical imaging was modeled as a BSS problem. ICA, PCA and NMF were used to decompose the data matrix, and locate the targets embedded in a highly scattering turbid medium. Only the components corresponding to the targets were extracted from a large dataset for target detection and localization.

4.5.1. Computational complexity

It may be instructive to compare the objectives, scope and computational complexity of these decomposition methods with model-based reconstruction methods. Decomposition methods obtain the 3-D locations of targets (the number of targets are generally small). Based on the retrieved locations, the methods may then be further extended to retrieve size and optical property information of the targets [9]. The common practice of model-based inverse reconstruction methods is to discretize the sample volume into $N \times N \times N$ voxels, and estimate absorption and/or scattering coefficient in each voxel iteratively. Voxels with significantly different optical properties than the surrounding are regions of interest, and may be identified as targets. While estimating the optical properties, the forward model is solved repeatedly to calculate the intensity of the multiply-scattered light on the sample boundary. The difference between the intensity of the multiply scattered light predicted by the forward model and the experimental measurements is minimized by seeking an optimal set of the optical properties of every voxel in the sample volume. The number of variables thus is on the order N^3. To determine location(s) of target(s) in three dimensions, the decomposition methods process the data matrix to retrieve the main components (A and S). Here A and S are two-dimensional matrices with the number of unknowns on the order

of N^2. The number of unknowns is, hence, reduced N times in the decomposition methods compared to the model-based approaches, which leads to a substantial saving in the computational time when N is large. No repeated solution of the forward model is involved in decomposition methods. Consequently, decomposition methods are considerably faster.

A comparison of the computational complexity of these two types of approaches may shed further light on their relative computation economy. For a model-based iterative reconstruction method, an equation of the form $b = Wx$ is solved to find the targets, where W is a weight matrix of *size* $N_dN_s \times N_v$, N_d, N_s, and N_v are the numbers of detectors, sources and voxels, respectively, b is an $N_dN_s \times 1$ vector describing the perturbation in the detected light intensity due to the presence of targets, and x is the perturbation in the optical properties from the background values with dimension of $N_v \times 1$. The computational complexity is typically $O(N_dN_sN_v^2)$ for a single iteration. For the decomposition approach, b is written as a 2-*D* matrix X with dimension $N_d \times N_s$. To decompose matrix X, the computational complexity per iteration is typically of order $O(N_dN_k)$ for ICA [36], and $O(N_dN_sN_k)$ for NMF [16], where N_k is the number of components that relates to the number of targets and is usually a small number. For PCA using SVD, the complexity is $O(N_s^2N_k)$ [36]. The computational complexity of the intrinsic iterative process involved in the matrix decomposition algorithms is much lower than that in the model-based inverse reconstruction methods.

4.5.2. Comparison of the decomposition methods

All three matrix decomposition methods presented in this chapter can potentially be used in *in-vivo* real-time breast cancer imaging. The three algorithms have different assumptions, which may lead to different favored conditions. In this study, the algorithms were evaluated using simulative and experimental data using model scattering media and absorptive and scattering targets. The (*x*,

y, *z*) positions of the targets were retrieved with good accuracy. The decomposition provided by ICA is "cleaner" than that of the PCA. PCA did not clearly separate the two absorptive targets used in the first two experiments. NMF decomposition seems to provide residue-free "cleaner" images than the other two methods in this study. However, since NMF is based on non-negativity assumption, the results might deteriorate when such a non-negativity assumption does not hold well. Similar consistent results from experiment and simulation are shown in Chapter 5, for fluorescent targets. Since fluorescence signal is inherently positive, the non-negativity assumption automatically holds. While continuous wave measurements were used in the work presented in this chapter, the approaches could be used with frequency domain and time-domain measurements as well.

The work presented here focuses on detecting and locating small targets, which derive impetus from the need to detect tumors in early stages of growth when those are more amenable to treatment. All three methods are applicable for extended targets as well, and are expected to provide the "center of optical strength" as the location of the target.

All three approaches are applicable for both scattering and absorbing targets, and may be used in clinical setting. The contrast between a tumor and surrounding normal tissue can be due to differences in absorption, scattering, or both absorption and scattering properties and may depend significantly on the wavelength of light used. However, *a priori* knowledge of the optical characteristics (absorptive or scattering) is not crucial. As has been shown [Eq. (4.2) and Eq. (4.3)] the expression for elements of the data matrix for absorptive targets involves Green's Functions *G*, while that for scattering targets involves $\partial G/\partial z \approx -\kappa G$, where $\kappa = \sqrt{\mu_a/D}$ in CW [9]. This relationship with *G* provides basis for detection and localization of target(s), whether contrast is due to absorption, scattering, or both. We are using transillumination geometry, which is one of

the approaches used by other researchers, and adequate signal for *in vivo* breast imaging is obtained [31, 37-40].

In this chapter, we presented results when the approaches were used to detect and obtain three-dimensional location information of the targets. We have demonstrated, while developing OPTICA [11] that a back-projection formalism can be further implemented to get a cross-section image of the target [11], or the retrieved target locations can be fed into other DOI methods as *a priori* information to get three-dimensional tomographic images. Since the approaches are suited for small targets, these hold promise for detecting and locating breast tumors in early stages of growth, which is crucially important for effective treatment. Further work involving *ex vivo* (model) and *in vivo* imaging of cancerous breast will be needed to establish the full potential of these approaches.

References

1. X. R. Cao, and R.-W. Liu, "General approach to blind source separation," IEEE Trans. Signal Process. **44**, 562-571 (1996).
2. J. F. Cardoso, "Blind signal separation: statistical principle," Proc IEEE **86**, 2009-2025 (1998).
3. A. Hyv ärinen, J. Karhunen, and E. Oja, *Independent Component Analysis* (Wiley, New York, 2001).
4. I. T. Jolliffe, *Principal Component Analysis* (Springer, New York, 1986).
5. D. D. Lee, and H. S. Seung, "Learning the parts of objects by non-negative matrix factorization," Nature **401**, 788-791 (1999).

6. M. W. Berry, M. Browne, A. N. Langville, V. P. Pauca, and R. J. Plemmons, "Algorithms and applications for approximate nonnegative matrix factorization," Comp. Stat. Data Anal. **52**, 155-173 (2007).
7. M. Xu, M. Alrubaiee, S. K. Gayen, and R. R. Alfano, "Optical imaging of turbid media using independent component analysis: theory and simulation," J. Biomed. Opt. **10**, 051705 (2005).
8. M. Xu, M. Alrubaiee, S. K. Gayen, and R. R. Alfano, "Three-dimensional localization and optical imaging of objects in turbid media with independent component analysis," Appl. Opt. **44**, 1889-1897 (2005).
9. M. Xu, M. Alrubaiee, S. K. Gayen, and R. R. Alfano, "Optical diffuse imaging of an *ex vivo* model cancerous human breast using independent component analysis," IEEE J. Select. Topics Quantum Electron. **14**, 43-49 (2008).
10. M. Alrubaiee, M. Xu, S. K. Gayen, M. Brito, and R. R. Alfano, "Three-dimensional optical tomographic imaging of scattering objects in tissue-simulating turbid media using independent component analysis," Appl. Phys. Lett. **87**, 191112 (2005).
11. M. Alrubaiee, M. Xu, S. K. Gayen, and R. R. Alfano, "Localization and cross section reconstruction of fluorescent targets in *ex vivo* breast tissue using independent component analysis," Appl. Phys. Lett. **89**, 133902 (2006).
12. D. L. Massart, B. G. M. Vandeginste, S. M. Deming, Y. Michotte, and L. Kaufman, *Chemometrics: A Textbook* (Elsevier, Amsterdam, 1988).
13. M. Turk, and A. Pentland, "Eigenfaces for recognition," J. Cogn. Neurosci. **3**, 71-86 (1991).
14. L. K. Hansen, J. Larsen, F. A. Nielsen, S. C. Strother, E. Rostrup, R. Savoy, N. Lange, J. Sidtis, C. Svarer, and O. B. Paulson, "Generalizable patterns in neuroimaging: how many principal components?," Neuroimage **9**, 534-544 (1999).

15. J.-P. Brunet, P. Tamayo, T. R. Golub, and J. P. Mesirov, "Metagenes and molecular pattern discovery using matrix factorization," Proc. Natl. Acad. Sci. **101**, 4164-4169 (2004).

16. V. P. Pauca, J. Piper, and R. J. Plemmons, "Nonnegative matrix factorization for spectral data analysis," Lin. Alg. Appl. **416**, 29-47 (2006).

17. A. Ishimaru, "Diffusion of a pulse in densely distributed scatterers," J. Opt. Soc. Am. **68**, 1045-1050 (1978).

18. K. Furutsu, "Diffusion equation derived from the space-time transport equation," J. Opt. Soc. Am. **70**, 360-366 (1980).

19. M. S. Patterson, B. Chance, and B. C. Wilson, "Time resolved reflectance and transmittance for the non-invasive measurement of tissue optical properties," Appl. Opt. **28**, 2331-2336 (1989).

20. S. Chandrasekhar, *Radiative Transfer* (Clarendon Press, Oxford, 1950).

21. A. Ishimaru, *Wave Propagation and Scattering in Random Media, Volume 1: Single Scattering and Transport Theory* (Academic, New York, 1978).

22. S. R. Arridge, and J. C. Schotland, "Optical tomography: forward and inverse problems," Inverse Probl. **25**, 123010 (2009).

23. S. R. Arridge, "Photon-measurement density functions. part I: analytical forms," Appl. Opt. **34**, 7395-7409 (1995).

24. P. C. Hansen, "Analysis of discrete ill-posed problems by means of the L-curve," SIAM Rev. **34**, 561-580 (1992).

25. P. Paatero, and U. Tapper, "Positive matrix factorization: a non-negative factor model with optimal utilization of error estimates of data values," Environmetrics **5**, 111–126 (1994).

26. P. Paatero, "The multilinear engine: a table-driven least squares program for solving multilinear problems, including the *n*-way parallel factor analysis model," J. Comp. Graph. Stat. **8**, 854–888 (1999).

27. http://cogsys.imm.dtu.dk/toolbox/.

28. A. N. Tikhonov, "Solution of incorrectly formulated problems and the regularization method," Soviet Math. Dokl. **4**, 1035-1038 (1963).

29. H. J. van Staveren, C. J. M. Moes, J. van Marle, S. A. Prahl, and M. J. C. van Gemert, "Light scattering in Intralipid-10% in the wavelength range of 400--1100 nm," Appl. Opt. **31**, 4507-4514 (1991).

30. C. Bordier, C. Andraud, J. Lafait, E. Charron, M. Anastasiadou, and A. de Martino, "Illustration of a bimodal system in Intralipid 20% by polarized light scattering: experiments and modelling," Appl. Phys. A **94**, 347-355 (2009).

31. T. Nielsen, B. Brendel, R. Ziegler, M. van Beek, F. Uhlemann, C. Bontus, and T. Koehler, "Linear image reconstruction for a diffuse optical mammography system in a noncompressed geometry using scattering fluid," Appl. Opt. **48**, D1-D13 (2009).

32. Y. Ardeshirpour, N. Biswal, A. Aguirre, and Q. Zhu, "Artifact reduction method in ultrasound-guided diffuse optical tomography using exogenous contrast agents," J. Biomed. Opt. **16**, 046015 (2011).

33. B. W. Pogue, M. S. Patterson, H. Jiang, and K. D. Paulsen, "Initial assessment of a simple system for frequency domain diffuse optical tomography," Phys. Med. Biol. **40**, 1709-1729 (1995).

34. A. Poellinger, J. C. Martin, S. L. Ponder, T. Freund, B. Hamm, U. Bick, and F. Diekmann, "Near-infrared laser computed tomography of the breast first clinical experience," Acad. Radiol. **15**, 1545–1553 (2008).

35. Binlin Wu, W. Cai, M. Alrubaiee, M. Xu, and S. K. Gayen, "Time reversal optical tomography: locating targets in a highly scattering turbid medium," Opt. Express **19**, 21956-21976 (2011).

36. T. Ristaniemi, and J. Joutsensalo, "Advanced ICA-based receivers for block fading DS-CDMA channels," Signal Processing **82**, 417-431 (2002).

37. M. Cutler, "Transillumination as an aid in the diagnosis of breast lesions," Surg. Gynecol. Obstet. **48**, 721–729 (1929).

38. R. Choe, A. Corlu, K. Lee, T. Durduran, S. D. Konecky, M. Grosicka-Koptyra, S. R. Arridge, B. J. Czerniecki, D. L. Fraker, A. DeMichele, B. Chance, M. A. Rosen, and A. G. Yodh, "Diffuse optical tomography of breast cancer during neoadjuvant chemotherapy: a case study with comparison to MRI," Med. Phys. **32**, 1128-1139 (2005).

39. A. Pifferi, P. Taroni, A. Torricelli, F. Messina, R. Cubeddu and G. Danesini, "Four-wavelength time-resolved optical mammography in the 680–980-nm range," Opt. Lett. **28**, 1138-1140 (2003).

40. B. J. Tromberg, B. W. Pogue, K. D. Paulsen, A. G. Yodh, D. A. Boas, and A. E. Cerussi, "Assessing the future of diffuse optical imaging technologies for breast cancer management," Med. Phys. **35**, 2443-2451 (2008).

Chapter 5

Near-infrared optical imaging for detection of tumors in a "realistic model breast"

5.1. Introduction

Time reversal optical tomography (TROT) [1-5] and nonnegative matrix factorization (NMF) based optical tomography (NMF-OT) have been developed in previous chapters as fast diffusive optical imaging methods to detect and localize target(s) embedded in highly scattering turbid media, such as tumor(s) in human breast. The efficacy of both methods has been evaluated using simulated data and experimental data. We have since tested the methods on *ex vivo* biological tissues with embedded cancerous breast tissues as targets. This chapter presents the results of our study on a "realistic model breast" assembled using *ex vivo* breast tissues with two pieces of human breast tumors of different sizes embedded. A multi-source, multiple wavelength probing and multi-detector signal acquisition scheme was realized to acquire data for analysis using TROT [3, 4] as well as NMF-OT [6] and optical imaging using independent component analysis (OPTICA) [7-9], two of the decomposition methods presented in Chapter 4. We also investigated the model breast using magnetic resonance imaging (MRI) to serve as a point of reference for optical measurement.

5.2. Formalism

The formalism of TROT has been detailed in Chapter 2 and Chapter 3, while those for NMF-OT and OPTICA have been presented in Chapter 4. These formalisms have been used to analyze the data on the *ex vivo* samples mentioned above. All three approaches use the same data acquired

using a multi-source illumination and multi-detector signal acquisition scheme. For small absorptive and scattering targets, the contribution due to the targets is a perturbation in the light intensities measured on the boundary of the sample. This perturbation data $-\Delta I = I - I_0$, where I and I_0 are the transmitted light intensity distributions on the sample boundary with and without target embedded, is the starting point for all three methods.

In the TROT formalism, the response matrix K is constructed using the perturbation data, $-\Delta I$, and describes the transport of light from multiple sources through the embedded target(s) to the array of detectors.

For multi-wavelength TROT, datasets collected using different wavelengths are put together in the same data matrix K. The elements of K are $K_{ij}^{\lambda} = -\Delta I^{\lambda}\left(\boldsymbol{r}_d^{(i)}, \boldsymbol{r}_s^{(j)}\right)$ corresponding to i^{th} detector and j^{th} source using light source of wavelength λ. The response matrix is constructed as

$$K = \begin{bmatrix} K^{\lambda_1} & 0 & 0 \\ 0 & K^{\lambda_2} & 0 \\ 0 & 0 & \ddots \end{bmatrix} \tag{1}$$

The time reversal (TR) matrix T is then constructed by multiplying the response matrix by its transpose for continuous-wave (CW) illumination, *i.e.* $T_{DSSD} = KK^T$ (DSSD scheme), where K^T is the transpose matrix of K. By solving an eigenvalue equation of TR matrix T_{DSSD}, eigenvalues and eigenvectors of T_{DSSD} are calculated. The eigenvectors with leading non-zero eigenvalues form the signal subspace, and correspond to the targets, while the eigenvectors with near-zero eigenvalues form the noise subspace which is complementary and orthogonal to the signal subspace. The signal and noise subspaces are separated using an L-curve method [10-12]. For multi-wavelengths data, the eigenvectors in the signal and noise subspaces include those for different wavelengths. A MUSIC pseudo-spectrum P for DSSD scheme is then calculated using Green's functions for slab geometry

$$P(\boldsymbol{X}_p)=\sum_{\lambda}\frac{<g_p{}^{\lambda},\mathrm{g}_p{}^{\lambda}>}{\left|<\mathrm{g}_p{}^{\lambda},\mathrm{g}_p{}^{\lambda}>-\sum_{m=1}^{M}\left|<u_m,\mathrm{g}_p{}^{\lambda}>\right|^2\right|}. \tag{2}$$

where $\mathrm{g}_p{}^{\lambda_k}$ is Green's function vector (GFV) at voxel p for k^{th} wavelength λ_k, and u_m ($1 \le m \le M$) is the m^{th} leading eigenvector. The locations of the targets are determined using the poles in the pseudo spectrum [1, 4]. As explained in Chapter 2, there are four types of GFVs corresponding to each voxel p, one for absorption and three for scattering. For a single wavelength, the GFV associated with the detector plane for an absorptive target at $\boldsymbol{r}$ is formed as $g_d(\boldsymbol{r}, \lambda) = \{G^d(\boldsymbol{r}_i, \boldsymbol{r}, \lambda), i = 1, \ldots, N_d\}$, which describes light propagation from target position $\boldsymbol{r}$ to detectors located at $\boldsymbol{r}_i$; while for each scattering target, three GFVs are constructed as, $\partial_\alpha g_d$, $\alpha = x, y, z$, respectively [4]. For multiple wavelengths, the GFV associated with the detector plane is constructed as

$$g_d{}^{\lambda_1}=\begin{pmatrix} g_d(\boldsymbol{r},\lambda_1)\\ 0\\ 0\\ \vdots\end{pmatrix},\ g_d{}^{\lambda_2}=\begin{pmatrix} 0\\ g_d(\boldsymbol{r},\lambda_2)\\ 0\\ \vdots\end{pmatrix},\ \ldots \tag{3}$$

Three dimensional tomographic pseudo images of sample are generated using the pseudo spectrum. The target locations are determined using the poles associated with specific GFVs, which is then used to characterize the targets in principle. For example, if the overall peak shows up in the pseudo spectrum calculated using the GFV for an absorptive target, the target is considered to be an absorptive target (absorptive contrast dominates), otherwise, a scattering target. In this study, we mainly focus on locating the targets. We use the maxima in the pseudo spectrum to determine the target position. The full-width-at-half-maximum (FWHM) of the poles is used to estimate dimension of the target(s).

The NMF and ICA analysis were carried using the multi-wavelength datasets, separately. The target locations were retrieved using each dataset. The average value of the retrieved positions was used to determine the position of a target. As discussed in Chapter 4, NCIDs and

ICIDs were obtained using NMF and ICA. The target locations were estimated by fitting the NCIDs and ICIDs, particularly on the detector plane, to the Green's functions that describe light propagation from targets to the detectors. The NCIDs were then back-projected to the *z* plane of the target positions to generate cross-section images. The size of a target was then estimated using the FWHM in the cross-section images.

5.3. Experimental Methods and Materials

5.3.1. Experiments

Two sets of experiments were carried out on the realistic model breast. First set involved NIR imaging measurements using 750 nm, 800 nm and 830 nm probe beams. The second set was corroborating MRI measurements.

5.3.1.1. *NIR Imaging Experiments*

The experimental arrangement is shown schematically in Fig. 5.1. The model breast was assembled using two pieces of normal *ex vivo* female human breast tissues and two pieces of cancerous tissues provided by National Disease Research Interchange (NDRI) under an Internal Review Board approval at the City College of New York. The normal breast tissue specimens weighed 119 grams and 127 grams and consisted primarily of adipose tissue, while each tumor (infiltrating ductal carcinoma) pieces weighed approximately 1 gram. Two incisions ~ 3 cm apart were made in the mid-plane (along the *z*-axis, which was the shortest dimension) of normal tissue pieces and a small amount of tissue was removed from the core region to make two small pouches. The tumor pieces were inserted into these pouches, and the incisions were closed by moderate compression of the tissue-tumor composite from all directions. The sample was placed inside a cylindrical transparent plastic container with a movable end face of diameter 110 mm, which was moved to slightly compress the tissue along the z-axis and hold it in place. The

resulting slab sample filled over 75% of the lateral dimension of the cylinder and had a uniform thickness of 40 mm. It was treated as a single entity in the subsequent imaging experiments.

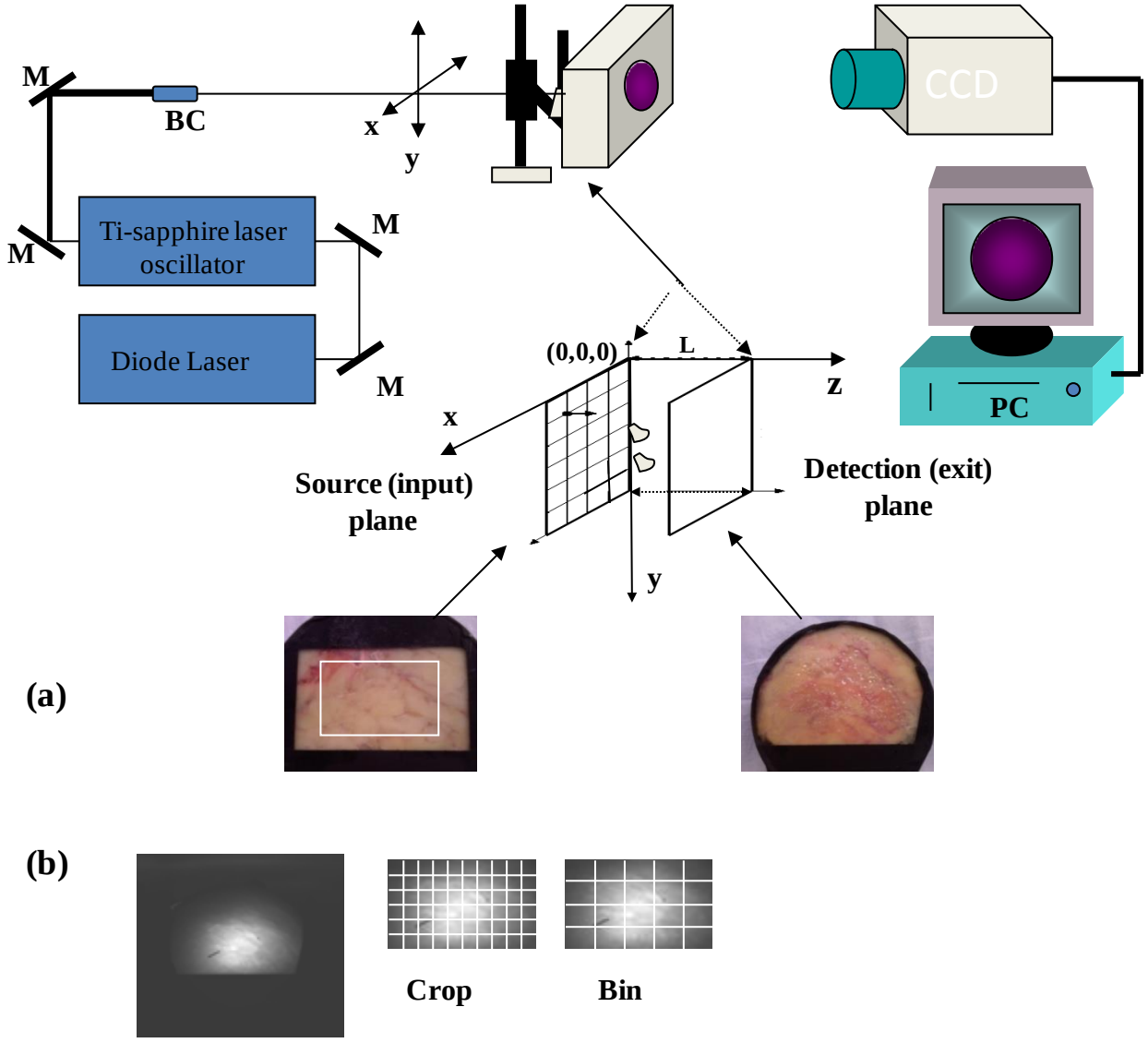

Fig. 5.1. (a) Schematic diagram of the experimental arrangement. (Key: BC = beam collimator, CCD = charge coupled device, M = mirror.) Inset below shows the expanded view of the source (input) plane with the scanning grid points. (b) Photographs of the source plane (left) showing the scanned area, and detection plane (right) of the model breast sample. (c) (Upper pane) A typical raw CCD image of the detection plane, and how it is cropped and binned for analysis.

The nominal dimension of the tumor piece located at the left side of the sample ('left tumor') was 8 mm × 5 mm × 3 mm and that located on the right side ('right tumor') was 10 mm × 10 mm × 5 mm. The positions of the tumor pieces within the sample, and the distance between the pieces were known approximately, as those were placed in position as discussed above. The axial orientation of the plastic container and sample within it was preserved for magnetic resonance imaging (MRI) experiments following the optical measurements.

The optical imaging experiments were carried out using the 750-nm, 800-nm, and 830-nm near-infrared (NIR) beams from a continuous wave (CW) Ti:Sapphire laser. The average beam power was maintained at 10 mW for every wavelength. The light beam at any of these wavelengths was collimated to a 1-mm spot onto the entrance face (henceforth referred to as the 'source plane') of the slab sample. Multiple source illumination was realized in practice by step scanning the slab sample along the horizontal (x) and vertical (y) directions across the laser beam in an x-y array of grid points using a computer controlled translation stage. A camera lens collected the diffusely transmitted light on the opposite face of the sample (henceforth referred to as the 'detection plane') and projected it onto the sensing element of the cooled 16-bit, 1024 × 1024 charged couple device (CCD) camera. Each illuminated pixel of the 1024 × 1024 pixels of the CCD camera could be regarded as a detector. For illumination of every scanned point on the source plane, the CCD camera recorded the diffusely transmitted intensity pattern on the detection plane. A 62.5 mm × 37.5 mm area of the source plane was scanned in a 26 × 16 array of x-y grid points with a step size of 2.5 mm, while the CCD camera imaged the entire detection plane.

The average of all 26 × 16 images was used to assess the average optical properties of the *ex vivo* model breast. The radial profile of the transmitted light intensity of the average image was

fitted to the predictions of a diffusion model of light propagation inside a slab. Assuming a typical value of 1 mm^{-1} for the reduced scattering coefficient for breast tissues, the average absorption coefficient, μ_a of the entire model breast was found to be 0.00338 mm^{-1}, 0.00238 mm^{-1} and 0.00350 mm^{-1} for wavelengths of 750, 800 and 830 nm, respectively. While the entire detection plane was imaged, each raw image was cropped to retain the region within ~ 50 mm × 50 mm for carrying out image reconstruction. The size of 1 pixel in the raw image was ~160 μm × 160 μm. The raw images were binned by merging 5 × 5 pixels into one to enhance the signal-to-noise ratio. All the binned images corresponding to probing of the grid points in sequence were then stacked. The difference between each individual image and the average image was calculated, which is the perturbation due to tumors in the measured light intensity distribution on the sample exit surface. The response data matrix *K* was then constructed for subsequently analysis.

5.3.1.2. *MRI experiment*

For MRI experiments, the breast model sample in the plastic container was taken to Memorial Sloan-Kettering Cancer Center (MSKCC) small animal MRI facility. The facility currently utilizes a 4.7-T 33-cm bore magnet imaging/spectroscopy system (Bruker BioSpin) operating at 200 MHz for 1-H (standard) imaging experiments. The tissue container was fixed inside the radio-frequency coil (RFC) and placed inside the bore magnet. MR images of the sample were recorded in 2.0-mm slice thick sagittal slices.

5.3.2. Analysis & Results

5.3.2.1. *TROT analysis*

In the TROT analysis, the TR matrix $T_{DSSD} = KK^T$ was calculated. Eigenvalues and eigenvectors of the *T* were found by solving the eigenvalue equation of *T*. Signal and noise subspaces were

separated with a proper threshold level. The pseudo spectrum was then calculated. The positions of the targets were determined using the poles in the pseudo spectrum.

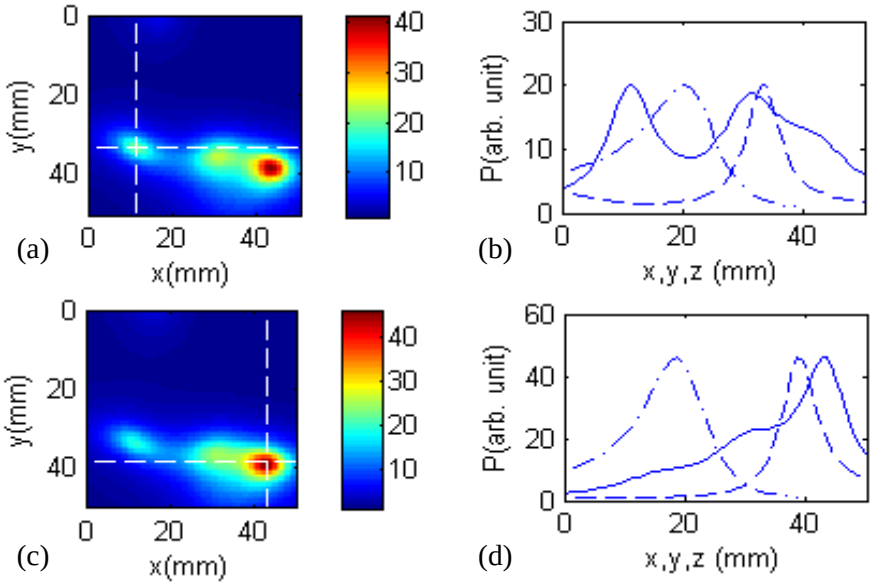

Fig. 5.2. (a) and (c) are TROT-generated pseudo images at the z = 20.5 mm and 18.5 mm for the left and right tumors, respectively, using 750 nm; (b) and (d) are profiles of the pseudo image through the target along x(-), y(--) and z(-.) directions.

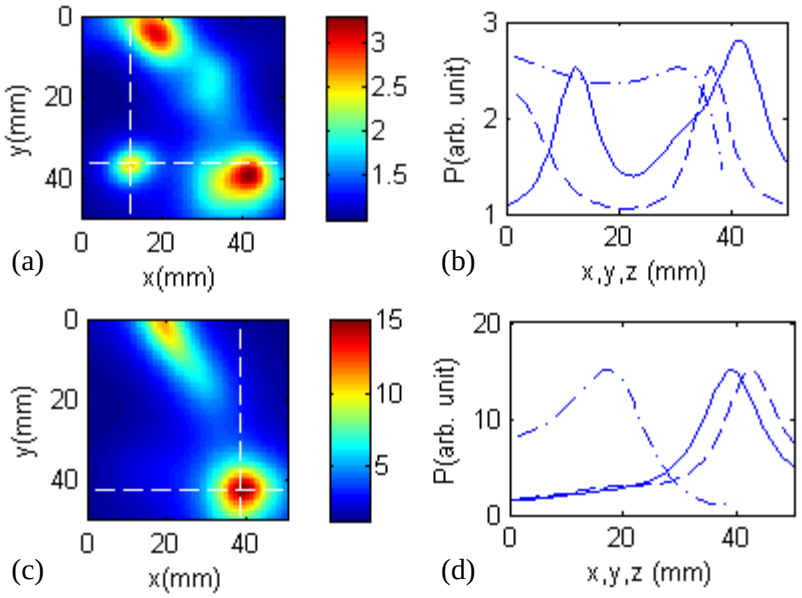

Fig. 5.3. (a) and (c) are TROT-generated pseudo images for the left and right tumors using 800 nm; (b) and (d) are profiles of the pseudo image through the target along x(-), y(--) and z(-.) directions.

TROT was used to analyze the dataset for each individual wavelength first. Then all three datasets were put together as one multi-wavelength dataset and analyzed accordingly. The TROT-generated pseudo image at the *z*-coordinates of the positions of the tumors for wavelength 750 nm is shown in Fig. 5.2(a) and 5.2(c). Profiles through the tumor position in the *x*, *y* and *z* directions are plotted in Fig. 5.2(b) and 5.2(d). Similar images were obtained for wavelengths of 800 nm and 830 nm in Figs. 5.3 and 5.4.

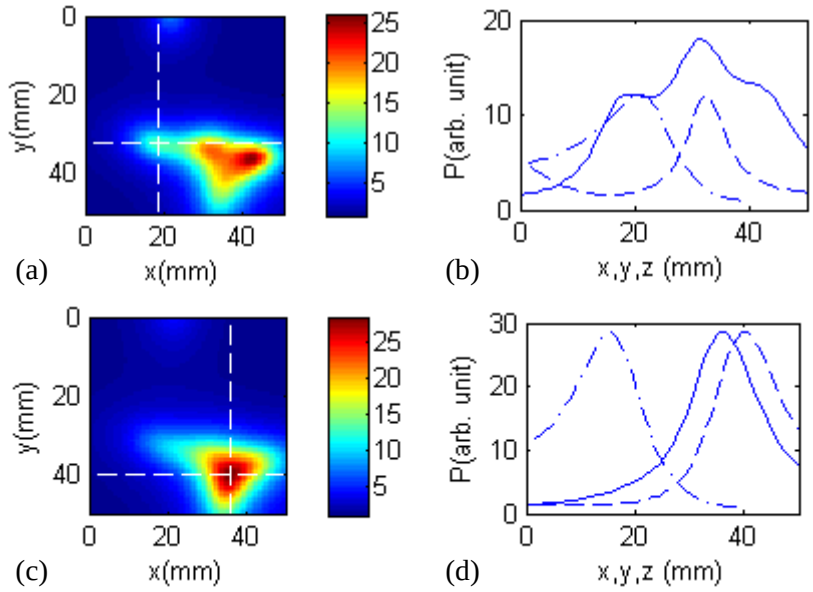

Fig. 5.4. (a) and (c) are TROT-generated pseudo images for the left and right tumors using 830 nm; (b) and (d) are profiles of the pseudo image through the target along x(-), y(--) and z(-.) directions.

For 800-nm measurements, a black tape was placed on the exit surface of the sample for testing. Even though there was a local maximum position located at (12.3, 36.2, 30.5) mm, the global maximum position along the axial direction at the same lateral position is located on the detector plane (exit surface) of the sample, which is the same as the known location of the tape, as shown in Fig. 5.5. The target shown in Fig. 5.3(a) could be an artifact due to the tape, or a combination effect due to the tape and the left tumor. Since the left tumor is relatively smaller, as shown in the MRI images, and located at about the same location of the tape, it is hard to detect

and localize it accurately. The target shown on the top of the reconstructed image using 800 nm is another artifact probably due to the boundary.

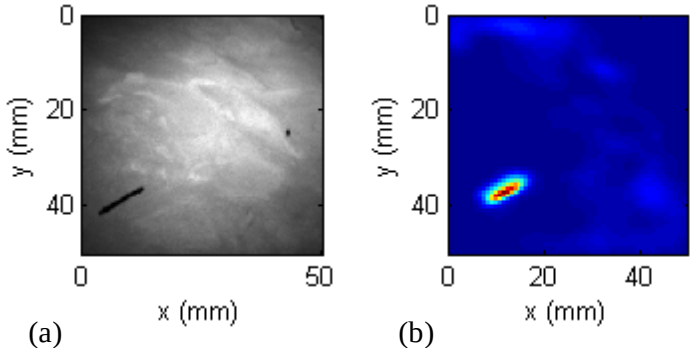

Fig. 5.5. (a) The raw image which shows the tape placed on the exit surface of the sample. (b) TROT-generated pseudo image at z = 39 mm which the neighbor plane of the detector plane using 800 nm.

When all three wavelengths were combined, similar images were also obtained and shown in Fig. 5.6.

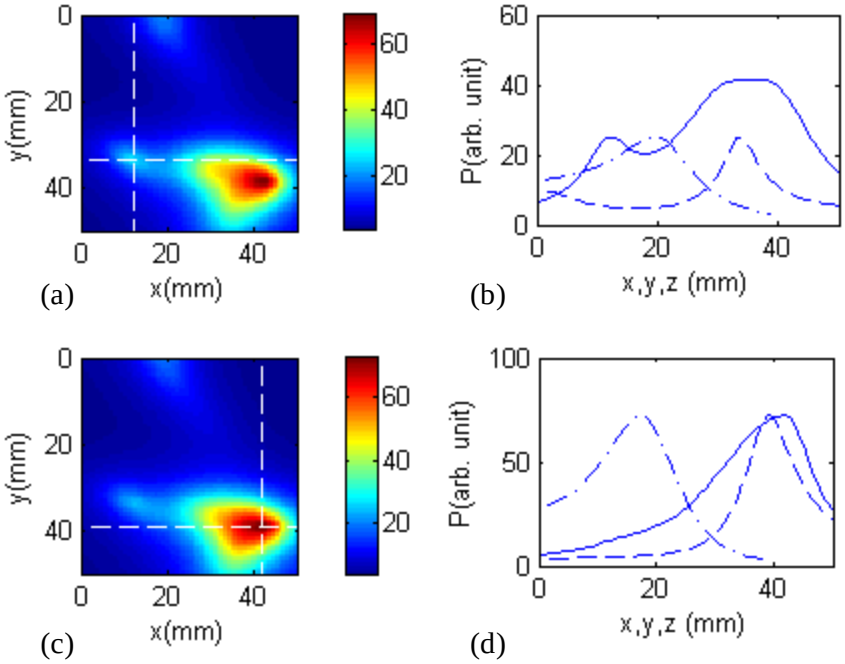

Fig. 5.6. (a) and (c) are TROT-generated pseudo images for the left and right tumors using all three wavelengths; (b) and (d) are pseudo value profiles through the target along x(-), y(--) and z(-.) directions.

The peaks in the pseudo spectrum (pseudo images) were used to represent the locations of the tumors (targets). The locations of the tumors found respectively for the three wavelengths were listed in Table 5.1.

Table 5.1. Coordinates (x, y, z) of the tumors retrieved by TROT

Wavelength (nm)	Left Tumor Position [(x, y, z) (mm)]	Right Tumor Position [(x, y, z) (mm)]
750	11.5, 33.1, 20.5	43.4, 38.6, 18.5
800	12.3, 36.2, 30.5	38.6, 42.6, 17.5
830	18.7, 32.3, 20.5	36.2, 40.2, 15.5
Combined	12.3, 33.9, 19.5	41.8, 39.4, 17.5

FWHM of the peaks in the multi-wavelength pseudo spectrum was used to estimate the dimensions of the tumors. The lateral dimensions of the left tumor were estimated to be 7.2 mm × 7.6 mm, and the right tumor, 16.7 mm × 8.8 mm. These estimated dimensions of both tumors are comparable to the known dimensions of the tumors.

5.3.2.2. ***NMF-OT and OPTICA analysis***

The experimental data from Section 5.3.1 were then analyzed using NMF-OT and OPTICA. The NCIDs and ICIDs for the 750-nm illumination of are shown in Fig. 5.7 and Fig. 5.8, respectively.

The profiles in the NCIDs and ICIDs were fitted to Green's functions to retrieve the target positions. The Green's function fits for the profiles in the x direction through the maxima in the intensity distributions are shown in Figs. 5.7(b) and 5.7(d) for NCIDs, and Figs. 5.8(b) and 5.8(d) for ICIDs, respectively. Similar fits for the profiles in the y direction were obtained (not shown

here). Figs. 5.7(e) and 5.7(f) show the NCIDs for the left and right targets, respectively on the source plane. Similar images for ICIDs were obtained (not shown here). The source plane was relatively small and had much lower resolution. Therefore, only the NCIDs and ICIDs on the detector plane were used for further analysis.

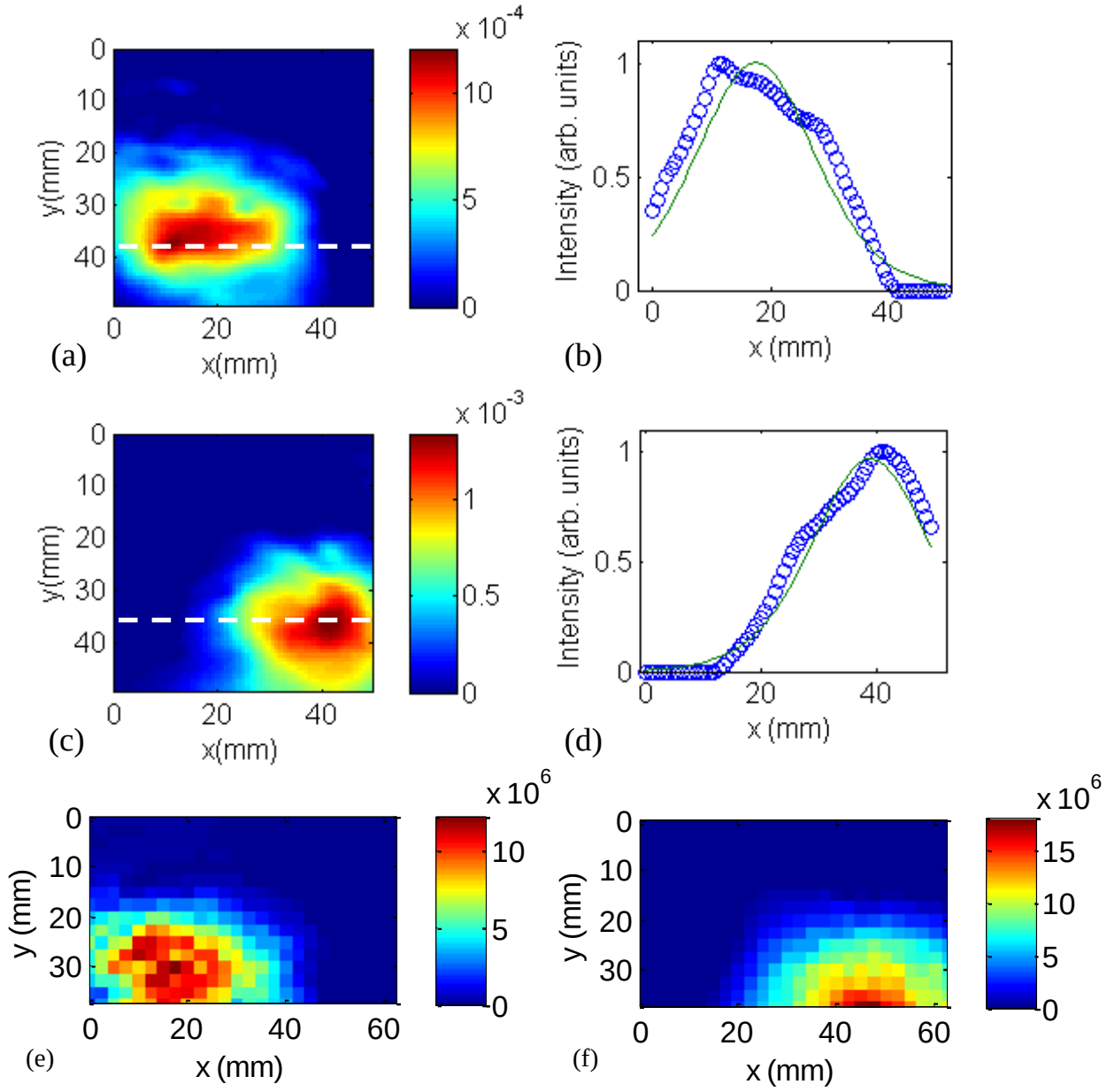

Fig. 5.7. (a) and (c) are NCIDs of the left and right targets, respectively on the detector plane, for 750-nm measurements. (b) and (d) are Green's function fits of the profiles through the white lines. (e) and (f) are the corresponding NCIDs for the left and right targets, respectively on the source plane.

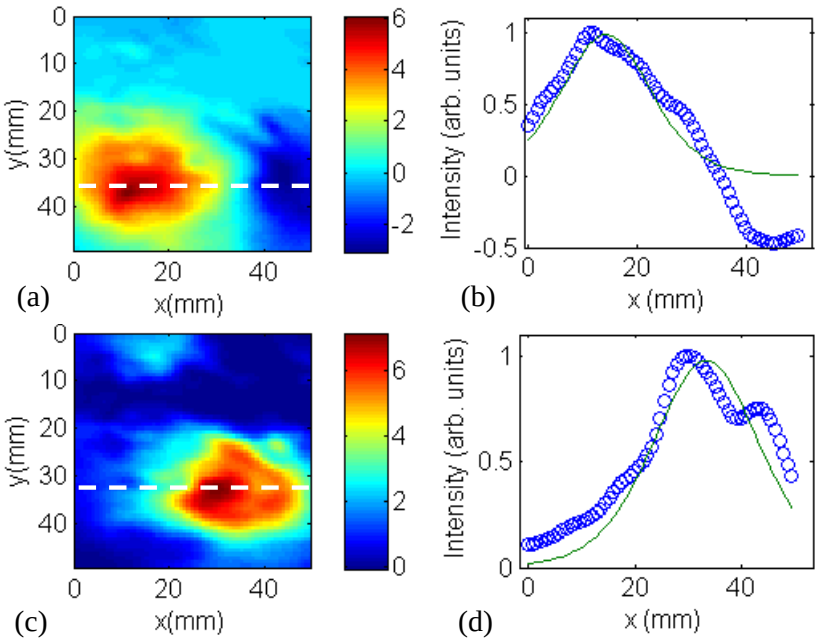

Fig. 5.8. (a) and (c) are ICIDs of the left and right targets respectively on the detector plane, for 750-nm measurements. (b) and (d) are Green's function fits of the profiles through the white lines.

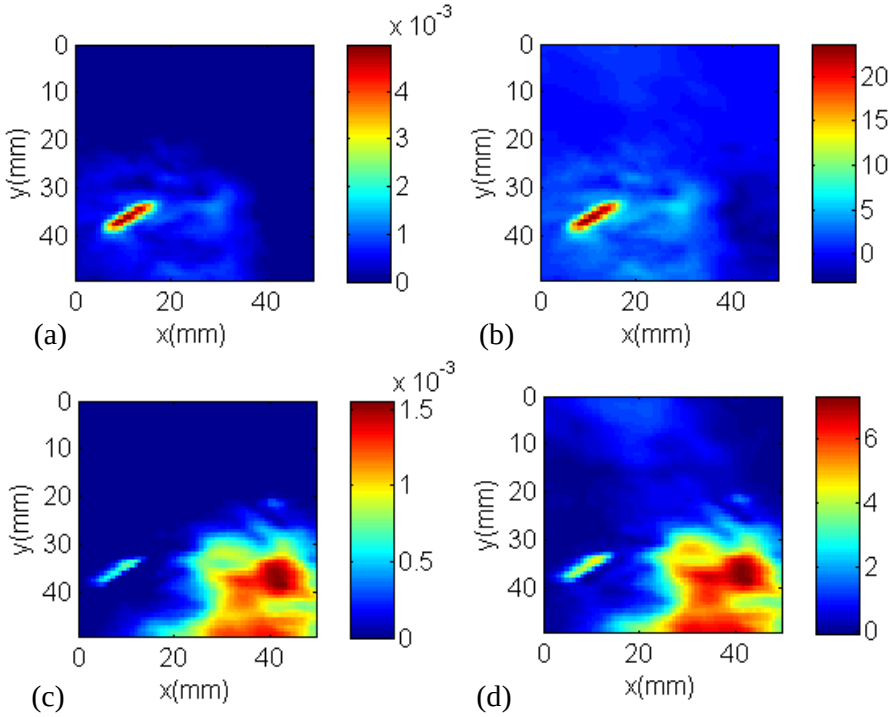

Fig. 5.9. (a) and (c) are NCIDs of the left and right targets, respectively on the detector plane, for 800-nm measurements, and (b) and (d) are the corresponding ICIDs.

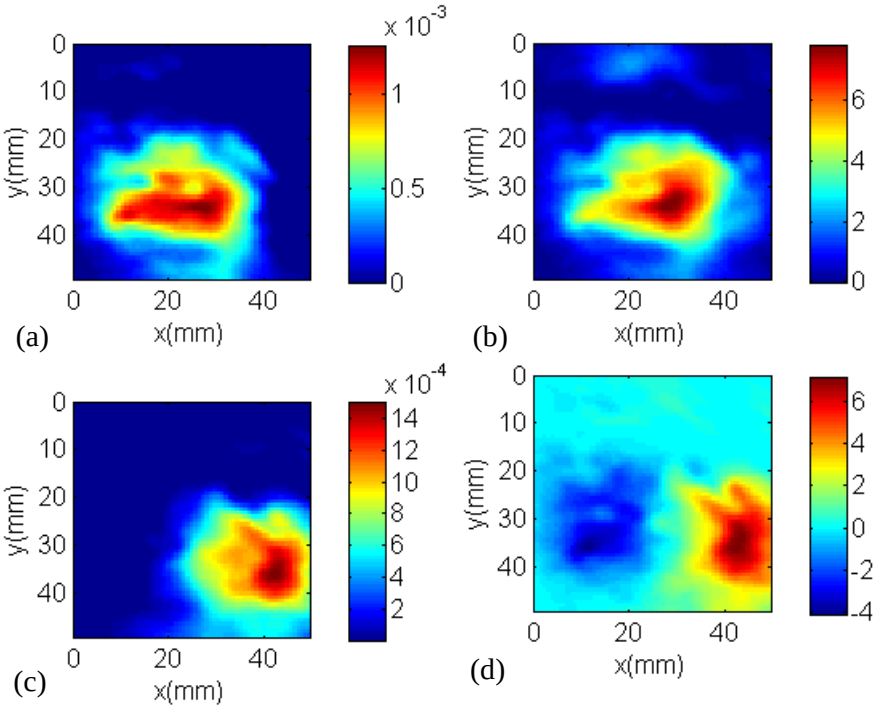

Fig. 5.10. (a) and (c) are NCIDs of the left and right targets, respectively on the detector plane, for 830-nm measurements, and (b) and (d) are the corresponding ICIDs.

NCIDs and ICIDs on the detector plane for illumination of 800 nm and 830 nm are shown in Fig. 5.9 and Fig. 5.10, respectively. Similar NCIDs and ICIDs on the source plane were also obtained (not shown here).

Table 5.2. Target positions retrieved by NMF-OT and OPTICA

Illumination wavelength (nm)	Left Target Position [(*x*, *y*, *z*) mm]		Right Target Position [(*x*, *y*, *z*) mm]	
	NMF-OT	OPTICA	NMF-OT	OPTICA
750	18.0, 35.9, 16.7	14.6, 35.9, 21.9	39.3, 38.1, 16.6	33.7, 33.5, 17.2
800	N/A	N/A	39.2, 40.3, 21.2	38.2, 40.6, 20.4
830	17.9, 36.1, 17.1	14.6, 35.9, 21.9	39.4, 38.1, 16.7	33.7, 33.5, 17.2
Average	18.0, 36.0, 16.9	14.6, 35.9, 21.9	39.3, 38.7, 17.8	35.2, 35.9, 18.3

As shown in Fig. 5.9, due to the black tape which has approximately same lateral position as the left target on the exit surface of the sample, the left target (small tumor piece) was not obtained.

The target positions were also obtained for 800 nm and 830 nm illumination using Green's function fit. The retrieved positions are shown in Table 5.2.

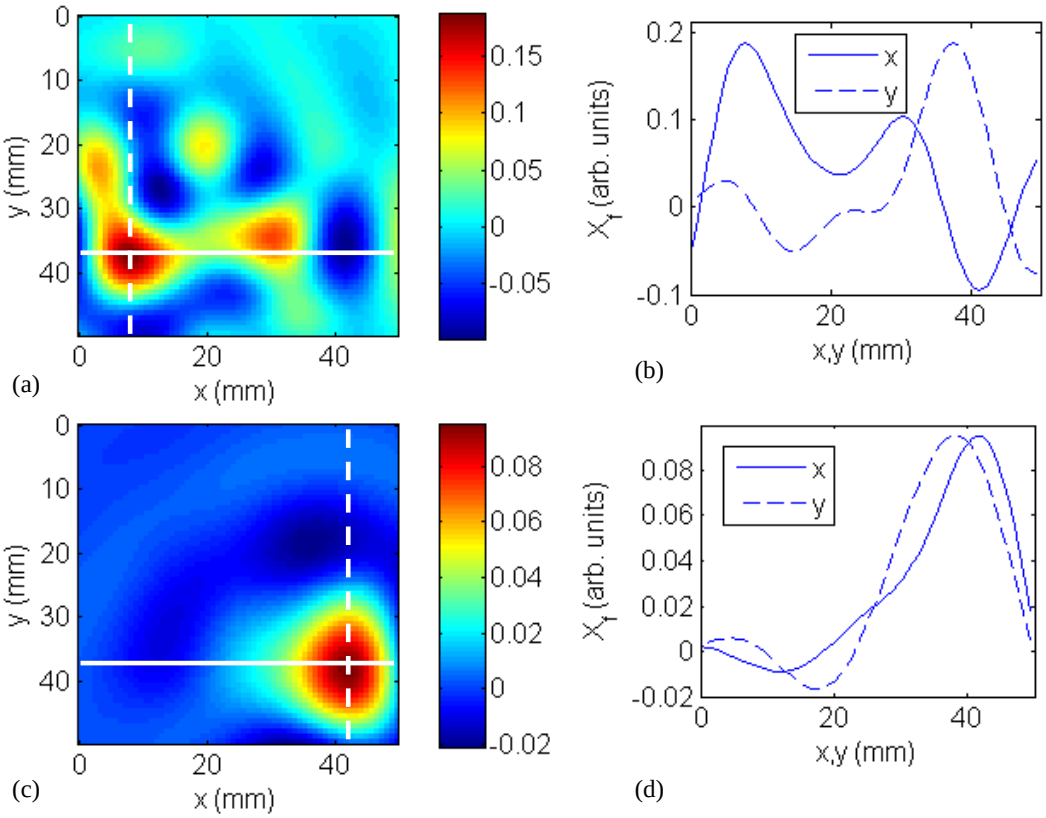

Fig. 5.11. (a) and (c) are cross-section images of the left and right targets, respectively generated using backprojection of the NCIDs; (b) and (d) are the profiles through the maximum in the images, whose FWHMs are used to estimate the target dimensions.

The lateral distance between the two targets is found to be 21.5 mm and 20.6 mm using NMF-OT and OPTICA respectively. These retrieved values of the distance are about ~1cm less than that detected by MRI. It is probably because the tissue heterogeneity around the embedded tumors, particularly the left tumor, caused the NCIDs and ICIDs to spread out significantly.

When the weighted center of the optical property was used to describe the target location, it led to difficulty in accurate localization of the target.

The cross-section images of the targets were generated using the backprojection of NCIDs for 750-nm measurements, and shown in Fig. 5.11. Similar cross-section images were generated using measurements with other wavelengths. The profiles through the maxima in the cross-section images are also shown in Fig. 5.11, FWHMs of which are used to estimate the lateral dimension of the targets. Similar cross-section images of the targets and the profiles in the images were also generated using backprojection of ICIDs, and shown in Fig. 5.12. The estimated values are shown in Table 5.3.

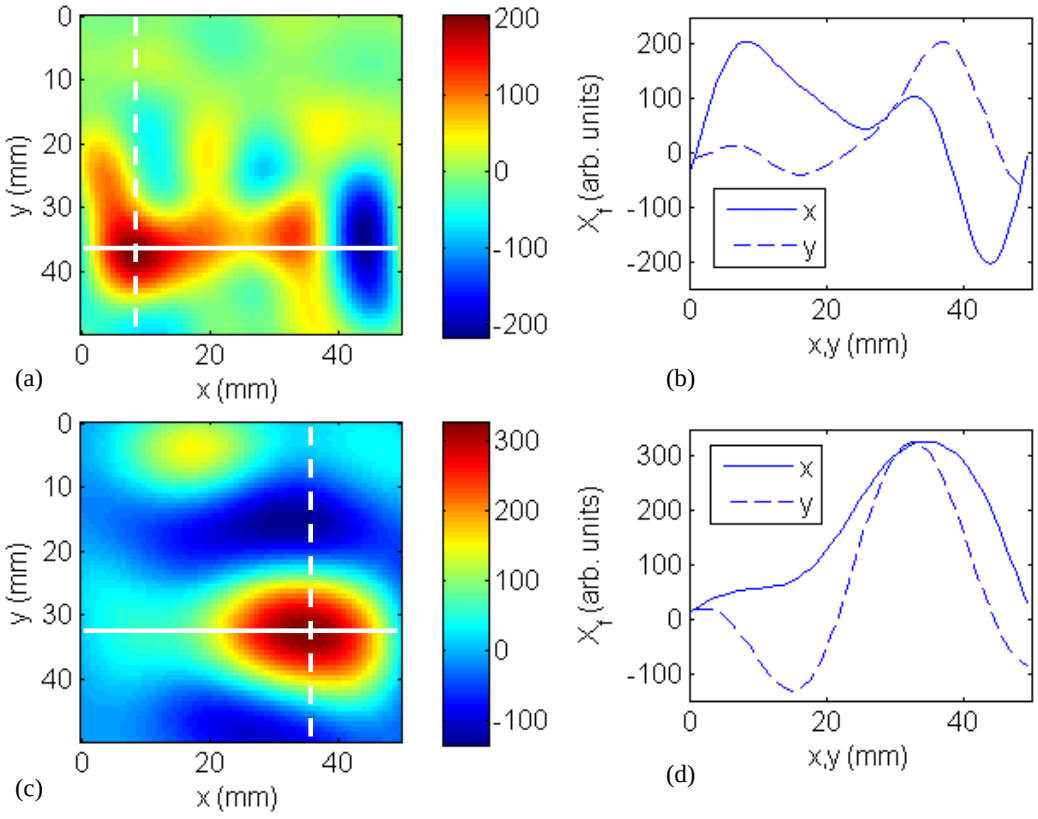

Fig. 5.12. (a) and (c) are cross-section images of the left and right targets, respectively generated using backprojection of the ICIDs; (b) and (d) are the profiles through the maximum in the images, whose FWHMs are used to estimate the target dimensions.

Table 5.3. Estimated positions and dimensions of the targets using cross-section images

Method	Left Target		Right Target	
	Position [(x, y) mm]	Dimensions [(Δx, Δy) mm]	Position [(x, y) mm]	Dimensions [(Δx, Δy) mm]
NMF-OT	8.4, 37.8	11.2, 9.6	41.8, 38.6	14.3, 16.3
OPTICA	8.4, 37.8	12.7, 11.2	34.6, 33.1	22.3, 14.3

The estimated target dimension using the FWHMs of the profiles of the cross-section images generated using NCIDs and ICIDs are approximately up to twice as big as the actual target dimensions. The dimensions estimated using NMF-OT are smaller than those using OPTICA. This happens since the cross-section image is highly sensitive to the background heterogeneity, and flexibility exists in the regularization process.

For this dataset, even though the modified *L*-curve is used, the regularization parameter is from around the corner. If lower regularization is used, the target cannot be distinguished from artifacts in the cross-section image. Therefore, the maxima in the cross-section images can also be used to estimate the target positions, since it is not shifted due to regularization. The lateral distance between the two targets is estimated to be 33.4 mm and 26.6 mm, for NMF-OT and OPTICA respectively, which are close to the actual distance (~ 30 mm), and better than those estimated by Green's function fit. This could be due to the higher resolution in the cross-section image than the component intensity distributions.

5.3.2.3. *MRI Results*

The MRI images of the two targets were recorded for 2-mm-thick slices, and placed around the mid-plane in two sagittal slices that are 4 mm apart. The MRI images of the sample through the known *z* positions of the two tumors are shown in Fig. 5.13.

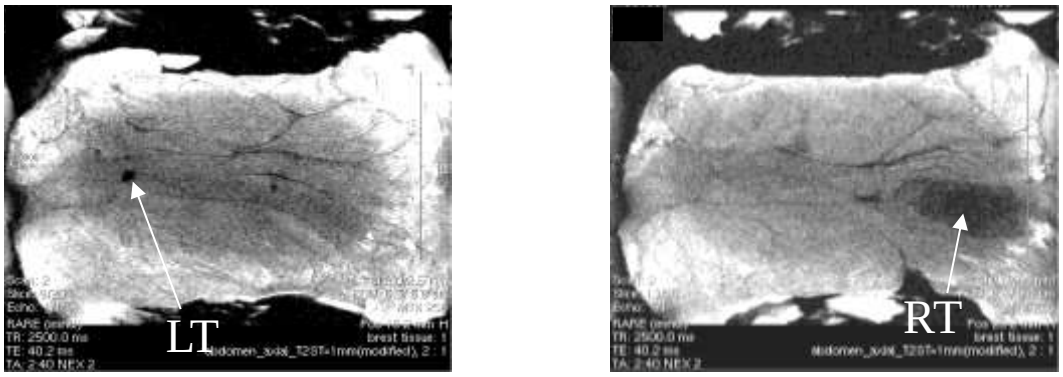

(a) (b)

Fig. 5.13. Magnetic resonance images of the left tumor and the right tumor pieces (LT: left tumor, RT: right tumor)

5.4. Discussion

The efficacy of TROT and NMF-OT for detection and localization of tumors was tested and compared to MRI and OPTICA. In realistic conditions, the perturbations in the measured light intensities due to absorptive and scattering inhomogeneities are very similar and difficult to distinguish, which was also reported by other groups [13, 14]. The situation may be improved using frequency-domain measurements. The results from the experiments showed that TROT and NMF-OT could detect, locate and estimate the dimension of targets (breast tumors) inside biological tissue (normal tissue). The locations of the targets retrieved by NMF-OT are comparable to that retrieved by OPTICA. However, the locations retrieved by NMF-OT and OPTICA using Green's function fit are not as accurate as those retrieved by TROT, particularly

when significant background heterogeneity is present around the targets. This need be verified by further experiments.

The dimensions of the targets estimated by NMF-OT are comparable to OPTICA. In the experiment, the NMF-OT and OPTICA-estimated target dimensions are less accurate than the TROT-estimated values, which is probably also due to the influence of the background heterogeneity. Tikhonov regularization using a modified *L*-curve method is used in inverse Fourier transform algorithm for NMF-OT and OPTICA. However, this method is highly sensitive to the background heterogeneity (signal-to-background ratio), since the regularization parameter is selected by comparing the target to the rest part of the cross-section image which is sensitive to the boundary condition, noise and background heterogeneity. For this dataset, the cross-section images generated using backprojection algorithm used regularization parameter around the "corner" of the *L*-curve, since higher-resolution images cannot be generated using lower regularization. Then the cross-section images were also used to locate the targets, which resulted in improved accuracy in the localization. This may be due to higher resolution in the cross-section image than the component intensity distributions.

The experiments showed the multi-wavelength data may help to improve the localization of targets. The MRI images of the sample displayed in Fig. 5.13 were obtained to serve as reference for testing the validity of the TROT, NMF-OT and OPTICA measurements. The MRI measurements corroborate the assessments of TROT, NMF-OT and OPTCA in terms of the number of targets, the distance separating them, and their depth (*z*-position). TROT and NMF-OT-retrieved positions are within 3 mm from the mid-plane (z = 20 mm). OPTICA-retrieved positions are within 2 mm from the mid-plane. This is a good agreement between the results

from all the methods. Similarly, all the approaches provide comparable estimates for overall distance between the tumor pieces.

In TROT analysis, when each individual wavelength was used, the two targets were clearly detected and accurately localized when 750 nm was used; while the image of left tumor was hardly separated from the right tumor when 830 nm was used. For 800-nm illumination, when a black tape was placed on the exit surface of the sample around the same lateral position of the left tumor, the left tumor was not accurately localized in the reconstructed image. This mimics a dynamic condition in *in-vivo* experiments where instability may be present. When all three wavelengths were combined, two tumors were detected with accurate positions retrieved. The black tape as a "random false target" was filtered out and not shown in images anymore. At the same time, the artifact was suppressed by the TROT algorithm automatically, and not shown as a prominent "false" target. The left tumor was shown to be much smaller and difficult to detect than the right tumor. The distance between the centers of the left and right tumors was found to be ~ 30 mm. The result is comparable to that from MRI images.

TROT is a fast approach for DOT with no iterations of forward model involved. *A priori* information of the targets was not used for the approach. Even though, the slab geometry, diffusion model and CW measurements were used in this study, TROT is applicable to different geometries, different forward models, and different measurement modes such as frequency-domain and time-domain. TROT has a potential to be used in real-time breast cancer detection and imaging.

In NMF-OT and OPTICA analysis, while the three wavelengths that we used were not targeted for obtaining diagnostic molecular spectroscopic information, we observed some instructive and clarifying advantages of employing light of different wavelengths. In addition to

the two tumor pieces shown in Fig. 5.7 – Fig. 5.10, another NCID and ICID (not shown in any figure) appeared prominently in both NMF-OT and OPTICA analysis conducted using all three wavelengths. However, strength of two of the NCIDs and ICIDs corresponding to tumor pieces decreased monotonically with increasing wavelength of the probing light, but no such wavelength dependence was observed in the strength of the third independent component. We tentatively ascribe this feature to an embedded water pocket within the sample. Multi-wavelength measurements helped sort out this artifact. The monotonic decrease in strength of the tumor pieces with increasing wavelength is consistent with the wavelength dependence of light scattering by tissue and tumor constituents.

References

1. W. Cai, M. Alrubaiee, S. K. Gayen, M. Xu, and R. R. Alfano, "Three-dimensional optical tomography of objects in turbid media using the round-trip matrix," Proc. SPIE **5693**, 4-9 (2005).
2. B. Wu, M. Alrubaiee, W. Cai, M. Xu, and S. K. Gayen, "Optical imaging of objects in turbid media using principal component analysis and time reversal matrix methods," in *Computational Optical Sensing and Imaging, OSA Technical Digest (CD) (Optical Society of America, 2009), paper JTuC10*(San Jose, California, 2009).
3. B. Wu, W. Cai, M. Alrubaiee, M. Xu, and S. K. Gayen, "Three dimensional time reversal optical tomography," Proc. SPIE **7892**, 78920G (2011).
4. B. Wu, W. Cai, M. Alrubaiee, M. Xu, and S. K. Gayen, "Time reversal optical tomography: locating targets in a highly scattering turbid medium," Opt. Express **19**, 21956-21976 (2011).

5. B. Wu, M. Xu, W. Cai, and S. K. Gayen, "Time-reversal optical tomography: detecting and locating extended targets in a turbid medium," Proc. SPIE **8216**, 82160K (2012).
6. B. Wu, M. Alrubaiee, W. Cai, M. Xu, and S. K. Gayen, "Diffuse optical imaging using decomposition methods," Int. J. Opt. **2012**, 185435 (2012).
7. M. Xu, M. Alrubaiee, S. K. Gayen, and R. R. Alfano, "Optical imaging of turbid media using independent component analysis: theory and simulation," J. Biomed. Opt. **10**, 051705 (2005).
8. M. Xu, M. Alrubaiee, S. K. Gayen, and R. R. Alfano, "Three-dimensional localization and optical imaging of objects in turbid media using independent component analysis," Appl. Opt. **44**, 1889-1897 (2005).
9. M. Xu, M. Alrubaiee, S. K. Gayen, and R. R. Alfano, "Optical diffuse imaging of an *ex vivo* model cancerous human breast using independent component analysis," IEEE J. Sel. Top. Quantum Electron. **14**, 43-49 (2008).
10. P. C. Hansen, "Analysis of discrete ill-posed problems by means of the L-curve," SIAM Rev. **34**, 561-580 (1992).
11. W. Cai, S. K. Gayen, M. Xu, M. Zevallos, M. Alrubaiee, M. Lax, and R. R. Alfano, "Optical tomographic image reconstruction from ultrafast time-sliced transmission measurements," Appl. Opt. **38**, 4237-4246 (1999).
12. E. A. Marengo, F. K. Gruber, and F. Simonetti, "Time reversal MUSIC imaging of extended targets," IEEE Trans. Image Process. **16**, 1967-1984 (2007).
13. S. R. Arridge, "Optical tomography in medical imaging," Inverse Probl. **15**, R41-R93 (1999).

14. S. R. Arridge, and W. R. B. Lionheart, "Non-uniqueness in diffusion-based optical tomography," Opt.Lett. **23**, 882-884 (1998).

Chapter 6

Fluorescence imaging using time reversal optical tomography and non-negative matrix factorization

6.1. Introduction

Near-infrared (NIR) fluorescence imaging is emerging as a promising modality for early detection of cancer for a variety of reasons [1-13]. Fluorescence signals are generally noninvasive, and have the intrinsic potential to provide molecular information about biological tissues and changes in significant physiological parameters associated with the onset and progression of disease. Fluorescence imaging is characterized by higher detection sensitivity and specificity, as well as, higher target-to-background ratio and spatial resolution than absorption and scattering contrast-based optical imaging approaches. The problem of limited tissue depth penetration may be considerably resolved by operating in the NIR spectral range of 700 – 1000 nm. Development of target-specific exogenous contrast agents holds the promise for tumor detection and characterization with high specificity. Much recent effort has gone into the development of fluorescent contrast agents, such as, dyes [2, 7], nanoparticles [3], and molecular beacons [4]. Concomitant developments have taken place in imaging instrumentation and numerical algorithms for image reconstruction [5-13]. These advances have culminated in contrast-enhanced fluorescence tomography approaches that are used more often for *in vivo* studies on animal models[5, 7, 9] than for human subjects[6, 11] or realistic phantoms.[8, 10, 11].

In this chapter, we report on two fluorescence tomography approaches. One is the extension of time reversal optical tomography (TROT) [14] to fluorescent targets embedded in a turbid

medium, where, the contrast is based on the difference in fluorescence between the target and the intervening medium. We refer to it as *fluorescence* TROT. We build on the TROT formalism introduced in Chapter 2 for locating small absorptive and scattering targets. TROT combines the methodology of time reversal (TR) imaging[15] with multiple signal classification (MUSIC),[16] a subspace based processing methodology to locate unknown targets from measurements using multiple probes. We demonstrate that with a nominal modification of experimental arrangement fluorescence TROT and transillumination TROT measurements can be carried out in consecutive runs providing complementary approaches to target detection and localization. [14]

The other approach is based on non-negative matrix factorization (NMF) [17], which is the extension of the NMF decomposition approach introduced in Chapter 4 to fluorescent targets. The NMF based fluorescence tomography approach treats detecting and locating targets within a turbid medium (such as, tumors inside human breast) as a blind source separation (BSS) problem [18], and seeks a solution based on non-negative matrix factorization (NMF) [17, 19]. BSS is a general problem in information theory that involves retrieval of "component" signals from measured signals. The measured signals are weighted mixtures of the component signals contributed by the targets ("blind sources") and may be expressed as:

$$X = AS, \tag{6.1}$$

where rows of X represent the measured mixed signals, rows of S represent the component signals, and A is the mixing matrix.

Fig. 6.1 schematically illustrates the measurement scheme of the proposed fluorescence tomography approach for a slab sample that consists of fluorescent targets embedded in a highly scattering turbid medium. The scheme uses multi-source illumination of a part of the sample ("*source plane*") by excitation light of wavelength λ_x and multi-detector acquisition of the induced fluorescence signals of wavelength λ_m that emerge from the opposite face ("*detector plane*"). The excitation light beam incident

at a point on the source plane diffusely transits through the sample and induces the embedded targets to fluoresce. Fluorescence from the targets diffusely transits through the sample and gives rise to a two-dimesional (2-*D*) spatial intensity distribution of fluorescence signal on the detector plane, which is recorded by a multiple-detector arrangement. Similar signals are recorded for excitation beam incident on other points on the source plane. We realize the multi-source illumination scheme by step-scanning the sample across the excitation light beam in a two-dimensional (2-*D*) array of grid points, and implement the multi-detector signal acquisition scheme by imaging the detector plane onto the sensing element of a charge coupled device (CCD) camera with every pixel acting as a detector. Every recorded fluorescence signal is a weighted mixture of component signals from the fluorescent targets. Such a multi-source probing and multi-detector siganl acquisition culminates in a robust data set for retrieving target information.

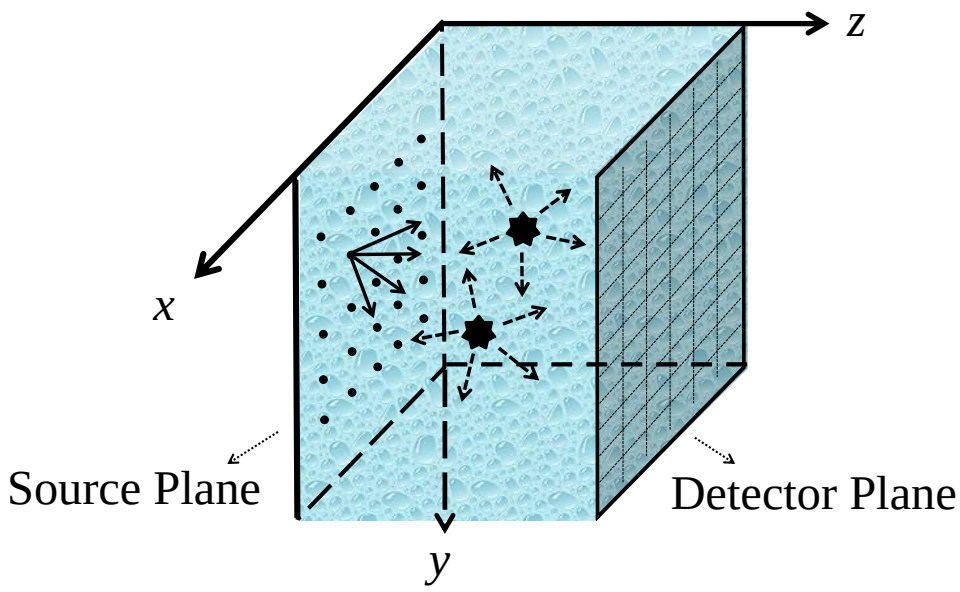

Fig. 6.1. Multi-detector acquisition of fluorescence (wavelength, λ_m) intensity distribution on the detector plane following multi-source illumination (wavelength, λ_x) of the source plane of the sample.

The task of retrieving target information from these mixtures is a BSS problem and here we adapt NMF for the task. The non-negativity constraint makes NMF particularly suited for fluorescence tomography because in principle fluorescence signal appears on a dark background, and in common practice measured on a weak background, and hence is expected to be intrinsically positive.

We test the efficacy of the *fluorescence* TROT and the NMF-based fluorescence tomography using experimental data on a "human breast-simulating phantom", that is, a sample whose size and key optical properties are similar to the average values of those parameters for a typical human breast.

6.2. Theoretical formalism

6.2.1. Fluorescence TROT

Fluorescence TROT uses a multi-source illumination and multi-detector signal acquisition scheme to acquire multiple angular views of the sample that consists of a target (or, targets) embedded in a turbid medium, such as, a tumor in human breast. Excitation beam of light sequentially illuminates an array of N_s source points on the source plane of the sample realizing multiple-source probing. Once any of these N_s points ("excitation sources") is illuminated the diffusely propagating excitation beam of wavelength λ_x induces the targets ("fluorescent sources") embedded in the medium to fluoresce. The fluorescent signal at the opposite boundary ("detector plane") is recorded by N_d detectors. The focus is to detect the target(s) and retrieve three-dimensional (3-*D*) location information.

Light propagation in a highly scattering medium with embedded fluorescent targets excited by an external light source is approximately described by coupled diffusion equations at the excitation wavelength (λ_x) and emission wavelength (λ_m) [20, 21]:

$$-\nabla\cdot\left[D_x(\mathbf{r},\omega)\nabla\phi_x(\mathbf{r},\omega)\right]+\left[\mu_{a_x}(\mathbf{r},\omega)-i\,\omega/c\right]\phi_x(\mathbf{r},\omega)=\delta(\mathbf{r}-\mathbf{r}_s), \tag{6.2a}$$

$$-\nabla\cdot\left[D_m(\mathbf{r},\omega)\nabla\phi_m(\mathbf{r},\omega)\right]+\left[\mu_{a_m}(\mathbf{r},\omega)-i\omega/c\right]\phi_m(\mathbf{r},\omega)=\phi_x(\mathbf{r},\omega)\gamma(\mathbf{r})/\left[1-i\omega\tau(\mathbf{r})\right], \quad (6.2b)$$

where the subscripts *x* and *m* denote parameters pertaining to excitation wavelength and emission wavelength, respectively; ω is the modulation angular frequency; $\phi_x(\mathbf{r},\omega)$ and $\phi_m(\mathbf{r},\omega)$ are photon densities at position $\mathbf{r}$; μ_{a_x} and μ_{a_m} are absorption coefficients of the medium; $D_x(\mathbf{r}, \omega)$ and $D_m(\mathbf{r}, \omega)$ are the diffusion coefficients of the medium; $\gamma(\mathbf{r}) = \eta\mu_{a_f}(\mathbf{r})$ is the fluorescent yield of the fluorophore in the target; and η, μ_{a_f} and $\tau(\mathbf{r})$ are the quantum yield, absorption coefficient at the excitation wavelength, and fluorescence lifetime of the fluorophore, respectively.

Assuming fluorescent targets are localized, that is, the j^{th} target is contained in volume V_j centered at $\mathbf{r}_j$, the fluorescence signal under illumination by a point source of unit power at $\mathbf{r}_s$ is given by,

$$U_m(\mathbf{r}_d,\mathbf{r}_s,\omega)=\sum_j G_m(\mathbf{r}_d,\mathbf{r}_j,\omega)\,f_j(\omega)G_x(\mathbf{r}_j,\mathbf{r}_s,\omega), \quad (6.3)$$

where $G_x(\mathbf{r}_j, \mathbf{r}_s, \omega)$ is a Green's function that describes the propagation of the excitation light of wavelength λ_x from the source at $\mathbf{r}_s$ to the j^{th} target contained in volume V_j centered at $\mathbf{r}_j$; $G_m(\mathbf{r}_d, \mathbf{r}_j, \omega)$ is a Green's function that describes the propagation of the fluorescence of wavelength λ_m from j^{th} target to the detector at $\mathbf{r}_d$;

$$f_j(\omega) = \gamma(\mathbf{r}_j)c_m V_j / \left[1-i\omega\tau(\mathbf{r}_j)\right], \quad (6.4)$$

is the fluorescence strength of the j^{th} target, where γ is the fluorescence yield, c_m is the speed of light in the medium, and τ is the fluorescence lifetime..

The fluorescence signal can be re-written in a matrix form as

$$X=\sum_j g_d(\mathbf{r},\omega)\,f_j(\omega)g_s{}^T(\mathbf{r},\omega), \quad (6.5)$$

where $g_s(\mathbf{r}, \omega) = \{G_x(\mathbf{r}, \mathbf{r}_s, \omega\}^T$ and $g_d(\mathbf{r}, \omega) = \{G_m(\mathbf{r}_d, \mathbf{r}, \omega\}^T$, (the superscript ^{T} denotes transpose) are Green's function vectors. X describes the diffuse propagation of the excitation light beam of wavelength, λ_x, from the sources through the medium to the targets, and then the propagation of fluorescence of wavelength, λ_m from the targets to the detectors. It also holds that X^T describes the virtual process of fluorescent light propagation from the positions of detectors to the targets, and then the propagation of the excitation light of wavelength λ_x, from the positions of the targets to the sources. A time reversal matrix $T_{SDDS} = X^{\dagger}X$ [$T_{DSSD} = (X^T)^{\dagger}X^T = X^*X^T$] in frequency domain is then constructed, where the superscript † denotes Hermitian conjugate, or $T_{SDDS} = X^TX$ ($T_{DSSD} = XX^T$) when using the continuous wave (CW) illumination, *i.e.* $\omega = 0$. T_{SDDS} and T_{DSSD} describe two virtual time-reversed light propagations between the sources and detectors through targets, as described in Section 2.2.3. In Section 2.2.3, the light propagating between sources and targets and the light between targets and detectors have the same wavelengths, while here they are at different wavelengths, namely, one at excitation wavelengths, and the other at emission wavelengths. T_{DSSD} and T_{SDDS} have eigenvectors $\{u_k, k = 1, \ldots, N_d\}$ and $\{v_l, l = 1, \ldots, N_s\}$, respectively, with a common set of eigenvalues $\{\mu_j, j = 1, \ldots, \min(N_s, N_d)\}$, where N_s and N_d are numbers of sources and detectors, respectively [14]. If the fluorescent targets are well resolved, the eigenvalues are proportional to squared fluorescence strengths of the targets,

$$\mu_j = \left| f_j \right|^2 \left\| g_d(\mathbf{r}_j, \omega) \right\|^2 \left\| g_s(\mathbf{r}_j, \omega) \right\|^2; \tag{6.6}$$

otherwise, they are linear combinations of the fluorescence strengths, similar to what is the case for absorptive and scattering targets.[14]

The eigenvectors are separated into signal and noise subspaces using an *L*-curve method with an eigenvalue threshold ε.[22] More details of the *L*-curve method has been provided in Section 3.2. The locations of targets are poles in the MUSIC pseudo spectrum [14]

$$P_d\left(\boldsymbol{X}_p,\omega\right)=1\Big/\sum_{\mu_j<\varepsilon}\left|u_j{}^T\,\frac{g_d\left(\boldsymbol{X}_p,\omega\right)}{\left\|g_d\left(\boldsymbol{X}_p,\omega\right)\right\|}\right|^2, \tag{6.7a}$$

associated with the detector plane, where $\boldsymbol{X}_p$ runs over positions of all voxels in the sample. A similar pseudo spectrum for the source plane $P_s(\boldsymbol{X}_p, \omega)$,

$$P_s\left(\boldsymbol{X}_p,\omega\right)=1\Big/\sum_{\mu_j<\varepsilon}\left|v_j{}^T\,\frac{g_s\left(\boldsymbol{X}_p,\omega\right)}{\left\|g_s\left(\boldsymbol{X}_p,\omega\right)\right\|}\right|^2, \tag{6.7b}$$

or for both detector and source planes,

$$P(\boldsymbol{X}_p,\omega)=1\Big/\sum_{\mu_j<\varepsilon}\left(\left|u_j{}^T\,\frac{g_d\left(\boldsymbol{X}_p,\omega\right)}{\left\|g_d\left(\boldsymbol{X}_p,\omega\right)\right\|}\right|^2+\left|v_j{}^T\,\frac{g_s\left(\boldsymbol{X}_p,\omega\right)}{\left\|g_s\left(\boldsymbol{X}_p,\omega\right)\right\|}\right|^2\right), \tag{6.7c}$$

may also be used to retrieve the target position.

From Eq. (6.5), the fluorescence strengths of the targets may then be retrieved by unmixing the data matrix using Green's functions associated with the retrieved positions of the targets, as introduced in Chapter 3,

$$diag(f_1, f_2,\cdots)=\{g_d(\boldsymbol{r}_1,\omega), g_d(\boldsymbol{r}_2,\omega),\cdots\}^{-1}X\{\{g_s(\boldsymbol{r}_1,\omega), g_s(\boldsymbol{r}_2,\omega),\cdots\}^T\}^{-1}, \tag{6.8}$$

where the data matrix could be rank-reduced data matrix as introduced in Chapter 3.

In this work, we used the pseudo spectrum, P_d associated with the detector plane because: (a) the images naturally reside in the co-ordinate system based on the field of view of the charge-coupled device (CCD) camera (*detectors*) making data analysis easier; and (b) the use of many more detectors than sources in our experimental arrangement provides a more robust data set for

superior noise-resistant and artifact-tolerant reconstruction in the detector plane than the source plane. We set $\omega = 0$ as a CW laser beam was used in the experiment.

6.2.2. NMF-based Fluorescence Tomography

The formalism considers this fluorescence signal to be a weighted mixture of signals arriving from the embedded targets. A different signal is obtained when another source point is illuminated. The fluorescence signal measured by the detector at $\boldsymbol{r}_d$ for illumination of the source point at $\boldsymbol{r}_s$ may be expressed as the following form of Eq. (6.1):

$$x\left(\boldsymbol{r}_d, \boldsymbol{r}_s\right) = \sum_j a_j(\boldsymbol{r}_d) s_j(\boldsymbol{r}_s), \tag{6.8}$$

where $a_j(\boldsymbol{r}_d)$ is the mixing vector and $a_j(\boldsymbol{r}_d)s_j(\boldsymbol{r}_s)$ represents the contribution of the j^{th} target to the signal [10, 23] and the sum is over all the targets ("fluorescent sources"). NMF retrieves $s_j(\boldsymbol{r}_s) = [s_j(\boldsymbol{r}_{s1}), s_j(\boldsymbol{r}_{s2}), \ldots, s_j(\boldsymbol{r}_{sN_s})]$ and $a_j(\boldsymbol{r}_d) = [a_j(\boldsymbol{r}_{d1}), a_j(\boldsymbol{r}_{d2}), \ldots, a_j(\boldsymbol{r}_{dN_d})]^T$ assuming those to be non-negative, where superscript (^{T}) denotes transpose. Commonly used NMF algorithms include the multiplicative update method [17] and alternating least squares (ALS) method [24, 25]. We implement the ALS method that uses alternating least squares steps to estimate *A* (or *S*), and use that estimate to optimize *S* (or *A*), and keep repeating the alternative steps until the desired optimization is obtained. Non-negativity is ensured by setting any negative element of *A* or *S* equal to 0. We used an available NMF toolbox [26] to carry out the computation.

Comparing Eq. (6.3) and Eq. (6.8) we find,

$$s_j\left(\boldsymbol{r}_s\right) = \alpha_j G_x\left(\boldsymbol{r}_j, \boldsymbol{r}_s, \omega\right), \tag{6.9a}$$

and

$$a_j\left(\boldsymbol{r}_d\right) = \beta_j G_m\left(\boldsymbol{r}_d, \boldsymbol{r}_j, \omega\right), \tag{6.9b}$$

where α_j, β_j are scaling factors. One refers to $s_j(\boldsymbol{r}_s)$ and $a_j(\boldsymbol{r}_d)$ as non-negative component intensity distributions (NCIDs) on the source plane and detector plane, respectively, since those are proportional to the corresponding light intensity distributions and from reciprocity $G_x(\boldsymbol{r}_j, \boldsymbol{r}_s, \omega) = G_x(\boldsymbol{r}_s, \boldsymbol{r}_j, \omega)$. Since we used a slab sample in the experiment, the Green's functions to be used in above equations are those for slab geometry in the diffusion approximation assuming a uniform background medium, as detailed elsewhere [23, 27].

The task of retrieving the locations of the targets involves fitting of the NCIDs to the Green's functions, and we use the following least square fitting for the j^{th} target

$$\arg\min_{\alpha_j,\beta_j,\boldsymbol{r}_j}\{\sum_{\boldsymbol{r}_s}[\alpha_j^{-1}s_j(\boldsymbol{r}_s)-G_x(\boldsymbol{r}_j,\boldsymbol{r}_s,\omega)]^2+\sum_{\boldsymbol{r}_d}[\beta_j^{-1}a_j(\boldsymbol{r}_d)-G_m(\boldsymbol{r}_d,\boldsymbol{r}_j,\omega)]^2\}. \tag{6.10}$$

The fitting using Eq. (6.10) provides optimal estimates of the two scaling factors α_j and β_j and the location $\boldsymbol{r}_j$ of the j^{th} target. The fluorescence strength then is

$$f_j = \alpha_j \beta_j. \tag{6.11}$$

Another important consideration is the size of the targets. A back projection of $U_{m_j}(\boldsymbol{r}_d, \boldsymbol{r}_s, \omega)$ from the detection plane onto the "target plane" ($z = z_j$ plane) provides an estimate of the target size [10]. The fluorescence signal due to the j^{th} target can be approximated by [10]

$$U_{m_j}(\boldsymbol{r}_d, \boldsymbol{r}_s, \omega) = \int_{z=z_j} G_m(\boldsymbol{\rho}_d - \boldsymbol{\rho}, \omega)\chi_j(\boldsymbol{\rho})G_x(\boldsymbol{\rho} - \boldsymbol{\rho}_s, \omega)d\boldsymbol{\rho}, \tag{6.12}$$

where $\boldsymbol{\rho}_s$ and $\boldsymbol{\rho}_d$ are the lateral coordinates of the source and the detector, and the integration is over the $z = z_j$ plane. In the Fourier space $\chi_j(\boldsymbol{q})$ follows from Eq. (6.12) as,

$$\chi_j(\boldsymbol{q}) = \frac{U_{m_j}(\boldsymbol{q}-\boldsymbol{q}_s, \boldsymbol{q}_s, \omega)}{G_m(\boldsymbol{q}-\boldsymbol{q}_s, \omega)G_x^*(\boldsymbol{q}_s, \omega)}, \tag{6.13}$$

where $\boldsymbol{q}$ and $\boldsymbol{q}_s$ are the spatial frequencies on the x-y plane and * denotes complex conjugate. The inverse Fourier transform of $\chi_j(\boldsymbol{q})$ provides the cross-section image of the j^{th} target at the $z = z_j$ plane.

This NMF-based optical imaging approach may be realized with slab, cylindrical and other geometries; and time-resolved, frequency domain and continuous wave (CW) measurement schemes. Data collected in backscattering mode may be used as well. In this article, we focus on localization of targets with CW ($\omega = 0$) measurements in forward propagation mode.

6.3. Experimental Materials and Methods

The experimental arrangement for fluorescence imaging of targets in a turbid medium is shown schematically in Fig. 6.2. It used a multi-source sample excitation and multi-detector fluorescence signal acquisition scheme to acquire multiple angular views of the sample. The fluorescence light intensities were measured on the boundary of the medium by a two-dimensional detector array when an external point source (laser beam) scanned the other side of the medium.

The sample consisted of a 250 mm × 250 mm × 60 mm transparent plastic container filled with Intralipid-20% (Baxter, Product 2B6023) in water suspension in water as a slab of scattering medium. Separate experiments were carried out with one and two 4.2-mm-diameter × 10-mm cylindrical glass tubes filled with a solution of Indo-cyanine green (ICG) dye (Sigma-Aldrich, Product I2633) as fluorescent targets. In both cases, the target(s) was (were) embedded in the mid-plane (z = 30 mm) of the sample cell.

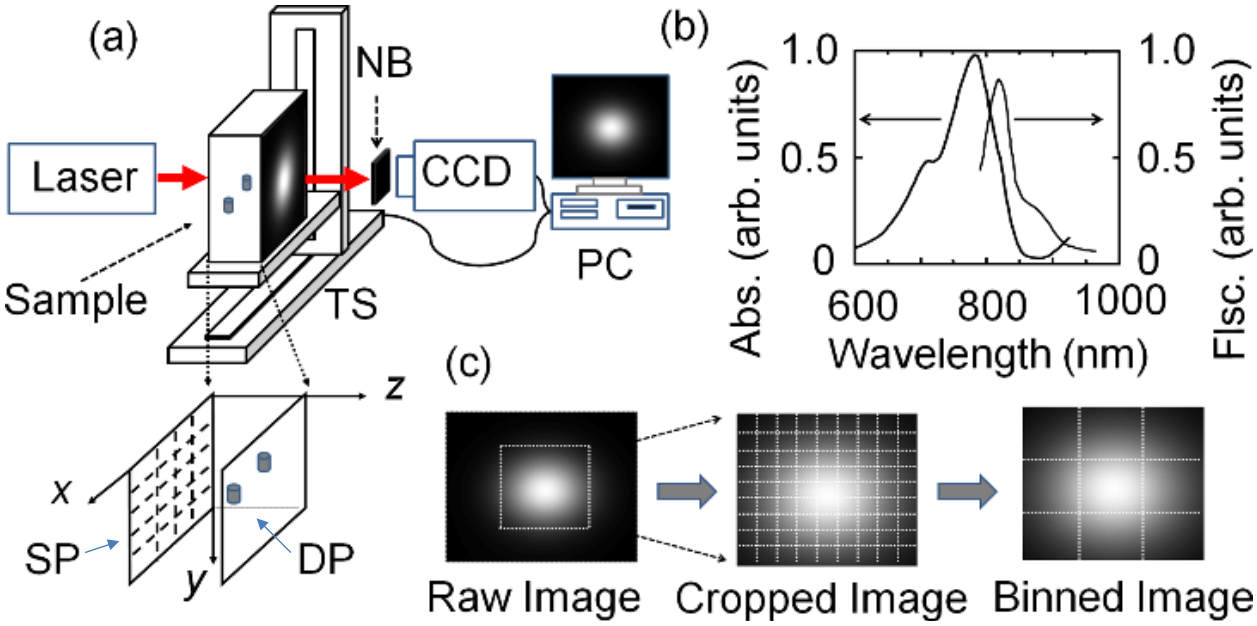

Fig. 6.2. (a) A schematic diagram of the experimental arrangement for imaging objects embedded in a turbid medium. [Key: NB = narrow band pass filter (830 nm), TS = translational stage, CCD = charge coupled device, PC = personal computer, SP = source plane, DP = detector plane] Inset (below) shows the 2-*D* array in the input plane that was scanned across the incident laser beam, and a typical raw image is shown in the PC monitor. (b) The absorption and fluorescence spectra of ICG in water. (c) A typical raw image detected by the CCD camera is cropped and binned.

The concentration of Intralipid-20% was adjusted [28] to provide a transport mean free path l_t of ~0.99 mm at λ_x = 790 nm, and 1.05 mm at λ_m = 830 nm. More details about Intralipid suspension have been presented in Section 2.5.1. We chose the optical properties and the thickness (60 mm) of the sample cell to emulate average values of those parameters for a compressed human breast and the size of the target to resemble that of small tumors. The ICG concentration in the targets was 1 μM which provided an absorption coefficient of $0.027 mm^{-1}$ at 790 nm [29-32, 33]. The absorption coefficient of ICG was measured in aqueous solution. The absorption spectrum, shown in Fig. 6.3(a), spans 500 - 860 wavelength range with a peak at 780 nm. The fluorescence spectrum for 620-nm excitation is shown in Fig. 6.3(b). It spans the 790 -

966 nm wavelength range and peaks around 815 nm. The quantum yield of ICG is 0.016 [33]. The Intralipid-20% concentration in the target was same as that of the background to ensure that both had the same scattering characteristics. The targets were placed in the mid-plane of the sample cell and their known locations appear in Table 6.1. The targets were treated as fluorescent targets for the measurements using emitted light in a narrow band around 830 nm, and as absorptive targets for transillumination measurements using light at the excitation wavelength of 790 nm.

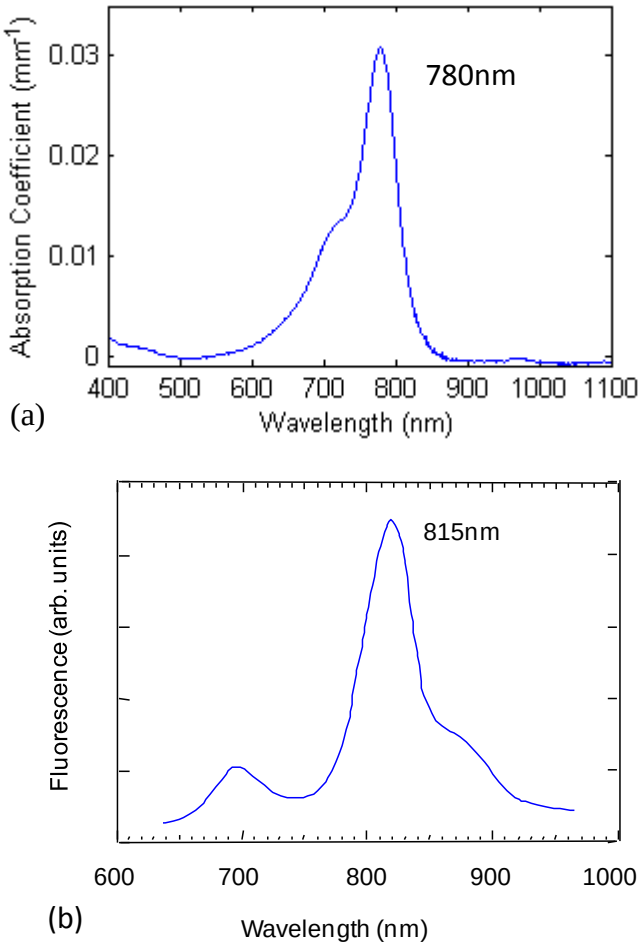

Fig. 6.3. Room-temperature (a) absorption spectrum, and (b) fluorescence spectrum of 1μM ICG aqueous solution.

A computerized translation stage (Aerotech Model ATS02015-M-40L with Unidex 511 controller) scanned the sample across a 790-nm, 100-mW, CW diode-laser (Power Technology, Model IQ1C100G2) beam in a two-dimensional (*x*-*y*) array of 15 × 11 grid points, with a step size of 5 mm to realize the multi-source probing scheme. We refer to the 250-mm × 250-mm sample surface that faced the laser beam as the *source plane*, and the opposite face as the *detector plane*. The forward-propagating fluorescence (or, transmitted) signal was collected by imaging the detector plane onto the sensing element of a 1024 × 1024 pixels cooled CCD camera (Photometrics CH350) using a 60-mm focal-length camera lens. Each illuminated 24-μm pixel of the CCD camera served as a detector. For fluorescence imaging, the signal was passed through a narrow-band interference filter centered at 830 nm (FWHM 10 nm, 50% transmission) to effectively block the scattered 790-nm pump light. The integration time is 60 seconds. An interfaced personal computer (PC) controlled the sample scanning, as well as, data acquisition and storage operations. The PC recorded the raw images for each scan position, and stored those for subsequent analysis. Each illuminated pixel of the CCD camera could be regarded as a detector. A typical image, which is a 2-*D* intensity distribution, is shown in the left frame of Fig. 6.2(c). The same arrangement then acquired another set of images with the narrow band filter removed. The camera integration time is 2.3 seconds. Since the diffusely transmitted 790-nm signal was ~1500 times stronger than the fluorescence signal, we considered this later set of images to be transillumination images, and used those in two different ways. First, analysis of these transillumination images provided estimate of the average value of $\kappa_x = \sqrt{\mu_{a_x} / D_x}$ for the excitation light. The values of these optical parameters of Intralipid-20% suspension in water happened to be very close for the excitation beam and fluorescence light. Second, the images provided a complementary set of raw data for obtaining information about the targets based on

their absorption contrast. The experimental arrangement thus enables correlated imaging and retrieval of target location using both fluorescence and transmission measurements.

6.4. Analysis

The transmission images were analyzed to estimate the average value of $\kappa = \sqrt{3\mu_a \mu_s'}$ (where μ_a and μ_s' are the absorption and reduced scattering coefficients at 790 nm, respectively). The values of these optical parameters of Intralipid-20% suspension in water happened to be very close for excitation and fluorescence wavelengths.

From each fluorescence image, a region of interest was cropped out and then every 5×5 pixels in the cropped image were binned to one pixel to enhance the signal-to-noise ratio. The fluorescence data was normalized [8, 21, 34] using $U/I = \phi_0/I_0$ to remove the contribution of unaccounted factors (such as, light-source strength, collection geometry, attenuation in the optical filters and components etc.), where U and I were the computed and measured fluorescence signals with targets inside the background medium, respectively; and ϕ_0 and I_0 were the computed and measured transmitted signals at the excitation wavelength through the background medium "without" targets inside. As it is not practical to remove the target in real life situations, I_0 was estimated as an average of all images acquired at different scan positions [14]. The data matrix, $X = \{x(\boldsymbol{r}_d, \boldsymbol{r}_s)\}$ was then constructed using the normalized fluorescence signals for all scan positions. One column of X corresponds to signal accumulated for one scan position.

For comparison, the transmission data were also analyzed using both approaches as detailed in Chapter 2 [14, 19]. In that case, the targets were treated to be absorptive, and the contrast was mainly due to higher absorption of the excitation beam by the target(s). It should be noted that

absorption measurement involves changes in the intensity of the excitation beam, and consequently the TROT and NMF analysis used the difference images between the raw transmission images and a reference image for the background medium. The background image was an average of images acquired at all scan positions.

As was done for the fluorescence signal, the transmission data were also normalized using $\Delta\phi/\Delta I = \phi_0/I_0$ [21, 35, 36], where ΔI is the measured perturbation in I_0 due to the presence of targets; and $\Delta\phi$ is the computed perturbation in ϕ_0. Since the targets were more absorptive than the background, $\Delta\phi$ was intrinsically negative, so we used $-\Delta\phi$ for constructing the data matrix to satisfy the non-negativity constraint of NMF [19].

Then the data matrix generated using either fluorescence or transmission data is then used for the further analysis using TROT or NMF.

6.4.1. Fluorescence TROT

A TR matrix was generated using the data matrix X. An eigenvalue equation of the TR matrix was then solved. The pseudo spectrum P_d was calculated over all voxels in the sample space using one dominant eigenvector for the one-target experiment, and two dominant eigenvectors for the two-target experiment, using Eq. (6.7a). The voxel size was 0.77 mm × 0.77 mm × 1 mm. Three-dimensional tomographic pseudo images were generated using the pseudo spectrum. The positions of target(s) were determined using the maxima in the pseudo spectrum. The fluorescence strengths of the targets were calculated by unmixing the data matrix using Eq. (6.8).

6.4.2. NMF-based fluorescence tomography

The acquired data were processed using the following steps.

(i) NMF decomposition of the data matrix using ALS algorithm [24, 25] was carried out. The fluorescence signal due to each target and the mixing vector, $s_j(\boldsymbol{r}_s)$ and $a_j(\boldsymbol{r}_d)$ were retrieved, which are NCIDs on the source and detector planes, respectively.

(ii) NCIDs $s_j(\boldsymbol{r}_s)$ and $a_j(\boldsymbol{r}_d)$ were then fitted to Green's functions $G_x(\boldsymbol{r}_j, \boldsymbol{r}_s)$, and $G_m(\boldsymbol{r}_d, \boldsymbol{r}_j)$, respectively, using Eq. (6.10) to find the positions of the targets.

(iii) The transmission images were then analyzed using the NMF formalism and similar steps to those above for the fluorescent case.

(iv) The NMF-generated NCIDs from both fluorescence and transmission data were used to calculate the cross-section images of the targets using the back-projection algorithm. Because of the diffuse nature of light propagation in the turbid medium, the estimated cross section is expected to be considerably larger than the actual target size. The calculation of $\chi_j(\boldsymbol{q})$ using Eq. (6.13) employed Tikhonov regularization [37], with a modified *L*-curve method [22] to determine the optimal regularization parameter. However, this optimization is a tradeoff between obtaining a closer estimate of target cross section and fewer artifacts in the back-projection image. Since the positions of the targets were obtained from the previous steps, any artifacts cropping up in the back-projection process could be readily identified from their positions. So, instead of using the "corner" of the *L*-curve to find the optimal regularization parameter, we settled for a lower regularization using the criterion that the highest artifact peak reaches ~50% of the target peak to improve the size estimate of the cross-section images. The full width at half maximum (FWHM) of the spatial profile of the cross-section image was used as an estimate of the target size.

6.5. Results

6.5.1. Single target

6.5.1.1. *Fluorescence TROT*

The three-dimensional pseudo images were generated. The single target was detected, and the position of the target was determined using the peak in the pseudo spectrum and listed in Table 6.1, with comparison to the actual position. The image at the retrieved *z*-coordinate of the target position (z = 30.5 mm) plotted using the pseudo spectrum is shown in Fig. 6.4(a). Further calculation showed that when more eigenvectors were used, the pseudo spectrum still clearly detected one single target. The determination of the number of targets is not sensitive to the choice of the threshold in the eigenvalue spectrum.

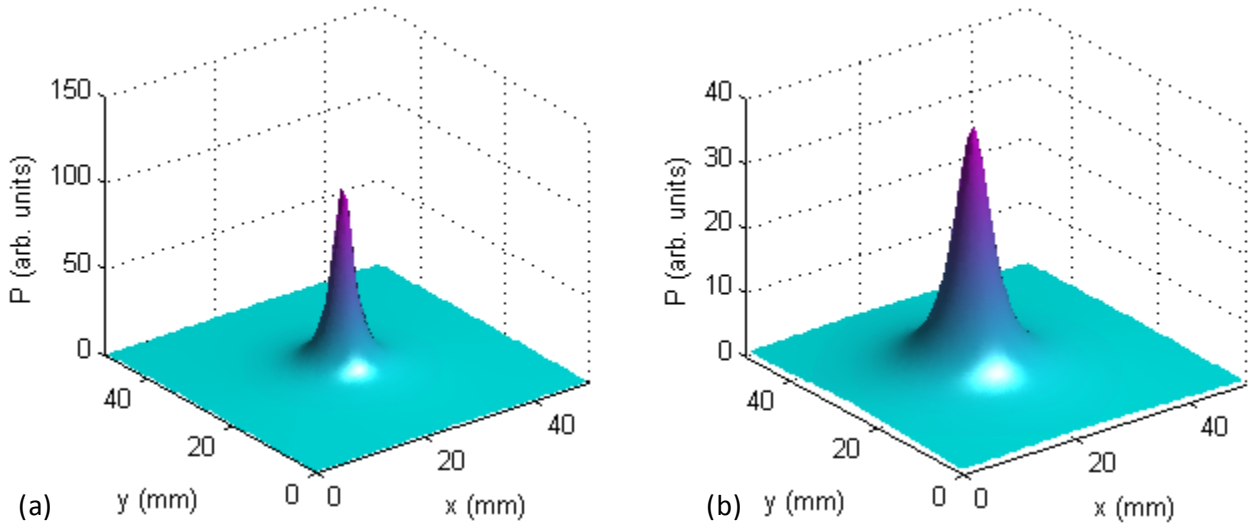

Fig. 6.4. TROT-reconstructed image at z = 30.5 mm using *fluorescence* data is shown in (a), and at z = 29.5.mm using transmission data shown in (b).

Following Eq. (6.4), the actual fluorescence strengths f of the targets was 13.5 mm^3/ns (*i.e.* m^3/s). Using Green's functions corresponding to the retrieved target positions along with Eq. 6.6, the fluorescence strengths of the target was directly retrieved to be 5.3 mm^3/ns, with 60.7% error.

Since the fluorescence signal decayed by a factor of 2.6 during the experiments for the fluorescence and transmission measurements, the fluorescence strength was corrected using a multiplication factor 2.6 and retrieved to be 13.8 mm^3/ns, with 2.2% error.

Table 6.1. Known and TROT-retrieved target positions

	Known	Retrieved	
		Fluorescence	Transmission
Position [x, y, z (mm)]	25.1, 25.7, 30.0	24.1, 25.6, 30.5	21.8, 25.6, 29.5
Error [Δx, Δy, Δz (mm)]	-	1.0, 0.1, 0.5	3.3, 0.1, 0.5
FWHM [δx, δy (mm)]	-	3.8, 3.8	6.9, 6.9

The transmission data was then analyzed for comparison. The target was also detected and its retrieved location is listed in Table 6.1 for comparison. The image of the target at z = 29.5 mm is shown in Fig. 6.4(b).

As shown in Table 6.1, the location of the target retrieved from the fluorescence data is in excellent agreement with the known position, and is consistent with that retrieved using transmission data. The pole of the pseudo image using fluorescence data is sharper than that obtained using transmission data. The FWHM of the pole in both x and y directions is 3.8 mm in the fluorescence-TROT image and 6.9 mm in the transmission-TROT image.

The absorption strength of the target was also retrieved using the transmission data similarly. The known value of the absorption strength of the targets is 842.8 mm^3/ns. The retrieved value for the target was 749.1 mm^3/ns, with 11.1% error.

The retrieved fluorescence and absorption strengths of the target are shown in Table 6.2 with comparison to the known values.

Table 6.2. TROT retrieved optical strength of the target

Measurement Mode	Known strength (mm^3/ns)	Retrieved strength (mm^3/ns)	Error (%)
Fluorescence	13.5	13.8	2.2
Transmission	842.8	749.1	11.1

6.5.1.2. *NMF-based fluorescence tomography*

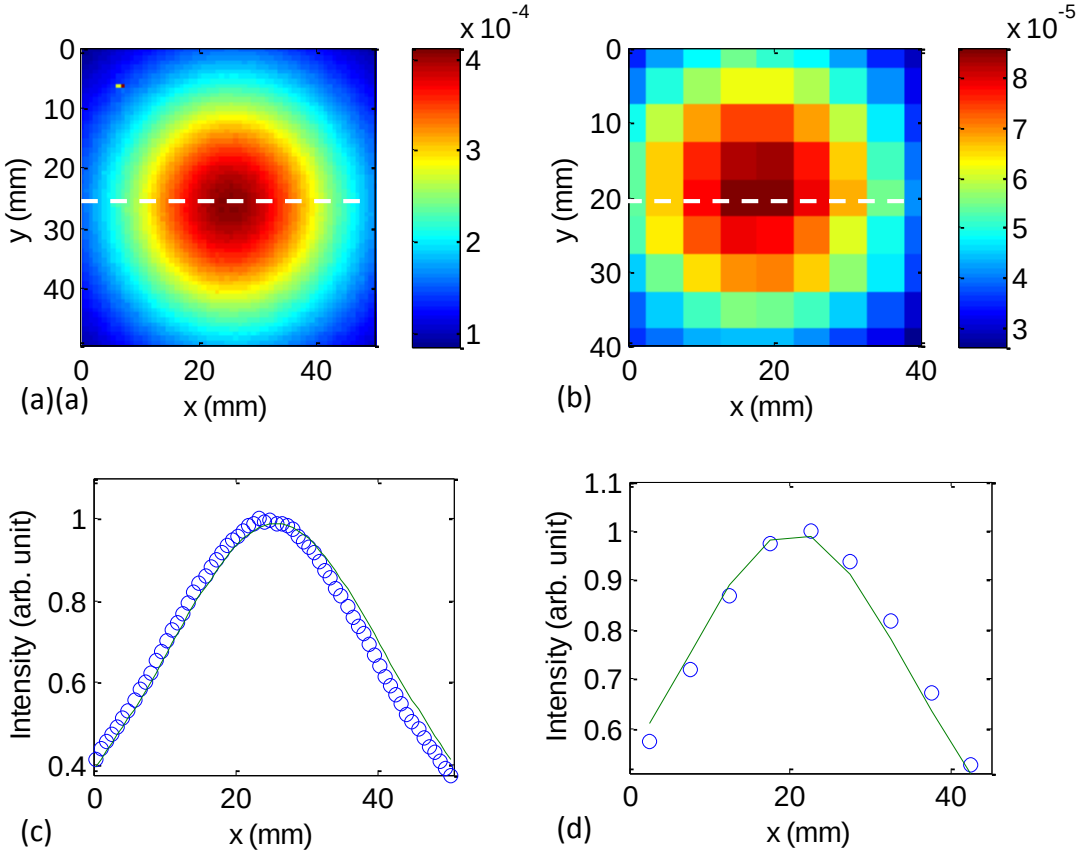

Fig. 6.5. (a) and (b) are NCIDs retrieved from the fluorescence data corresponding to the target on the detector and source planes, respectively; (c) and (d) are least squares fits to the spatial profiles along the white dashed lines in (a) and (b), respectively.

The data matrix was then analyzed using NMF-based approach. The NCIDs of the target on the detector and source planes are shown in Fig. 6.5(a) and 6.5(b). The target position is determined by fitting the NCIDs to Green's functions using Eq. (6.10). The fitted profiles in the NCIDs through the target in the x direction on the detector and source planes are shown in Fig. 6.5(c) and 6.5(d), respectively. The retrieved position is shown in Table 6.3.

Table 6.3. Known and NMF retrieved target positions

Measurement Mode	Known positions [x, y, z (mm)]	Retrieved positions [x, y, z (mm)]	Error [Δx, Δy, Δz] (mm)
Fluorescence	25.1, 25.7, 30.0	25.5, 26.4, 29.9	0.4, 0.7, 0.1
Transmission		22.0, 26.9, 33.7	3.1, 1.2, 3.7

The scaling factors α and β were generated in the least squares fitting using Eq. (6.10), and the fluorescence strength was estimated using Eq. (6.11) to be 3.7 mm^3/ns. With the fluorescence decay considered, the corrected fluorescence strength is 9.6 mm^3/ns, with 28.9% error. The retrieved fluorescence strength is listed in Table 6.4, with comparison to the known value.

Table 6.4. Known and NMF-retrieved optical strengths of the targets

Measurement Mode	Known strength (mm^3/ns)	Retrieved strength (mm^3/ns)	Error (%)
Fluorescence	13.5	4.1	28.9
Transmission	733.1	509.3	30.5

A cross-section image at the z-coordinate (z = 29.9 mm) of the target position was generated using the back-projection method. The modified L-curve method was used with a lower

regularization instead of the regularization at the "corner" of the *L*-curve, as introduced in Chapter 4. The cross-section image is shown in Fig. 6.6(a). The full-width-at-half-maximum (FWHM) of the profile through the maximum in the image is used to estimate the dimension of the target, as shown in Fig. 6.6(b). The edges of in the image shows very intense values due to the boundary effect. Therefore the boundary has been left out in the profiles. The FWHM were found to be 13.4 mm in both *x* and *y* directions. The FWHM is close to the actual dimension of the target in the *y* direction, with ~ 30% error. But the FWHM in the *x* direction is about 3 times of the actual dimension of the target (4.2 mm). Due to the diffusive nature of light transmission, 4.2 mm is considered to be small, and it is hard to detect its boundary. The retrieved FWHMs are shown in Table 6.5.

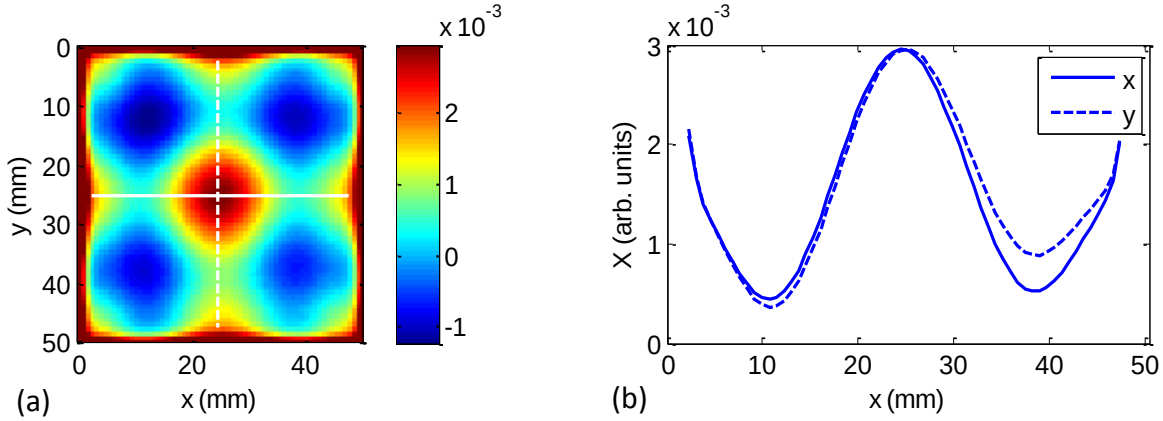

Fig. 6.6. (a) is the cross-section images at the z = 29.9 cm plane. (b) is the spatial profiles of the cross-sectiona image along the *x* and *y* directions shown by the white lines.

The transmission data were similarly analyzed. The NCIDs and the Green's function fits of the profiles in the NCIDs are shown in Fig. 6.7. The retrieved target position is also shown in Table 6.3. The absorption strength of the target was estimated from the transmission data to be 509.3 mm^3/ns, with 30.5% error. The retrieved absorption strength is also listed in Table 6.4, with comparison to the known value.

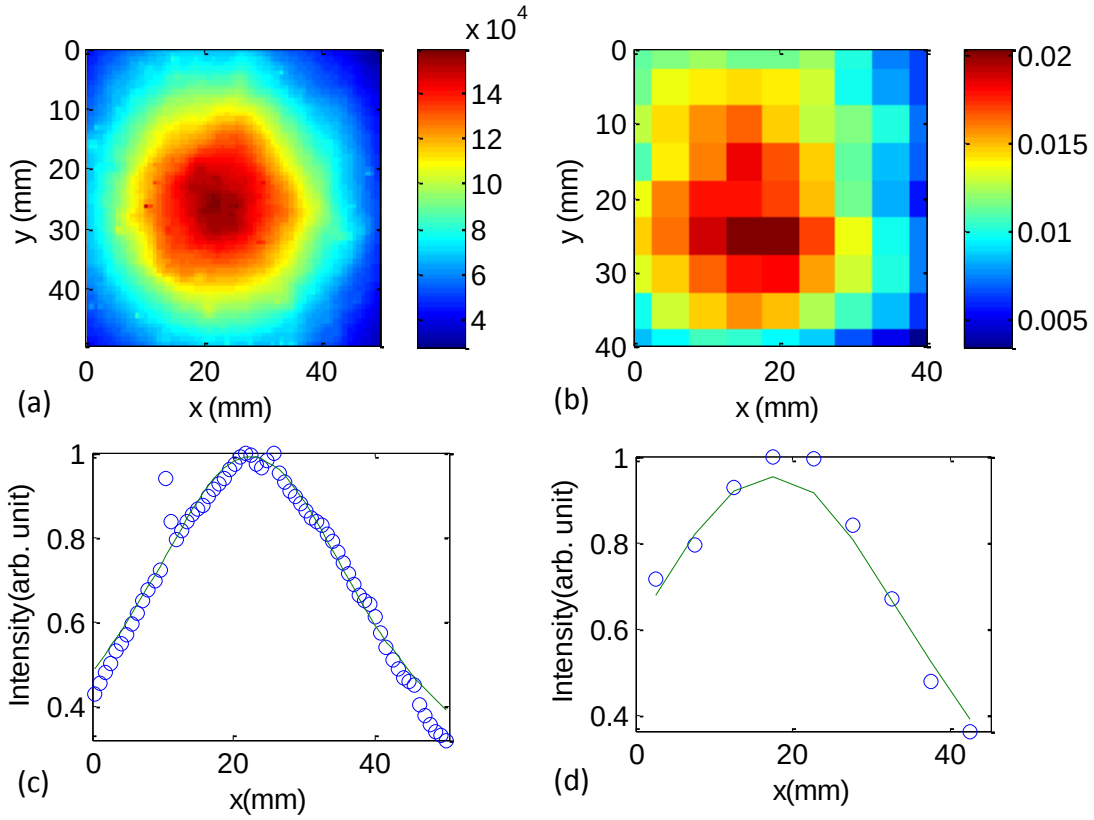

Fig. 6.7. (a) and (b) are NCIDs retrieved from the transmission data corresponding to the target on the detector and source planes, respectively; (c) and (d) are least squares fits to the spatial profiles along the white dashed lines in (a) and (b), respectively.

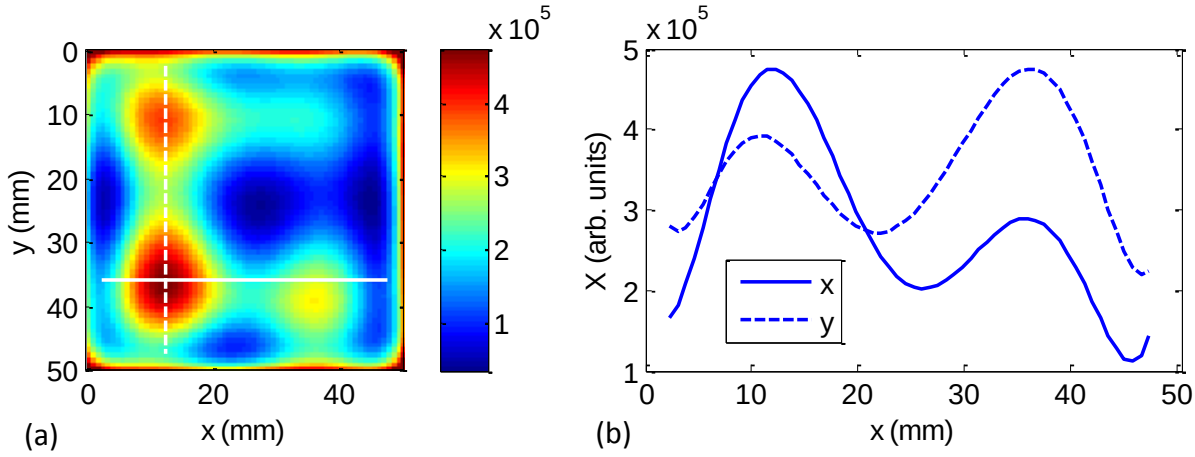

Fig. 6.8. (a) is the cross-section images at the z = 33.7 cm plane. (b) is the spatial profiles of the cross-sectiona image along the x and y directions shown by the white lines.

Table 6.5. Estimated target size using FWHM of the cross-section image of the targets

Measurement Mode	Known size [δx, δy] (mm)	Retrieved size [δx, δy] (mm)
Fluorescence	4.2, 10	13.4, 13.4
Transmission		12.3, 13.0

The cross-section image with low regularization was also generated using back-projection, as shown in Fig. 6.8. In the cross-section image, the target position shifted to the left and to the bottom by ~ 1 cm in both *x* and *y* directions, which may be due to the noise (distortion) in the NCIDs that corresponds to high spatial frequency. The FWHMs of the profiles through the maximum in the cross-section image were found to be 12.3 mm and 13.0 mm in the *x* and *y* directions, respectively, which are similar to those obtained using fluorescence data. The retrieved FWHMs using transmission data are listed in Table 6.5. If the regularization at the "corner" of the L-curve is used, the location of the target shown in the cross-section image becomes more accurate (image not shown here). However the resolution degrades.

6.5.2. Two targets

6.5.2.1. *Fluorescence TROT*

The TR matrix was generated by multiplying the response matrix by its transpose for our CW probing scheme. The eigenvalue equation of TR matrix was solved.

The first 20 eigenvalues plotted in Fig. 6.9 demonstrate that only two eigenvalues are dominant, and consequently those two were included in the signal subspace and separated from the noise subspace.

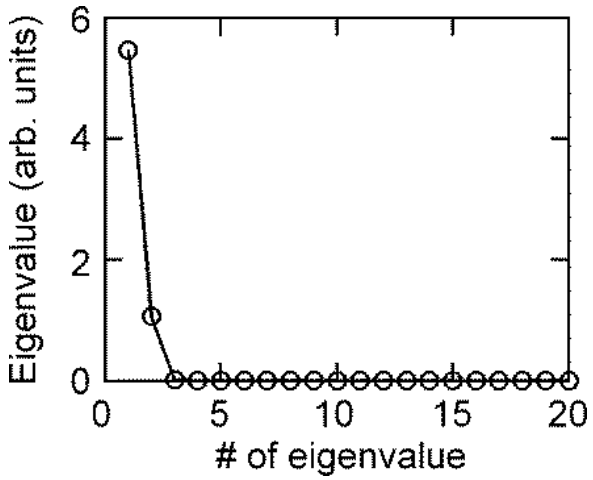

Fig. 6.9. Eigenvalue spectrum of TR matrix

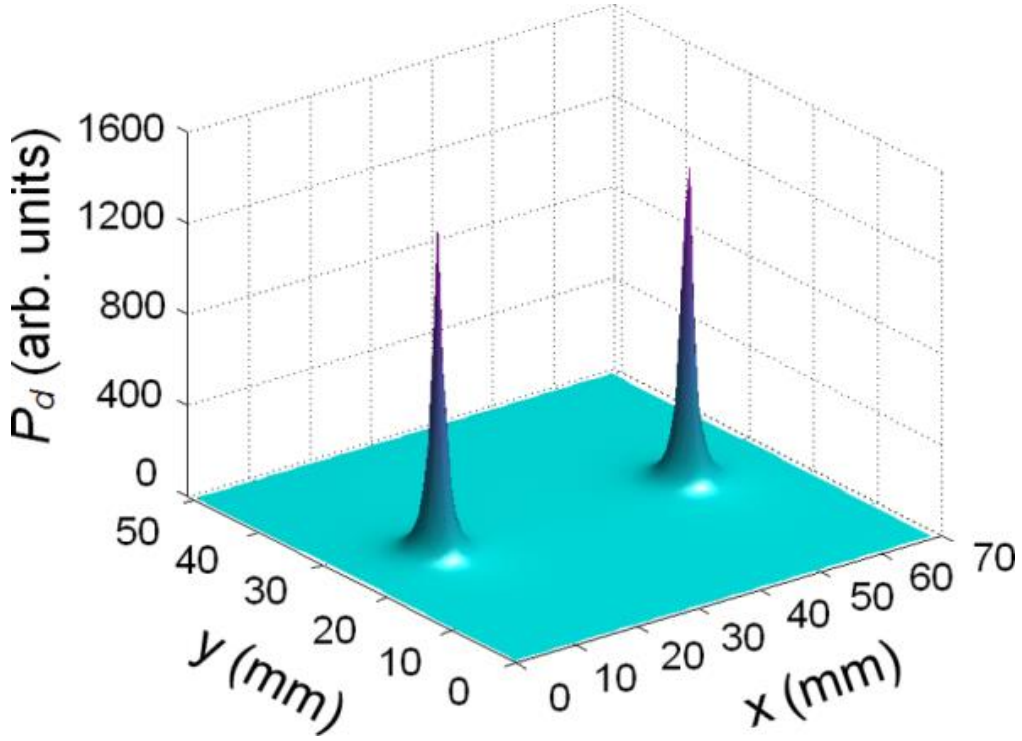

Fig 6.10. TROT-reconstructed pseudo image at z = 29.5 mm using *fluorescence* data.

MUSIC algorithm [16] was then used to calculate the pseudo spectrum for all voxels in the 3-*D* space of the sample. The voxel size was 0.77 mm × 0.77 mm × 1 mm. Three-dimensional tomographic pseudo images were generated using the pseudo spectrum. Fig. 6.10 shows one such tomographic image for z = 29.5 mm. The locations of targets taken to correspond to the peaks of

the pseudo images are listed and compared with known positions in Table 6.6. The single point that the method identifies as the location of a target may be considered to be the "center of fluorescence strength" of the target, which may coincide with the geometrical center for a homogeneous target, but would be weighted by the distribution of fluorescence strength for a heterogeneous target.

Table 6.6. Known and retrieved target positions

		Left target	Right target
Known Position [x, y, z (mm)]		14.2, 25.0, 30.0	54.2, 25.0, 30.0
Fluorescence-TROT retrieved	Position [x, y, z (mm)]	13.4, 24.9, 29.5	53.9, 24.1, 30.5
	Error [Δx, Δy, Δz (mm)]	0.8, 0.1, 0.5	0.3, 0.9, 0.5
Transmission-TROT retrieved	Position [x, y, z (mm)]	12.6, 27.2, 30.5	53.9, 27.2, 29.5
	Error [Δx, Δy, Δz (mm)]	1.6, 2.2, 0.5	0.3, 2.2, 0.5
FWHM [δx, δy (mm)] using	Fluorescence-TROT	2.0, 1.5	1.7, 1.8
	Transmission-TROT	5.7, 4.2	6.4, 5.0

The retrieved positions are in good agreement with the known locations of the targets. Further experimentation and simulation reveal that TROT achieves better resolution in the lateral (x, y) directions than in the axial (z) direction, and that the resolution depends on separation between the targets and other experimental parameters. We estimate that under the reported experimental conditions and parameters, the same two targets could be resolved even when the closest lateral (x, y) distance between their surfaces were 2 mm (center-to-center distance of 6 mm) with a noise level of ~10%. If the targets had the same lateral position but different z-positions, the separation between them could be determined within 2 mm even with 50% additive random

noise when the separation was 30 mm. As the axial distance between the two targets was reduced to 20 mm, the approach retrieved the separation to be smaller, such as, 18 mm for up to 20% noise, 11 mm for 40% noise, and fail to resolve for 45% or higher noise. For a separation of 17 mm the targets could not be resolved even with 0 noise. The axial resolution could be improved if data were acquired in a wider angular view (for example, additional measurements across an adjacent (*y*-*z*) side), or using cylindrical geometry.

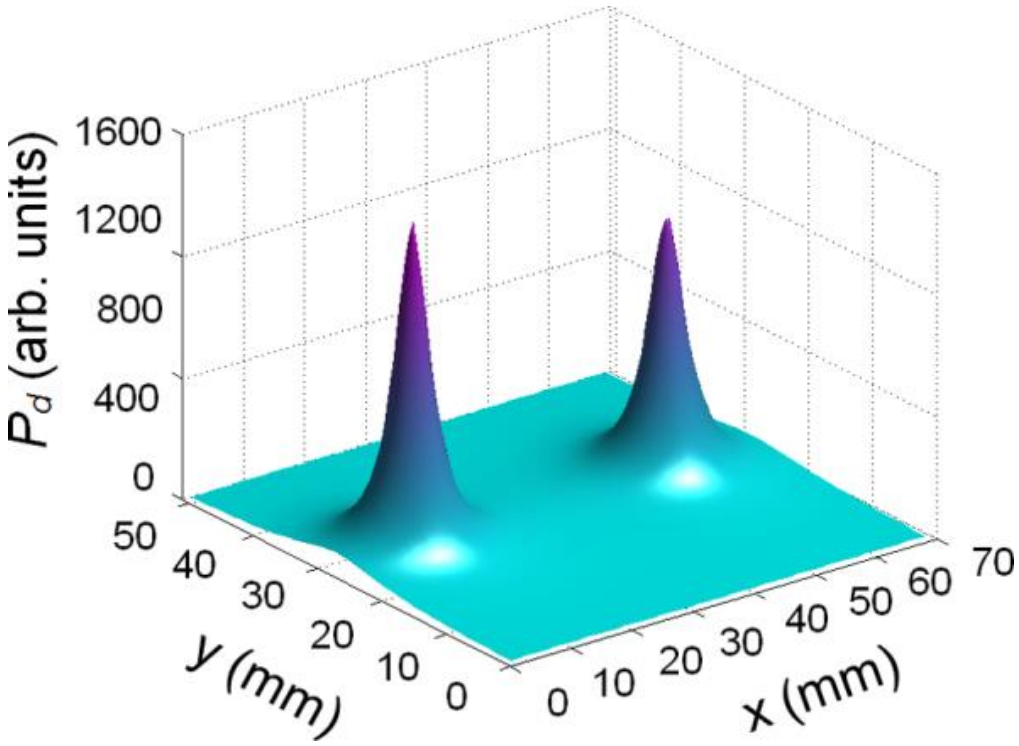

Fig. 6.11. TROT-reconstructed pseudo image at z = 29.5 mm using transmission data.

Since an excited fluorescent target emits light in all directions, the method can be readily used in back-propagation geometry and is not restricted to transmission mode reported here. We have used CW illumination and rectangular slab sample geometry in experiments reported here, but the approach can be extended to frequency-domain and time-domain measurements and other sample geometries (cylindrical, spherical, and hemispherical) as well.

The TROT reconstructed image at the z = 29.5 mm plane using the transmission data is shown in Fig. 6.11, and the retrieved locations of targets are listed and compared with those obtained from fluorescence data in Table 6.6.

It follows from Table 6.6, that the positions of the targets retrieved using fluorescence measurements are in very good agreement (uncertainty <1 mm) with the known locations, and are quite consistent with those retrieved using transmission measurements. However, the peaks in the reconstructed images using fluorescence data are sharper than those using transmission data. Since only one eigen component was used to reconstruct a target, the targets are treated as point targets, and the pseudo images only carry location information. The FWHMs of the peaks in the fluorescence-TROT and transmission-TROT images are shown also in Table 6.6. It is shown the FWHM of the peaks in the transmission-TROT images are about 2.8 times of those in the fluorescence-TROT images. The width of the profile of each target reflects on the uncertainty in determination of location of the corresponding target. We tentatively ascribe this better resolution of fluorescence TROT result than that of transmission TROT result to the difference in the background level between fluorescence and transmission signals. Fluorescence signal, in principle, has zero background, while transmission signal involves measurement of changes on a strong background, and such changes for targets in a turbid medium can be rather small. This set of measurements suggests that higher resolution may be achieved with TROT using fluorescence data than that using transmission data, an observation reported by other researchers as well.[6, 8] However, the overall level of fluorescence signal is an important factor in imaging applications, and more work involving different types of samples and target contrast will be needed to obtain a more definitive conclusion.

Following Eq. (6.4), the fluorescence strengths *f* of the targets were found to be 13.5 mm^3/ns. Using Green's functions corresponding to the retrieved target positions along with Eq. 6.8, the fluorescence strengths of the targets were retrieved to be 13.8 mm^3/ns and 15.0 mm^3/ns, with 2.2% and 11.1% errors for the left and right targets, respectively. The absorption strength of the targets were also retrieved similarly. The retrieved values for the two targets were 668.8 and 622.7 mm^3/ns, with 20.6% and 26.1% errors, respectively. The retrieved fluorescence and absorption strengths are listed in Table 6.7 with comparison to the known values.

Table 6.7. Retrieved optical strengths of the targets

Target	Measurement Type	Known strength (mm^3/ns)	Retrieved strength (mm^3/ns)	Error (%)
Left	Fluorescence	13.5	13.8	2.2
	Transmission	842.8	668.8	20.6
Right	Fluorescence	13.5	15.0	11.1
	Transmission	842.8	622.7	26.1

6.5.2.2. *NMF-based fluorescence tomography*

Fig. 6.12(a) and Fig. 6.12(b) show NCIDs of the left target on the detector and source planes, respectively. Fig. 6.12(c) and Fig. 6.12(d) present the corresponding spatial profiles along the white dashed lines. The solid curves in Fig. 6.12(c) and Fig. 6.12(d) are the least squares fits of the experimental profiles denoted by circles to Green's functions using Eq. (6.9). Table 6.8 lists the three-dimensional (3-*D*) locations of the targets extracted from this fitting procedure. Similar NCIDs are obtained for the right target as shown in Figs. 6.12(e) and 6.12(f), and the retrieved

target positions are also listed in Table 6.8. The retrieved positions agree within ~ 1mm of the known positions.

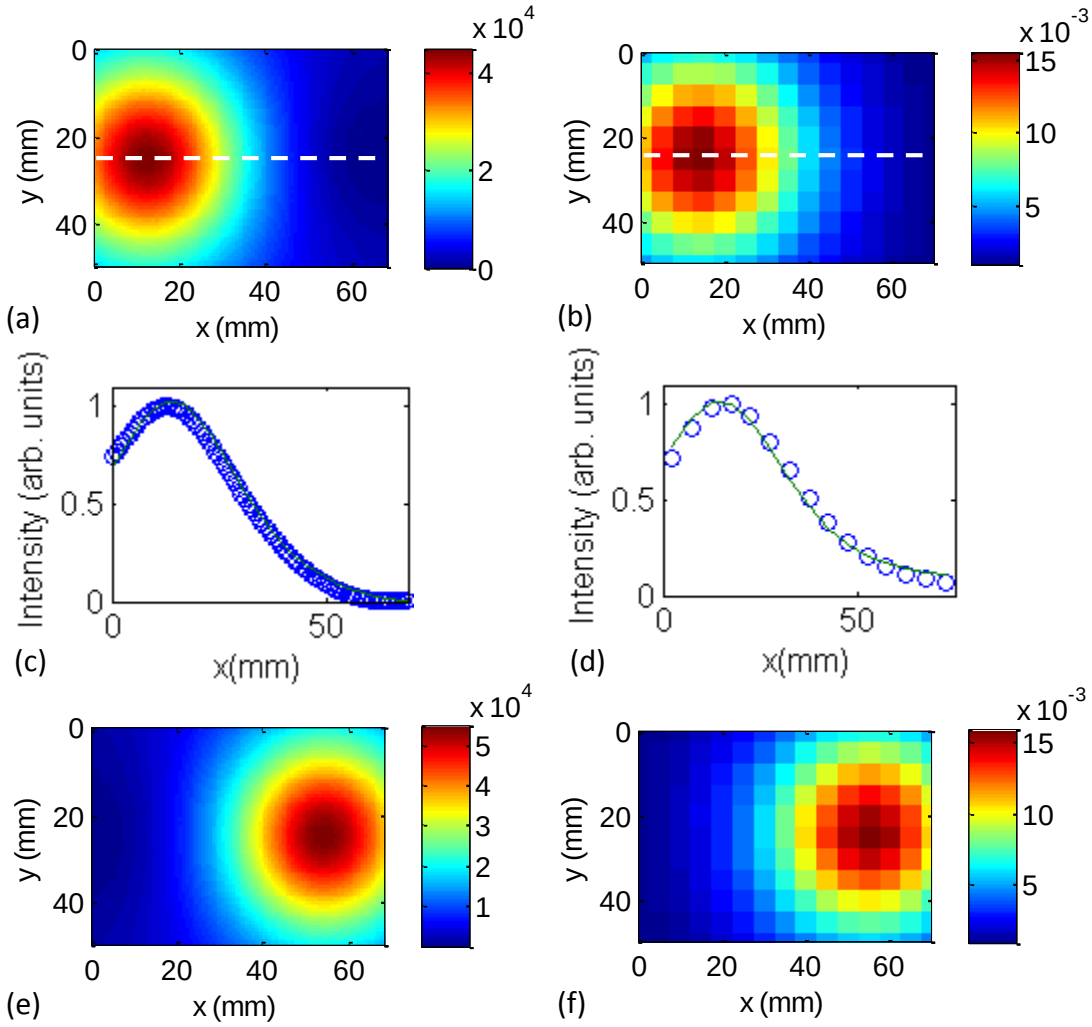

Fig. 6.12. (a) and (b) are NCIDs corresponding to the left target on the detector plane and on the source plane, respectively; (c) and (d) are least squares fits to the spatial profiles along the white dashed lines in (a) and (b), respectively; (e) and (f) are NCIDs corresponding to the right target on the detector and source planes, respectively.

The NCIDs retrieved from the transmission data are shown in Fig. 6.13. Table 6.8 further lists the NMF-retrieved target positions using transillumination data for comparison with those obtained from fluorescence data. There are some small differences in the accuracy of retrieved *x*

and *y* coordinates (that is in the values of Δx and Δy) for two inclusions. We attribute those to random measurement/ reconstruction error.

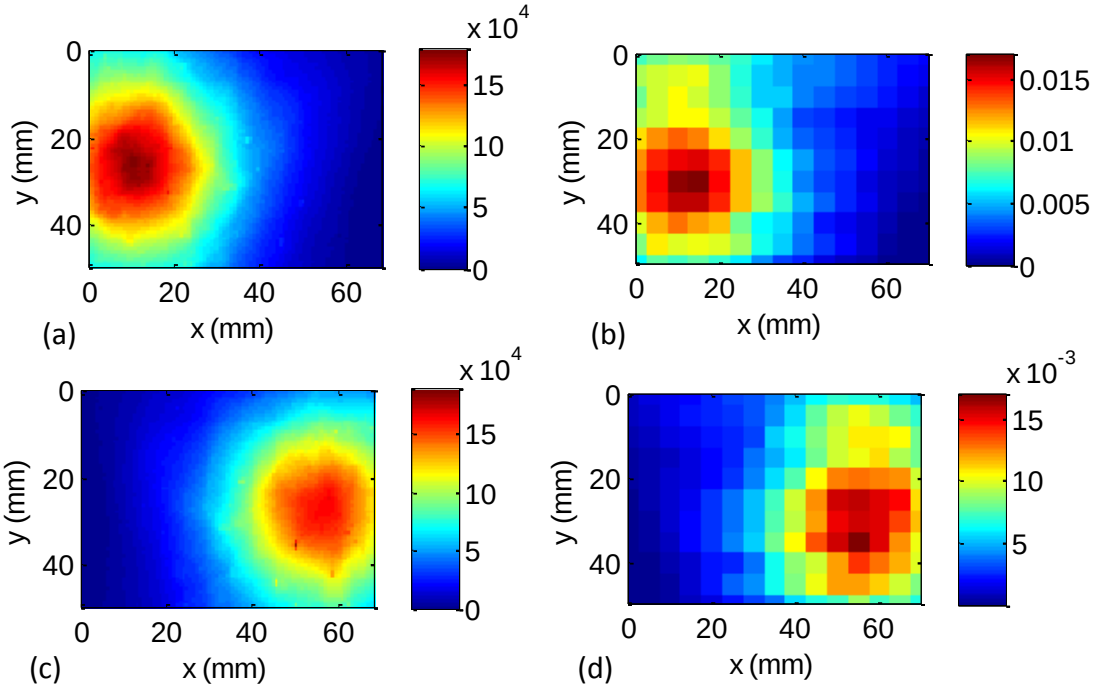

Fig. 6.13. (a) and (b) are NCIDs corresponding to the left target on the detector and source planes, respectively; (c) and (d) are NCIDs corresponding to the right target on the detector and source planes, respectively.

NMF-based fluorescence and transillumination approaches both retrieve locations of the targets well. However, as Table 6.8 show, errors in position coordinates of the targets retrieved from fluorescence data are significantly smaller than those obtained from transillumination data. We attribute this difference to the role played by the background in the two cases. Ideally, the fluorescence signal is a measurement of emitted light on a dark background, while the transillumination signal is a perturbation on a strong background. In practice, the background is significantly smaller in fluorescence imaging than in transillumination imaging. Other researchers have reported on similar superior performance of fluorescence tomography as well [8]. If the background is substantial (as in the case of fluorescence from contrast agent up taken

by normal tissue, or tissue autofluorescence) the fluorescence tomography may not retain this edge over the transilllumination imaging.

Table 6.8. Known and NMF retrieved target positions

Mode	Target	Known positions [x, y, z (mm)]	Retrieved positions [x, y, z (mm)]	Error [Δx, Δy, Δz] (mm)
Fluorescence	Left	14.2, 25.0, 30.0	13.9, 25.8, 30.5	0.3, 0.8, 0.5
	Right	54.2, 25.0, 30.0	55.8, 25.5, 29.2	1.6, 0.5, 0.8
Transmission	Left	14.2, 25.0, 30.0	11.7, 28.0, 31.7	2.5, 3.0, 1.7
	Right	54.2, 25.0, 30.0	55.9, 29.7, 32.2	1.7, 4.7, 2.2

Table 6.9. Retrieved optical strengths of the targets

Target	Measurement Type	Known strength (mm^3/ns)	Retrieved strength (mm^3/ns)	Error (%)
Left	Fluorescence	13.5	11.5	14.8
	Transmission	842.8	589.7	30.0
Right	Fluorescence	13.5	14.6	8.1
	Transmission	842.8	584.6	30.6

The scaling factors α and β were generated in the least squares fitting using Eq. (6.10), and the fluorescence strengths were estimated using Eq. (6.11) to be 11.5 mm^3/ns and 14.6 mm^3/ns for the left and right targets, respectively. The uncertainties in the estimated values are 14.8% and 8.1% compared to known values. Similarly, the absorption strength of the targets were

estimated from the transmission data to be 583 mm^3/ns and 582 mm^3/ns for the left and right targets, respectively, which were within ~30% of the known value. The retrieved fluorescence and absorption strengths are listed in Table 6.9, with comparison to known values.

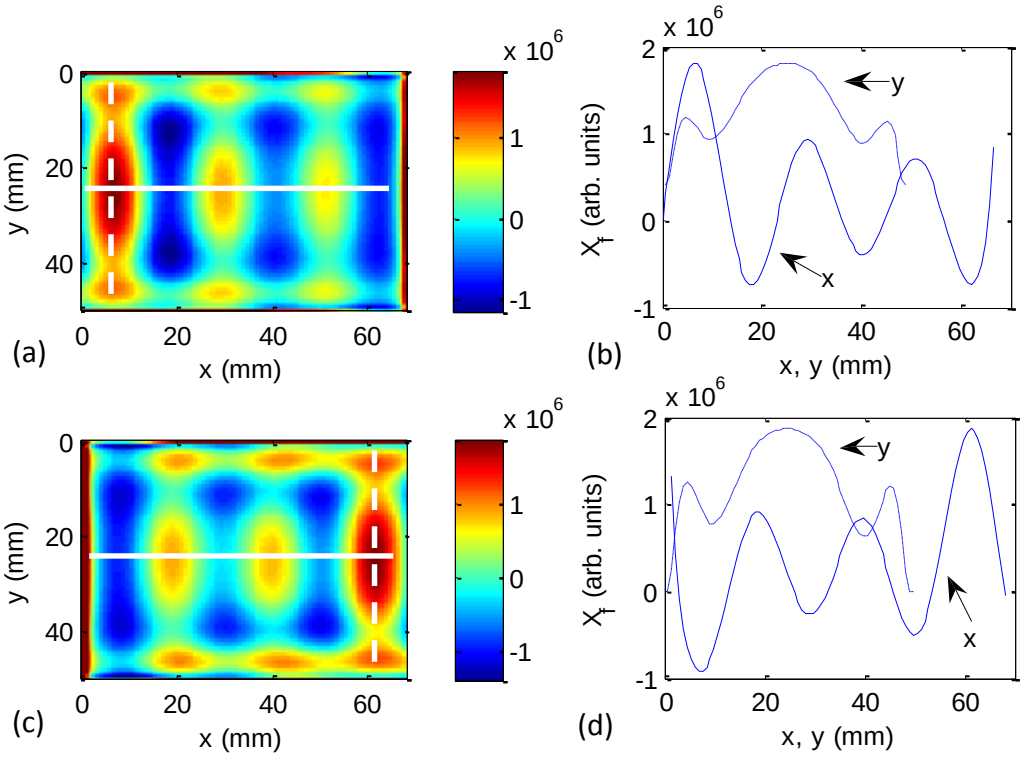

Fig. 6.14. (a) and (c) are cross sectional images at the z = 30.5 cm and 29.2 cm planes, respectively. (b) and (d) are spatial profiles of the cross sectional images along the x and y directions shown by the white lines.

Cross-section images of the targets were generated using the back-projection method. Fig. 6.14(a) displays a cross-section image of the left target at the z = 30.5 mm plane generated from the fluorescence data. The real cross section image of the target is at the left of the frame (confirmed by its location obtained from the previous step), while other two are artifacts whose strength depends in part on the regularization parameter. Similar cross-section image was obtained for the right target. The FWHM of the spatial profiles of the cross-section images were found to be 8.8 mm and 19.1 mm for the left target, and 8.8 mm and 18.4 mm for the right target in x and y directions, respectively. The cross-section images estimate the lateral dimensions of

the targets to be approximately twice their known values. We presume it a consequence of the diffusive nature of light propagation. However, the ratio between the *y* and *x* dimensions of the targets estimated to be 2.2 and 2.1 for the left and right targets, respectively, are close to the actual value of ~2.4 for both targets. The FWHMs retrieved from fluorescence as the estimate of the sizes of the targets, are listed in Table 6.10.

For comparison, similar cross section images were generated using the transmission data, as shown in Fig. 6.15.

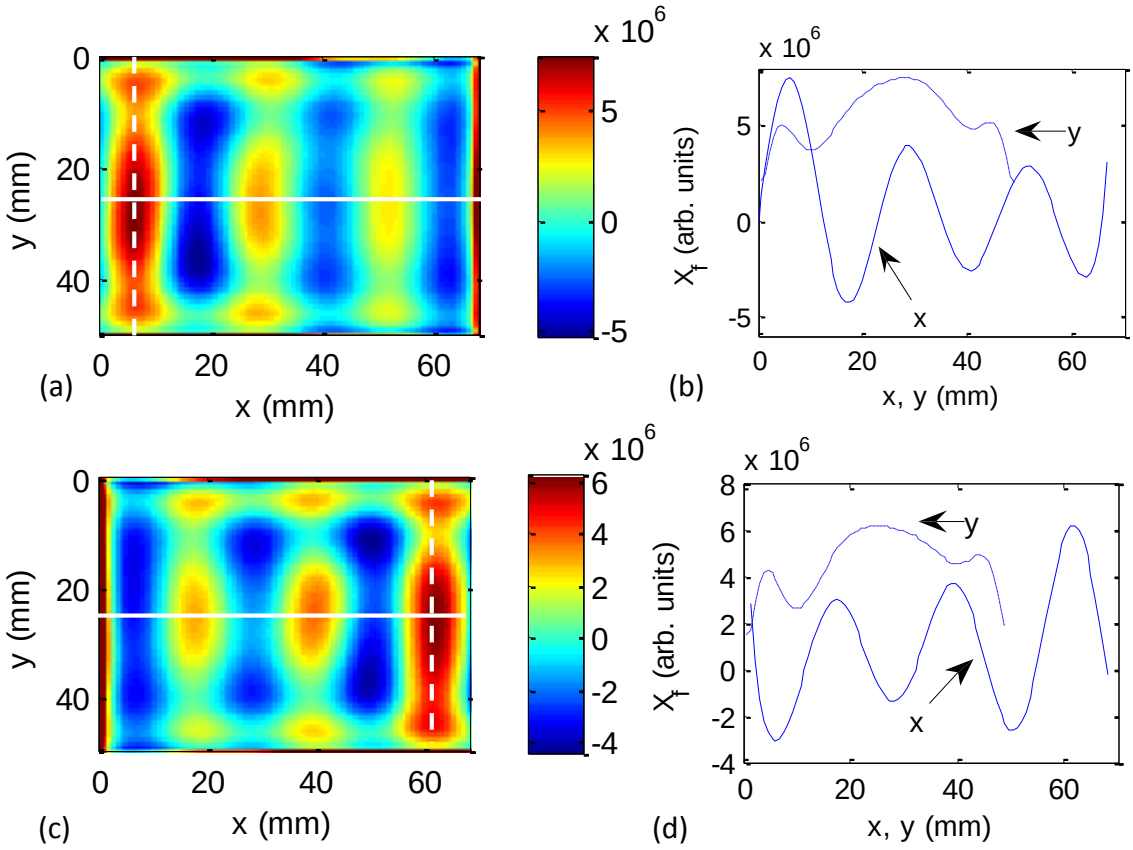

Fig. 6.15. (a) and (c) are cross sectional images generated at the *z*-positions of the two targets (*z* = 31.7 mm and 32.2 mm), respectively. (b) and (d) are spatial profiles of the cross sectional images along the *x* and *y* directions shown by the lines.

We found the FWHM to be 7.7 mm and 18.4 mm for the left target, and 8.4 mm and 19.1 mm for the right target in x and y directions, respectively. The ratio between the y and x dimensions of the targets estimated to be 2.4 and 2.3 for the left and right targets, respectively. The cross section estimates are comparable for both the fluorescence and transillumination approaches. The FWHMs retrieved from transmission data are also all listed in Table 6.10 for comparison.

Table 6.10. Estimated target size using FWHM of the cross-section image of the targets

Target	Measurement Type	Known size [δx, δy] (mm)	Retrieved size [δx, δy] (mm)
Left	Fluorescence	4.2, 10	8.8, 19.1
	Transmission		7.7, 18.4
Right	Fluorescence		8.8, 18.4
	Transmission		8.4, 19.1

6.6. Discussion

Compared to the case with two targets present, when only one target was presented, the cross-section image of the target was almost round, *i.e.* the ratio between the estimated dimensions of the target in the x and y directions was about 1. This distortion in the shape of the image in the single target case is probably due to the noise in the weaker signal of the single target.

Minimum detectable fluorophore concentration and target size are useful considerations for application of the TROT method. While we present data on ICG concentration of 1 μM in the target following the common practice [6, 8] with our current experimental configuration we have tested with ICG at various concentrations. Fluorescence signal due to a 1-cm-long and a 2-cm-

long, 4.2-mm-diameter target embedded in the mid-plane of the 60-mm container was measured with various concentrations (20 nM, 50 nM, 100 nM, 250 nM, 500 nM, 1 μM), respectively. The peak values in the measured signals are shown in Fig. 6.16(a). The fluorescence signal due to the 2-cm-long target was approximately twice as much as the 1-cm-long target with ICG at the same concentrations. When the ICG concentrations was 20 nM, 50 nM and 100 nM, the images of the 1-cm long target are shown in Fig. 6.16(b), 6.16(c) and 6.16(d), respectively. Fig. 6.16 shows even with 20-nM ICG, the 1-cm-long target could be detected. However, the signal-to-noise ratio was significantly lower than that with 100-nM ICG, as shown in Fig. 6.16.

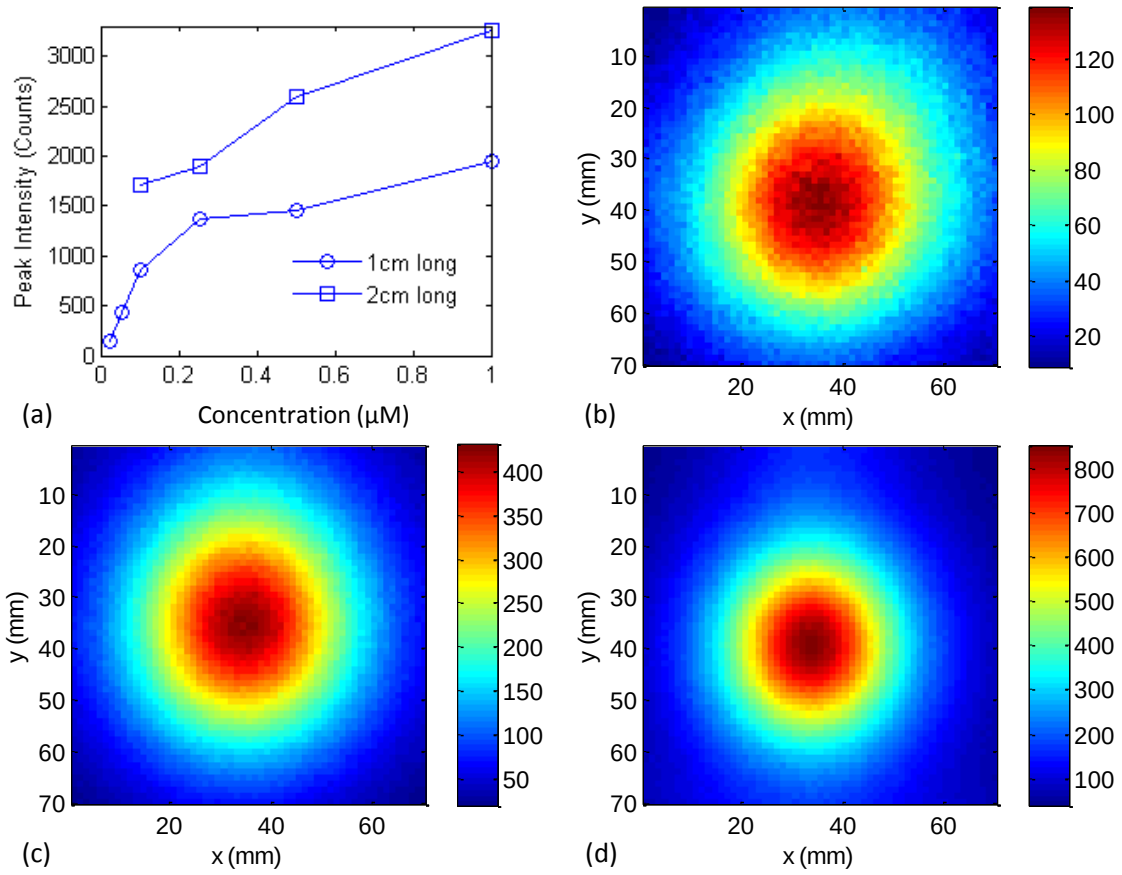

Fig. 6.16. (a) The two curves show the peak values in the fluorescence signal using different ICG concentrations for the 1-cm-long and 2-cm-long fluorescent targets, respectively; (b), (c) and (d) show the fluorescence signal with ICG at concentrations of 20 nM, 50 nM, and 100 nM, respectively.

Both TROT and NMF-OT approaches retrieve locations of targets based on their fluorescence strength, which is a product of the fluorescence yield and the volume of the target. However, it is impractical to use a point target and make the fluorescence yield arbitrarily large. Based on experimental conditions we anticipate being able to locate targets of size 0.04 cm^3, 4-times smaller than what we used with same ICG concentration. In clinical applications involving detecting and locating tumors, these sizes are more than adequate for early detection of cancer.

This set of experiments was done with no background ICG uptake. Background fluorescence is seldom zero for *in vivo* experiments and is a common concern for fluorescence DOT [6]. For uniform distribution of fluorophore in the background medium, simulation shows that the present methods would provide target location that is quite accurate in the lateral directions, but is shifted towards the detector plane, and the shift would depend on the target-to-backbround fluorescence ratio. The fluorescence signal was examined experimentally when there was fluorophore distribution in the background. The peak value in the measured fluorescence light intensity distribution is used to represent the strength of fluorescence. The measured fluorescence signals due to ICG in the background at different concentrations and a fitted curve are plotted in Fig. 6.17(a). Small sections of the curve in Fig. 6.17(a) are plotted in 6.17(b) – 6.17(d). As described by Yuan *et al.* [32], quantum quenching in the fluorescence was observed. Fig. 6.17 shows the fluorescence signal becomes detectable at 1 nM, and increases linearly within 10 nM. Then it continues to increase nonlinearly and reaches maximum at 80 nM. After that, the fluorescence decreases with concentration. This effect is expected to vary with the scattering and absorption properties of the medium, and the volume, particularly thickness of the medium. For smaller medium with lower absorption and scattering properties, a larger linear signal-increasing range is expected.

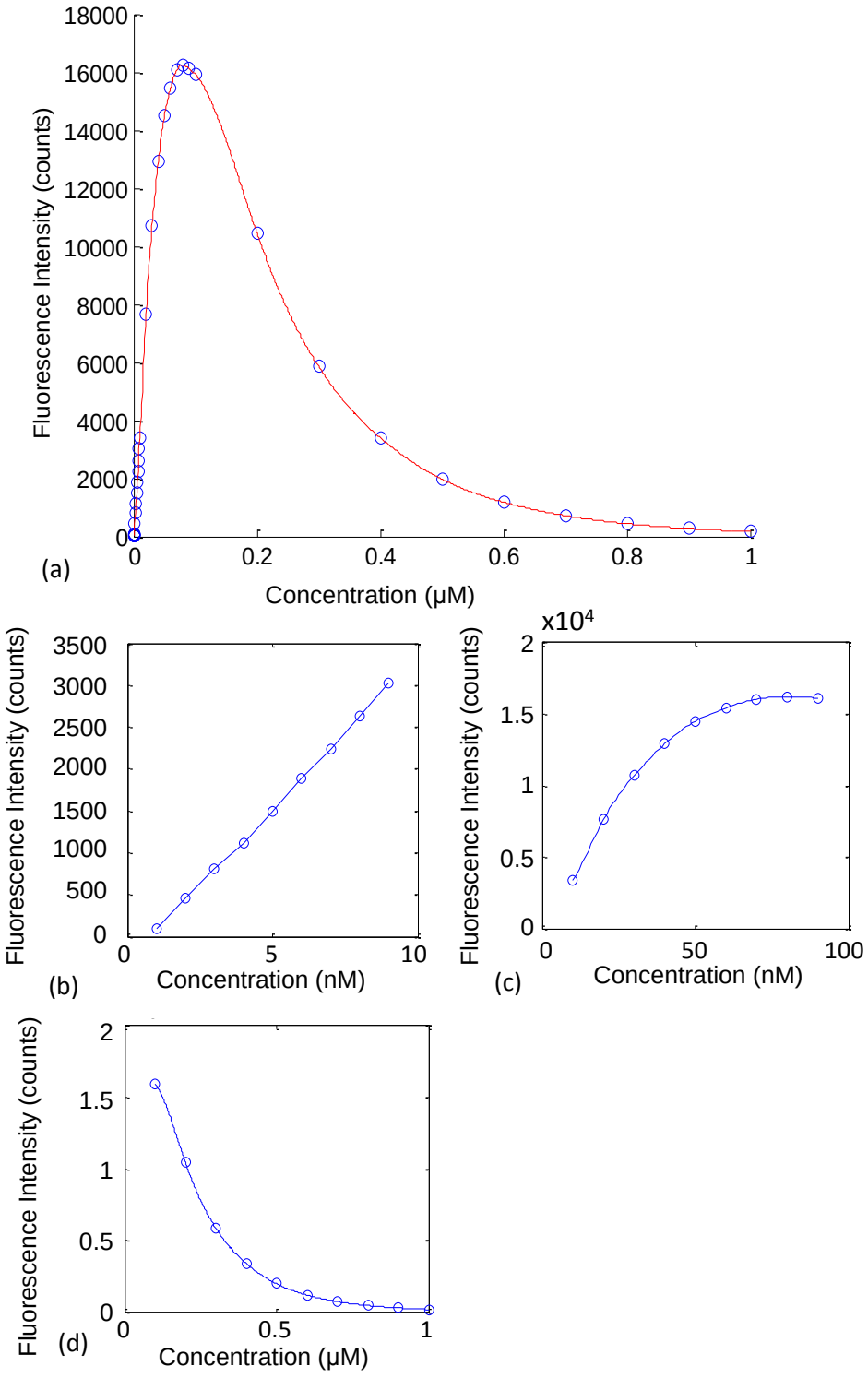

Fig. 6.17(a) shows measured fluorescence signal (o) and fitted curve (-) due to the ICG in the background medium at different concentrations. (b), (c) and (d) show different sections of the curve in (a).

The results above (Figs. 6.16 and 6.17) show that the fluorescence signal due to the background medium in the 250 mm × 250 mm × 60 mm container has much higher signal before quantum quenching takes place for the same concentration in the background and in the target. For instance, for a concentration of 50 nM, the fluorescence signal from the background is ~30 times of that from the target. 5-nM ICG in the background produces similar level of fluorescence signal as 500-nM ICG in the target. The target-to-background fluorescence signal ratio should be higher for a target inside a smaller sample. However, in realistic experimental conditions, the background fluroescence is usually significant and cannot be neglected. Analyzing the data using TROT or NMF directly with background fluroescence neglected will lead to significant error in the resutls.

The situation may improve if an appropriate background subtraction method may be employed [8, 38, 39]. In *in vivo* studies, background fluorescence due to fluorophore uptake by normal tissues may be significantly reduced by adjusting the time delay between administration of fluorophore and the measurements, since the fluorophore gets removed from the normal tissue faster than from the tumor [6]. The method uses the diffusion model of light propagation, which takes into account the effect of background absorption and scattering in the intervening medium.

As explained in Chapter 2 and Chapter 4 respectively, both TROT and NMF are fast reconstruction methods, since they use data matrix with lower dimension than that used in other inverse image reconstruction (IIR) approaches, do not involve iterations of the forward model, and do not attempt to find optical properties for every voxel. The same advantages of these approaches over other IIR methods hold true for fluorescence imaging. The computational complexity of both approaches is less than what it is even for a single iteration of an iterative IIR method. Even though a limited number of acquisition angles were used for the slab geometry,

locations of the fluorescence targets were retrieved by both approaches within ~1 mm of known positions for a sample with similar thickness and average optical properties of a typical compressed human breast, which is a significant result.

In summary, *fluorescence* TROT and NMF-based fluorescence tomography approaches have been developed and used to retrieve the target location and relative fluorescence strength of one and two small fluorescent targets embedded in a breast-simulating turbid medium. Locations of targets were retrieved in 3-*D* with an accuracy of ~1 mm under the favorable condition of well-separated targets. Achievable spatial resolution is better for assessment of lateral separation between the targets than for axial separation in the forward propagation mode of signal acquisition using slab geometry. Fluorescence signal appeared to provide better resolution than transillumination signal. The results further suggest the potential of TROT and NMF-based fluorescence tomography for retrieving three-dimensional location information of contrast-enhanced tumors in a human breast at early development stages.

References

1. B. P. Joshi, and T. D. Wang, "Exogenous molecular probes for targeted imaging in cancer: focus on multi-modal imaging," Cancers **2**, 1251-1287 (2010).
2. S. Luo, E. Zhang, Y. Su, T. Cheng, and C. Shi, "A review of NIR dyes in cancer targeting and imaging," Biomaterials **32**, 7127 -7138 (2011).
3. X. He, K. Wang, and Z. Cheng, "In vivo near-infrared fluorescence imaging of cancer with nanoparticle-based probes," WIREs Nanomed. Nanobiotechnol. **2**, 349–366 (2010).
4. S. Tyagi, S. A. E. Marras, and F. R. Kramer, "Wavelength-shifting molecular beacons," Nat. Biotechnol. **18**, 1191-1196 (2000).

5. E. E. Graves, J. Ripoll, R. Weissleder, and V. Ntziachristos, "A submillimeter resolution fluorescence molecular imaging system for small animal imaging," Med. Phys. **30**, 901 (2003).

6. A. Corlu, R. Choe, T. Durduran, M. A. Rosen, M. Schweiger, S. R. Arridge, M. D. Schnall, and A. G. Yodh, "Three-dimensional in vivo fluorescence diffuse optical tomography of breast cancer in humans," Opt. Express **15**, 6696-6716 (2007).

7. S. Bloch, F. Lesage, L. McIntosh, A. Gandjbakhche, K. Liang, and S. Achilefu, "Whole-body fluorescence lifetime imaging of a tumor-targeted near infrared molecular probe in mice," J. Biomed. Opt. **10**, 054003 (2005).

8. A. Godavarty, M. J. Eppstein, C. Zhang, S. Theru, A. B. Thompson, M. Gurfinkel, and E. M. Sevick-Muraca, "Fluorescence-enhanced optical imaging in large tissue volumes using a gain-modulated ICCD camera," Phys. Med. Biol. **48**, 1701-1720 (2003).

9. I. Gannot, A. Garashi, V. Chernomordik, and A. Gandjbachkhe, "Quantitative optical imaging of the pharmacokinetics of fluorescent-specific antibodies to tumor markers through tissuelike turbid media," Opt. Lett. **29**, 742-744 (2004).

10. M. Alrubaiee, M. Xu, S. K. Gayen, and R. R. Alfano, "Localization and cross section reconstruction of fluorescent targets in *ex vivo* breast tissue using independent component analysis," Appl. Phys. Lett. **89**, 133902 (2006).

11. A. Liebert, H. Wabnitz, J. Steinbrink, M. Moller, R. Macdonald, H. Rinneberg, A. Villringer, and H. Obrig, "Bed-side assessment of cerebral perfusion in stroke patients based on optical monitoring of a dye-bolus by time-resolved diffuse reflectance," Neuroimage **24**, 426-435 (2005).

12. A. D. Klose, and A. H. Hielscher, "Fluorescence tomography with simulated data based on the equation of radiative transfer," Opt. Lett. **28**, 1019–1021 (2003).

13. J. Wu, L. Perelman, R. R. Dasari, and M. S. Feld, "Fluorescence tomographic imaging in turbid media using early-arriving photons and Laplace transforms," Proc. Natl. Acad. Sci. USA **94**, 8783–8788 (1997).

14. B. Wu, W. Cai, M. Alrubaiee, M. Xu, and S. K. Gayen, "Time reversal optical tomography: locating targets in a highly scattering turbid medium," Opt. Express **19**, 21956-21976 (2011).

15. M. Fink, D. Cassereau, A. Derode, C. Prada, P. Roux, M. Tanter, J.-L. Thomas, and F. Wu, "Time-reversed acoustics," Rep. Prog. Phys. **63**, 1933-1995 (2000).

16. A. J. Devaney, "Time reversal imaging of obscured targets from multistatic data," IEEE Trans. Antenn. Propag. **53**, 1600-1610 (2005).

17. D. D. Lee, and H. S. Seung, "Learning the parts of objects by non-negative matrix factorization," Nature **401**, 788-791 (1999).

18. J.-F. Cardoso, "Blind signal separation: statistical principles," Proc. IEEE **86**, 2009-2025 (1998).

19. B. Wu, M. Alrubaiee, W. Cai, M. Xu, and S. K. Gayen, "Diffuse optical imaging using decomposition methods," Int. J. Opt. **2012**, 185435 (2012).

20. M. S. Patterson, and B. W. Pogue, "Mathematical model for time-resolved and frequency-domain fluorescence spectroscopy in biological tissues," Appl. Opt. **33**, 1963-1974 (1994).

21. A. B. Milstein, S. Oh, K. J. Webb, C. A. Bouman, Q. Zhang, D. A. Boas, and R. P. Millane, "Fluorescence optical diffusion tomography," Appl. Opt. **42**, 3081-3094 (2003).

22. P. C. Hansen, "Analysis of discrete ill-posed problems by means of the *L*-curve," SIAM Rev. **34**, 561-580 (1992).

23. M. Xu, M. Alrubaiee, S. K. Gayen, and R. R. Alfano, "Three-dimensional localization and optical imaging of objects in turbid media with independent component analysis," Appl. Opt. **44**, 1889-1897 (2005).

24. P. Paatero, "The multilinear engine: a table-driven least squares program for solving multilinear problems, including the n-way parallel factor analysis model," J. Comp. Graph. Stat. **8**, 854-888 (1999).

25. P. Paatero, and U. Tapper, "Positive matrix factorization: a non-negative factor model with optimal utilization of error estimates of data values," Environmetrics **5**, 111-126 (1994).

26. http://cogsys.imm.dtu.dk/toolbox/nmf/.

27. M. Lax, V. Narayanamurti, and R. C. Fulton, "Classical diffusion photon transport in a slab," in *Laser Optics of Condensed Matter*, J. L. Birman, H. Z. Cummins, and A. A. Kaplyanskii, eds. (Plenum, New York, 1987), pp. 229-237.

28. H. J. v. Staveren, C. J. M. Moes, J. v. Marle, S. A. Prahl, and M. J. C. v. Gemert, "Light scattering in Intralipid-10% in the wavelength range of 400--1100 nm," Appl. Opt. **31**, 4507-4514 (1991).

29. M. L. J. Landsman, G. Kwant, G. A. Mook, and W. G. Zijlstra, "Light- absorbing properties, stability, and spectral stabilization of indocyanine green," J. Appl. Physiol. **40**, 575-583 (1976).

30. J. T. Alander, I. Kaartinen, A. Laakso, T. Pätilä, T. Spillmann, V. V. Tuchin, M. Venermo, and P. Välisuo, "A review of indocyanine green fluorescent imaging in surgery," Int. J. Biomed. Opt. **2012**, 940585 (2012).

31. R. C. Benson, and H. A. Kues, "Fluorescence properties of indocyanine green as related to angiography," Phys. Med. Biol. **23**, 159-163 (1978).

32. B. Yuan, and Q. Zhu, "Emission and absorption properties of indocyanine green in Intralipid solution," J Biomed Opt. **9**, 497-503 (2004).

33. E. M. Sevick-Muraca, G. Lopez, J. S. Reynolds, T. L. Troy, and C. L. Hutchinson, "Fluorescence and absorption contrast mechanisms for biomedical optical imaging using frequency-domain techniques," Photochem. Photobiol. **66**, 55-64 (1997).

34. V. Ntziachristos, and R. Weissleder, "Experimental three-dimensional fluorescence reconstruction of diffuse media by use of a normalized Born approximation," Opt. Lett. **26**, 893-895 (2001).

35. D. S. Kepshire, S. C. Davis, H. Dehghani, K. D. Paulsen, and B. W. Pogue, "Subsurface diffuse optical tomography can localize absorber and fluorescent objects but recovered image sensitivity is nonlinear with depth," Appl. Opt. **46**, 1669-1678 (2007).

36. S. D. Konecky, G. Y. Panasyuk, K. Lee, V. Markel, A. G. Yodh, and J. C. Schotland, "Imaging complex structures with diffuse light," Opt. Express **7**, 5048-5060 (2008).

37. A. N. Tikhonov, "Solution of incorrectly formulated problems and the regularization method," Soviet Math. Dokl. **4**, 1035-1038 (1963).

38. M. Xu, Y. Pu, and W. Wang, "Clean image synthesis and target numerical marching for optical imaging with backscattering light," Biomed. Opt. Express **2**, 850-857 (2011).

39. J. Lee, and E. M. Sevick-Muraca, "Three-dimensional fluorescence enhanced optical tomography using referenced frequency domain photon migration measurements at emission and excitation wavelengths," J. Opt. Soc. Am. A **19**, 759-771 (2002).

Chapter 7

Summary and future work

7.1. Summary

In this thesis, the time reversal optical tomography (TROT) and non-negative matrix factorization (NMF) based optical tomography (NMF-OT) were developed and used for imaging through highly scattering turbid media with embedded absorptive, scattering or fluorescent targets. The efficacy of the methods was evaluated using simulations, and experiments using human-breast-simulating phantoms, and *ex vivo* model human breast. The methods were shown to be able to provide three-dimensional location of the targets with high accuracy. The optical characteristics and dimensions of the targets may also be estimated with reasonable accuracy. CW laser and transillumination slab geometry were used in the study. The advantage is that the experimental arrangement is relatively simple, and such an imaging system is easy to build and more affordable. However, more sophisticated experimental arrangements could be developed to improve the imaging efficacy and provides interesting ground for further exploration.

7.2. Future work

The results obtained in the work presented in this thesis suggest further steps for development. Some steps may improve the results of the proposed approaches. Some are necessary to realize the goal of optical mammography ultimately. Our future work includes the following.

(a) Time-resolved and frequency-domain TROT

Time-resolved and frequency-domain measurements may provide more information of the sample and lead to higher resolution and more robust results. Time domain measurements can be

converted to frequency domain using Fourier transform. Phase information in the photon density wave will be obtained. A real "time reversal matrix" can be obtained instead of the one used currently which only involves "round-trip" of light propagation without "time reversal" (phase conjugate).

(b) Cylindrical or semi-spherical geometry

Since the slab geometry provides limited angular view of the sample, the resolution, particularly along the axial direction is not optimized. By using cylindrical or semi-spherical geometry, experimental data in a larger angular view are obtained. This may lead to higher resolution, particularly in the axial direction. The accuracy in the estimate of the shape (size) of an extended target may also be improved.

(c) Multi-wavelength studies using key wavelengths

Key wavelengths which correspond to the spectral features of the key fluorophores in the human breast tissue may be chosen for multi-wavelength measurements. The spectral information of the inhomogeneity may be used for diagnosis, particularly to distinguish cancer from benign growth or other irregularities which behave as an inhomogeneity.

(d) Combining FEM with TROT

The currently proposed TROT approach is mainly used for detection of localized small target such as a tumor. It provides limited information about the structure (heterogeneity) in the target. On the contrary, the widely used finite-element-method (FEM) based approach provides with a distribution of optical property in the sample. However, it is computation intensive. Combining these two methods may provide an optimal solution without aid of traditional imaging modality such as CT or MRI. First, TROT will be used to accurately determine the location, and estimate

the dimension of the target. Then a relatively small region around the target may be chosen for reconstruction using FEM. An optical property distribution will be obtained in the region, which uses much less computational time than that for reconstruction of the whole sample.

(e) Animal study

In vivo live animal study can be used to test the proposed approaches in a more realistic condition before it is eventually tested on human body.

(f) *In vivo* study on volunteers

The ultimate usefulness of the approaches may only be assessed by conducting *in vivo* study on volunteers before the approaches are used in clinical trials.

Appendix A

TROT Computer Program

main.m

```
function main

%read_in data for geometry
fid = fopen('geometry.txt', 'r');
ISNX = fscanf(fid,'%f',1);
ISNY = fscanf(fid,'%f',1);
IDNX = fscanf(fid,'%f',1);
IDNY = fscanf(fid,'%f',1);
MX = fscanf(fid,'%f',1);
MY = fscanf(fid,'%f',1);
LL = fscanf(fid,'%f',1);
fclose(fid);


fid = fopen('input_data.txt', 'r');

%read_in data
n1 = fscanf(fid,'%f',2);        %the reflective index of scattering medium
n2 = fscanf(fid,'%f',2);        %the reflective index of wall (i.e. glass)
n3 = fscanf(fid,'%f',2);        %the reflective index of outside (i.e. air)
lld = fscanf(fid,'%f',1);       %scattering medium thickness
mua = fscanf(fid,'%f',1);       %absorption coefficient
lt = fscanf(fid,'%f',1);        %transport length
nd = fscanf(fid,'%f',1);        %scattering medium refraction index
omega = fscanf(fid,'%f',1);     %modulation frequency, 0 for cw
z0 = fscanf(fid,'%f',1);        %depth of the center of the first voxel
dz = fscanf(fid,'%f',1);        %z direction division of the scattering medium
zs = fscanf(fid,'%f',1);        %source position
zd = fscanf(fid,'%f',1);        %detector position
delta = fscanf(fid,'%f',6);     %step interval in x and y
rate = fscanf(fid,'%f',2);      %noise level (for simulation)
dmu = fscanf(fid,'%f',2);       %change in mu of the inhomogeneities(abs, sca)
key = fscanf(fid,'%d',1);       %switch for judging the signal from the noise
space, either by readin number r_mm or automatic judging with r_ratio
r_mm = fscanf(fid,'%d',1);      %signal space rank
r_ratio = fscanf(fid,'%f',1);   %cutoff threshold for signal space
key2 = fscanf(fid,'%d',1);      %switch for normalization of the pseudo
spectrum
fclose(fid);

%calculate the extrapolated coefficient from the reflective index
%the galss wall is included
ze = calc_ze(n1,n2,n3);

%exp data
disp('enter exp data');
ryd=zeros(IDNY,IDNX,ISNY,ISNX);
```

```
fid = fopen('signal.txt','r');
ryd(:) = fscanf(fid,'%f')';
fclose(fid);

disp('enter trev');
pseudo =
trev1(ryd,key,key2,r_mm,r_ratio,ze,lld,mua,lt,nd,omega,z0,zd,dz,delta);
save trev0.mat pseudo;
[latt_pp] = sort_data(pseudo);
save trev.mat latt_pp;
```

gr.m

```
function s = createhandles
%Call: s = gr;
%s.cgrb(ze,mua,lt,nd,omega,x_xs,y_ys,z,zs)
%s.cgrd(ze,lld,mua,lt,nd,omega,x_xs,y_ys,z,zs)
%s.sgrb(ze,mua,lt,nd,omega,x_xs,y_ys,z,zs)
%s.sgrd(ze,lld,mua,lt,nd,omega,x_xs,y_ys,z,zs)
%
%ze=[ze(1),ze(2)]
%omega is modulation frequency, omega = 0 for CW
%
s.cgrb = @cgrb;
s.cgrd = @cgrd;
s.sgrb = @sgrb;
s.sgrd = @sgrd;

%cgrb.r
%This is for diffusion model
%The source position should move 1 lt  from real source position
%along incident direction.
%The follwing formula is little differet from Xu.
%In my formula, z=0 is defined from the real boundary
%In Xu's formula z=0 is defined at -ze(1), the extrapolated boundary.

function [rcgrb,icgrb] = cgrb(ze,mua,lt,nd,omega,x_xs,y_ys,z,zs)
%This is background Green's function for absorptive object.
%This is a frequency domain Green's function in real space.
%This Green's function is for a semi-infinite medium
%omegas: the modulated Frequency, Unit:  GHz.
%nd: the refractive index in the medium
%c: the light speed in medium, Unit: mm/nsec

ccgrb = zeros(size(x_xs));
rcgrb = ccgrb;
icgrb = ccgrb;

kext=ze(1)*lt;
dd=1/3*lt;
c=2.998*100/nd;
kapa=complex(mua/dd, -2*pi*omega/(dd*c));
kapa=sqrt(kapa);
rr=x_xs.^2+y_ys.^2;
```

```
r1=sqrt(rr+(z-zs)^2);
r2=sqrt(rr+(z+zs+2*kext)^2);
ccgrb=exp(-kapa*r1)./r1 - exp(-kapa*r2)./r2;
rcgrb=real(ccgrb)/(4*pi*dd);
icgrb=imag(ccgrb)/(4*pi*dd);
return


function [rcgrd,icgrd] = cgrd(ze,lld,mua,lt,nd,omega,x_xs,y_ys,z,zs)
%function rcgrd = cgrd(ze,lld,mua,lt,nd,omega,x_xs,y_ys,z,zs)
%This is background Green's function for absorptive object.
%This is a frequency domain Green's function in the real space
%This Green's function for a slab (thick: lld) medium
%omegas: the modulated Frequency, Unit:  GHz.
%nd: the refractive index in the medium
%c: the light speed in medium, Unit: mm/nsec

ccgrd = zeros(size(x_xs));
rcgrd = ccgrd;
icgrd = ccgrd;

kext=(ze(1)+ze(2))*lt;
dd=1/3*lt;
c=2.998*100/nd;
kapa=complex(mua/dd, -2*pi*omega/(dd*c));
kapa=sqrt(kapa);
rr=(x_xs).^2+(y_ys).^2;
for m=-4:4
    r1=sqrt(rr+(z-zs+2*m*(lld+kext))^2);
    r2=sqrt(rr+(z+zs+2*ze(1)*lt-2*m*(lld+kext))^2);
    ccgrd=ccgrd+exp(-kapa*r1)./r1 - exp(-kapa*r2)./r2;
end
rcgrd = real(ccgrd)/(4*pi*dd);
icgrd = imag(ccgrd)/(4*pi*dd);
return


function [rsgrb,isgrb] = sgrb(ze,mua,lt,nd,omega,x_xs,y_ys,z,zs)
%This is background Green's function for scattering object.
%This is a frequency domain Green's function in real space.
%This Green's function is for a semi-infinite medium.
%omegas: the modulated Frequency, Unit:  GHz.
%nd: the refractive index in the medium
%c: the light speed in medium, Unit: mm/nsec

rsgrb = zeros([3 size(x_xs)]);
isgrb = rsgrb;
rsgrb1 = zeros(size(x_xs));
rsgrb2 = rsgrb1;
rsgrb3 = rsgrb1;
isgrb1 = zeros(size(x_xs));
isgrb2 = isgrb1;
isgrb3 = isgrb1;

kext=ze(1)*lt;
```

```
dd=1/3*lt;
c=2.998*100/nd;
kapa=complex(mua/dd, -2*pi*omega/(dd*c));
kapa=sqrt(kapa);
rr=x_xs.^2+y_ys.^2;
z1=z-zs;
r1=sqrt(rr+z1*z1);
r1_3=r1.*r1.*r1;
z2=z+zs+2*kext;
r2=sqrt(rr+z2*z2);
r2_3=r2.*r2.*r2;
tt1=(kapa*r1+1).*exp(-kapa*r1)./r1_3;
tt2=(kapa*r2+1).*exp(-kapa*r2)./r2_3;

rsgrb1=x_xs.*real(tt1-tt2)/(4*pi*dd);
rsgrb(1,:) = rsgrb1(:);
rsgrb2 = y_ys.*real(tt1-tt2)/(4*pi*dd);
rsgrb(2,:) = rsgrb2(:);
rsgrb3=(z1*real(tt1)-z2*real(tt2))/(4*pi*dd);
rsgrb(3,:) = rsgrb3(:);
isgrb1=x_xs.*imag(tt1-tt2)/(4.*pi*dd);
isgrb(1,:) = isgrb1(:);
isgrb2=y_ys.*imag(tt1-tt2)/(4.*pi*dd);
isgrb(2,:) = isgrb2(:);
isgrb3=(z1*imag(tt1)-z2*imag(tt2))/(4.*pi*dd);
isgrb(3,:) = isgrb3(:);
return


function [rsgrd,isgrd] = sgrd(ze,lld,mua,lt,nd,omega,x_xs,y_ys,z,zs)
%This is background Green's function for scattering object.
%This is a frequency domain Green's function in the real space
%This Green's function for a slab (thick: lld) medium
%omegas: the modulated Frequency, Unit:  GHz.
%nd: the refractive index in the medium
%c: the light speed in medium, Unit: mm/nsec

csgrd = zeros([3 size(x_xs)]);
isgrd = csgrd;
rsgrd = csgrd;
csgrd1 = zeros(size(x_xs));
csgrd2 = csgrd1;
csgrd3 = csgrd1;

kext=(ze(1)+ze(2))*lt;
dd=1/3*lt;
c=2.998*100/nd;
kapa=complex(mua/dd, -2*pi*omega/(dd*c));
kapa=sqrt(kapa);
rr=x_xs.^2+y_ys.^2;

for m=-4:4
   z1=z-zs+2*m*(lld+kext);
   r1=sqrt(rr+z1*z1);
   r1_3=r1.*r1.*r1;
   z2=z+zs+2*ze(1)*lt-2*m*(lld+kext);
```

```
    r2=sqrt(rr+z2*z2);
    r2_3=r2.*r2.*r2;
    tt1=(kapa*r1+1).*exp(-kapa*r1)./r1_3;
    tt2=(kapa*r2+1).*exp(-kapa*r2)./r2_3;
    csgrd1=csgrd1+(tt1-tt2).*x_xs;
    csgrd(1,:) = csgrd1(:);
    csgrd2=csgrd2+(tt1-tt2).*y_ys;
    csgrd(2,:) = csgrd2(:);
    csgrd3=csgrd3+(z1*tt1-z2*tt2);
    csgrd(3,:) = csgrd3(:);
end
for i=1:3
  rsgrd(i,:)= real(csgrd(i,:))/(4*pi*dd);
  isgrd(i,:)= imag(csgrd(i,:))/(4*pi*dd);
end
```

trev1.m

```
function pseudo =
trev(ryd,key,key2,r_mm,r_ratio,ze,lld,mua,lt,nd,omega,z0,zd,dz,delta)

%read_in data for geometry
fid = fopen('geometry.txt', 'r');
ISNX = fscanf(fid,'%f',1);
ISNY = fscanf(fid,'%f',1);
IDNX = fscanf(fid,'%f',1);
IDNY = fscanf(fid,'%f',1);
MX = fscanf(fid,'%f',1);
MY = fscanf(fid,'%f',1);
LL = fscanf(fid,'%f',1);
fclose(fid);

fprintf('%s\n','enter T-matrix');
ryd = reshape(ryd,IDNX*IDNY,ISNX*ISNY);

%calculate the eigen value and eigen vector of T-matrix
fprintf('%s\n','enter eigen');

[u,s]=svd(ryd);
E = diag(s).^2;

fid = fopen('eigen.txt','w');
fprintf(fid,'%s \r\n', 'eigen value = ');
for i=1:IDNX*IDNY
    fprintf(fid,' %1.15E \r\n',E(i));
end
fclose(fid);

%determine mm: the signal space from the noise space
if(key == 1)
    mm=r_mm;   %judged the signal space by readin number
else
    mm=1;
    for k=1:IDNX*IDNY
```

```
        if (E(k) > E(1)*r_ratio)
            %eigen value is large, as signal
            mm=k;
        end
    end
end
fprintf('mm_estimated = %d \n',mm);

%determine the pseudo-spectum
fprintf('%s\n','enter pseudo-spectrum');

pseudo=zeros(4,LL,MY,MX);

x_xd = zeros(IDNY,IDNX);
y_yd = zeros(IDNY,IDNX);
ii = 1:IDNX;
jj = 1:IDNY;

rgd = zeros([4 size(x_xd)]);
gp = zeros(1,4);
gpu = zeros(mm,4);
gu = gp;

grhandles = gr;
for i=1:MX
    for j=1:MY
        for l=1:LL
            x=delta(2)*(i-1);
            y=delta(2)*(j-1);
            z=z0+dz*(l-1);

            x_xd=ones(IDNY,1)*(delta(3)*(ii-1)-x);
            y_yd=(delta(3)*(jj-1)-y)'*ones(1,IDNX);

            %calculate for absorption
            rcgrd = zeros(size(x_xd));
            icgrd = rcgrd;
            [rcgrd,icgrd] =
grhandles.cgrd(ze,lld,mua,lt,nd,omega,x_xd,y_yd,z,zd);
            rgd(1,:)=rcgrd(:);

            %calculate for scattering
            rsgrd = zeros([3 size(x_xd)]);
            isgrd = rsgrd;
            [rsgrd,isgrd] =
grhandles.sgrd(ze,lld,mua,lt,nd,omega,x_xd,y_yd,z,zd);
            rgd(2:4,:) = rsgrd(:,:);

            gp = sum(rgd(:,:)'.^2,1);
            gpu = u(:,1:mm)'*rgd(:,:)';
            gu = sum(gpu.^2,1);

            if(key2==1)
                pseudo(:,l,j,i)=gp./abs(gp-gu);
            else
```

```
                pseudo(:,l,j,i)=1./abs(gp-gu);
            end
        end
    end
end
```

cal_ze.m

```
function ze = calcze(n1,n2,n3)

for j=1:2
    R1=0;
    R2=0;
    for i=1:1001
        cosi=(double(i)-0.99999)/1000.0002;
        sini=sqrt(1-cosi*cosi);
        if(abs(n1(j)-n2(j)) < 1e-06)
            r12=0;
        else
            sinr=sini*n1(j)/n2(j);
            if(sinr > 0.999999999)
                re_par=1;
                re_pen=1;
            else
                cosr=sqrt(1-sinr*sinr);
                re_par=(n2(j)*n2(j)*cosi-
n1(j)*n2(j)*cosr)/(n2(j)*n2(j)*cosi+n1(j)*n2(j)*cosr);
                re_pen=(n1(j)*cosi-n2(j)*cosr)/(n1(j)*cosi+n2(j)*cosr);
            end
            r12=0.5*(re_par*re_par+re_pen*re_pen);
        end
        if(abs(n2(j)-n3(j)) < 1e-06)
            r23=0;
        else
            if(n3(j)-n2(j)*sinr < 1e-06)
                re_par=1;
                re_pen=1;
            else
                cosr=sqrt(1.-sinr*sinr);
                temp=sqrt(n3(j)*n3(j)-n2(j)*n2(j)*sinr*sinr);
                re_par=(n3(j)*n3(j)*cosr-
n2(j)*temp)/(n3(j)*n3(j)*cosr+n2(j)*temp);
                re_pen=(n2(j)*cosr-temp)/(n2(j)*cosr+temp);
            end
            r23=0.5*(re_par*re_par+re_pen*re_pen);
        end
        RR=(r12+r23-2*r12*r23)/(1-r12*r23);
        if(i==1 || i==1001)
            R1=R1+0.5*2.*cosi*RR;
            R2=R2+0.5*3*cosi*cosi*RR;
        else
            R1=R1+2*cosi*RR;
```

```
            R2=R2+3*cosi*cosi*RR;
        end
    end
    ze(j)=2*(1+R2/1000)/3/(1-R1/1000);
end
```

sort.m

```
function latt_pp = sort_data(pseudo)

DIM = size(pseudo);
MX = DIM(4);
MY = DIM(3);
LL = DIM(2);

% sorting the pseudo-spectrum
fprintf('enter sort pseudo-spectrum\n');

xx = [1:LL]; yy = [1:MY]; zz = [1:MX];

xx2 = xx'*ones(1,MY);
xx3 = ones(LL,MY,MX);
xx3(:) = xx2(:)*ones(1,MX);

yy2 = ones(LL,1)* yy;
yy3 = ones(LL,MY,MX);
yy3(:) = yy2(:)*ones(1,MX);

zz2 = ones(LL,MY);
zz3 = ones(LL,MY,MX);
zz3(:) = zz2(:)*zz;

latt_pp = ones(LL*MY*MX*4,5);
latt_pp = [[zz3(:) yy3(:) xx3(:) ones(LL*MY*MX,1) pseudo(1,:)'];[zz3(:)
yy3(:) xx3(:) 2*ones(LL*MY*MX,1) pseudo(2,:)'];[zz3(:) yy3(:) xx3(:)
3*ones(LL*MY*MX,1) pseudo(3,:)'];[zz3(:) yy3(:) xx3(:) 4*ones(LL*MY*MX,1)
pseudo(4,:)']];

latt_pp = sortrows(latt_pp,-5);
latt_pp = latt_pp';

fid = fopen('pseudo.txt','w');
fprintf(fid,'%4s %4s %4s %4s  %s \r\n\r\n','x','y','z','A/S','Pseudo');
fprintf(fid,'%4d %4d %4d %4d  %1.15E \r\n',latt_pp);

fclose(fid);
```

Appendix B

PCA and NMF based computer programs

pca1.m

```
function [A S E] = pca(n,type)

%n: objects numbers

fid = fopen('input_data.txt', 'r');
prm = fscanf(fid,'%f',21);       %the reflective index of scattering medium
delta = prm(16:21);
fclose(fid);

fid = fopen('geometry.txt', 'r');
ISNX = fscanf(fid,'%f',1);
ISNY = fscanf(fid,'%f',1);
IDNX = fscanf(fid,'%f',1);
IDNY = fscanf(fid,'%f',1);
MX = fscanf(fid,'%f',1);
MY = fscanf(fid,'%f',1);
LL = fscanf(fid,'%f',1);
fclose(fid);

disp('enter exp data');
ryd=zeros(IDNY,IDNX,ISNY,ISNX);
fid = fopen('signal.txt','r');
ryd(:) = fscanf(fid,'%f')';
fclose(fid);

x = reshape(ryd,IDNY*IDNX,ISNY*ISNX);
if type==1
    x(x<0)=0;
end

M = ISNY*ISNX;
N = IDNY*IDNX;

MM = mean(x,2);
Y=x-repmat(MM,1,M);

[A,D] = svd(Y,0);
E = dot(D',D');
E = E/N;

A = A(:,1:n); E = E(1:n);
S = pinv(A)*x;

for ii = 1:n
    if max(A(:,ii))*max(S(ii,:))<min(A(:,ii))*min(S(ii,:))
        A(:,ii)=-A(:,ii);S(ii,:)=-S(ii,:);
```

```
    end
    figure; set(gcf,'position',[100 300 500 200]);

    a1 = A(:,ii);
    s1 = S(ii,:);
    x1 = a1*s1;

    a11 = reshape(a1,IDNY,IDNX);
    s11 = reshape(s1,ISNY,ISNX);
    x11 = reshape(x1,IDNY,IDNX,ISNY,ISNX);

    for nsy = 1:ISNY
        for nsx = 1:ISNX
            x12 = squeeze(x11(:,:,nsy,nsx));

            [ym, jm] = max(x12);
            [yM, im] = max(ym);
            jm = jm(im);
            %xi(ii) = im;
            %yj(ii) = jm;
            jmn(nsy,nsx) = jm;
            imn(nsy,nsx) = im;
        end
    end

    im = mean(imn(:));
    jm = mean(jmn(:));

    fprintf('The component intensity is peaked at i = %d and j
= %d\n',int16(im),int16(jm));
    subplot(1,2,1);
    imagesc(a11);
    colormap(gray);
    title('Image on detector plane');
    xlabel('x(mm)');
    ylabel('y(mm)');
    set(get(gca,'children'),'xdata',delta(5)*[0 IDNX-1]);
    set(get(gca,'children'),'ydata',delta(6)*[0 IDNY-1]);
    axis equal;
    set(gca,'xlim',delta(5)*[0 IDNX-1]);
    set(gca,'ylim',delta(6)*[0 IDNY-1]);
    set(gca,'fontsize',12);
    set(get(gca,'title'),'fontsize',12);

    subplot(1,2,2);
    imagesc(s11);
    colormap(gray);
    title('Image on source plane');
    xlabel('x(mm)');
    ylabel('y(mm)');
    set(get(gca,'children'),'xdata',delta(1)*[0.5 ISNX-0.5]);
    set(get(gca,'children'),'ydata',delta(2)*[0.5 ISNY-0.5]);
    axis equal;
    set(gca,'xlim',delta(1)*[0.5 ISNX-0.5]);
    set(gca,'ylim',delta(2)*[0.5 ISNY-0.5]);
```

```
    set(gca,'fontsize',12);
    set(get(gca,'title'),'fontsize',12);

end
```

fitpos.m

```
function [pars,fitdata,resnorm] = fitpos(a,s,type,dx,dy)
% [pars,resnorm] = fitpos(a,s) %fit position of an object(source)
% find the location of the target r and scaling factors by fitting a and s;
%
% a is a certain column of the mixing matrix A
% s is a certain row of component in source matrix B
% type: 0/'abs' - absorption 1/'sca' - scattering
% dx, dy: coordinates mapping - coordinates of the origin of source plane in
the
%   detector plane, x - dx = x', y - dy = y', where x,y are detector plane
%   coordinates, x',y' are source plane coordinates
% by: Binlin Wu 06/2008
% CCNY-CUNY

global dx0 dy0
dx0 = dx; dy0 = dy;

if type==0 || isequal(type,'abs')
    kkey = 0; % for absorption
elseif type ==1 || isequal(type,'sca')
    kkey = 1; % for scattering
else
    disp('fitpos(a,s,type) where type is 0/''abs'' or 1/''sca''');
    return
end

%%read in geometry
fid = fopen('geometry.txt', 'r');
ISNX = fscanf(fid,'%f',1);
ISNY = fscanf(fid,'%f',1);
IDNX = fscanf(fid,'%f',1);
IDNY = fscanf(fid,'%f',1);
MX = fscanf(fid,'%f',1);
MY = fscanf(fid,'%f',1);
%LL = fscanf(fid,'%f',1);
fclose(fid);

%%read in parameters
fid = fopen('input_data.txt', 'r');

%read_in data
n1 = fscanf(fid,'%f',2);        %the reflective index of scattering medium
n2 = fscanf(fid,'%f',2);        %the reflective index of wall (i.e. glass)
n3 = fscanf(fid,'%f',2);        %the reflective index of outside (i.e. air)
lld = fscanf(fid,'%f',1);       %scattering mediu thickness
```

```
mua = fscanf(fid,'%f',1);       %absorption coefficient
lt = fscanf(fid,'%f',1);        %transport length
nd = fscanf(fid,'%f',1);        %scattering medium refraction index
omega = fscanf(fid,'%f',1);     %modulation frequency, 0 for cw
z0 = fscanf(fid,'%f',1);        %depth of the center of the first voxel
dz = fscanf(fid,'%f',1);        %z direction division of the scattering medium
zs = fscanf(fid,'%f',1);        %source position
zd = fscanf(fid,'%f',1);        %detector position
delta = fscanf(fid,'%f',6);     %step interval in x and y
rate = fscanf(fid,'%f',2);      %noise level
dmu = fscanf(fid,'%f',2);       %change in mu of the inhomogeneities
key = fscanf(fid,'%d',1);       %switch for judging the signal from the noise
space, either by readin number r_mm or automatic judging with r_ratio
r_mm = fscanf(fid,'%d',1);      %signal space rank
r_ratio = fscanf(fid,'%f',1);   %cutoff threshold for signal space
key2 = fscanf(fid,'%d',1);      %switch for normalization of the pseudo
spectrum

fclose(fid);

%calculate extrapolation distance
ze = calc_ze(n1,n2,n3);

%find maxima
x = a*s;
a = reshape(a,IDNY,IDNX);
s = reshape(s,ISNY,ISNX);
x1 = reshape(x,IDNY,IDNX,ISNY,ISNX);
for nsy = 1:ISNY
    for nsx = 1:ISNX
        x2 = squeeze(x1(:,:,nsy,nsx));
        [ym, jm] = max(x2);
        [yM, im] = max(ym);
        jm = jm(im);
        jmn(nsy,nsx) = jm;
        imn(nsy,nsx) = im;
    end
end

% im = mean(imn(:));
% jm = mean(jmn(:));

x12 = squeeze(x1(:,:,ceil(ISNY/2),ceil(ISNX/2)));
[ym, jm] = max(x12);
[yM, im] = max(ym);
jm = jm(im);

x=(im-1)*delta(3);
y=(jm-1)*delta(4);

[ym, jma] = max(a);
[yM, ima] = max(ym);
jma = jma(ima);
xma=(ima-1)*delta(5);
yma=(jma-1)*delta(6);
```

```
[ym, jms] = max(s);
[yM, ims] = max(ym);
jms = jms(ims);
xms=(ims-1)*delta(1);
yms=(jms-1)*delta(2);

%%%%%% first normalize a and s %%%%%%
gamma1 = 1/max(s(:));
gamma2 = 1/max(a(:));
s = s*gamma1;
a = a*gamma2;

%%%%% generate positions %%%%%%%%%
x_xs = zeros(ISNY,ISNX);
y_ys = zeros(ISNY,ISNX);
nsx = 1:ISNX;
nsy = 1:ISNY;

x_xd = zeros(IDNY,IDNX);
y_yd = zeros(IDNY,IDNX);
ndx = 1:IDNX;
ndy = 1:IDNY;

%2d positions
x_xs = ones(ISNY,1)*(delta(1)*(nsx-1)-xms+dx0) + srcX;
y_ys = (delta(2)*(nsy-1)-yms+dy0)'*ones(1,ISNX) + srcY;

x_xd = ones(IDNY,1)*(delta(5)*(ndx-1)-xma) + dtrX;
y_yd = (delta(6)*(ndy-1)-yma)'*ones(1,IDNX) + dtrY;


%%%%%%%%%% initialization %%%%%%%%%%%%

%kkey = 0; %0: abs; 1: sca

% set z initial value in the middle of the volume
l=fix(lld/dz/2);
z = z0+(l-1)*dz;

% calculate alpha_inv, beta_inv, b1 and b2 initial values
grhandles = gr;
if (kkey == 0)
    rcgrd = zeros(size(x_xs));
    icgrd = rcgrd;
    rbb = rcgrd;
    ibb = rcgrd;
    [rcgrd,icgrd] = grhandles.cgrd(ze,lld,mua,lt,nd,omega,x_xs,y_ys,z,zs);
    rbb = rcgrd;
    alpha =
sign(mean(s(:)))*sign(mean(rcgrd(:)))*max(abs(s(:)))/max(abs(rcgrd(:)));
    b1 = std(s(:) - alpha*rcgrd(:));
else
    rsgrd = zeros([3 size(x_xs)]);
    isgrd = rsgrd;
```

```
    rsb = rsgrd;
    isb = rsgrd;
    [rsgrd,isgrd] = grhandles.sgrd(ze,lld,mua,lt,nd,omega,x_xs,y_ys,z,zs);
    rsb = rsgrd;
    alpha =
sign(mean(s(:)))*sign(mean(rsgrd(3,:)))*max(abs(s(:)))/max(abs(rsgrd(3,:)));
    b1 = std(s(:) - alpha*rsgrd(3,:)');
end

%calculate green's functions G(rm,rd)

if(kkey == 0)
    rcgrd = zeros(size(x_xd));
    icgrd = rcgrd;
    [rcgrd,icgrd] = grhandles.cgrd(ze,lld,mua,lt,nd,omega,x_xd,y_yd,z,zd);
    beta =
sign(mean(a(:)))*sign(mean(rcgrd(:)))*max(abs(a(:)))/max(abs(rcgrd(:)));
    b2 = std(a(:) - beta*rcgrd(:));
else
    rsgrd = zeros([3 size(x_xd)]);
    isgrd = rsgrd;
    [rsgrd,isgrd] = grhandles.sgrd(ze,lld,mua,lt,nd,omega,x_xd,y_yd,z,zd);
    beta = -
sign(mean(a(:)))*sign(mean(rsgrd(3,:)))*max(abs(a(:)))/max(abs(rsgrd(3,:)));
    b2 = std(a(:) - beta*rsgrd(3,:)');
end

pars0=[x y z alpha beta b1 b2];


options = optimset('MaxFunEvals',1e4,'MaxIter',1e4,'TolX',1e-7);
err =
@(pars)fitpos_err(pars,s,a,ze,lld,mua,lt,nd,omega,zs,zd,delta,kkey,xms,yms,xm
a,yma);
[pars,resnorm] = fminsearch(err,pars0,options);

x = pars(1);
y = pars(2);
z = pars(3);
alpha = pars(4);
beta = pars(5);
b1 = pars(6);
b2 = pars(7);

%%%%%%%%%%%%%%%%%%%%%%%%%%%%%%%% plot %%%%%%%%%%%%%%%%%%%%%%%%%%%%%%%%

%%%%% generate positions %%%%%%%%%
x_xs = zeros(ISNY,ISNX);
y_ys = zeros(ISNY,ISNX);
nsx = 1:ISNX;
nsy = 1:ISNY;

x_xd = zeros(IDNY,IDNX);
y_yd = zeros(IDNY,IDNX);
ndx = 1:IDNX;
```

```
ndy = 1:IDNY;

%2d positions
x_xs = ones(ISNY,1)*(delta(1)*(nsx-1)-x+dx0);
y_ys = (delta(2)*(nsy-1)-y+dy0)'*ones(1,ISNX);

x_xd = ones(IDNY,1)*(delta(5)*(ndx-1)-x);
y_yd = (delta(6)*(ndy-1)-y)'*ones(1,IDNX);


grhandles = gr;
%calculate green functions G(rm,rs)

if (kkey == 0)
    rcgrd = zeros(size(x_xs));
    icgrd = rcgrd;
    rbb = rcgrd;
    ibb = rcgrd;
    [rcgrd,icgrd] = grhandles.cgrd(ze,lld,mua,lt,nd,omega,x_xs,y_ys,z,zs);
    rbb = rcgrd;
else
    rsgrd = zeros([3 size(x_xs)]);
    isgrd = rsgrd;
    rsb = rsgrd;
    isb = rsgrd;
    [rsgrd,isgrd] = grhandles.sgrd(ze,lld,mua,lt,nd,omega,x_xs,y_ys,z,zs);
    rsb = rsgrd;
end

%calculate green functions G(rm,rd)
if(kkey == 0)
    rcgrd = zeros(size(x_xd));
    icgrd = rcgrd;
    [rcgrd,icgrd] = grhandles.cgrd(ze,lld,mua,lt,nd,omega,x_xd,y_yd,z,zd);

    subplot(2,2,1);
    plot(delta(1)*(nsx-1),s(jms,1:ISNX),'o',delta(1)*(nsx-
1),alpha*rbb(jms,1:ISNX)+b1);
    title('Fitting image on source plane along x through peak');
    set(gca,'fontsize',12);
    set(get(gca,'title'),'fontsize',12);
    xlabel('x(mm)');
    ylabel('Intensity(arb. unit)');
    set(get(gca,'xlabel'),'fontsize',12);
    xlim([0 delta(1)*ISNX]);
    ylim([min([s(:); alpha*rbb(:)+b1]) max([s(:); alpha*rbb(:)+b1])]);

    subplot(2,2,2);
    plot(delta(2)*(nsy-1),s(1:ISNY,ims),'o',delta(2)*(nsy-
1),alpha*rbb(1:ISNY,ims)+b1);
    title('Fitting image on source plane along y through peak');
    set(gca,'fontsize',12);
    set(get(gca,'title'),'fontsize',12);
    xlabel('y(mm)');
    ylabel('Intensity(arb. unit)');
```

```
    set(get(gca,'ylabel'),'fontsize',12);
    xlim([0 delta(2)*ISNY]);
    ylim([min([s(:); alpha*rbb(:)+b1]) max([s(:); alpha*rbb(:)+b1])]);

    subplot(2,2,3);
    plot(delta(5)*(ndx-1),a(jma,1:IDNX),'o',delta(5)*(ndx-
1),beta*rcgrd(jma,1:IDNX)+b2);
    title('Fitting image on detector plane along x through peak');
    set(gca,'fontsize',12);
    set(get(gca,'title'),'fontsize',12);
    xlabel('x(mm)');
    ylabel('Intensity(arb. unit)');set(get(gca,'xlabel'),'fontsize',12);
    xlim([0 delta(5)*IDNX]);
    ylim([min([a(:); beta*rcgrd(:)+b2]) max([a(:); beta*rcgrd(:)+b2])]);

    subplot(2,2,4);
    plot(delta(6)*(ndy-1),a(1:IDNY,ima),'o',delta(6)*(ndy-
1),beta*rcgrd(1:IDNY,ima)+b2);
    title('Fitting image on detector plane along y through peak');
    set(gca,'fontsize',12);
    set(get(gca,'title'),'fontsize',12);
    xlabel('y(mm)');
    ylabel('Intensity(arb. unit)');set(get(gca,'ylabel'),'fontsize',12);
    xlim([0 delta(6)*IDNY]);
    ylim([min([a(:); beta*rcgrd(:)+b2]);max([a(:); beta*rcgrd(:)+b2])]);
else
    rsgrd = zeros([3 size(x_xd)]);
    isgrd = rsgrd;
    [rsgrd,isgrd] = grhandles.sgrd(ze,lld,mua,lt,nd,omega,x_xd,y_yd,z,zd);

    subplot(2,2,1);
    plot(delta(1)*(nsx-1),s(jms,1:ISNX),'o',delta(1)*(nsx-
1),alpha*squeeze(rsb(3,jms,1:ISNX)+b1)');
    title('Fitting image on source plane along x through peak');  %2d
    set(gca,'fontsize',12);
    set(get(gca,'title'),'fontsize',12);
    xlabel('x(mm)');
    ylabel('Intensity(arb. unit)');
    set(get(gca,'xlabel'),'fontsize',12);
    xlim([0 delta(1)*ISNX]);
    ylim([min([s(:)' alpha*rsb(3,:)+b1]) max([s(:)'
alpha*rsb(3,:)+b1])]); %2d

    subplot(2,2,2);
    plot(delta(2)*(nsy-1),s(1:ISNY,ims),'o',delta(2)*(nsy-
1),alpha*rsb(3,1:ISNY,ims)+b1);
    title('Fitting image on source plane along y through peak'); %2d
    set(gca,'fontsize',12);
    set(get(gca,'title'),'fontsize',12);
    ylabel('y(mm)');
    ylabel('Intensity(arb. unit)');
    set(get(gca,'ylabel'),'fontsize',12);
    xlim([0 delta(2)*ISNY]);
    ylim([min([s(:)' alpha*rsb(3,:)+b1]) max([s(:)' alpha*rsb(3,:)+b1])]);

    subplot(2,2,3);
```

```
    plot(delta(5)*(ndx-1),a(jma,1:IDNX),'o',delta(5)*(ndx-
1),beta*squeeze(rsgrd(3,jma,1:IDNX)+b2)');
    title('Fitting image on detector plane along x through peak'); %2d
    set(gca,'fontsize',12);
    set(get(gca,'title'),'fontsize',12);
    xlabel('x(mm)');
    ylabel('Intensity(arb. unit)');
    set(get(gca,'xlabel'),'fontsize',12);
    xlim([0 delta(5)*IDNX]);
    ylim([min([a(:)' beta*rsgrd(3,:)+b2]) max([a(:)' beta*rsgrd(3,:)+b2])]);

    subplot(2,2,4);
    plot(delta(6)*(ndy-1),a(1:IDNY,ima),'o',delta(6)*(ndy-
1),beta*rsgrd(3,1:IDNY,ima)+b2);
    title('Fitting image on detector plane along y through peak'); %2d
    set(gca,'fontsize',12); set(get(gca,'title'),'fontsize',12);
    ylabel('y(mm)');
    ylabel('Intensity(arb. unit)');set(get(gca,'ylabel'),'fontsize',12);
    xlim([0 delta(6)*IDNY]);
    ylim([min([a(:)' beta*rsgrd(3,:)+b2]) max([a(:)'
beta*squeeze(rsgrd(3,:)+b2)'])]); %2d
end


%%%%%% print results %%%%%%%%%
alpha = pars(4)/gamma1;
beta = pars(5)/gamma2;
strength = alpha*beta;
fprintf('\nObject location: x = %fmm; y = %fmm; z = %fmm\r\n',x,y,z);
fprintf('Scaling factors: alpha = %1.14f; beta = %1.14f; strength
= %1.14f\r\n',alpha,beta,strength);
fprintf('Intercept/Background: b1 = %1.14f; b2 = %1.14f\r\n',b1,b2);

if type == 0
    fitdata = rcgrd;
else
    fitdata = rsgrd;
end

return


function err =
fitpos_err(pars,s,a,ze,lld,mua,lt,nd,omega,zs,zd,delta,kkey,xms,yms,xma,yma)
global dx0 dy0

%%read in geometry
fid = fopen('geometry.txt', 'r');
ISNX = fscanf(fid,'%f',1);
ISNY = fscanf(fid,'%f',1);
IDNX = fscanf(fid,'%f',1);
IDNY = fscanf(fid,'%f',1);
MX = fscanf(fid,'%f',1);
MY = fscanf(fid,'%f',1);
LL = fscanf(fid,'%f',1);
```

```
fclose(fid);
grhandles = gr;

x = pars(1);
y = pars(2);
z = pars(3);
alpha = pars(4);
beta = pars(5);
b1 = pars(6);
b2 = pars(7);

%%%%% generate positions %%%%%%%%%
x_xs = zeros(ISNY,ISNX); %only a horizontal line
y_ys = zeros(ISNY,ISNX); %only a vertical line
nsx = 1:ISNX;
nsy = 1:ISNY;

x_xd = zeros(IDNY,IDNX); %only a horizontal line
y_yd = zeros(IDNY,IDNX); %only a vertical line
ndx = 1:IDNX;
ndy = 1:IDNY;

x_xs = ones(ISNY,1)*(delta(1)*(nsx-1)-x+dx0);
y_ys = (delta(2)*(nsy-1)-y+dy0)'*ones(1,ISNX);

x_xd = ones(IDNY,1)*(delta(5)*(ndx-1)-x);
y_yd = (delta(6)*(ndy-1)-y)'*ones(1,IDNX);

%calculate green functions G(rs,rm)
if (kkey == 0)
    rcgrd = zeros(size(x_xs));
    icgrd = rcgrd;
    rbb = rcgrd;
    ibb = rcgrd;
    [rcgrd,icgrd] = grhandles.cgrd(ze,lld,mua,lt,nd,omega,x_xs,y_ys,z,zs);
    rbb = rcgrd;
else
    rsgrd = zeros([3 size(x_xs)]);
    isgrd = rsgrd;
    rsb = rsgrd;
    isb = rsgrd;
    [rsgrd,isgrd] = grhandles.sgrd(ze,lld,mua,lt,nd,omega,x_xs,y_ys,z,zs);
    rsb = rsgrd;
end

%calculate green functions G(rm,rd)
if(kkey == 0)
    rcgrd = zeros(size(x_xd));
    icgrd = rcgrd;
    [rcgrd,icgrd] = grhandles.cgrd(ze,lld,mua,lt,nd,omega,x_xd,y_yd,z,zd);
    err11 = (s(:) - alpha*rbb(:) - b1).^2;
    err12 = (a(:) - beta*rcgrd(:) - b2).^2;
    err =
sum(err11(:))/length(s(:))/var(s(:))+sum(err12(:))/length(a(:))/var(a(:));
```

```
else
    rsgrd = zeros([3 size(x_xd)]);
    isgrd = rsgrd;
    [rsgrd,isgrd] = grhandles.sgrd(ze,lld,mua,lt,nd,omega,x_xd,y_yd,z,zd);

    err11 = (s(:) - alpha*rsb(3,:)' - b1).^2;
    err12 = (a(:) - beta*rsgrd(3,:)' - b2).^2;
    err =
sum(err11(:))/length(s(:))/var(s(:))+sum(err12(:))/length(a(:))/var(a(:));
end
```

backprojection.m

```
function backproj(A,z,lambda)
% A is the NCID/ICID/PCID
% z is the z-position of the target
% lambda is the optimal regularization number chosen from the L-curve

close all
% ---------------- initialization -------------------------
fid = fopen('geometry.txt', 'r');
ISNX = fscanf(fid,'%f',1);
ISNY = fscanf(fid,'%f',1);
IDNX = fscanf(fid,'%f',1);
IDNY = fscanf(fid,'%f',1);
MX = fscanf(fid,'%f',1);
MY = fscanf(fid,'%f',1);
fclose(fid);

fid = fopen('input_data.txt', 'r');
n1 = fscanf(fid,'%f',2);       %the reflective index of scattering medium
n2 = fscanf(fid,'%f',2);       %the reflective index of wall (i.e. glass)
n3 = fscanf(fid,'%f',2);       %the reflective index of outside (i.e. air)
lld = fscanf(fid,'%f',1);      %scattering mediu thickness
mua = fscanf(fid,'%f',1);      %absorption coefficient
lt = fscanf(fid,'%f',1);       %transport length
nd = fscanf(fid,'%f',1);       %scattering medium refraction index
omega = fscanf(fid,'%f',1);    %modulation frequency, 0 for cw
z0 = fscanf(fid,'%f',1);       %depth of the center of the first voxel
dz = fscanf(fid,'%f',1);       %z direction division of the scattering medium
zs = fscanf(fid,'%f',1);       %source position
zd = fscanf(fid,'%f',1);       %detector position
delta = fscanf(fid,'%f',6);    %step interval in x and y
rate = fscanf(fid,'%f',2);     %noise level
dmu = fscanf(fid,'%f',2);      %change in mu of the inhomogeneities
key = fscanf(fid,'%d',1);      %switch for judging the signal from the noise
space, either by readin number r_mm or automatic judging with r_ratio
r_mm = fscanf(fid,'%d',1);     %signal space rank
r_ratio = fscanf(fid,'%f',1);  %cutoff threshold for signal space
key2 = fscanf(fid,'%d',1);     %switch for normalization of the pseudo
spectrum
fclose(fid);
```

```
ze = calc_ze(n1,n2,n3);
grhandles = gr;

%% ---------------- Initialization --------------------------------------
x_xd = ones(IDNY*2-1,1)*(-IDNX+1:IDNX-1)*delta(5);
y_yd = (-IDNY+1:IDNY-1)'*delta(6)*ones(1,IDNX*2-1);
gd = grhandles.cgrd(ze,lld,mua,lt,nd,omega,x_xd,y_yd,z,zd);
gd1 = [gd zeros(2*IDNY-1,2*IDNX-2);zeros(2*IDNY-2,2*IDNX-1+2*IDNX-2)];
gd1f = fft2(gd1);

A1 = zeros(4*IDNY-3,4*IDNX-3);
A1(IDNY:2*IDNY-1,IDNX:2*IDNX-1)=reshape(A(:,1),IDNY,IDNX);
A1f = fft2(A1);

%% -- Tikholov regularization on Ax = b, check in Fourier domain START
% (conj(A)A+lambda) x = conj(A)b => x = conj(A)b/(conj(A)A+lambda)
k = 1;
h = waitbar(0,'Please wait...');
clear A1f_recon X1f

for lambda = 1:100
X1f(:,:) = conj(gd1f).*A1f./(conj(gd1f).*gd1f +
min(min(real(conj(gd1f).*gd1f)))*10^lambda);
A1f_recon(:,:) = X1f(:,:).*gd1f;

resNorm(k) = log(sqrt(squeeze(sum(sum(abs((A1f_recon(:,:)-A1f).^2))))));
solNorm(k) = log(sqrt(squeeze(sum(sum(abs(X1f(:,:).^2))))));

waitbar((lambda)/100,h);
k = k + 1;
end
close(h)

% plot L-curve
figure(1)
plot(resNorm,solNorm)
set(gca,'fontsize',12); set(get(gca,'title'),'fontsize',12);
xlabel('Residue norm (arb. units)')
ylabel('Solution norm (arb. units)')

%% choose corner from L-curve
%lambda = 25
X1f(:,:) = conj(gd1f).*A1f./(conj(gd1f).*gd1f +
min(min((real(conj(gd1f).*gd1f))))*10^lambda);
X1_recon = ifft2(X1f(:,:));

%% -- plot cross section image --
X1s = X1_recon(1:IDNY,1:IDNX);
% X1s([1 end],:) = 0; X1s(:,[1 end]) = 0;
figure(2)

[yy,xx]=find(X1s==max(X1s(:)));
set(gcf,'position',[100 300 900 250]);

subplot(1,2,2);
```

```
plot((0:IDNX-1)*delta(5),X1s(yy,:),'linewidth',2);
hold on
plot((0:IDNY-1)*delta(6),X1s(:,xx),'--','linewidth',2);
xlim([0 IDNX*delta(5)])
set(gca,'fontsize',12);
xlabel('x (mm)');
ylabel('X (arb. units)');
legend('x','y')

subplot(1,2,1);
imagesc(X1s,'xdata',delta(5)*[0:IDNX-1],'ydata',delta(6)*[0:IDNY-1]);
colorbar
axis equal tight;
hold on
plot((0:IDNX-1)*delta(5),ones(1,IDNX)*(yy-1)*delta(5),'w','LineWidth',2)
plot(ones(1,IDNY)*(xx-1)*delta(6),(0:IDNY-1)*delta(6),'w--','LineWidth',2)
set(gca,'fontsize',12);
set(get(gca,'title'),'fontsize',12);
set(get(gca,'xlabel'),'FontSize',12);
set(get(gca,'ylabel'),'FontSize',12);
xlabel('x (mm)');
ylabel('y (mm)');



%% find FWHM in the cross section image

[xm,xM]=searchMin(X1s(yy,:),xx);
[ym,yM]=searchMin(X1s(:,xx),yy);
if X1s(yy,xm) < 0
x1 = interp1(X1s(yy,xm:xx),xm:xx,(X1s(yy,xx))/2);
else
x1 = interp1(X1s(yy,xm:xx),xm:xx,(X1s(yy,xx)+X1s(yy,xm))/2);
end



if X1s(yy,xM) < 0
x2 = interp1(X1s(yy,xx:xM),xx:xM,(X1s(yy,xx))/2);
else
x2 = interp1(X1s(yy,xx:xM),xx:xM,(X1s(yy,xx)+X1s(yy,xM))/2);
end

if X1s(ym,xx) < 0
y1 = interp1(X1s(ym:yy,xx),ym:yy,(X1s(yy,xx))/2);
else
y1 = interp1(X1s(ym:yy,xx),ym:yy,(X1s(yy,xx)+X1s(ym,xx))/2);
end

if X1s(yM,xx) < 0
y2 = interp1(X1s(yy:yM,xx),yy:yM,(X1s(yy,xx))/2);
else
y2 = interp1(X1s(yy:yM,xx),yy:yM,(X1s(yy,xx)+X1s(yM,xx))/2);
end

dX = (x2-x1)*delta(5)
```

```
dY = (y2-y1)*delta(6)


function [xm,xM]=searchMin(y,x0)
D = length(y);
x = x0;
while 1
    if x - 1 < 1
        xm = x;
        break
    end
    if y(x-1)>=y(x)
        xm = x;
        break
    end
    x = x-1;
end

x = x0;
while 1
    if x+1 > D
        xM = x;
        break
    end
    if y(x+1)>=y(x)
        xM = x;
        break
    end
    x = x+1;
end
return
```

Appendix C

List of Patents, Publications and Presentations

List of Patents

Binlin Wu, Wei Cai, and Swapan K. Gayen, "*Time reversal optical tomography*," U.S. Patent Provisional Application Serial No. 61/716,762.

List of Publications

Journal Articles

1. **Binlin Wu**, W. Cai, S. K. Gayen, "Three-dimensional optical fluorescence imaging using time reversal optical tomography," Appl. Phys. Lett. **101**, 251103 (2012).
2. **Binlin Wu**, W. Cai, S. K. Gayen, "Time Reversal Optical Tomography," Optics and Photonics News (OPN), Vol. 23, Optics in 2012 (Issue 12), pp. 41-41 (2012). (Selected by the Editors for publication in the Virtual Journal for Biomedical Optics (VJBO), Volume 8, Issue 1, Topic "Diffuse Imaging, Tissue Optics, and Scattering". http://www.opticsinfobase.org/vjbo/abstract.cfm?uri=opn-23-12-41).
3. **Binlin Wu**, M. Alrubaiee, W. Cai, M. Xu and S. K. Gayen, "Diffuse optical imaging using decomposition methods," Int. J. Opt. **2012**, 185435 (2012).
4. **Binlin Wu**, W. Cai, M. Alrubaiee, M. Xu and S. K. Gayen, "Time reversal optical tomography: locating targets in a highly scattering turbid medium," Opt. Express **19**, 21956-21976 (2011). (Selected by the Editors, Andrew Dunn and Anthony Durkin, for publication in the Virtual Journal for Biomedical Optics (VJBO), Volume 6, Issue 11, Topic "Diffuse Imaging, Tissue Optics, and Scattering". http://www.opticsinfobase.org/vjbo/abstract.cfm?uri=oe-19-22-21956).

5. **Binlin Wu** and S. K. Gayen, “Fluorescence tomography of targets in a turbid medium using nonnegative matrix factorization”, submitted to Phys. Rev. E (2013).

Conference Proceedings

1. **Binlin Wu**, W. Cai, S. K. Gayen, “Time reversal optical tomography locates fluorescent targets in a turbid medium,” in Multimodal Biomedical Imaging VIII. Proceedings of SPIE, vol. 8574, 85740N-1 – 85740N-8 (2013).
2. **Binlin Wu**, W. Cai, M. Xu and S. K. Gayen, “Time-reversal optical tomography: detecting and locating extended targets in a turbid medium”, in Multimodal Biomedical Imaging VI. Proceeding of SPIE, vol. 8216, 82160K-1 – 82160K-5 (2012).
3. **Binlin Wu**, W. Cai, M. Alrubaiee, M. Xu and S. K. Gayen, “Three-dimensional time-reversal optical tomography”, in Multimodal Biomedical Imaging VI. Proceeding of SPIE, vol. 7892, pp. 78920G-1 – 78920G-6 (2011).
4. M. Alrubaiee, **B. Wu**, M. Xu, W. Cai, and S. K. Gayen, “Independent component analysis and time reversal algorithms”, in Diffuse Optical Imaging III. Proceeding of SPIE-OSA, vol. 8088, pp. 80880Y-1 – 80880Y-5 (2011).

List of Presentations

1. **Binlin Wu**, W. Cai, S. K. Gayen, “Time reversal optical tomography locates fluorescent targets in a turbid Medium,” Paper 8574-1 presented at the SPIE’s International Symposium on Multimodal Biomedical Imaging VIII, BIOS’13/Photonics West, 2-7 January, San Francisco, California.
2. **Binlin Wu**, W. Cai, M. Xu, and S. K. Gayen, “Time-reversal optical tomography: detecting and locating extended targets in a turbid medium,” Paper 8216-19 presented at the SPIE’s

International Symposium on Multimodal Biomedical Imaging VII, BIOS'12/Photonics West, 21-26 January, San Francisco, California.

3. **Binlin Wu**, W. Cai, M. Alrubaiee, M. Xu, and S. K. Gayen, "Time reversal optical tomography for breast tumor detection", Paper BC060114-2962 presented at the 6th Era of Hope 2011 conference of Department of Defense (DOD) Breast Cancer Research Program (BCRP), 2 – 5 August, Orlando, Florida.
4. M. Alrubaiee, **Binlin Wu**, M. Xu, W. Cai, S. K. Gayen, "Multi-wavelength diffusive optical tomography using independent component analysis and time reversal algorithms", Paper 8088-33 presented at the SPIE's International Symposium on Diffuse Optical Imaging III, European Conferences on Biomedical Optics (ECBO) 2011, 22-26 May, Munich, Germany.
5. **Binlin Wu**, W. Cai, M. Alrubaiee, M. Xu and S. K. Gayen, "Three-dimensional time-reversal optical tomography ", Paper 7892-15 presented at the SPIE's International Symposium on Multimodal Biomedical Imaging VI, BIOS'11/Photonics West, 22-27 January, San Francisco, California.
6. **Binlin Wu**, M. Alrubaiee, W. Cai, M. Xu, and S. K. Gayen, "Optical imaging of objects in turbid media using principal component analysis and time reversal matrix methods," paper JTuC10 presented at Frontier in Optics (FiO), OSA's Annual Meeting on Computational Optical Sensing and Imaging, October 11, 2009, San Jose, California.
7. **Binlin Wu**, S. K. Gayen, and M. Xu, "Native excitation and emission matrix fluorescence spectroscopy for quantification of tissue native fluorophores and cancer diagnosis," submitted to Therapeutics and Diagnostics in Urology, SPIE Photonics West (2014).

Bibliography

Chapter 1

1. A. Ishimaru, *Wave Propagation and Scattering in Random Media* (Academic Press, New York, 1978).
2. S. K. Gayen, and R. R. Alfano, "Emerging optical biomedical imaging techniques," Opt. Photonics News **7**, 22 (1996).
3. S. K. Gayen, and R. R. Alfano, "Sensing lesions in tissues with light," Opt. Express **4**, 475 (1999).
4. S. Chandrasekhar, *Radiative Transfer* (Clarendon, Oxford, 1950).
5. M. S. Patterson, B. Chance, and B. C. Wilson, "Time resolved reflectance and transmittance for the noninvasive measurement of tissue optical properties," Appl. Opt. **28**, 2331-2336 (1989).
6. A. Ishimaru, "Diffusion of a pulse in densely distributed scatterers," J. Opt. Soc. Am. A **68**, 1045-1050 (1978).
7. K. Furutsu, "On the diffusion equation derived from the space-time transport equation," J. Opt. Soc. Am. A **70**, 360-366 (1980).
8. S. R. Arridge, "Optical tomography in medical imaging," Inverse Probl. **15**, R41-R93 (1999).
9. S. R. Arridge, and J. C. Hebden, "Optical imaging in medicine: II. Modelling and reconstruction," Phys. Med. Biol. **42** 841-853 (1997).
10. S. R. Arridge, and J. C. Schotland, "Optical tomography: forward and inverse problems," Inverse Probl. **25**, 123010 (2009).
11. J. C. Hebden, S. R. Arridge, and D. T. Delpy, "Optical imaging in medicine: I. Experimental techniques," Phys. Med. Biol. **42** 825-840 (1997).

12. A. Hyvärinen, J. Karhunen, and E. Oja, *Independent Component Analysis* (Wiley, New York, 2001).

13. M. Xu, M. Alrubaiee, S. K. Gayen, and R. R. Alfano, "Optical imaging of turbid media using independent component analysis: theory and simulation," J. Biomed. Opt. **10**, 051705 (2005).

14. M. Xu, M. Alrubaiee, S. K. Gayen, and R. R. Alfano, "Three-dimensional localization and optical imaging of objects in turbid media using independent component analysis," Appl. Opt. **44**, 1889-1897 (2005).

15. M. Xu, M. Alrubaiee, S. K. Gayen, and R. R. Alfano, "Optical diffuse imaging of an *ex vivo* model cancerous human breast using independent component analysis," IEEE J. Sel. Top. Quantum Electron. **14**, 43-49 (2008).

16. I. T. Jolliffe, *Principal Component Analysis* (Springer, New York, 1986).

17. B. Wu, M. Alrubaiee, W. Cai, M. Xu, and S. K. Gayen, "Diffuse optical imaging using decomposition methods," Int. J. Opt. **2012**, 185435 (2012).

18. D. D. Lee, and H. S. Seung, "Learning the parts of objects by non-negative matrix factorization," Nature **401**, 788-791 (1999).

19. M. W. Berry, M. Browne, A. N. Langville, V. P. Pauca, and R. J. Plemmons, "Algorithms and applications for approximate nonnegative matrix factorization," Comp. Stat. Data Anal. **52**, 155-173 (2007).

20. A. Corlu, R. Choe, T. Durduran, M. A. Rosen, M. Schweiger, S. R. Arridge, M. D. Schnall, and A. G. Yodh, "Three-dimensional *in vivo* fluorescence diffuse optical tomography of breast cancer in humans," Opt. Express **15**, 6696-6716 (2007).

21. A. Godavarty, M. J. Eppstein, C. Zhang, S. Theru, A. B. Thompson, M. Gurfinkel, and E. M. Sevick-Muraca, "Fluorescence-enhanced optical imaging in large tissue volumes using a gain modulated ICCD camera," Phys. Med. Biol. **48**, 1701-1720 (2003).

22. A. B. Milstein, S. Oh, K. J. Webb, C. A. Bouman, Q. Zhang, D. A. Boas, and R. P. Millane, "Fluorescence optical diffusion tomography," Appl. Opt. **42**, 3081-3094 (2003).

23. M. S. Patterson, and B. W. Pogue, "Mathematical model for time-resolved and frequency-domain fluorescence spectroscopy in biological tissues," Appl. Opt. **33**, 1963-1974 (1994).

24. V. Ntziachristos, and R. Weissleder, "Experimental three-dimensional fluorescence reconstruction of diffuse media by use of a normalized Born approximation," Opt. Lett. **26**, 893-895 (2001).

25. I. D. Campbell, and R. A. Dwek, *Biological Spectroscopy* (Benjamin/Cummins Publishing Co. Inc., California, 1984).

26. R. R. Alfano, S. K. Gayen, and A. Katz, "Advances in mediphotonic imaging and biopsy," IS&T/OSA Optics & Imaging in the Information Age **299** (1997).

27. L. Rayleigh, "On the scattering of light by small particles," Phil. Mag. **41**, 447 (1871).

28. M. I. Mishchenko, L. D. Travis, and A. A. Lacis, *Scattering, Absorption, and Emission of Light by Small Particles* (Cambridge University Press, 2002).

29. G. Mie, "Beitrâge zur optik truber Medien, speziell kolloidaler Metalolsungen," Ann. Phys. **25**, 377 (1908).

30. A. Ishimaru, "Diffusion of light in turbid material," Appl. Opt. **28**, 2210 (1989).

31. S. L. Jacques, C. A. Alter, and S. A. Prahl, "Angular dependence of HeNe laser light scattering by human dermis," Lasers Life Sci. **1**, 309-333 (1987).

32. P. Taroni, G. Danesini, A. Torricelli, A. Pifferi, L. Spinelli, and R. Cubeddu, "Clinical trial of time-resolved scanning optical mammography at 4 wavelengths between 683 and 975 nm," J. Biomed. Opt. **9**, 464-473 (2004).

33. R. Weissleder, "A clearer vision for *in vivo* imaging," Nat. Biotechnol. **19**, 316-317 (2001).

34. F. A. Marks, "Optical determination of the hemoglobin oxygenation state of breast biopsies and human breast cancer xenografts in nude mice," Proc. SPIE **1641**, 227-237 (1992).

35. http://www.cancer.org/cancer/breastcancer/detailedguide/breast-cancer-key-statistics.

36. A. G. Yodh, and D. A. Boas, "Functional imaging with diffusing light," in *Biomedical Photonics*, T. Vo-Dinh, ed. (CRC Press, Boca Raton, 2003).

37. M. Cutler, "Transillumination as an aid in the diagnosis of breast lesions," Surg. Gynecol. Obstet. **48**, 721-729 (1929).

38. A. O. Wist, P. P. Fatouros, and S. L. Herr, "Increased spatial resolution in transillumination using collimated light," IEEE Trans. Med. Imaging **12**, 751-757 (1993).

39. W. R. Hendee, and E. R. Ritenour, *Medical Imaging Physics* (Wiley-Liss, 2002).

40. A. P. Gibson, J. C. Hebden, and S. R. Arridge, "Recent advances in diffuse optical imaging," Phys. Med. Biol. **50**, R1-R43 (2005).

41. M. Lax, V. Narayanamurti, and R. C. Fulton, "Classical diffusive photon transport in a slab," in *Proc. Symp. on Laser Optics and Condensed Matter*, J. L. Birman, H. Z. Cummins, and A. A. Kaplyanskii, eds. (Plenum, New York, 1987), pp. 229-235.

42. W. Cai, M. Lax, and R. R. Alfano, "Analytical solution of the polarized photon transport equation in an infinite uniform medium using cumulant expansion," Phys. Rev. E **63**, 016606 (2000).

43. S. R. Arridge, "Photon-measurement density functions. Part I: Analytical forms," Appl. Opt. **34**, 7395-7409 (1995).

44. K. M. Yoo, F. Liu, and R. R. Alfano, "When does the diffusion approximation fail to describe photon transport in random media?," Phys. Rev. Lett. **64**, 2647 (1990).

45. J. Crank, *The Mathematics of Diffusion* (Clarendon Press, Oxford, 1956).

46. M. Xu, "Optical image reconstruction in highly scattering media," (PhD Thesis, City University of New York, 2001).

47. X. D. Li, T. Durduran, A. G. Yodh, B. Chance, and D. N. Pattanayak, "Diffraction tomography for biochemical imaging with diffuse-photon density waves," Opt. Lett. **22**, 573-575 (1997).

48. D. A. Boas, M. A. O'Leary, B. Chance, and A. G. Yodh, "Scattering of diffuse photon density waves by spherical inhomogeneities within turbid media: analytic solution and applications," Proc. Natl. Acad. Sci. USA **91** 4887-4891 (1994).

49. S. R. Arridge, M. Cope, and D. T. Delpy, "The theoretical basis for the determination of optical pathlengths in tissue: temporal and frequency analysis," Phys. Med. Biol. **37** 1531-1559 (1992).

50. W. Cai, M. Xu, and R. R. Alfano, "Analytical form of the particle distribution based on the cumulant solution of the elastic Boltzmann transport equation," Phys. Rev. E **71**, 041202 (2005).

51. W. Cai, M. Lax, and R. R. Alfano, "Cumulant solution of the elastic Boltzmann transport equation in an infinite uniform medium," Phys. Rev. E **61**, 3871-3876 (2000).

52. W. Cai, X. Ni, S. K. Gayen, and R. R. Alfano, "Analytical cumulant solution of the vector radiative transfer equation investigates backscattering of circularly polarized light from turbid media," Phys. Rev. E **74**, 056605 (2006).

53. S. R. Arridge, M. Schweiger, M. Hiraoka, and D. T. Delpy, "A finite element approach to modeling photon transport in tissue," Med. Phys. **20**, 299-309 (1993).

54. S. R. Arridge, and M. Schweiger, "Photon-measurement density functions. Part 2: finite-element-method calculations," Appl. Opt. **34**, 841-853 (1995).

55. B. W. Pogue, M. S. Patterson, H. Jiang, and K. D. Paulsen, "Initial assessment of a simple system for frequency domain diffuse optical tomography," Phys. Med. Biol. **40** 1709-1729 (1995).

56. J. P. Culver, R. Choe, M. J. Holboke, L. Zubkov, T. Durduran, A. Slemp, V. Ntziachristos, B. Chance, and A. G. Yodh, "Three-dimensional diffuse optical tomography in the parallel plane transmission geometry: evaluation of a hybrid frequency domain/continuous wave clinical system for breast imaging," Med. Phys. **30**, 235-247 (2003).

57. A. H. Hielscher, A. D. Klose, A. K. Scheel, B. Moa-Anderson, M. Backhaus, U. Netz, and J. Beuthan, "Sagittal laser optical tomography for imaging of rheumatoid finger joints," Phys. Med. Biol. **49**, 1147-1163 (2004).

58. K. Ren, G. S. Abdoulaev, G. Bal, and A. H. Hielscher, "Algorithm for solving the equation of radiative transfer in the frequency domain," Opt. Lett. **29**, 578-580 (2004).

59. S. A. Prahl, M. Keijzer, S. L. Jacques, and A. J. Welch, "A Monte Carlo model of light propagation in tissue," in *SPIE Proceedings of Dosimetry of Laser Radiation in Medicine and Biology*, G. Mueller, and D. Sliney, eds. (1989), pp. 102-111.

60. L. Wang, and S. L. Jacques, "Hybrid model of Monte Carlo simulation and diffusion theory for light reflectance by turbid media," J. Opt. Soc. Am. A **10**, 1746-1752 (1993).

61. L. Wang, and S. L. Jacques, "Optimized radial and angular positions in Monte Carlo modeling," Med. Phys. **21**, 1081-1083 (1994).

62. L. Wang, S. L. Jacques, and L. Zheng, "MCML-Monte Carlo modeling of light transport in multi-layered tissues," Comput. Methods Programs Biomed. **47**, 131-146 (1995).

63. W. Cai, S. K. Gayen, M. Xu, M. Zevallos, M. Alrubaiee, M. Lax, and R. R. Alfano, "Optical tomographic image reconstruction from ultrafast time-sliced transmission measurements," Appl. Opt. **38**, 4237-4246 (1999).

64. A. N. Tikhonov, "Solution of incorrectly formulated problems and the regularization method," Soviet Math. Dokl. **4**, 1035-1038 (1963).

65. J. C. Schotland, "Continuous-wave diffusion imaging " J. Opt. Soc. Am. A **14**, 275-279 (1997).

66. J. C. Schotland, and V. A. Markel, "Inverse scattering with diffusing waves," J. Opt. Soc. Am. A **18**, 2767-2777 (2001).

67. V. A. Markel, and J. C. Schotland, "Symmetries, inversion formulas and image reconstruction for optical tomography," Phys. Rev. E **70**, 056616 (2004).

68. S. D. Konecky, G. Y. Panasyuk, K. Lee, V. Markel, A. G. Yodh, and J. C. Schotland, "Imaging complex structures with diffuse light," Opt. Express **16**, 5048-5060 (2008).

69. M. Xu, M. Lax, and R. R. Alfano, "Time-resolved Fourier optical diffuse tomography," J. Opt. Soc. Am. A **18**, 1535-1542 (2001).

70. M. A. O'Leary, D. A. Boas, B. Chance, and A. G. Yodh, "Experimental images of heterogeneous turbid media by frequency-domain diffusing-photon tomography," Opt. Lett. **20**, 426–428 (1995).

71. N. Kroman, J. Wohlfahrt, H. T. Mouridsen, and M. Melbye, "Influence of tumor location on breast cancer prognosis," Int. J. Cancer **105**, 542-545 (2003).

72. B. A. Brooksby, H. Dehghani, B. W. Pogue, and K. D. Paulsen, "Near-infrared (NIR) tomography breast image reconstruction with *a priori* structural information from MRI: algorithm development for reconstructing heterogeneities," IEEE J. Sel. Top. Quantum Electron. **9**, 199-209 (2003).

73. Y. Tao, Y. Wang, Y. Pei, W. Zhu, and R. L. Barbour, "Frequency-domain optical imaging of absorption and scattering distributions by a Born iterative method," J. Opt. Soc. Am. A. **14**, 325-342 (1997).

74. D. S. Kepshire, S. C. Davis, H. Dehghani, K. D. Paulsen, and B. W. Pogue, "Subsurface diffuse optical tomography can localize absorber and fluorescent objects but recovered image sensitivity is nonlinear with depth," Appl. Opt. **46**, 1669-1678 (2007).

75. P. Mohajerani, A. A. Eftekhar, and A. Adibi, "Object localization in the presence of a strong heterogeneous background in fluorescent tomography," J. Opt. Soc. Am. A **25**, 1467-1479 (2008).

76. A. Godavarty, A. B. Thompson, R. Roy, M. Gurfinkel, M. J. Eppstein, C. Zhang, and E. M. Sevick-Muraca, "Diagnostic imaging of breast cancer using fluorescence-enhanced optical tomography: phantom studies," J. Biomed. Opt. **9**, 488-496 (2004).

77. Q. Zhao, L. Ji, and T. Jiang, "Improving depth resolution of diffuse optical tomography with a layer-based sigmoid adjustment method," Opt. Express **15**, 4018-4029 (2007).

78. M. Alrubaiee, M. Xu, S. K. Gayen, M. Brito, and R. R. Alfano, "Three-dimensional optical tomographic imaging of scattering objects in tissue-simulating turbid medium using independent component analysis," Appl. Phys. Lett. **87**, 191112 (2005).

79. M. Alrubaiee, M. Xu, S. K. Gayen, and R. R. Alfano, "Localization and cross section reconstruction of fluorescent targets in *ex vivo* breast tissue using independent component analysis," Appl. Phys. Lett. **89**, 133902 (2006).

80. A. Poellinger, J. C. Martin, S. L. Ponder, T. Freund, B. Hamm, U. Bick, and F. Diekmann, "Near-infrared laser computed tomography of the breast: first clinical experience," Acad. Radiol. **15** (2008).

81. V. Ntziachristos, A. G. Yodh, M. Schnall, and B. Chance, "Concurrent MRI and diffuse optical tomography of breast after indocyanine green enhancement," Proc. Natl. Acad. Sci. **97**, 2767-2772 (2000).

82. Q. Zhu, M. Huang, N. G. Chen, K. Zarfos, B. Jagjivan, M. Kane, P. Hedge, and S. H. Kurtzman, "Ultrasound-guided optical tomographic imaging of malignant and benign breast lesions - initial clinical results of 19 cases," Neoplasia **5**, 379-388 (2003).

83. A. Li, E. L. Miller, M. E. Kilmer, T. J. Brukilacchio, T. Chaves, J. Stott, Q. Zhang, T. Wu, M. Chorlton, R. H. Moore, D. B. Kopans, and D. A. Boas, "Tomographic optical breast imaging guided by three-dimensional mammography," Appl. Opt. **42**, 5181-5190 (2003).

84. C. Prada, J.-L. Thomas, and M. Fink, "The iterative time reversal process: analysis of the convergence," J. Acoust. Soc. Am. **97** (1995).

85. A. J. Devaney, "Time reversal imaging of obscured targets from multistatic data," IEEE Trans. Antenn. Propag. **53**, 1600-1610 (2005).

86. B. Wu, W. Cai, M. Alrubaiee, M. Xu, and S. K. Gayen, "Time reversal optical tomography: locating targets in a highly scattering turbid medium," Opt. Express **19**, 21956-21976 (2011).

Chapter 2

1. W. Cai, M. Alrubaiee, S. K. Gayen, M. Xu, and R. R. Alfano, "Three-dimensional optical tomography of objects in turbid media using the round-trip matrix," Proc. SPIE **5693**, 4-9 (2005).
2. Binlin Wu, M. Alrubaiee, W. Cai, M. Xu, and S. K. Gayen, "Optical imaging of objects in turbid media using principal component analysis and time reversal matrix methods," in *Computational Optical Sensing and Imaging, OSA Technical Digest (CD) (Optical Society of America, 2009), paper JTuC10* (San Jose, California, 2009).
3. Binlin Wu, W. Cai, M. Alrubaiee, M. Xu, and S. K. Gayen, "Three dimensional time reversal optical tomography," Proc. SPIE **7892**, 78920G (2011).
4. C. Prada, F. Wu, and M. Fink, "The iterative time reversal mirror: a solution to self-focusing in the pulse echo mode," J. Acoust. Soc. Am. **90**, 1119-1129 (1991).
5. M. Fink, C. Prada, F. Wu, and D. Cassereau, "Self-focusing in inhomogeneous media with time-reversal acoustic mirrors," Proc. IEEE Ultrason. Symp. **2**, 681-686 (1989).
6. M. Fink, "Time reversal of ultrasonic fields -- part I: basic principles," IEEE Trans. Ultrason. Ferroelec. Freq. Control **39**, 555-556 (1992).
7. M. Fink, "Time reversal mirrors," J. Phys. D: Appl. Phys. **26**, 1333-1350 (1993).
8. C. Prada, J.-L. Thomas, and M. Fink, "The iterative time reversal process: analysis of the convergence," J. Acoust. Soc. Am. **97**, 62-71 (1995).
9. F. K. Gruber, E. A. Marengo, and A. J. Devaney, "Time-reversal-based imaging and inverse scattering of multiply scattering point targets," J. Acoust. Soc. Am. **118**, 3129-3138 (2005).

10. M. Fink, D. Cassereau, A. Derode, C. Prada, P. Roux, M. Tanter, J.-L. Thomas, and F. Wu, "Time-reversed acoustics," Rep. Prog. Phys. **63**, 1933-1995 (2000).
11. W. A. Kuperman, W. S. Hodgkiss, H. C. Song, T. Akal, C. Ferla, and D. R. Jackson, "Phase conjugation in the ocean: experimental demonstration of an acoustic time reversal mirror," J. Acoust. Soc. Am. **103**, 25-40 (1998).
12. G. Lerosey, J. de Rosny, A. Tourin, and M. Fink, "Focusing beyond the diffraction limit with far-field time reversal," Science **315**, 1120-1122 (2007).
13. A. J. Devaney, "Super-resolution processing of multi-static data using time reversal and MUSIC," (available online: http://www.ece.neu.edu/faculty/devaney/) (2000).
14. H. Lev-Ari, and A. J. Devaney, "The time reversal techniques re-interpreted: subspace-based signal processing for multi-static target location," in *Proc. IEEE sensor array and multichannel signal processing workshop*(2000), pp. 509-513.
15. S. K. Lehman, and A. J. Devaney, "Transmission mode time-reversal super-resolution imaging," J. Acoust. Soc. Am. **113**, 2742-2753 (2003).
16. F. K. Gruber, E. A. Marengo, and A. J. Devaney, "Time-reversal imaging with multiple signal classification considering multiple scattering between the targets," J. Acoust. Soc. Am. **115**, 3042-3047 (2004).
17. C. Prada, and J. Thomas, "Experimental subwavelength localization of scatterers by decomposition of the time reversal operator interpreted as a covariance matrix," J. Acoust. Soc. Amer. **114**, 235-243 (2003).
18. P. C. Hansen, "Analysis of discrete ill-posed problems by means of the *L*-curve," SIAM Rev. **34**, 561-580 (1992).

19. E. A. Marengo, F. K. Gruber, and F. Simonetti, "Time reversal MUSIC imaging of extended targets," IEEE Trans. Image Process. **16**, 1967-1984 (2007).

20. W. Cai, S. K. Gayen, M. Xu, M. Zevallos, M. Alrubaiee, M. Lax, and R. R. Alfano, "Optical tomographic image reconstruction from ultrafast time-sliced transmission measurements," Appl. Opt. **38**, 4237-4246 (1999).

21. A. Ishimaru, "Diffusion of a pulse in densely distributed scatterers," J. Opt. Soc. Am. **68**, 1045-1050 (1978).

22. K. Furutsu, "Diffusion equation derived from the space-time transport equation," J. Opt. Soc. Am. **70**, 360-366 (1980).

23. M. S. Patterson, B. Chance, and B. C. Wilson, "Time resolved reflectance and transmittance for the non-invasive measurement of tissue optical properties," Appl. Opt. **28**, 2331-2336 (1989).

24. S. Chandrasekhar, *Radiative Transfer* (Clarendon Press, Oxford, 1950).

25. A. Ishimaru, *Wave Propagation and Scattering in Random Media, Volume 1: Single Scattering and Transport Theory* (Academic, New York, 1978).

26. S. R. Arridge, and J. C. Schotland, "Optical tomography: forward and inverse problems," Inverse Probl. **25**, 123010 (2009).

27. S. R. Arridge, "Photon-measurement density functions. part I: analytical forms," Appl. Opt. **34**, 7395-7409 (1995).

28. M. Xu, M. Alrubaiee, S. K. Gayen, and R. R. Alfano, "Three-dimensional localization and optical imaging of objects in turbid media using independent component analysis," Appl. Opt. **44**, 1889-1897 (2005).

29. R. C. Haskell, L. O. Svaasand, T.-T. Tsay, T.-C. Feng, M. S. McAdams, and B. J. Tromberg, "Boundary conditions for the diffusion equation in radiative transfer," J. Opt. Soc. Am. A **11**, 2727-2741 (1994).

30. M. Lax, V. Nayaramamurti, and R. C. Fulton, "Classical diffusion photon transport in a slab," in *Laser Optics of Condensed Matter*, J. L. Birman, H. Z. Cummins, and A. A. Kaplyanskii, ed. (Plenum, NewYork, 1987), pp. 229-237.

31. C. Prada, S. Manneville, D. Spoliansky, and M. Fink, "Decomposition of the time reversal operator: detection and selective focusing on two scatterers," J. Acoust. Soc. Am. **99**, 2067-2076 (1996).

32. A. J. Devaney, "Time reversal imaging of obscured targets from multistatic data," IEEE Trans. Antenn. Propag. **53**, 1600-1610 (2005).

33. N. Bourbaki, *Topological Vector Spaces: Chapters 1-5* (Springer-Verlag, Berlin-Heidelberg-New York, 1987).

34. H. J. v. Staveren, C. J. M. Moes, J. v. Marle, S. A. Prahl, and M. J. C. v. Gemert, "Light scattering in Intralipid-10% in the wavelength range of 400--1100 nm," Appl. Opt. **31**, 4507-4514 (1991).

35. C. Bordier, C. Andraud, J. Lafait, E. Charron, M Anastasiadou, and A. de Martino, "Illustration of a bimodal system in Intralipid 20% by polarized light scattering: experiments and modelling," Appl. Phys. A **94**, 347-355 (2008).

36. I. Driver, J. W. Feather, P. R. King, and J. B. Dawson, "The optical properties of aqueous suspensions of Intralipid, a fat emulsion," Phys. Med. Biol. **34**, 1927-1930 (1989).

37. S. D. Konecky, G. Y. Panasyuk, K. Lee, V. Markel, A. G. Yodh, and J. C. Shotland, "Imaging complex structures with diffuse light," Opt. Express **16**, 5048-5060 (2008).

38. M. Xu, Y. Pu, and W. Wang, "Clean image synthesis and target numerical marching for optical imaging with backscattering light," Biomed. Opt. Express **2**, 850-857 (2011).

39. T. Nielsen, B. Brendel, R. Ziegler, M. van Beek, F. Uhlemann, C. Bontus, and T. Koehler, "Linear image reconstruction for a diffuse optical mammography system in a noncompressed geometry using scattering fluid," Appl. Opt. **48**, D1-D13 (2009).

40. Y. Ardeshirpour, N. Biswal, A. Aguirre, and Q. Zhu, "Artifact reduction method in ultrasound-guided diffuse optical tomography using exogenous contrast agents," J. Biomed. Opt. **16**, 046015 (2011).

41. B. W. Pogue, M. S. Patterson, H. Jiang, and K. D. Paulsen, "Initial assessment of a simple system for frequency domain diffuse optical tomography," Phys. Med. Biol. **40**, 1709-1729 (1995).

42. A. Poellinger, J. C. Martin, S. L. Ponder, T. Freund, B. Hamm, U. Bick, and F. Diekmann, "Near-infrared laser computed tomography of the breast: first clinical experience," Acad. Radiol. **15**, 1545-1553 (2008).

43. S. Hou, K. Solna, and H. Zhao, "Imaging of location and geometry for extended targets using the response matrix," J. Comput. Phys. **199**, 317-338 (2004).

44. F. K. Gruber, and E. Marengo, "Reinterpretation and enhancement of signal-subspace-based imaging methods for extended scatterers," SIAM J. Imaging Sciences **3**, 434-461 (2010).

Chapter 3

1. Binlin Wu, W. Cai, M. Alrubaiee, M. Xu, and S. K. Gayen, "Time reversal optical tomography: locating targets in a highly scattering turbid medium," Opt. Express **19**, 21956-21976 (2011).

2. A. J. Devaney, "Time reversal imaging of obscured targets from multistatic data," IEEE Trans. Antenn. Propag. **53**, 1600-1610 (2005).
3. M. Fink, D. Cassereau, A. Derode, C. Prada, P. Roux, M. Tanter, J. L. Thomas, and F. Wu, "Time-reversed acoustics," Rep. Prog. Phys. **63**, 1933-1995 (2000).
4. S. Hou, K. Solna, and H. Zhao, "A Direct Imaging Algorithm For Extended Targets," Inverse Probl. **22**, 1151-1178 (2006).
5. S. Hou, K. Solna and H. Zhao, "Imaging of location and geometry for extended targets using the response matrix," J. Comput. Phys. **199**, 317-338 (2004).
6. F. K. Gruber, and E. Marengo, "Reinterpretation and enhancement of signal-subspace-based imaging methods for extended scatterers," SIAM J. Imaging Sci. **3**, 434-461 (2010).
7. E. A. Marengo, F. K. Gruber, and F. Simonetti, "Time reversal MUSIC imaging of extended targets," IEEE Trans. Image Process. **16**, 1967-1984 (2007).
8. C. Ramananjaona, M. Lambert, D. Lesselier, and J.-P. Zolesio, "Shape reconstruction of buried obstacles by controlled evolution of a level set: from a min-max formulation to numerical experimentation," Inverse Prob. **17**, 1087-1111 (2001).
9. M. Burger, "A level set method for inverse problems," Inverse Prob. **17**, 1327-1355 (2001).
10. O. Dorn, and D. Lesselier, "Level set methods for inverse scattering," Inverse Problems **22**, R67-R131 (2006).
11. P. C. Hansen, "Analysis of discrete ill-posed problems by means of the L-curve," Soc. Ind. Appl. Math. Rev. **34**, 561-580 (1992).
12. S. K. Lehman, and A. J. Devaney, "Transmission mode time-reversal super-resolution imaging," J. Acoust. Soc. Am. **113**, 2742-2753 (2003).

13. A. N. Tikhonov, "Solution of incorrectly formulated problems and the regularization method," Soviet Math. Dokl. **4**, 1035-1038 (1963).

14. M. Xu, M. Alrubaiee, S. K. Gayen, and R. R. Alfano, "Three-dimensional localization and optical imaging of objects in turbid media with independent component analysis," Appl. Opt. **44**, 1889-1897 (2005).

15. S. J. Osher, and R. P. Fedkiw, *Level Set Methods and Dynamic Implicit Surfaces* (Springer-Verlag, New York, 2002).

Chapter 4

1. X. R. Cao, and R.-W. Liu, "General approach to blind source separation," IEEE Trans. Signal Process. **44**, 562-571 (1996).

2. J. F. Cardoso, "Blind signal separation: statistical principle," Proc IEEE **86**, 2009-2025 (1998).

3. A. Hyv ärinen, J. Karhunen, and E. Oja, *Independent Component Analysis* (Wiley, New York, 2001).

4. I. T. Jolliffe, *Principal Component Analysis* (Springer, New York, 1986).

5. D. D. Lee, and H. S. Seung, "Learning the parts of objects by non-negative matrix factorization," Nature **401**, 788-791 (1999).

6. M. W. Berry, M. Browne, A. N. Langville, V. P. Pauca, and R. J. Plemmons, "Algorithms and applications for approximate nonnegative matrix factorization," Comp. Stat. Data Anal. **52**, 155-173 (2007).

7. M. Xu, M. Alrubaiee, S. K. Gayen, and R. R. Alfano, "Optical imaging of turbid media using independent component analysis: theory and simulation," J. Biomed. Opt. **10**, 051705 (2005).

8. M. Xu, M. Alrubaiee, S. K. Gayen, and R. R. Alfano, "Three-dimensional localization and optical imaging of objects in turbid media with independent component analysis," Appl. Opt. **44**, 1889-1897 (2005).

9. M. Xu, M. Alrubaiee, S. K. Gayen, and R. R. Alfano, "Optical diffuse imaging of an *ex vivo* model cancerous human breast using independent component analysis," IEEE J. Select. Topics Quantum Electron. **14**, 43-49 (2008).

10. M. Alrubaiee, M. Xu, S. K. Gayen, M. Brito, and R. R. Alfano, "Three-dimensional optical tomographic imaging of scattering objects in tissue-simulating turbid media using independent component analysis," Appl. Phys. Lett. **87**, 191112 (2005).

11. M. Alrubaiee, M. Xu, S. K. Gayen, and R. R. Alfano, "Localization and cross section reconstruction of fluorescent targets in *ex vivo* breast tissue using independent component analysis," Appl. Phys. Lett. **89**, 133902 (2006).

12. D. L. Massart, B. G. M. Vandeginste, S. M. Deming, Y. Michotte, and L. Kaufman, *Chemometrics: A Textbook* (Elsevier, Amsterdam, 1988).

13. M. Turk, and A. Pentland, "Eigenfaces for recognition," J. Cogn. Neurosci. **3**, 71-86 (1991).

14. L. K. Hansen, J. Larsen, F. A. Nielsen, S. C. Strother, E. Rostrup, R. Savoy, N. Lange, J. Sidtis, C. Svarer, and O. B. Paulson, "Generalizable patterns in neuroimaging: how many principal components?," Neuroimage **9**, 534-544 (1999).

15. J.-P. Brunet, P. Tamayo, T. R. Golub, and J. P. Mesirov, "Metagenes and molecular pattern discovery using matrix factorization," Proc. Natl. Acad. Sci. **101**, 4164-4169 (2004).

16. V. P. Pauca, J. Piper, and R. J. Plemmons, "Nonnegative matrix factorization for spectral data analysis," Lin. Alg. Appl. **416**, 29-47 (2006).

17. A. Ishimaru, "Diffusion of a pulse in densely distributed scatterers," J. Opt. Soc. Am. **68**, 1045-1050 (1978).

18. K. Furutsu, "Diffusion equation derived from the space-time transport equation," J. Opt. Soc. Am. **70**, 360-366 (1980).

19. M. S. Patterson, B. Chance, and B. C. Wilson, "Time resolved reflectance and transmittance for the non-invasive measurement of tissue optical properties," Appl. Opt. **28**, 2331-2336 (1989).

20. S. Chandrasekhar, *Radiative Transfer* (Clarendon Press, Oxford, 1950).

21. A. Ishimaru, *Wave Propagation and Scattering in Random Media, Volume 1: Single Scattering and Transport Theory* (Academic, New York, 1978).

22. S. R. Arridge, and J. C. Schotland, "Optical tomography: forward and inverse problems," Inverse Probl. **25**, 123010 (2009).

23. S. R. Arridge, "Photon-measurement density functions. part I: analytical forms," Appl. Opt. **34**, 7395-7409 (1995).

24. P. C. Hansen, "Analysis of discrete ill-posed problems by means of the L-curve," Rev. **34**, 561-580 (1992).

25. P. Paatero, and U. Tapper, "Positive matrix factorization: a non-negative factor model with optimal utilization of error estimates of data values," Environmetrics **5**, 111–126 (1994).

26. P. Paatero, "The multilinear engine: a table-driven least squares program for solving multilinear problems, including the *n*-way parallel factor analysis model," J. Comp. Graph. Stat. **8**, 854–888 (1999).

27. http://cogsys.imm.dtu.dk/toolbox/.

28. A. N. Tikhonov, "Solution of incorrectly formulated problems and the regularization method," Soviet Math. Dokl. **4**, 1035-1038 (1963).

29. H. J. van Staveren, C. J. M. Moes, J. van Marle, S. A. Prahl, and M. J. C. van Gemert, "Light scattering in Intralipid-10% in the wavelength range of 400--1100 nm," Appl. Opt. **31**, 4507-4514 (1991).

30. C. Bordier, C. Andraud, J. Lafait, E. Charron, M. Anastasiadou, and A. de Martino, "Illustration of a bimodal system in Intralipid 20% by polarized light scattering: experiments and modelling," Appl. Phys. A **94**, 347-355 (2009).

31. T. Nielsen, B. Brendel, R. Ziegler, M. van Beek, F. Uhlemann, C. Bontus, and T. Koehler, "Linear image reconstruction for a diffuse optical mammography system in a noncompressed geometry using scattering fluid," Appl. Opt. **48**, D1-D13 (2009).

32. Y. Ardeshirpour, N. Biswal, A. Aguirre, and Q. Zhu, "Artifact reduction method in ultrasound-guided diffuse optical tomography using exogenous contrast agents," J. Biomed. Opt. **16**, 046015 (2011).

33. B. W. Pogue, M. S. Patterson, H. Jiang, and K. D. Paulsen, "Initial assessment of a simple system for frequency domain diffuse optical tomography," Phys. Med. Biol. **40**, 1709-1729 (1995).

34. A. Poellinger, J. C. Martin, S. L. Ponder, T. Freund, B. Hamm, U. Bick, and F. Diekmann, "Near-infrared laser computed tomography of the breast first clinical experience," Acad. Radiol. **15**, 1545–1553 (2008).

35. Binlin Wu, W. Cai, M. Alrubaiee, M. Xu, and S. K. Gayen, "Time reversal optical tomography: locating targets in a highly scattering turbid medium," Opt. Express **19**, 21956-21976 (2011).

36. T. Ristaniemi, and J. Joutsensalo, "Advanced ICA-based receivers for block fading DS-CDMA channels," Signal Processing **82**, 417-431 (2002).

37. M. Cutler, "Transillumination as an aid in the diagnosis of breast lesions," Surg. Gynecol. Obstet. **48**, 721–729 (1929).

38. R. Choe, A. Corlu, K. Lee, T. Durduran, S. D. Konecky, M. Grosicka-Koptyra, S. R. Arridge, B. J. Czerniecki, D. L. Fraker, A. DeMichele, B. Chance, M. A. Rosen, and A. G. Yodh, "Diffuse optical tomography of breast cancer during neoadjuvant chemotherapy: a case study with comparison to MRI," Med. Phys. **32**, 1128-1139 (2005).

39. A. Pifferi, P. Taroni, A. Torricelli, F. Messina, R. Cubeddu and G. Danesini, "Four-wavelength time-resolved optical mammography in the 680–980-nm range," Opt. Lett. **28**, 1138-1140 (2003).

40. B. J. Tromberg, B. W. Pogue, K. D. Paulsen, A. G. Yodh, D. A. Boas, and A. E. Cerussi, "Assessing the future of diffuse optical imaging technologies for breast cancer management," Med. Phys. **35**, 2443-2451 (2008).

Chapter 5

1. W. Cai, M. Alrubaiee, S. K. Gayen, M. Xu, and R. R. Alfano, "Three-dimensional optical tomography of objects in turbid media using the round-trip matrix," Proc. SPIE **5693**, 4-9 (2005).

2. B. Wu, M. Alrubaiee, W. Cai, M. Xu, and S. K. Gayen, "Optical imaging of objects in turbid media using principal component analysis and time reversal matrix methods," in *Computational Optical Sensing and Imaging, OSA Technical Digest (CD) (Optical Society of America, 2009), paper JTuC10*(San Jose, California, 2009).

3. B. Wu, W. Cai, M. Alrubaiee, M. Xu, and S. K. Gayen, "Three dimensional time reversal optical tomography," Proc. SPIE **7892**, 78920G (2011).
4. B. Wu, W. Cai, M. Alrubaiee, M. Xu, and S. K. Gayen, "Time reversal optical tomography: locating targets in a highly scattering turbid medium," Opt. Express **19**, 21956-21976 (2011).
5. B. Wu, M. Xu, W. Cai, and S. K. Gayen, "Time-reversal optical tomography: detecting and locating extended targets in a turbid medium," Proc. SPIE **8216**, 82160K (2012).
6. B. Wu, M. Alrubaiee, W. Cai, M. Xu, and S. K. Gayen, "Diffuse optical imaging using decomposition methods," Int. J. Opt. **2012**, 185435 (2012).
7. M. Xu, M. Alrubaiee, S. K. Gayen, and R. R. Alfano, "Optical imaging of turbid media using independent component analysis: theory and simulation," J. Biomed. Opt. **10**, 051705 (2005).
8. M. Xu, M. Alrubaiee, S. K. Gayen, and R. R. Alfano, "Three-dimensional localization and optical imaging of objects in turbid media using independent component analysis," Appl. Opt. **44**, 1889-1897 (2005).
9. M. Xu, M. Alrubaiee, S. K. Gayen, and R. R. Alfano, "Optical diffuse imaging of an *ex vivo* model cancerous human breast using independent component analysis," IEEE J. Sel. Top. Quantum Electron. **14**, 43-49 (2008).
10. P. C. Hansen, "Analysis of discrete ill-posed problems by means of the L-curve," SIAM Rev. **34**, 561-580 (1992).
11. W. Cai, S. K. Gayen, M. Xu, M. Zevallos, M. Alrubaiee, M. Lax, and R. R. Alfano, "Optical tomographic image reconstruction from ultrafast time-sliced transmission measurements," Appl. Opt. **38**, 4237-4246 (1999).
12. E. A. Marengo, F. K. Gruber, and F. Simonetti, "Time reversal MUSIC imaging of extended targets," IEEE Trans. Image Process. **16**, 1967-1984 (2007).

13. S. R. Arridge, "Optical tomography in medical imaging," Inverse Probl. **15**, R41-R93 (1999).
14. S. R. Arridge, and W. R. B. Lionheart, "Non-uniqueness in diffusion-based optical tomography," Opt.Lett. **23**, 882-884 (1998).

Chapter 6

1. B. P. Joshi, and T. D. Wang, "Exogenous molecular probes for targeted imaging in cancer: focus on multi-modal imaging," Cancers **2**, 1251-1287 (2010).
2. S. Luo, E. Zhang, Y. Su, T. Cheng, and C. Shi, "A review of NIR dyes in cancer targeting and imaging," Biomaterials **32**, 7127 -7138 (2011).
3. X. He, K. Wang, and Z. Cheng, "In vivo near-infrared fluorescence imaging of cancer with nanoparticle-based probes," WIREs Nanomed. Nanobiotechnol. **2**, 349–366 (2010).
4. S. Tyagi, S. A. E. Marras, and F. R. Kramer, "Wavelength-shifting molecular beacons," Nat. Biotechnol. **18**, 1191-1196 (2000).
5. E. E. Graves, J. Ripoll, R. Weissleder, and V. Ntziachristos, "A submillimeter resolution fluorescence molecular imaging system for small animal imaging," Med. Phys. **30**, 901 (2003).
6. A. Corlu, R. Choe, T. Durduran, M. A. Rosen, M. Schweiger, S. R. Arridge, M. D. Schnall, and A. G. Yodh, "Three-dimensional in vivo fluorescence diffuse optical tomography of breast cancer in humans," Opt. Express **15**, 6696-6716 (2007).
7. S. Bloch, F. Lesage, L. McIntosh, A. Gandjbakhche, K. Liang, and S. Achilefu, "Whole-body fluorescence lifetime imaging of a tumor-targeted near infrared molecular probe in mice," J. Biomed. Opt. **10**, 054003 (2005).
8. A. Godavarty, M. J. Eppstein, C. Zhang, S. Theru, A. B. Thompson, M. Gurfinkel, and E. M. Sevick-Muraca, "Fluorescence-enhanced optical imaging in large tissue volumes using a gain-modulated ICCD camera," Phys. Med. Biol. **48**, 1701-1720 (2003).

9. I. Gannot, A. Garashi, V. Chernomordik, and A. Gandjbachkhe, "Quantitative optical imaging of the pharmacokinetics of fluorescent-specific antibodies to tumor markers through tissuelike turbid media," Opt. Lett. **29**, 742-744 (2004).

10. M. Alrubaiee, M. Xu, S. K. Gayen, and R. R. Alfano, "Localization and cross section reconstruction of fluorescent targets in *ex vivo* breast tissue using independent component analysis," Appl. Phys. Lett. **89**, 133902 (2006).

11. A. Liebert, H. Wabnitz, J. Steinbrink, M. Moller, R. Macdonald, H. Rinneberg, A. Villringer, and H. Obrig, "Bed-side assessment of cerebral perfusion in stroke patients based on optical monitoring of a dye-bolus by time-resolved diffuse reflectance," Neuroimage **24**, 426-435 (2005).

12. A. D. Klose, and A. H. Hielscher, "Fluorescence tomography with simulated data based on the equation of radiative transfer," Opt. Lett. **28**, 1019–1021 (2003).

13. J. Wu, L. Perelman, R. R. Dasari, and M. S. Feld, "Fluorescence tomographic imaging in turbid media using early-arriving photons and Laplace transforms," Proc. Natl. Acad. Sci. USA **94**, 8783–8788 (1997).

14. B. Wu, W. Cai, M. Alrubaiee, M. Xu, and S. K. Gayen, "Time reversal optical tomography: locating targets in a highly scattering turbid medium," Opt. Express **19**, 21956-21976 (2011).

15. M. Fink, D. Cassereau, A. Derode, C. Prada, P. Roux, M. Tanter, J.-L. Thomas, and F. Wu, "Time-reversed acoustics," Rep. Prog. Phys. **63**, 1933-1995 (2000).

16. A. J. Devaney, "Time reversal imaging of obscured targets from multistatic data," IEEE Trans. Antenn. Propag. **53**, 1600-1610 (2005).

17. D. D. Lee, and H. S. Seung, "Learning the parts of objects by non-negative matrix factorization," Nature **401**, 788-791 (1999).

18. J.-F. Cardoso, "Blind signal separation: statistical principles," Proc. IEEE **86**, 2009-2025 (1998).

19. B. Wu, M. Alrubaiee, W. Cai, M. Xu, and S. K. Gayen, "Diffuse optical imaging using decomposition methods," Int. J. Opt. **2012**, 185435 (2012).

20. M. S. Patterson, and B. W. Pogue, "Mathematical model for time-resolved and frequency-domain fluorescence spectroscopy in biological tissues," Appl. Opt. **33**, 1963-1974 (1994).

21. A. B. Milstein, S. Oh, K. J. Webb, C. A. Bouman, Q. Zhang, D. A. Boas, and R. P. Millane, "Fluorescence optical diffusion tomography," Appl. Opt. **42**, 3081-3094 (2003).

22. P. C. Hansen, "Analysis of discrete ill-posed problems by means of the *L*-curve," SIAM Rev. **34**, 561-580 (1992).

23. M. Xu, M. Alrubaiee, S. K. Gayen, and R. R. Alfano, "Three-dimensional localization and optical imaging of objects in turbid media with independent component analysis," Appl. Opt. **44**, 1889-1897 (2005).

24. P. Paatero, "The multilinear engine: a table-driven least squares program for solving multilinear problems, including the n-way parallel factor analysis model," J. Comp. Graph. Stat. **8**, 854-888 (1999).

25. P. Paatero, and U. Tapper, "Positive matrix factorization: a non-negative factor model with optimal utilization of error estimates of data values," Environmetrics **5**, 111-126 (1994).

26. http://cogsys.imm.dtu.dk/toolbox/nmf/.

27. M. Lax, V. Narayanamurti, and R. C. Fulton, "Classical diffusion photon transport in a slab," in *Laser Optics of Condensed Matter*, J. L. Birman, H. Z. Cummins, and A. A. Kaplyanskii, eds. (Plenum, New York, 1987), pp. 229-237.

28. H. J. v. Staveren, C. J. M. Moes, J. v. Marle, S. A. Prahl, and M. J. C. v. Gemert, "Light scattering in Intralipid-10% in the wavelength range of 400--1100 nm," Appl. Opt. **31**, 4507-4514 (1991).

29. M. L. J. Landsman, G. Kwant, G. A. Mook, and W. G. Zijlstra, "Light- absorbing properties, stability, and spectral stabilization of indocyanine green," J. Appl. Physiol. **40**, 575-583 (1976).

30. J. T. Alander, I. Kaartinen, A. Laakso, T. Pätilä, T. Spillmann, V. V. Tuchin, M. Venermo, and P. Välisuo, "A review of indocyanine green fluorescent imaging in surgery," Int. J. Biomed. Opt. **2012**, 940585 (2012).

31. R. C. Benson, and H. A. Kues, "Fluorescence properties of indocyanine green as related to angiography," Phys. Med. Biol. **23**, 159-163 (1978).

32. B. Yuan, and Q. Zhu, "Emission and absorption properties of indocyanine green in Intralipid solution," J Biomed Opt. **9**, 497-503 (2004).

33. E. M. Sevick-Muraca, G. Lopez, J. S. Reynolds, T. L. Troy, and C. L. Hutchinson, "Fluorescence and absorption contrast mechanisms for biomedical optical imaging using frequency-domain techniques," Photochem. Photobiol. **66**, 55-64 (1997).

34. V. Ntziachristos, and R. Weissleder, "Experimental three-dimensional fluorescence reconstruction of diffuse media by use of a normalized Born approximation," Opt. Lett. **26**, 893-895 (2001).

35. D. S. Kepshire, S. C. Davis, H. Dehghani, K. D. Paulsen, and B. W. Pogue, "Subsurface diffuse optical tomography can localize absorber and fluorescent objects but recovered image sensitivity is nonlinear with depth," Appl. Opt. **46**, 1669-1678 (2007).

36. S. D. Konecky, G. Y. Panasyuk, K. Lee, V. Markel, A. G. Yodh, and J. C. Schotland, "Imaging complex structures with diffuse light," Opt. Express **7**, 5048-5060 (2008).

37. A. N. Tikhonov, "Solution of incorrectly formulated problems and the regularization method," Soviet Math. Dokl. **4**, 1035-1038 (1963).

38. M. Xu, Y. Pu, and W. Wang, "Clean image synthesis and target numerical marching for optical imaging with backscattering light," Biomed. Opt. Express **2**, 850-857 (2011).

39. J. Lee, and E. M. Sevick-Muraca, "Three-dimensional fluorescence enhanced optical tomography using referenced frequency domain photon migration measurements at emission and excitation wavelengths," J. Opt. Soc. Am. A **19**, 759-771 (2002).